Nanoengineered polymer architectures for antimicrobial medical applications: Novel additives

Mark A. Isaacs

Submitted for the Degree of Doctor of Philosophy

Cardiff University

Department of Chemistry

June 2014

Abstract

Silver is a clinically important, broad spectrum antibacterial, whose use extends back over several millennia. Its potent antibacterial activity, range of susceptible microorganisms, and lack of developed resistances, elevate silver as an exciting weapon in the fight against hospital acquired infections and so-called 'superbugs'. The active, ionic form is efficacious at very low concentrations, thus controlling release rates offers potential durable, non-specific, antibacterial medical devices. This thesis examines a number of inorganic systems as potential slow-release, antibacterial silver nanocomposites for incorporation into polyurethane foam wound dressings.

A range of silver core-silica shell nanocomposites were synthesised with tuneable dimensions, with porosity introduced into the silica shells, via base-etching or surfactant-templating producing disordered or ordered architectures respectively. An alternative system based on mesoporous SBA-15 silica was also investigated, which was employed as a scaffold for subsequent multilayer titania functionalisation, onto which mixed silver/silver carbonate nanoparticles were subsequently deposited.

Detailed characterisation allowed fundamental structural-function relationships for silver dissolution kinetics and their associated impact upon antibacterial activity towards Gram-positive and Gram-negative bacteria including methicillin-resistant *Staphylococcus aureus*. Silver ion release rates are inversely proportional to silver crystallite size, with further governance via shell thickness and mesoporosity achievable in core shell systems. The intrinsic antibacterial activity of titania coated SBA-15 further enhances performance, independent of silver, whilst support macropore introduction increases silver particle dispersion. Antibacterial prowess of all materials demonstrates a strong activity correlation with dissolution kinetics, evidencing up to seven-fold logarithmic reductions in the bacterial concentrations within four hours. Materials were potent for > 24 hours, with the reverse micelle core-shell formulation showing continuous activity over a 14 day period. Comparative benchmarking indicates mesoporous silver core-silica shell architectures as promising candidates due to antibacterial longevity, manufacturing simplicity and cost, with their hydrophilic nature and small dimensions rendering them amenable to incorporation into compatible polyurethane foams.

Table of Contents

Acknowledgments

I would like to thank, first and foremost, my supervisors, Prof. Karen Wilson and Prof. Adam Lee, for all their help and kindness to and, most importantly, patience with, me over the course of my studies. I would like to thank Polymer Health Technology and the KESS scholarship for funding my PhD and the University of Cardiff for allowing me to carry out my postgraduate studies there. Thank you to all the group members with whom I have worked, in particular Dr. Chris Parlett, for your help and friendship.

I would like to thank all those involved with Polymer Health Technology, for the funding, and for making my time working within the company an enjoyable experience. In particular, Mr. Nick Woodman, for his input and time throughout my PhD.

I would also like to thank Prof. Anthony Hilton and Dr. Tony Worthington at Aston University for use of their microbiology labs, as well as Dr. Preena Mistry for all of the great help she gave me (best of luck to Villa next season).

I would also like to thank some colleagues from Cardiff, Drs. Ian Fallis and Nancy Dervisi for my master project, which ultimately inspired me to want to pursue research, Dr. Ian Morgan for his words of, uh, encouragement, and Post-Pre Dr. Steve Hughes and Pre-Dr. Owen Bonello for their company throughout my PhD.

Thanks to Puppy, Leanne and Jamie for their friendship throughout, it really helped. Thanks to Seb and Darv, as well as a big thanks to Bill and Kelly, for your friendship, and for making me the godfather to the adorable Jackson. I hope to see you all a lot more soon.

I would also like to thank Mr. Grimes and Mr. Rimmer for peaking my interest in the physical sciences during my school days, you guys were awesome teachers.

The biggest thanks goes to my family, without whom this would have all been impossible. Mum and Dad, you have been absolutely amazing to me, and always encouraged me to do whatever I want (which luckily turned out to be something positive!). But also to my nan Joy, aunty Katy (banned from chemistry class), uncle Phil and my cousin Lizzie, I love you all very much.

Finally, I want to thank Scoob. You have no idea how much you helped me. Bibbidyboppidy. X

DECLARATION

This work has not been submitted in substance for any other degree or award at this or any other university or place of learning, nor is being submitted concurrently in candidature for any degree or other award.

Signed Mark Isaacs…… (candidate) Date 01/12/2014……

STATEMENT 1

This thesis is being submitted in partial fulfillment of the requirements for the degree of PhD

Signed Mark Isaacs…… (candidate) Date 01/12/2014……

STATEMENT 2

This thesis is the result of my own independent work/investigation, except where otherwise stated.
Other sources are acknowledged by explicit references. The views expressed are my own.

Signed Mark Isaacs…… (candidate) Date 01/12/2014……

STATEMENT 3

I hereby give consent for my thesis, if accepted, to be available for photocopying and for inter-library loan, and for the title and summary to be made available to outside organisations.

Signed Mark Isaacs…… (candidate) Date 01/12/2014……

STATEMENT 4: PREVIOUSLY APPROVED BAR ON ACCESS

I hereby give consent for my thesis, if accepted, to be available for photocopying and for inter-library loans **after expiry of a bar on access previously approved by the Academic Standards & Quality Committee.**

Signed Mark Isaacs…… (candidate) Date 01/12/2014……

For

Irene, John

and Barbera

Chapter 1: Introduction

1. Introduction

1.1. Hospital acquired infections

Hospital acquired infections (HAIs), or alternately healthcare associated infections, is a term given to illnesses which arise in a patient as a direct result of a hospital stay. The spread of drug-resistant bacteria is a growing threat, attributed to around 150000 deaths per year in Europe,[1] an estimated 100000 per year in the USA and at any one time, over 1.4 million worldwide people are suffering from a hospital acquired infection.[1] With a large variety of drug-resistant bacteria, such as methicillin-resistant Staphylococcus Aureus (MRSA) and multi-drug-resistant tuberculosis (MDR-TB), a broad spectrum antibiotic is an ideal candidate for use in the fight against hospital acquired infections.

Approximately one third of all HAIs are preventable[2] and while in recent times standards in cleanliness in hospitals has significantly reduced the number of HAIs per year, the number of patients suffering from these infections remains as large as 6% of all administered patients in England.[3] As of December 2013, rates of infection of MRSA, MSSA (methicillin-susceptible *Staphylococcus aureus*) and *Escherichia coli* remain stable across English hospitals for the past 2 years and only *Clostridium difficile* rates have diminished.[4] The overall rate in HAI's has reduced due to guidelines developed on evidence from various hospitals, beginning in 2001.[5] These encourage standard principles for preventing HAI's, which include hospital environmental hygiene, hand hygiene, the use of personal protective equipment, and the safe use and disposal of sharps; preventing infections associated with the use of short-term indwelling urethral catheters; and preventing infections associated with central venous catheters.[6]

1.1.1. History of antibiotic resistance in bacterium

The penicillin family of compounds (**Figure 1.1**) was famously discovered by Sir Alexander Fleming in 1928 when he demonstrated that the fungi *Penicillum rubens* could be used to produce a substance which exhibited antibacterial effects.[7] Along with

its younger derivatives, it is classified as a β-lactam antibiotic, named after the β-lactam ring in its structure.

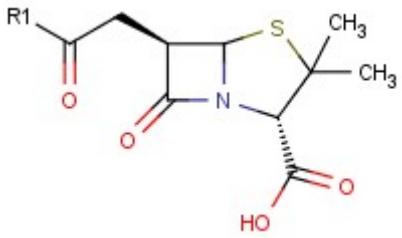

Figure 1.1: General structure of penicillin family of compounds.

The β-lactam group of broad-spectrum antibiotics (**Figure 1.2**) include penicillins, cephalosporins and related compounds. As a group, these drugs are active against many gram-positive, gram-negative and anaerobic organisms. These antibiotics exert their effect by interfering with the structural crosslinking of peptidoglycans in bacterial cell walls through binding of the β-lactam ring with the enzyme DD-transpeptidase.[8]

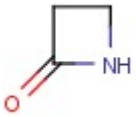

Figure 1.2: β-lactam ring, the active site in β-lactam antibiotics.

The spread of MRSA was initially not seen as a realistic threat, with the common view being that the particular strain was not as pathogenic as an abundant strain which was prevalent at the time, that of MSSA.[9] Opinion was that the replacement of MSSA with MRSA was also as inevitable as the initial spread of MSSA.[10] MRSA is now known to have a higher morbidity and mortality rate than MSSA (approximately double) making MRSA is one of the most significant antibiotic-resistant hospital acquired pathogen to have developed[11] and combined with its ability to evolve further makes it a real threat.[12] It is also worth noting that MRSA is not merely a replacement for MSSA, but an additional burden of staphylococcal infections.[13] Worse still, new strains are beginning to emerge into the community which are spreading widely and are more virulent than hospital acquired MRSA.[14]

1.1.2. Treatment and prevention

Hospital staff have been aware of the dangers of HAIs since the 1960s, following a staphylococcal pandemic, which began a search for greater control and prevention of harmful pathogenic infections in the intensive care environment.[15] The pandemic was caused by penicillin resistant microorganisms, and although quelled with the introduction of methicillin, began an age of developing techniques to prevent such infections, and this lead to the hospitals taking responsibility for the prevention of HAIs.[16]

It was not only staphylococcal strains which were causing widespread infections in hospitals, Gram negative bacteria such as *Escherichia*, *Klebsiella*, *Proteus* and *Pseudomonas* which possess very limited pathogenic abilities in a healthy host, were found to be thriving in hospital environments in the 1960s. With increased resistance to antibiotics and disinfectants, plus their ability to survive and multiply rapidly in inhospitable environments, they rapidly became very problematic organisms for the healthcare industry and patient wellbeing.[17]

In 1987, the first International Conference of the Hospital Infection Society was held, in which the opening address noted that not only are pathogens continuing to develop new resistances to more and more antibiotics and disinfectants, but that also, with medical progress advancing to tackle more complex problems, the barriers to infection are reducing. This is an important note, as it highlights the need to tackle the problem from two fronts; the need to develop new materials to kill harmful microorganisms, plus the need to develop practical techniques, to protect susceptible infection sites from possibly harmful pathogens. Nowadays, many professional bodies have strict guidelines to strive towards protecting patients from infections, such as the Royal College of Nursing, which includes activities such as strenuous hand sanitising and isolation of patients suspected of infection.

1.2. Microbiology

1.2.1. Bacterial cell structure

A typical bacterium is pictured in **Figure 1.3**, including its cell components.

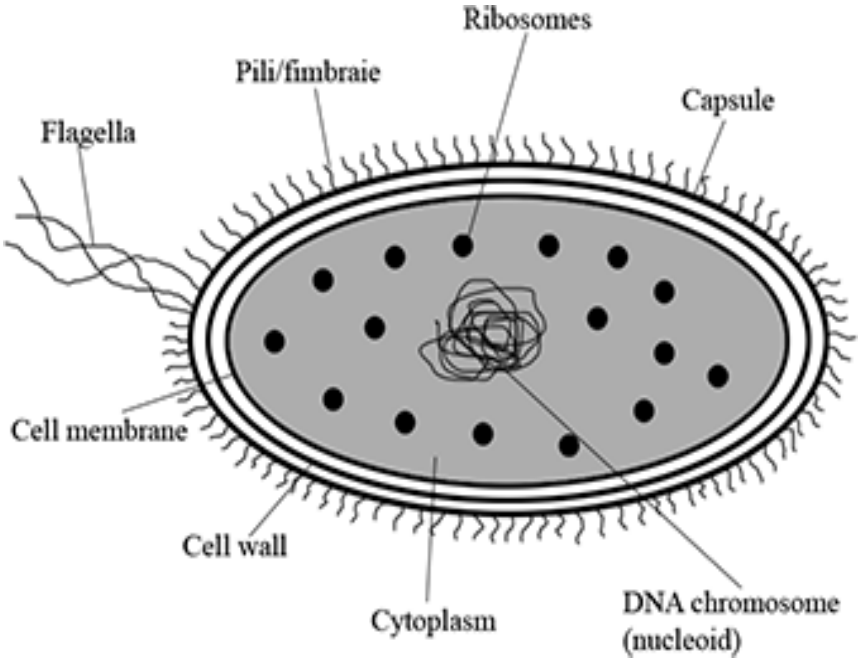

Figure 1.3: Schematic of a bacterium.

Surrounding the cell, is the cell wall, which can be split into two distinct types, to be covered in an upcoming section. The cell wall serves to protect the cell from external and internal osmotic forces, to maintain the shape of the cell and regulate the penetration and escape of macromolecules into and out of the cell.[18] The capsule encases the wall, and is responsible for the prevention of desiccation of the cell and the release of harmful toxins and bacterial viruses for the purpose of infecting nearby organisms.[19] On the outside of that, lie the pili/fimbriae, which are the components of the cell responsible for adhesion onto surfaces and the formation of biofilms, as well as allowing DNA transfer in certain strains of bacteria (e.g. *Escherichia coli*) during the process of bacterial conjugation.[20] Flagella are responsible for cell transport function.[21] Within this outer layer, the cell membrane separates the cell interior with the wall, and is responsible for the permeation of ions and molecules in and out of the cell.[22] The internal section of the cell is comprised of the DNA chromosome, which contains the

genetic material of the bacteria,[23] ribosomes, which are responsible for protein synthesis,[24] whilst the cytoplasm is the collective term for these internal sub structures (known as organelles) and the cytosol (gel-like substance) which encases the organelles, is comprised of water, salts and organic material and accounts for approximately 70% of the cytoplasm.[25]

1.2.2. Bacterial classification

Bacteria are classified according to many factors and organisms are grouped together based on similarities, such as cell structure, cell metabolism or on differences in cell components. They are typically between 0.5 - 5μm in length and can take a variety of forms. Common morphologies for bacteria to take include spheres (cocci), rods (bacilli), spirals (spirella) and comma-shapes (vibrio). Further to this, the grouping of the bacteria can be described by a variety of prefixes, including diplo (groups of two), strepto (chains) and staphylo (grape-like clusters). Further to this, there are two more important groups in which to divide bacteria; Gram-positive and Gram-negative bacteria.

1.2.3. Gram positive and Gram negative

In 1884, Hans Christian Gram was developing a method to stain bacteria to make them more visible whilst examining lung tissue from patients who had died from pneumonia.[26] During this process he actually developed a method to differentiate between the *Klebsiella pneumonia* and *Streptococcus pneumonia* bacteria present, a method which is still in use today. The method he discovered was to become known as the Gram-stain and involves staining a slide of bacteria with purple crystal violet solution, removing the excess and adding iodine (which fixes the crystal violet to the cell), adding alcohol or acetone and counterstaining with safranin.

Crystal violet dissociates into CV^+ and Cl^- in aqueous solutions and these ions penetrate the cell walls of both Gram-positive and Gram-negative bacteria. The CV^+ ion reacts with negatively charged components of the cell wall and the addition of iodine forms CV-I complexes and subsequently fixes the purple colour to the cell. A Gram-negative cell will lose its outer lipopolysaccharide membrane during an acetone

or alcohol wash, removing the colour from the cell revealing a thin peptidoglycan layer, which can be stained pink by the counter stain. This leaves the purple stain remains in the Gram-positive bacteria and a pink stain in the Gram-negative, allowing for differentiation (**Figure 1.4**).

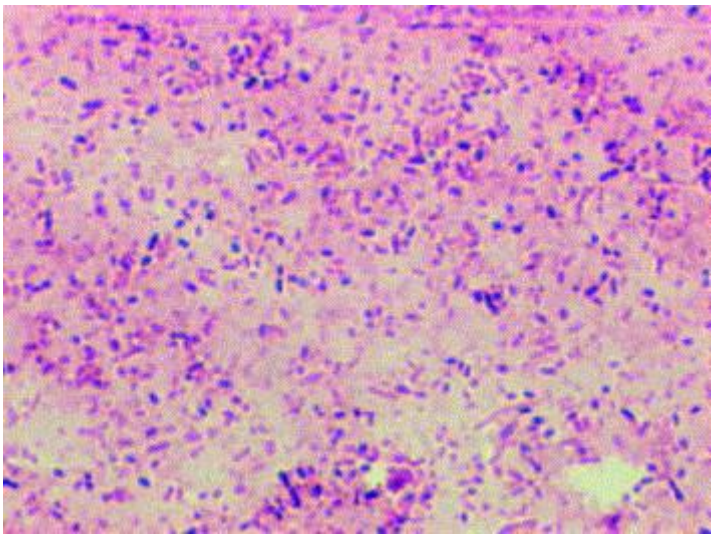

Figure 1.4: Gram staining of a mixture of Gram positive and Gram-negative bacteria.[27]

The difference in the cell wall structures are shown in **Figure 1.5**.

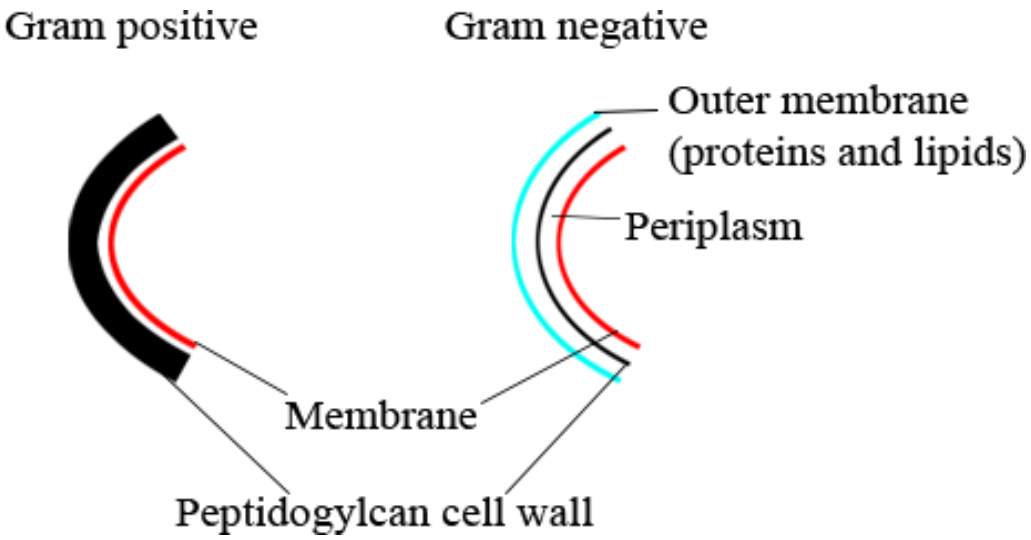

Figure 1.5: Cell wall structures of Gram-positive and Gram-negative bacteria.[28]

Gram-positive bacteria have a thick cell wall made of peptidoglycan, linear chains of N-acetyl glucosamine (NAG) and N-acetyl muramic acid (NAM) which makes up at least 40% of the mass of the cell wall and is responsible for the shape of the bacterium. These are accompanied by one or more non-peptidoglycan polymers, such as teichoic acids or teichuronic acids.[18] These thick cell walls (20-50 nm) stain purple during the Gram-stain test, whilst the Gram-negative bacteria have a thin peptidoglycan layer (around 10% of the cell wall), which stains pink. The other features of the Gram-negative cell wall are the protein and lipid based outer membrane and the periplasmic space between it and the cell wall.

In this work, the bacteria were chosen as representatives for Gram-positive and Gram-negative strains, both of which are commonly attributed to HAIs. *Pseudomonas aeruginosa* is a Gram-negative, aerobic bacterium with a semi-spherical, semi-rod-like which resides commonly in soil, skin flora and water. It is commonly found on medical equipment such as catheters, due to its tendency towards moist environments, which can result in the spread of HAIs. *Staphylococcus aureus* is a spherical, facultatively anaerobic Gram-positive bacterium which is commonly found on the skin and nasal passages.

1.3. Silver as an antimicrobial

1.3.1. History of silver as an antibacterial agent

Silver is a well-known broad spectrum antibiotic, effective against Gram-positive (e.g. MRSA, B.Subtilis) and Gram-negative bacteria (e.g. E. Coli, P.Aeruginosa).[29]

Silver has been known to exhibit antibacterial properties for a very long time, dating back to the ancient Greeks and Phoenicians,[30] who used silver pots to keep water fresh thanks to its broad antibacterial activity. Silver is used the world over, in Central America, it is painted onto village water filters, in Japan, it is applied to washing machines, deodorant and toilet seats amongst others, elsewhere, wound care products such as SilverIon (Argentum Products), Actisorb Silver (Johnson and Johnson),

Acticoat (Smith and Nephew) and Tegaderm (3M) and many more.[31] The history of silver as a medical application dates back to the 18th century, at which time it was used to treat ulcers, later in 1880, a paper was published on treating newborns with silver nitrate to prevent blindness caused by infections of Gonorrhoea in mothers.[30] After the discovery of penicillin in the 1940s, the use of silver as an antimicrobial diminished, however it made a comeback in the 1960's as 0.5% silver nitrate solution was used to treat burns.[32, 33] In 1968, Charles Fox combined silver nitrate with a sulphonamide antibiotic, to create a more broad spectrum antibiotic, the result was silver sulfadiazine and was the standard for burns treatment for a long time.[34-36] It has also been combined with polyurethane dressings in the past, creating an effective combination.[37] Silver sulfadiazine is now not recommended after a Cochrane review found it to increase healing times.[38] As well as many wound dressings and wound management systems incorporating some level of silver, it is also being incorporated into other systems susceptible to bactericidal attack, for example, catheters.[31] Silver also has the ability to kill virus's such as Herpes simplex 1 and the HIV virus.[39] Alongside this broad spectrum antimicrobial activity, silver is known to have a remarkably low toxicity to human cells.[40]

1.3.2. Silver nanoparticles as antimicrobial agents

Silver nanoparticles exhibit a high degree of cytotoxicity towards a broad range of microorganisms, and as such, are of particular interest in the field of antimicrobial research.[41-50] An advantage of silver in the form of nanoparticles is the slow release rate of ionic, biologically active silver species, which can be used to develop a material with a long lifetime of action against bacteria.[51, 52]

Silver nanoparticle formation is commonly achieved using chemical methods, thermal treatments and photolytic processes. Using a chemical method, Ag nanoparticles can be produced using a combination of a reducing agent and silver precursor in the presence of a stabilising agent or surfactant. Reducing protocols range from strong treatments with reagents such as sodium borohydride[53-57] and hydrazine[58-60] to milder, organic reducing agents, such as glucose,[61] ethylene glycol[62] and formaldehyde.[47, 63, 64] Stablizers and capping agents such as polyvinyl pyrollidone,

polyvinyl acetone and gelatin can be used to prevent the silver nanoparticles from agglomerating into large crystallites during synthesis.[65]

Using thermal treatments, silver nanoparticles can be prepared in a similar manner to many other metal nanoparticles, although this usually results in more monodispersity amongst prepared nanocomposites.[66] There has been suggestion that tuning of the pore size in the ordered oxide structure can be utilised to control resultant silver particle size.[67] Surface modifiers have also been used to further retard the size growth of resultant particles, by using amine groups as a stronger tether to the oxide surface, silver particles of greater monodispersity and smaller size range have been prepared (~ 2.5 nm).[68]

1.3.3. Mechanism of action

The mechanism of action of silver as an antimicrobial agent is the subject of some debate, and is thought to be a complex and broad one, with popular opinion weighted towards silver(I) ions being the active species.[69] The mechanism attributed to this action is denoted the oligodynamic effect, discovered in 1893 by Swiss botanist Karl Willhelm von Nägeli[70] and is described as the toxic effect of metal ions on living cells, algae, molds, spores, fungi, viruses, prokaryotic and eukaryotic microorganisms, even in relatively low concentrations. This effect is common in many metal ions, including mercury, copper, silver, gold and iron, to varying degrees.

The oligodynamic effect describes the ability of these metals to exhibit bacteriostatic or bacteriocidal activity, silver is thought to do this in its ionic form by interacting with the thiol groups of certain vital enzymes and inactivating them.[53] Silver ions have also been suggested to disrupt the ability of DNA to replicate, leading again to cell death. Further studies have reported the build-up of silver-sulfur, electron rich granules within the membrane and cell wall, resulting in structural changes.[71]

The motivation for continued current research interests into silver nanoparticles as antimicrobial agents mirrors that for nanoparticles in general, with their small size altering their physical properties, allowing for new and unique materials. Much of the success of silver nanoparticles in this field has been attributed to electronic effects, which are the result of the changes in the local electronic structure of the surfaces of the

smaller-sized particles. It is suggested that these effects contribute to the enhancement of the reactivity of the silver-nanoparticle surfaces, leading to improved dissolution kinetics and release of antimicrobial Ag^+ species.[72] Silver nanoparticles exhibit antimicrobial activity by releasing soluble ionic silver species into solution, effectively acting as drug delivery systems.[73] Complimentary to this, however, silver nanoparticles can produce reactive oxygen species, which exhibit additional antimicrobial effects, dependent on the nanoparticle diameter, and hence total available surface area.[74] This occurs via the oxidative dissolution process from which silver ions are released by silver nanoparticles into solution outlined in **figure 1.6**, hence both ROS generation and Ag ion dissolution are surface area dependent.

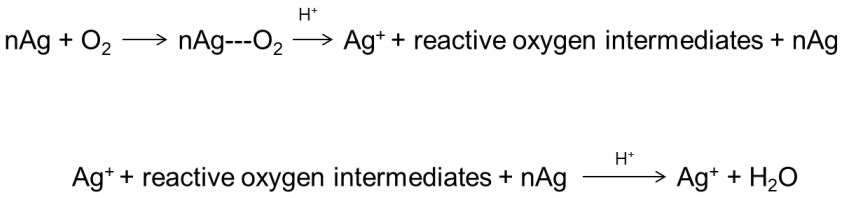

Figure 1.6: Oxidative release of silver ions from nanocrystalline silver particles.[75]

1.3.4. Silver in the wound care industry

Silver has been used in wound care products for some time now, with companies including Smith and Nephew and Johnson and Johnson producing silver containing products. Nanocrystalline materials have been of growing interest in this field, due to an intrinsic ability to overcome the limitations of existing silver based antimicrobial additives, such as silver nitrate and silver sulfadiazine, in fast silver dissolution rates resulting in fast inactivation of the active species, as well as the formation of a pseudo-eschar (a build-up of dead tissue).[54, 76, 77] Silver in its nanocrystalline form has been found to be not only an effective antimicrobial treatment, but also to decrease healing time and decrease inflammation.[78]

The form of silver differs between products, in Smith and Nephews Acticoat 7, the silver is in a high loading nanocrystalline form, whereas in Reliamed's Silver Alginate dressings, it is in an ionic form and lower loading (silver alginate, **Figure 1.67**).

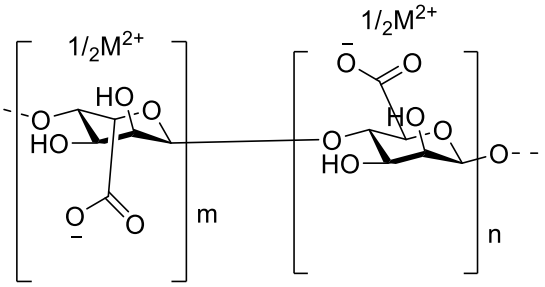

Figure 1.7: Metal alginate structure, cations are shared between layers of polymer.

The weight percentage of silver in these products varies from 0.5% in the ionic silver containing materials to 10% in the nanoparticulate based materials, as shown in **Figure 1.8**.

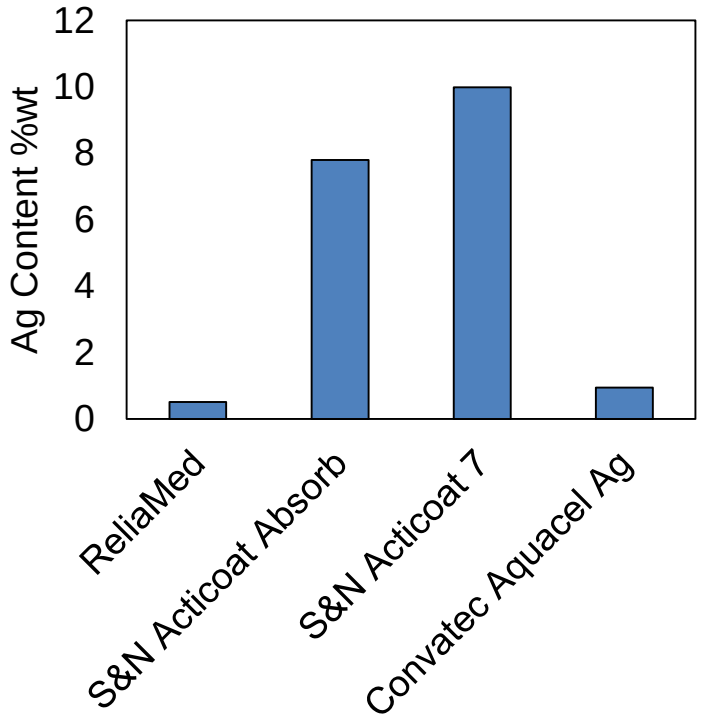

Figure 1.8: Silver contents of selected commercial products.[79]

Alongside the incredibly broad range of organisms targeted by the antimicrobial activity of silver, there is the added advantage that silver is a powerful agent, even at sub ppm concentrations.[80] It is for this reason that nanoparticular silver offers an advantage over silver based compounds, such as silver nitrate, as a slower, controlled release of silver species into solution can offer a solution to the fast dissolution kinetics offered by these materials.[43]

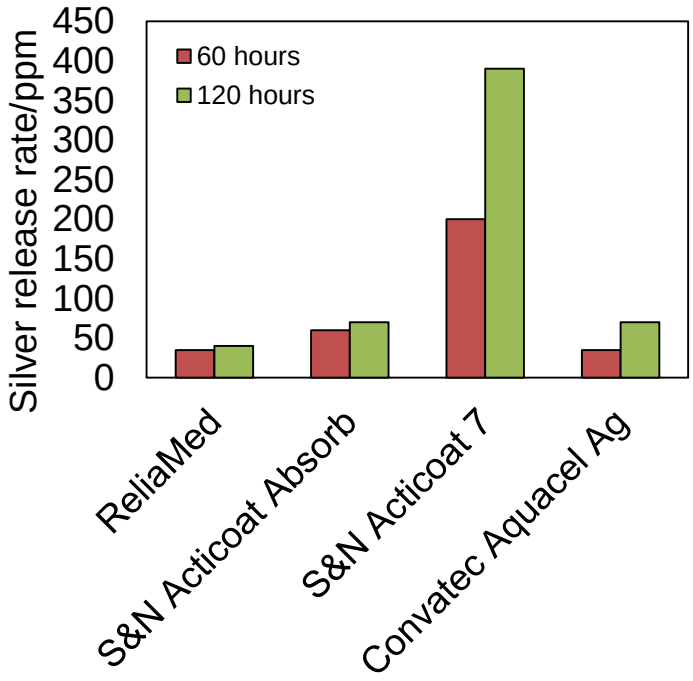

Figure 1.10: Silver release rates from selected commercial products.[79]

Control over dissolution of the silver species is vital in the production of silver wound care systems. As silver is active at very low levels, it is important to regulate the release of the ionic species to low levels, as prolonged exposure to large quantities of silver can result in damage to healthy human cells and cause argyria and hepatotoxicity in patients.[81] Although silver is to be found in the average human diet (27-80 μg per day), it is important to limit exposure due to these complications and, it is for this reason that the guidelines for safe drinking water are 50 ppb of Ag, as complications have been recorded in patients with blood-silver levels of 5 ppm.[82] Although severe cases of silver toxicity result from continued exposure to high levels of silver, this is due reason to take care to limit the silver release as much as possible.

1.3.5. Polyurethane foam wound dressings

Incorporating synthesised nanomaterials within existing wound care products is the end goal of this thesis. In collaboration with our industrial partners polymer health

technology (PHT), it is hoped that a suitable antimicrobial additive can be developed for use within existing products within PHT.

The products in question are polyurethane foam based wound care devices, which exhibit excellent absorption properties and provide a suitable environment for the healing process to occur.

Polyurethane is a long chain polymer formed from diisocyanate and polyol monomers, involving carbamate linkages between hydrocarbon chains (**figure 1.11**).[83]

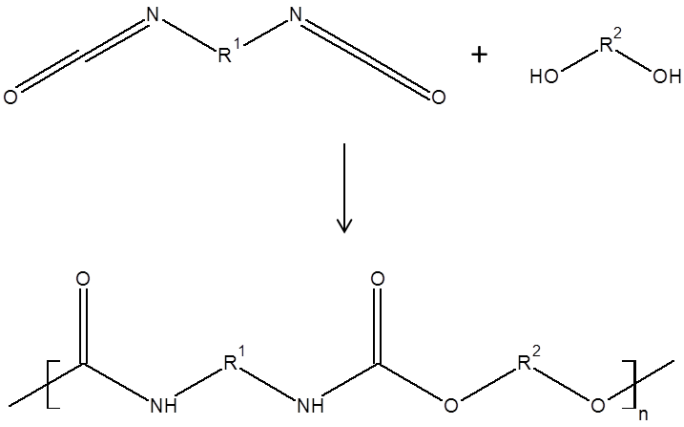

Figure 1.11: Polyurethane formation.[83]

Compatibility with these hydrophilic foams must be taken into consideration, as with the foam production procedure.

1.4. Nanocomposites

1.4.1. Definition of the nanoscale

The term ‘nano’ is becoming widely used as a prefix for many new and exciting research areas. There are, however, formal definitions for materials possessing one or more dimension in the sub-micron range. The accepted definitions for ‘nanomaterials’ involve materials with one or more dimension in the sub 100 nm range, including structures, agglomerates and aggregates.[84] The dimensions are merely arbitrary values, and do not necessarily dictate the appearance of the special properties which make

nanomaterials so appealing, as these may develop above or below the 100 nm boundary.

1.4.2. Silver nanoparticles

As well as finding use as antimicrobial agents, silver nanoparticles have been the subject of much research since the dawn of the age of nanotechnology, partly due to their large surface plasmon resonance band (a feature it shares with nanoparticles of its fellow noble metal, gold) which lends itself well to fields such as biological sensing and nanoscale photonics.[85]

Whilst not as active or popular as gold nanoparticulate catalysts, silver has found itself useful in a variety of select, mainly oxidative, reactions, such as CO oxidation,[86, 87] oxidation of organic compounds,[88-90] reduction[55, 91, 92] and dehydrogenations[93] as well as possessing capabilities for photocatalysis.[94-96]

As a result of finding many applications for silver nanoparticles, control over its size and morphology has been the subject of much research.[97-102] Using a variety of surfactants, protecting groups or capping agents the size and shape of silver nanoparticles can be controlled to give a selection of morphologies, including cubes, spheres, rods and dendrites.[100, 103, 104] The control over shape allows for different dominant facets of silver, which affect the antimicrobial efficacy of the resultant particles. Particles with a high number of facets with a large atom density, such as the (111) facet, which is in existence in a high degree within triangular particles, more so than spherical or rod shaped particles, exert a greater antimicrobial force.[98]

Size control is also of particular interest in this field, with methodologies developed to govern the dimensions of the produced silver crystallites with the purpose of controlling optical properties in the fields of photonics,[105] catalytic activity[55] and of course, antimicrobial activity.[106] Methodologies including laser ablation, photochemical and chemical treatments have been employed to control the dimensions of silver nanoparticles between a large range of sizes, in the presence of organic stabilising molecules.[107-109] These methods often produce materials of a relatively polydisperse size distribution when compared with advances in the use of reverse micelle

microreactor methodologies for producing very small (< 10 nm) monodisperse nanoparticles of a tuneable diameter within water-in-oil microemulsions.[110, 111]

1.4.3. Core-shell architectures

The coating of metal nanoparticles with a protective coating has been proven a useful and interesting development in recent times, finding applications in fields including bioimaging,[112] surface-enhanced raman spectroscopy,[113] and catalysis. One-pot or multi step methods of coating metal nanoparticles with inorganic layers have been developed which include, inorganic oxides such as silica,[114-117] titania[118, 119] and zirconia,[120] polymeric coatings[121] or encapsulation with biomolecules such as DNA.[122]

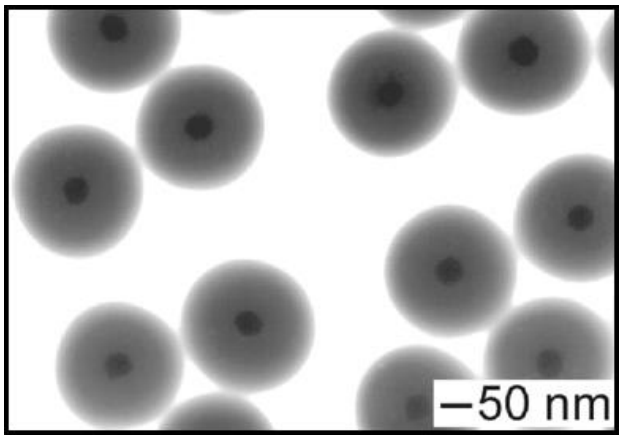

Figure 1.12: Example of a core-shell system, Au@SiO_2 nanocomposites.[123]

Metal nanoparticles exhibit interesting and novel electronic characteristics, attributed to surface plasmon resonance effects, control over the metal surface and high surface areas. The benefit of the inorganic shells is to vastly improve stability and prevent agglomeration of the metal nanoparticles to a more energetically favourable configuration. A high degree of control over dimensions and properties have been found for these composite materials, with protocols to govern eventual silica shell thickness and regulate core metal particle diameter,[124-127] as well as affect the density/porosity of the encasing material, or produce a so-called ‘rattle-type’ core shell material, in which the metal particles exist within a central void inside the inorganic shell.[128-130]

1.5. Porous structures

1.5.1. Micro, meso and macroporosity

Micropores, mesopores and macropores all describe different size ranges of pores within materials. The official IUPAC definitions for the three types of pore is as follows:[131, 132]

- Micropore: A pore with a diameter not exceeding 2.0 nm
- Mesopore: A pore with a diameter above 2.0 nm, but not exceeding 50 nm
- Macropore: A pore with a diameter above 50 nm

1.5.2. Mesoporous silicas

Introducing structured mesoporosity into silicas began a wave of research into the area, and was made famous by the Mobil corporation, who developed molecular sieves by the name of 'Mobil composition of matter'[133] and along with newer variants, such as SBA-15 and KIT-6, mesoporous silicas have found a strong foundation in applications such as catalyst support.[86, 88, 134-137]

Soft-templating is an incredibly useful tool for developing mesoporous materials as surfactant micelle arrangements can be controlled to a highly sophisticated degree to give a range of mesostructural materials, including hexagonally arranged, straight, discrete pores,[133] pore arrangements of a cubic, interconnected nature[138] or bicontinuous, enantiomeric arrangements, such as those found in KIT-6 and MCM-48 (**figure 1.9**).[139]

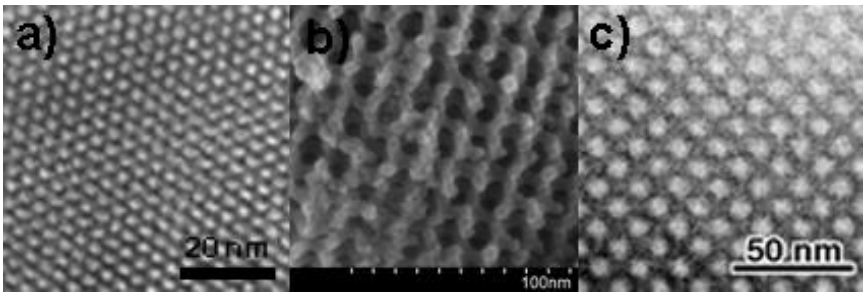

Figure 1.13: Electron micrographs of (a) MCM-41, (b) KIT-6 and (c) SBA-16 mesostructured silicas.[140-142]

These mesostructured materials bear significant advantages in fields such as catalysis, carbon capture and drug delivery.[143] Owing to high surface areas, monodisperse and easily accessible pores and the ability to easily functionalise the silica surfaces, they have become a common staple in the synthesis of inorganic structural materials. Added tuneability of material structure can be imparted in the form of variations in pore sizes. This has been achieved through various means, such as through temperature control,[144] the use of auxillary organics,[133] control over the concentration of ionic species within the reaction[145] or through systematic variation of surfactant chain lengths.[146]

The advantages of the utilisation of mesostructural silicas for antimicrobial applications include high stability, malleability and the fact that they are biologically inert.[147] Using well reported syntheses of surfactant-micelle template methods, followed by hydrolysis and condensation of an alkoxy silicate, well ordered mesopores of a narrow size distribution can be created within the silica matrix.[138]

1.5.3. Macroporous/hierarchically porous silicas

In addition to an ordered pore structure or narrow size distribution in the mesopore size range, many attempts to introduce macropores into these systems have been made, using large templates such as polystyrene beads,[135, 148, 149] polymer emulsions,[150-152] silica spheres[153] and even ice crystals.[154]

Macroporous and hierarchically porous materials have proven useful as adsorbents, separation materials and catalyst supports, due to enhanced mass transfer abilities,[154] as well as some unique optical properties which have found them use in photocatalytic devices.[155]

Advantages in macroporous materials stem from an increase to accessibility and mass transport, for example, hierarchically porous materials have been shown to improve reaction rates for acid and acid-base catalysts in biodiesel synthesis, by virtue of greater accessibility of active surface sites.[135, 156] Furthermore, improvements in dispersity of impregnated metal nanoparticles can be observed in these hierarchically porous materials.[157]

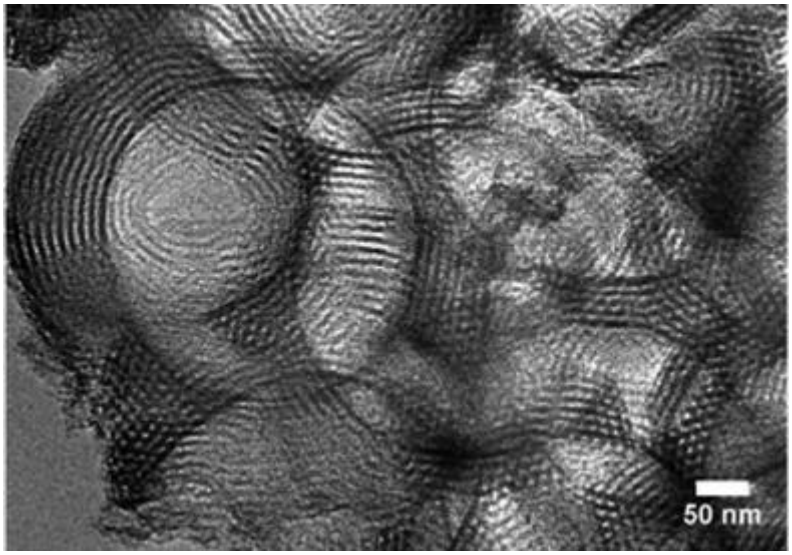

Figure 1.14: Hierarchically porous inorganic support structure.[158]

1.5.4. Silver doped mesoporous silica

The combination of silver and mesoporous silica has been studied extensively, due to the fact silica is such a robust and versatile support. This has come in many forms, the previously mentioned SBA-15 based materials being but one.[136, 159] Other common ordered mesostructured silicas have been developed as supports for catalytic and photocatalytic applications,[68, 160-162] however, these ordered mesoporous silicas are not frequently used supports for silver nanoparticles in antimicrobial applications.

Other mesostructured forms of silica, used in combination with silver include the popular mesostructured nanospheres, which have been developed as base supports, with silver nanoparticles decorating the external surface and pore channel matrix[163, 164] or as core-shell architectures in which preformed, or one-pot silver nanoparticles are coated with a mesoporous silica matrix, often of unordered pores of random orientations.[45, 165, 166]

1.5.5. Titania

Titania is well known to have photoactive properties, and has found much use as a photocatalyst.[167-170] However, in 1985, it was discovered that titania, irradiated with UV light, could also act as a photoactive antimicrobial agent.[171] Titania in the form of Anatase has a band gap of 3.2 eV and irradiation with electromagnetic radiation of greater energy than this promotes an electron from the valence band into the conduction band, leaving a free electron in the conduction band and a hole in the valence band which can then participate in oxidation and reduction processes either within the material itself, or with adsorbates at the surface of the material.[172]

Bacteria at the surface of titania based materials have been found to suffer oxidation of the Coenzyme A (CoA,, **Figure 1.9**) species photo-electrochemically, which inhibits the respiration of the cells, causing cell death.

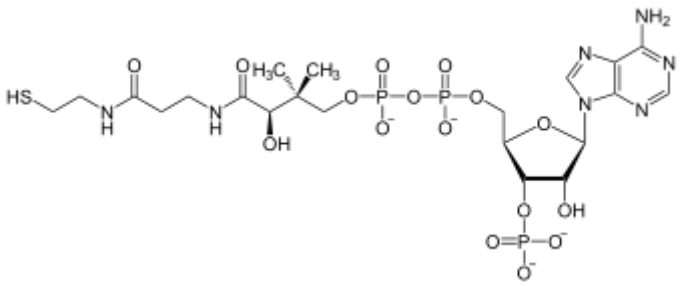

Figure 1.15: Coenzyme A, responsible for the oxidation of acetyl groups for energy production.

One of the common problems with titania based photocatalysts, is the recombination of electron hole and electron, although it is reported that this recombination can be avoided using a silver metal nanoparticle doping technique, which allows the excited electrons to 'jump' from the titania to the silver particles, thus stabilising the electron-hole formation.[173]

Although it has also been reported that there is a possibility that this stabilisation can depress silver ion release with the excited electrons reducing free silver ions back to silver metal,[174] there is a hope that these combination materials could lead to a highly active dual-functioning antimicrobial agent. The materials may require a short UV irradiation period prior to use, although titania is known to interact with approximately

3% of the solar spectrum, which it is hoped, could enhance the antimicrobial activity of silver-titania nanocomposites.[175]

1.6. Thesis aims

Silver has been known to be an effective antimicrobial agent for centuries, and yet is still a popular choice for wound management and antibacterial applications, thanks to its broad spectrum activity against a wide range of Gram positive and negative organisms, as well as yeasts, viruses and fungi. Whilst there have been studies suggesting alternative methods of action for the antimicrobial activity of silver nanoparticles, it is popular opinion that Ag^+ is the active species, and hence it is imperative that the nanocomposites developed release silver ions into the wound environment.[69]

Control over the silver release rate will be crucial to determining the lifetime of these materials as an antimicrobial agent, as release which is too fast may provide an effective antibiotic, but a material which does not last very long. Longer lifetimes for these materials would result in longer lifetimes for wound dressings and hence fewer dressing changes for chronic victims, thus reducing possible exposure to harmful pathogens. The silver release rate must also be high enough so as to exhibit antimicrobial activity, and so comparative studies of Ag^+ species dissolution and biological testing will be of high importance to attempt to optimise the performance of the developed materials.

It is for this reason that the core shell materials were the first material to be studies, with many parameters to control, such as silver nanoparticle size, silica shell size, porosity or pore size and possible further coatings, it was hypothesised that materials could be developed with very sensitive control over silver release and activity. Mesoporous silicas also gave a promising platform to work from, with the possibility of adding specific coatings to the biologically inert silica, plus introducing a hierarchically porous structure, allowed for more control over the support for the silver nanoparticles, rather than the silver itself. The development of a material with the malleability of silica and added biocompatibility or even antimicrobial activity, in combination with silver

nanoparticles, was thought to be an interesting and promising avenue. The added antimicrobial functionality of titania surface grafting alongside the study into the effects of macroporosity on these systems, will hopefully lead to the development of a highly effective antimicrobial agent with a dual mode of action.

1.7. References

1. World Health Organisation, *The Burden of Health Care-Associated Infection Worldwide* World Health Organisation, 2011.
2. A. Y. Peleg and D. C. Hooper, *New England Journal of Medicine*, 2010, **362**, 1804-1813.
3. English National Point Prevalence Survey on Healthcare-associated Infections and Antimicrobial Use, 2011: preliminary data. Health Protection Agency, May 23 2012, http://webarchive.nationalarchives.gov.uk/20140714084352/http://www.hpa.org.uk/webc/HPAwebFile/HPAweb_C/1317134305239
4. Healthcare associated infections (HCAI): guidance, data and analysis, Public health England, 2013, https://www.gov.uk/government/collections/healthcare-associated-infections-hcai-guidance-data-and-analysis
5. H. P. Loveday, J. A. Wilson, R. J. Pratt, M. Golsorkhi, A. Tingle, A. Bak, J. Browne, J. Prieto and M. Wilcox, *Journal of Hospital Infection*, 2014, **86, Supplement 1**, S1-S70.
6. R. J. Pratt, C. M. Pellowe, J. A. Wilson, H. P. Loveday, P. J. Harper, S. R. L. J. Jones, C. McDougall and M. H. Wilcox, *Journal of Hospital Infection*, 2007, **65, Supplement 1**, S1-S59.
7. J. Houbraken, J. C. Frisvad and R. A. Samson, *IMA Fungus*, 2011, **2**, 87-95.
8. O. Penicillins, *Am Fam Physician*, 2000, **62**, 611-620.
9. I. M. Gould, *International journal of antimicrobial agents*, 2006, **28**, 379-384.
10. R. W. Lacey, *The Journal of hospital infection*, 1987, **9**, 103-105.
11. D. J. Diekema, B. J. BootsMiller, T. E. Vaughn, R. F. Woolson, J. W. Yankey, E. J. Ernst, S. D. Flach, M. M. Ward, C. L. Franciscus, M. A. Pfaller and B. N. Doebbeling, *Clinical infectious diseases : an official publication of the Infectious Diseases Society of America*, 2004, **38**, 78-85.
12. J. C. Hageman, T. M. Uyeki, J. S. Francis, D. B. Jernigan, J. G. Wheeler, C. B. Bridges, S. J. Barenkamp, D. M. Sievert, A. Srinivasan, M. C. Doherty, L. K. McDougal, G. E. Killgore, U. A. Lopatin, R. Coffman, J. K. MacDonald, S. K. McAllister, G. E. Fosheim, J. B. Patel and L. C. McDonald, *Emerging infectious diseases*, 2006, **12**, 894-899.
13. I. M. Gould, *The Journal of hospital infection*, 2005, **61**, 277-282.
14. R. C. Moellering, Jr., *Annals of internal medicine*, 2006, **144**, 368-370.

15. D. K. Warren and M. H. Kollef, *Microbes and Infection*, 2005, **7**, 268-274.

16. R. E. Dixon, *Public Health Then and Now: Celebrating 50 Years of MMWR at CDC*, 2011, **60**, 58.

17. A. Ferder, *South African Medical Journal*, 2002, **92**.

18. G. D. Shockman and J. Barren, *Annual Reviews in Microbiology*, 1983, **37**, 501-527.

19. K. Yoshida, T. Matsumoto, K. Tateda, K. Uchida, S. Tsujimoto and K. Yamaguchi, *Journal of medical microbiology*, 2000, **49**, 1003-1010.

20. K. F. Jarrell, *Pili and flagella: current research and future trends*, Horizon Scientific Press, 2009.

21. C. Brennen and H. Winet, *Annual Review of Fluid Mechanics*, 1977, **9**, 339-398.

22. J. C. SKou, *Physiological Reviews*, 1965, **45**, 596-618.

23. M. Thanbichler, S. C. Wang and L. Shapiro, *Journal of Cellular Biochemistry*, 2005, **96**, 506-521.

24. P. B. Moore and T. A. Steitz, *Nature*, 2002, **418**, 229-235.

25. K. Luby-Phelps, F. Lanni and D. L. Taylor, *Annual review of biophysics and biophysical chemistry*, 1988, **17**, 369-396.

26. R. Austrian, *Bacteriological Reviews*, 1960, **24**, 261.

27. E. Lattuada, A. Zorzi, M. Lanzafame, D. Antolini, R. Fontana, S. Vento and E. Concia, *The Journal of infection*, 2005, **51**, E71-72.

28. M. T. Madigan, J. M. Martinko, J. Parker and T. D. Brock, *Biology of microorganisms*, prentice hall Upper Saddle River, NJ, 1997.

29. S. L. Percival, P. G. Bowler and J. Dolman, *International wound journal*, 2007, **4**, 186-191.

30. J. Duffy, *The Sanitarians: a History of American Public Health*, University of Illinois Press, 1992.

31. S. Silver, L. Phung and G. Silver, *Journal of Industrial Microbiology & Biotechnology*, 2006, **33**, 627-634.

32. W. R. Price and M. Wood, *The American Journal of Surgery*, 1966, **112**, 674-680.

33. C. A. MOYER, L. BRENTANO, D. L. GRAVENS, H. W. MARGRAF and W. W. MONAFO, JR., *AMA Arch Surg*, 1965, **90**, 812-867.

34. I. Chopra, *Journal of Antimicrobial Chemotherapy*, 2007, **59**, 587-590.

35. N. George, J. Faoagali and M. Muller, *Burns*, 1997, **23**, 493-495.

36. C. L. Fox, Jr., *AMA Arch Surg*, 1968, **96**, 184-188.

37. T. O. Stair, J. D'Orta, M. F. Altieri and M. S. Lippe, *The American Journal of Emergency Medicine*, 1986, **4**, 214-217.

38. J. C. Wasiak, Heather; Campbell, Fiona, *Dressings for superficial and partial thickness burns*, Cochrane Database of Systematic Reviews, 2008.

39. J. Elechiguerra, J. Burt, J. Morones, A. Camacho-Bragado, X. Gao, H. Lara and M. Yacaman, *Journal of Nanobiotechnology*, 2005, **3**, 6.

40. M. S. A. S. Shah, M. Nag, T. Kalagara, S. Singh and S. V. Manorama, *Chemistry of Materials*, 2008, **20**, 2455-2460.

41. T. Textor, M. M. G. Fouda and B. Mahltig, *Applied Surface Science*, 2010, **256**, 2337-2342.

42. J. J. Buckley, A. F. Lee, L. Olivi and K. Wilson, *Journal of Materials Chemistry*, 2010, **20**, 8056-8063.

43. J. J. Buckley, P. L. Gai, A. F. Lee, L. Olivi and K. Wilson, *Chemical Communications*, 2008, 4013-4015.

44. M. A. Maurer-Jones, M. P. S. Mousavi, L. D. Chen, P. Buhlmann and C. L. Haynes, *Chemical Science*, 2013, **4**, 2564-2572.

45. K. Xu, J.-X. Wang, X.-L. Kang and J.-F. Chen, *Materials Letters*, 2009, **63**, 31-33.

46. A. Panáček, L. Kvítek, R. Prucek, M. Kolář, R. Večeřová, N. Pizúrová, V. K. Sharma, T. j. Nevěčná and R. Zbořil, *The Journal of Physical Chemistry B*, 2006, **110**, 16248-16253.

47. I. Sondi and B. Salopek-Sondi, *Journal of Colloid and Interface Science*, 2004, **275**, 177-182.

48. S. M. Kelly, F. Cheng, J. Betts, J. Schaller and T. Heinze, *Green Chemistry*, 2013.

49. Y. H. Kim, D. K. Lee, H. G. Cha, C. W. Kim and Y. S. Kang, *The Journal of Physical Chemistry C*, 2007, **111**, 3629-3635.

50. A. Ivask, A. ElBadawy, C. Kaweeteerawat, D. Boren, H. Fischer, Z. Ji, C. H. Chang, R. Liu, T. Tolaymat, D. Telesca, J. I. Zink, Y. Cohen, P. A. Holden and H. A. Godwin, *ACS Nano*, 2013.

51. S. Luo, J. Chen, M. Chen, W. Xu and X. Zhang, 2012, vol. 380, pp. 254-259.

52. X. Zhao, Y. Xia, Q. Li, X. Ma, F. Quan, C. Geng and Z. Han, *Colloids and Surfaces A: Physicochemical and Engineering Aspects*, 2014, **444**, 180-188.

53. J. S. Kim, E. Kuk, K. N. Yu, J.-H. Kim, S. J. Park, H. J. Lee, S. H. Kim, Y. K. Park, Y. H. Park, C.-Y. Hwang, Y.-K. Kim, Y.-S. Lee, D. H. Jeong and M.-H. Cho, *Nanomedicine: Nanotechnology, Biology and Medicine*, 2007, **3**, 95-101.

54. T. Maneerung, S. Tokura and R. Rujiravanit, *Carbohydrate Polymers*, 2008, **72**, 43-51.

55. N. Pradhan, A. Pal and T. Pal, *Colloids and Surfaces A: Physicochemical and Engineering Aspects*, 2002, **196**, 247-257.

56. S. Tarimala, N. Kothari, N. Abidi, E. Hequet, J. Fralick and L. L. Dai, *Journal of Applied Polymer Science*, 2006, **101**, 2938-2943.

57. D. L. Van Hyning, W. G. Klemperer and C. F. Zukoski, *Langmuir*, 2001, **17**, 3128-3135.

58. M. L. Gulrajani, D. Gupta, S. Periyasamy and S. G. Muthu, *Journal of Applied Polymer Science*, 2008, **108**, 614-623.

59. Y. Li, Y. Wu and B. S. Ong, *Journal of the American Chemical Society*, 2005, **127**, 3266-3267.

60. A. Taleb, C. Petit and M. P. Pileni, *Chemistry of Materials*, 1997, **9**, 950-959.

61. H. Wang, X. Qiao, J. Chen and S. Ding, *Colloids and Surfaces A: Physicochemical and Engineering Aspects*, 2005, **256**, 111-115.

62. C. Luo, Y. Zhang, X. Zeng, Y. Zeng and Y. Wang, *Journal of Colloid and Interface Science*, 2005, **288**, 444-448.

63. S. L.-C. Hsu and R.-T. Wu, *Materials Letters*, 2007, **61**, 3719-3722.

64. H. Song, K. Ko, L. Oh and B. Lee, *Eur Cells Mater*, 2006, **11**, 58.

65. Q. Sun, X. Cai, J. Li, M. Zheng, Z. Chen and C.-P. Yu, *Colloids and Surfaces A: Physicochemical and Engineering Aspects*, 2014, **444**, 226-231.

66. P. Mukherjee, M. Roy, B. Mandal, G. Dey, P. Mukherjee, J. Ghatak, A. Tyagi and S. Kale, *Nanotechnology*, 2008, **19**, 075103.

67. V. Hornebecq, M. Antonietti, T. Cardinal and M. Treguer-Delapierre, *Chemistry of materials*, 2003, **15**, 1993-1999.

68. X.-G. Zhao, J.-L. Shi, B. Hu, L.-X. Zhang and Z.-L. Hua, *Materials Letters*, 2004, **58**, 2152-2156.

69. A. J. Miao, K. A. Schwehr, C. Xu, S. J. Zhang, Z. Luo, A. Quigg and P. H. Santschi, *Environmental pollution (Barking, Essex : 1987)*, 2009, **157**, 3034-3041.

70. C. Nägeli, *Über oligodynamische Erscheinungen in lebenen Zellen*, Zürcher & Furrer, 1900.

71. Q. L. Feng, J. Wu, G. Q. Chen, F. Z. Cui, T. N. Kim and J. O. Kim, *Journal of biomedical materials research*, 2000, **52**, 662-668.

72. J. Thiel, L. Pakstis, S. Buzby, M. Raffi, C. Ni, D. J. Pochan and S. I. Shah, *Small*, 2007, **3**, 799-803.

73. S. Elzey and V. Grassian, *J Nanopart Res*, 2010, **12**, 1945-1958.

74. O. Choi and Z. Hu, *Environmental Science & Technology*, 2008, **42**, 4583-4588.

75. J. Liu, D. A. Sonshine, S. Shervani and R. H. Hurt, *ACS Nano*, 2010, **4**, 6903-6913.

76. K. Dunn and V. Edwards-Jones, *Burns : journal of the International Society for Burn Injuries*, 2004, **30**, S1-S9.

77. M. A. A. O'Neill, G. J. Vine, A. E. Beezer, A. H. Bishop, J. Hadgraft, C. Labetoulle, M. Walker and P. G. Bowler, *International Journal of Pharmaceutics*, 2003, **263**, 61-68.

78. J. Tian, K. K. Y. Wong, C.-M. Ho, C.-N. Lok, W.-Y. Yu, C.-M. Che, J.-F. Chiu and P. K. H. Tam, *ChemMedChem*, 2007, **2**, 129-136.

79. Reliamed, *Silver Alginate / CMC Dressings*, http://www.reliamedproducts.com/sellsheets/reliamed_silveralginate.pdf.

80. M. Kawashita, S. Toda, H.-M. Kim, T. Kokubo and N. Masuda, *Journal of Biomedical Materials Research Part A*, 2003, **66A**, 266-274.

81. M. Trop, M. Novak, S. Rodl, B. Hellbom, W. Kroell and W. Goessler, *Journal of Trauma-Injury, Infection, and Critical Care*, 2006, **60**, 648-652.

82. A. Wadhera and M. Fung, *Dermatology online journal*, 2005, **11**.

83. E. Delebecq, J.-P. Pascault, B. Boutevin and F. Ganachaud, *Chemical Reviews*, 2012, **113**, 80-118.

84. W. G. Kreyling, M. Semmler-Behnke and Q. Chaudhry, *Nano Today*, 2010, **5**, 165-168.

85. Y. Lu, G. L. Liu and L. P. Lee, *Nano Letters*, 2004, **5**, 5-9.

86. D. Tian, G. Yong, Y. Dai, X. Yan and S. Liu, *Catal Lett*, 2009, **130**, 211-216.

87. H. Liu, D. Ma, R. A. Blackley, W. Zhou and X. Bao, *Chemical Communications*, 2008, 2677-2679.

88. L. Ma, l. Jia, X. Guo and L. Xiang, *Chinese Journal of Catalysis*, 2014, **35**, 108-119.

89. P. Christopher, H. Xin and S. Linic, *Nature chemistry*, 2011, **3**, 467-472.

90. R. Xu, D. Wang, J. Zhang and Y. Li, *Chemistry – An Asian Journal*, 2006, **1**, 888-893.

91. B. Baruah, G. J. Gabriel, M. J. Akbashev and M. E. Booher, *Langmuir : the ACS journal of surfaces and colloids*, 2013, **29**, 4225-4234.

92. T. Mitsudome, A. Noujima, Y. Mikami, T. Mizugaki, K. Jitsukawa and K. Kaneda, *Angewandte Chemie*, 2010, **122**, 5677-5680.

93. T. Mitsudome, Y. Mikami, H. Funai, T. Mizugaki, K. Jitsukawa and K. Kaneda, *Angewandte Chemie*, 2008, **120**, 144-147.

94. A. Wu, C. Tian, H. Yan, Y. Hong, B. Jiang and H. Fu, *Journal of Materials Chemistry A*, 2014.

95. K. Awazu, M. Fujimaki, C. Rockstuhl, J. Tominaga, H. Murakami, Y. Ohki, N. Yoshida and T. Watanabe, *Journal of the American Chemical Society*, 2008, **130**, 1676-1680.

96. L. Zhang, J. C. Yu, H. Y. Yip, Q. Li, K. W. Kwong, A.-W. Xu and P. K. Wong, *Langmuir : the ACS journal of surfaces and colloids*, 2003, **19**, 10372-10380.

97. Y. Takahashi, A. Suzuki, N. Zettsu, T. Oroguchi, Y. Takayama, Y. Sekiguchi, A. Kobayashi, M. Yamamoto and M. Nakasako, *Nano Letters*, 2013.

98. S. Pal, Y. K. Tak and J. M. Song, *Applied and environmental microbiology*, 2007, **73**, 1712-1720.

99. S. Zou and G. C. Schatz, *The Journal of Chemical Physics*, 2004, **121**, 12606-12612.

100. Y. Sun and Y. Xia, *Science*, 2002, **298**, 2176-2179.

101. J. J. Mock, M. Barbic, D. R. Smith, D. A. Schultz and S. Schultz, *The Journal of Chemical Physics*, 2002, **116**, 6755-6759.

102. K. L. Kelly, E. Coronado, L. L. Zhao and G. C. Schatz, *The Journal of Physical Chemistry B*, 2002, **107**, 668-677.

103. J. Zhu, S. Liu, O. Palchik, Y. Koltypin and A. Gedanken, *Langmuir : the ACS journal of surfaces and colloids*, 2000, **16**, 6396-6399.

104. B. Wiley, Y. Sun, B. Mayers and Y. Xia, *Chemistry – A European Journal*, 2005, **11**, 454-463.

105. W. Jiang, B. Y. Kim, J. T. Rutka and W. C. Chan, *Nature nanotechnology*, 2008, **3**, 145-150.

106. A. Panáček, L. Kvitek, R. Prucek, M. Kolar, R. Vecerova, N. Pizurova, V. K. Sharma, T. j. Nevečná and R. Zboril, *The Journal of Physical Chemistry B*, 2006, **110**, 16248-16253.

107. Z. S. Pillai and P. V. Kamat, *The Journal of Physical Chemistry B*, 2004, **108**, 945-951.

108. A. Callegari, D. Tonti and M. Chergui, *Nano Letters*, 2003, **3**, 1565-1568.

109. F. Mafune, J.-y. Kohno, Y. Takeda, T. Kondow and H. Sawabe, *The Journal of Physical Chemistry B*, 2000, **104**, 9111-9117.

110. J. Eastoe, M. J. Hollamby and L. Hudson, *Advances in colloid and interface science*, 2006, **128**, 5-15.

111. I. Capek, *Advances in colloid and interface science*, 2004, **110**, 49-74.

112. T. J. Yoon, K. N. Yu, E. Kim, J. S. Kim, B. G. Kim, S. H. Yun, B. H. Sohn, M. H. Cho, J. K. Lee and S. B. Park, *Small*, 2006, **2**, 209-215.

113. L. Chen, X. Han, J. Yang, J. Zhou, W. Song, B. Zhao, W. Xu and Y. Ozaki, *Journal of colloid and interface science*, 2011, **360**, 482-487.

114. S. Mun, B. Yoon, B. H. Cho and W. B. Ko, *Asian Journal of Chemistry*, 2012, **24**, 4804-4808.

115. K. Nischala, T. N. Rao and N. Hebalkar, *Colloids and Surfaces B-Biointerfaces*, 2011, **82**, 203-208.

116. J. E. Martin, A. A. Herzing, W. Yan, X. Q. Li, B. E. Koel, C. J. Kiely and W. X. Zhang, *Langmuir : the ACS journal of surfaces and colloids*, 2008, **24**, 4329-4334.

117. L. M. Liz-Marzán, M. Giersig and P. Mulvaney, *Langmuir : the ACS journal of surfaces and colloids*, 1996, **12**, 4329-4335.

118. H. Sakai, T. Kanda, H. Shibata, T. Ohkubo and M. Abe, *Journal of the American Chemical Society*, 2006, **128**, 4944-4945.

119. K. S. Mayya, D. I. Gittins and F. Caruso, *Chemistry of Materials*, 2001, **13**, 3833-3836.

120. R. T. Tom, A. S. Nair, N. Singh, M. Aslam, C. Nagendra, R. Philip, K. Vijayamohanan and T. Pradeep, *Langmuir : the ACS journal of surfaces and colloids*, 2003, **19**, 3439-3445.

121. P. Graf, A. Mantion, A. Haase, A. F. Thünemann, A. Mašić, W. Meier, A. Luch and A. Taubert, *ACS Nano*, 2011, **5**, 820-833.

122. Y. Cao, R. Jin and C. A. Mirkin, *Journal of the American Chemical Society*, 2001, **123**, 7961-7962.

123. Y. Lu, Y. Yin, Z.-Y. Li and Y. Xia, *Nano Letters*, 2002, **2**, 785-788.

124. N. Hagura, W. Widiyastuti, F. Iskandar and K. Okuyama, *Chemical Engineering Journal*, 2010, **156**, 200-205.

125. T. Li, J. Moon, A. A. Morrone, J. J. Mecholsky, D. R. Talham and J. H. Adair, *Langmuir : the ACS journal of surfaces and colloids*, 1999, **15**, 4328-4334.

126. C.-L. Chang and H. S. Fogler, *Langmuir : the ACS journal of surfaces and colloids*, 1997, **13**, 3295-3307.

127. K. Osseo-Asare and F. J. Arriagada, *Colloids and Surfaces*, 1990, **50**, 321-339.

128. Y. Hu, Q. Zhang, J. Goebl, T. Zhang and Y. Yin, *Phys Chem Chem Phys*, 2010, **12**, 11836-11842.

129. Q. Zhang, J. Ge, J. Goebl, Y. Hu, Z. Lu and Y. Yin, *Nano Res.*, 2009, **2**, 583-591.

130. Q. Zhang, T. Zhang, J. Ge and Y. Yin, *Nano Letters*, 2008, **8**, 2867-2871.

131. IUPAC, *Manual of Symbols and Terminology for Physicochemical Quantities and Units, Appendix II: Definitions, Terminology and Symbols in Colloid and Surface Chemistry*, 1972.

132. IUPAC, 1976.

133. J. S. Beck, J. C. Vartuli, W. J. Roth, M. E. Leonowicz, C. T. Kresge, K. D. Schmitt, C. T. W. Chu, D. H. Olson and E. W. Sheppard, *Journal of the American Chemical Society*, 1992, **114**, 10834-10843.

134. C. P. Vinod, K. Wilson and A. F. Lee, *Journal of Chemical Technology and Biotechnology*, 2011, **86**, 161-171.

135. J. Dhainaut, J.-P. Dacquin, A. F. Lee and K. Wilson, *Green Chemistry*, 2010, **12**, 296-303.

136. M. Boutros, J.-M. Trichard and P. Da Costa, *Applied Catalysis B: Environmental*, 2009, **91**, 640-648.

137. K. N. Rao, A. Sridhar, A. F. Lee, S. J. Tavener, N. A. Young and K. Wilson, *Green Chemistry*, 2006, **8**, 790-797.

138. D. Zhao, Q. Huo, J. Feng, B. F. Chmelka and G. D. Stucky, *Journal of the American Chemical Society*, 1998, **120**, 6024-6036.

139. F. Kleitz, S. Hei Choi and R. Ryoo, *Chemical Communications*, 2003, 2136-2137.

140. P. Van Der Voort, M. Benjelloun and E. F. Vansant, *The Journal of Physical Chemistry B*, 2002, **106**, 9027-9032.

141. H. Tüysüz, C. W. Lehmann, H. Bongard, B. Tesche, R. Schmidt and F. Schüth, *Journal of the American Chemical Society*, 2008, **130**, 11510-11517.

142. B. Muñoz, A. Rámila, J. Pérez-Pariente, I. Díaz and M. Vallet-Regí, *Chemistry of Materials*, 2002, **15**, 500-503.

143. M. Vallet-Regi, A. Rámila, R. P. del Real and J. Pérez-Pariente, *Chemistry of Materials*, 2000, **13**, 308-311.

144. A. Galarneau, H. Cambon, F. Di Renzo and F. Fajula, *Langmuir : the ACS journal of surfaces and colloids*, 2001, **17**, 8328-8335.

145. A. Corma, Q. Kan, M. T. Navarro, J. Pérez-Pariente and F. Rey, *Chemistry of Materials*, 1997, **9**, 2123-2126.

146. M. Kruk, M. Jaroniec, Y. Sakamoto, O. Terasaki, R. Ryoo and C. H. Ko, *The Journal of Physical Chemistry B*, 1999, **104**, 292-301.

147. J. C. Rooke, C. Meunier, A. Léonard and B.-L. Su, *Pure and Applied Chemistry*, 2008, **80**, 2345-2376.

148. S. Vaudreuil, M. Bousmina, S. Kaliaguine and L. Bonneviot, *Advanced Materials*, 2001, **13**, 1310-1312.

149. T. Sen, G. J. T. Tiddy, J. L. Casci and M. W. Anderson, *Chemistry of Materials*, 2004, **16**, 2044-2054.

150. R. Ravikrishna, R. Green and K. T. Valsaraj, *J Sol-Gel Sci Technol*, 2005, **34**, 111-122.

151. H. Zhang, G. C. Hardy, Y. Z. Khimyak, M. J. Rosseinsky and A. I. Cooper, *Chemistry of Materials*, 2004, **16**, 4245-4256.

152. B. P. Binks, *Advanced Materials*, 2002, **14**, 1824-1827.

153. H. Zhang and A. I. Cooper, *Industrial & Engineering Chemistry Research*, 2005, **44**, 8707-8714.

154. H. Nishihara, S. R. Mukai, D. Yamashita and H. Tamon, *Chemistry of Materials*, 2005, **17**, 683-689.

155. F. Iskandar, A. B. D. Nandiyanto, K. M. Yun, C. J. Hogan, K. Okuyama and P. Biswas, *Advanced materials*, 2007, **19**, 1408-1412.

156. J. J. Woodford, J.-P. Dacquin, K. Wilson and A. F. Lee, *Energy & Environmental Science*, 2012, **5**, 6145-6150.

157. B. Fang, J. H. Kim, M. Kim and J.-S. Yu, *Chemistry of Materials*, 2009, **21**, 789-796.

158. J. Dhainaut, J.-P. Dacquin, A. F. Lee and K. Wilson, *Green Chemistry*, 2010, **12**, 296-303.

159. W. Zhu, Y. Han and L. An, *Microporous and Mesoporous Materials*, 2005, **80**, 221-226.

160. H. Zhao, J. Zhou, H. Luo, C. Zeng, D. Li and Y. Liu, *Catal Lett*, 2006, **108**, 49-54.

161. S. Rodrigues, S. Uma, I. N. Martyanov and K. J. Klabunde, *Journal of Catalysis*, 2005, **233**, 405-410.

162. P. V. Adhyapak, P. Karandikar, K. Vijayamohanan, A. A. Athawale and A. J. Chandwadkar, *Materials Letters*, 2004, **58**, 1168-1171.

163. C. Dai, Y. Yuan, C. Liu, J. Wei, H. Hong, X. Li and X. Pan, *Biomaterials*, 2009, **30**, 5364-5375.

164. J.-X. Wang, L.-X. Wen, Z.-H. Wang and J.-F. Chen, *Materials Chemistry and Physics*, 2006, **96**, 90-97.

165. M. Liong, B. France, K. A. Bradley and J. I. Zink, *Advanced Materials*, 2009, **21**, 1684-1689.

166. L. Han, H. Wei, B. Tu and D. Zhao, *Chemical Communications*, 2011, **47**, 8536-8538.

167. C. M. Parlett, K. Wilson and A. F. Lee, *Chemical Society Reviews*, 2013.

168. D. Liu, Y. Fernández, O. Ola, S. Mackintosh, M. Maroto-Valer, C. Parlett, A. F. Lee and J. Wu, *Catalysis Communications*, 2012, **25**, 78-82.

169. P. Cheng, M. Zheng, Y. Jin, Q. Huang and M. Gu, *Materials Letters*, 2003, **57**, 2989-2994.

170. A. Fujishima, T. N. Rao and D. A. Tryk, *Journal of Photochemistry and Photobiology C: Photochemistry Reviews*, 2000, **1**, 1-21.

171. T. Matsunaga, R. Tomoda, T. Nakajima and H. Wake, *FEMS Microbiology Letters*, 1985, **29**, 211-214.

172. K. Page, R. G. Palgrave, I. P. Parkin, M. Wilson, S. L. P. Savin and A. V. Chadwick, *Journal of Materials Chemistry*, 2007, **17**, 95-104.

173. X. You, F. Chen, J. Zhang and M. Anpo, *Catal Lett*, 2005, **102**, 247-250.

174. X. Hu, X. Zhou, R. Wang, C. Hu and J. Qu, *Applied Catalysis B: Environmental*, 2014, **154–155**, 44-50.

175. J. C. Yu, W. Ho, J. Yu, H. Yip, P. K. Wong and J. Zhao, *Environmental Science & Technology*, 2005, **39**, 1175-1179.

Chapter 2: Experimental

2.1. Preparation of core-shell silver@silica materials

2.1.1. Parent core-shell materials

Silver/silica, core-shell nanocomposites were prepared using a modified preparation outlined by Adair et al.[1] In this procedure a microemulsion solution was prepared from cyclohexane (Sigma Aldrich ≥ 99%), Igepal co-520 (Sigma Aldrich) and deionised water in a 250 ml round bottomed flask with vigorous stirring (750 rpm) at room temperature and covered in foil under flowing N_2. Silver nitrate solution (0.1M, Sigma Aldrich) was added and the system left to equilibrate for 20 minutes. Hydrazine (Sigma Aldrich 50-60% vol) was added to reduce the silver. After 5 minutes stirring, ammonium hydroxide (Sigma Aldrich 35%) was added, followed by tetraethyl orthosilicate (Sigma Aldrich 98%). The solution was left stirring at 750 rpm for 24 hours under flowing nitrogen (1 ml/min).

The microemulsion was diluted with ethanol (Fisher 98%) at a 1:1 ratio of ethanol:cyclohexane, and centrifuged at 6000 rpm for 8 minutes to separate the solid particulate. The solution was decanted, leaving the product, which was redispersed in a 50:50 vol % mixture of water:ethanol by sonication. The resulting sol was again separated by centrifugation before being washed by a water/ethanol mixture twice more and obtained as a solid powder.

2.1.2. Surface protected etching

The procedure for introducing porosity into the materials was a modified procedure by Zhang et al.[2, 3] The isolated material from 2.1.1 was dispersed in a 50:50 mixture of ethanol and water (0.5g/L) and PVP K10 added at a 3:1 ratio by mass (PVP:Nanocomposite) and heated to 100^{o}C with stirring (750 rpm). After an hour, the solution was centrifuged at 8000 rpm for 15 minutes and the solid removed. The isolated solid material was dispersed in 0.01M sodium hydroxide (25 g/L) with vigorous stirring. One third of the solution was removed after 30, 60 and 120 minutes

before centrifugation at 8000 rpm for 5 minutes and the resultant solid washed with water 3 times.

2.2. Preparation of mesoporous core-shell silver@silica materials

2.2.1. Mesoporous core-shell silver@silica materials

The Ag@SiO_2-CTAB materials were prepared using a modified method developed by Han L. *et al*.[4] A solution of 0.2 %wt cetyltrimethylammonium bromide (CTAB, Sigma Aldrich, ≥99%) in water was made, sodium hydroxide (Sigma Aldrich, ≥98%),) and hydrazine hydrate (50-60 %vol, Sigma Aldrich) added at molar ratio of 1:2.5:15 CTAB:NaOH:Hydrazine. This was heated to 80 ^{o}C under vigorous stirring (900 rpm) for 30 minutes under flowing nitrogen (1 ml/min). Silver nitrate (Sigma Aldrich, 0.1 M) was added instantaneously (1:2.75 molar ratio silver nitrate to CTAB) quickly accompanied by a noticeable colour change in the solution, from a colourless, cloudy solution, to a dark red – orange, clear solution. After five minutes stirring (900 rpm), tetraethyl orthosilicate (Sigma Aldrich, 98%) was added in one go at a molar ratio of 20:1 TEOS:silver nitrate. The solution was left refluxing at 80^{o}C under nitrogen (1 ml/min) for 2 hours, before cooling. Addition of ethanol promoted the sedimentation of the silver-silica nanocomposite materials, allowing for quick filtration and separation of the particles. The material was washed twice with ethanol/ammonium carbonate mixture (6 g/L) and once with water water, before being allowed to dry in air at 100^{o}C. Following this, a pestle and mortar was used to grind the material into a fine powder, before a final ethanol washing and drying step was performed. The material was then treated thermally using a muffle furnace to calcine the material at 350 ^{o}C in air for 5 hours, with a ramp rate of 1 ^{o}C/min.

2.2.2. Pore swelling using organic additives

Materials with an increased pore diameter were synthesised using a mesitylene organic swelling agent to increase the diameter of the CTAB micelles, around which the silica condenses, forming pores[5]. Materials were synthesised using the method in 2.2.1, with the addition of mesitylene (Sigma Aldrich, 99%) to the CTAB/water/hydrazine/NaOH mixture at a molar ratio of 1.75 to 7:1 mesitylene:CTAB.

2.3. Preparation of SBA-15 based nanocomposites

2.3.1. Pure SBA-15 preparation

The preparation of SBA-15 was achieved using a modified method from Zhao et al.[6] A 2.6 wt% solution of Pluronic P123 triblock copolymer (poly(ethylene glycol)-poly(propylene glycol)-poly(ethylene glycol) (Sigma Aldrich), in 1.6 M HCl solution was stirred (500 rpm) at 35 ^{o}C. Tetraethyl orthosilicate (Sigma Aldrich, 98%) was then added to the mixture, at a molar ratio of 60:1[TEOS]:[P-123]. The mixture was aged at 80 ^{o}C for 24 hours without stirring in a sealed container in an oven. The resultant solid material was filtered, then washed with ethanol before drying in air at 100 ^{o}C overnight. Removal of the P123 framework was performed by calcination at 500 ^{o}C in a muffle furnace for 6 hours with a ramp rate of 1 ^{o}C/min.

2.3.2. Polystyrene bead synthesis

Polystyrene bead templates were synthesised using a method developed by Vaudreuil et al[7], in which styrene, divinyl benzene (co-monomer, Sigma Aldrich, 80%) and potassium persulphate (initiator, Sigma Aldrich, >99%) were the reagents. The reaction was performed on a large scale in a 2 litre jacketed Radleys' reactor ready system at 90 ^{o}C. Deionised water (1.5 L) was introduced to the reactor, along with a

Leibig condenser, thermocouple and a nitrogen line at 1.5 bar pressure. The reactor was stirred at 300 rpm overnight to outgas the solution. Styrene (140 ml, Sigma Aldrich, >99%) and divinylbenzene (27 ml) were washed with NaOH (0.1 M) three times in separate separating funnels and added to the reaction vessel. Potassium persulfate (Sigma Aldrich, 0.35 g) was dissolved in deionized water (20 ml) at 80 ^{o}C. After 30 minutes of stirring (300 rpm) in the reactor at 90 ^{o}C, the potassium persulfate solution was added. After stirring for 3 hours, the solid particles were recovered as a concentrated solution and stored in a freezer overnight, then the product was allowed to warm before being filtered, washed with ethanol and the beads dried at 80 ^{o}C overnight.

2.3.3. Macroporous SBA-15

To introduce the macroporosity into the mesoporous silicas, polystyrene beads were added to the SBA synthesis (2.3.1) at a weight ratio of 5.3:1 [PS beads]:[TEOS][7]. The polystyrene beads were introduced into the 2.6 %wt solution of P123 in 1.6 M HCl, before heating to 35 ^{o}C with stirring at 500 rpm. The resultant solid material was filtered, then washed with ethanol before drying in air at 100 ^{o}C overnight. Removal of the P123 framework was performed by calcination at 500 ^{o}C in a muffle furnace for 6 hours with a ramp rate of 1 ^{o}C/min.

2.3.4. Titania-grafting

The grafting of titania onto the surface of the prepared silica materials was done using a modified procedure by Landau et al[8] in which triethylamine is used to activate the surface silanols on the silica and allow the reaction to proceed at lower temperatures. To ensure a uniform coating of TiO_2, the reaction must be performed under completely dry conditions, due to the facile hydrolysis of the titania precursor, which will readily form large titania particles in the presence of water. The synthetic procedure involves mixing titanium isopropoxide (Sigma Aldrich,) in anhydrous toluene (Aldrich, water content <0.002%), adding triethylamine (Sigma Aldrich, >99%) and MM-SBA-15 or SBA-15 material whilst stirring at 85 ºC for 6 h under nitrogen flow. The concentration of titanium isopropoxide was 145 g/L, the molar ratio between

titanium isopropoxide and SBA-15 was fixed at 3.5 and the triethylamine:SBA-15 weight ratio at 1.5 on a scale of 5 g of SBA-15/MM-SBA-15. After the reaction, the solid was separated by filtration, washed with toluene (300 ml) and inserted in a 0.5 wt.% water-ethanol solution (500 ml) under stirring for 24 hours. The resultant solid was washed with ethanol, dried in air in an oven at 90 ^{o}C for 24 hours, then calcined for 1 hour at 250^{o}C, 1 hour 400^{o}C and finally for 4 h at 500^{o}C all at 1 ^{o}C/min.

2.3.5. Silver nanoparticle deposition

Silver nanoparticles were deposited onto the porous supports using a wet impregnation technique. This involves stirring the support with a metal salt solution of correct concentration to achieve the desired loading, drying, and then calcining to decompose the precursor to promote sintering and metal particle growth. In a typical synthesis, 1 gram of support was weighed out into a 50 ml round bottomed flask with stirring and a minimum amount of water was added to produce a slurry. An appropriate amount of silver nitrate was added to produce a material of the required weight percentage and the slurry left stirring overnight, before being dried at 100 ^{o}C for 24 hours. The material was then calcined in air at 500 ^{o}C for 3 hours with a ramp rate of 1 ^{o}Cmin^{-1}.

2.4. Dissolution studies

Silver species dissolution experiments are performed in deionized water. 10 mg of sample was weighed out and dispersed in 50 ml of deionised water with stirring (500 rpm) at 35 oC with 5 ml samples removed and filtered at set time intervals before silver ion concentrations are measured using ICP-MS. The plots are then normalised to initial silver concentration to measure total dissolved silver as a percentage of total silver.

2.5. Microbiological assays

In order to determine the antimicrobial activity of the material developed, two widely recognised techniques were employed. The zone of inhibition test is a simple determination of if a material exhibits any activity at all, and is a semi-quantitative method of strength of activity. The logarithmic reduction method is a quantitative method of determining the amount of bacteria killed over a certain time frame.

2.5.1. Zone of Inhibition

Zone of inhibition testing is a standard, semi-quantitative method of determining antibacterial activity. Agar plates are inoculated with a known number of bacteria (~10^8 colony forming units (cfu)/ml) and test materials are loaded onto the plate before the plates are incubated to encourage bacterial growth. During the incubation period, the antimicrobial agents will diffuse through the agar and inhibit bacterial growth, which is visualised by a clear area surrounding the material indicating inhibited bacteria. These areas can be measured and compared against other materials on this same plate. The size of the zones not only depends on the strength of the material as an antimicrobial agent, but also on the number of bacteria on the plate and the diffusion of the agent through the agar, hence zones should be compared only on the same plate.

The tests were performed against *Staphylococcus aureas* ATCC 6538, *Escherichea Coli* ATCC 15224, MRSA ATCC 33591 and *Pseudomonus aeruginosa* ATCC 15442 as these bacteria represent common problematic organisms in hospital environments and give representation to both Gram-positive and Gram-negative bacteria.

The organisms were harvested from overnight cultures grown at 37 ^oC on nutrient agar. The harvested organisms were added to simulated body fluid (SBF, **Table 2.1**) and diluted to give a bacterial inoculum containing approximately 10^7 cfu/ml by use of a spectrophotometer and a calibration curve, with concentrations determined accurately using serial dilution and colony counting. The bacterial concentration is confirmed using a viable counts method, which involves serial dilution of the broth down to 10^2 cfu/ml and subsequent plating of the 3 solutions of lowest

concentration. These plates are incubated at 37 ^{o}C for 24 hours then the number of bacteria counted, by taking into account the dilution factors, the number of bacteria in the mother broth can be determined.

Agar plates are made up using a nutrient broth and agar powder, which is autoclaved at 120 ^{o}C. Samples are prepared for the experiment by dispersing 10 mg of solid in 1 ml of SBF (**Table 2.1**). Bacterial cultures are grown overnight and diluted to ~10^{8} cfu and spread over the agar surface using sterile spreaders before 5.5 mm wells are bored into the agar using a sterilised cutter. Following this, 50 µl of the dispersed sample is pipetted into the hole using a Gilson pipette and the plates are incubated at 37 ^{o}C for 24 hours. This is repeated in triplicate.

Ion	Simulated Body Fluid	Blood Plasma
Na^{+}	142	142
K^{+}	5	5
Mg^{2+}	1.5	1.5
Ca^{2+}	2.5	2.5
Cl^{-}	148.8	103
HCO_3^{-}	4.2	27
HPO_4^{2-}	1	1
SO_4^{2-}	0.5	0.5

Table 2.1: Ion concentrations mM in SBF solution.[9]

The plates are removed after the 24 hour incubation period and photographed alongside a rule. The zone size is then analysed using ImageJ software and normalised against silver content. Silver nitrate standards are used on all plates in order to determine semi-consistency between plates. **Figure 2.1** shows the clear zones caused by the bacterial inhibition. The arrows indicate the area which is measured, discounting the central well.

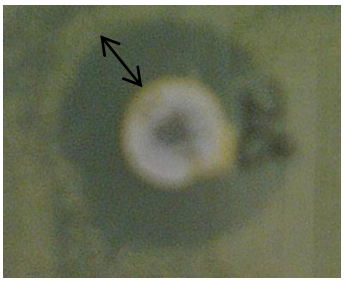

Figure 2.1: Example of zone of inhibition.

2.5.2. Minimum inhibitory concentration

Determination of a minimum inhibitory concentration was important in the quantitative analysis of the bactericidal activity of the materials, as suitable concentrations of materials were required to allow for bacterial growth.

The premise behind these tests was to measure the antimicrobial activity of the materials at different concentrations, to determine a breakpoint at which the activity was no longer seen. This involved serial dilution of a solution of the materials in SBF, followed by plating and incubation. A control was used to determine the point at which bacterial growth was similar in the sample containing potential antimicrobial agents to that without.

Staphylococcus aureas ATCC 6538 and *Pseudomonus aeruginosa* ATCC 15442 were all harvested as described in section 2.7.1. The test organism was prepared to solutions containing ~10^8 cfu/ml. Sample materials were prepared to a concentration of 10 mg/ml in bacterial inoculum before serial dilution was performed to give resultant solutions of 5 mg/ml, 1 mg/ml, 0.1 mg/ml, 0.5mg/ml and 0.01 mg/ml. These solutions were incubated at 37 ^{o}C for 4 hours, before being spread onto agar plates were incubated at 37 ^{o}C for 24 hours. The plates were removed and the colonies counted manually to determine a quantitative effectiveness as a function of concentration and determine a lower limit for antimicrobial activity.

2.5.3. Validity of neutralisation

In order to perform the logarithmic reduction experiments, a neutralising agent was required to avoid any continued antimicrobial activity affecting the results. The role of the neutraliser was to ensure that the antimicrobial species was rendered incapable of killing additional bacteria, effectively allowing for a snapshot of the percentage of bacteria killed at that moment in time. The test involves plating out bacteria in solution with neutraliser, neutraliser and sample, and a buffer solution, to ensure that not only does the neutraliser prevent antimicrobial activity, but also that it does not exhibit any of its own. If the bacterial growth on all plates is similar, the neutraliser can be considered effective.

Staphylococcus aureas ATCC 6538, *Pseudomonus aeruginosa* ATCC 15442 and *Escherichia coli* NCTC 10418 were all harvested by the same method as in section 2.7.1. The test organism was diluted to a resultant ~1000 cfu/ml of bacteria. Sulphur and chloride based salts were chosen as agents, due to the ability of sulphate and chlorides to bind strongly with silver and render it inactive.

A solution of tween 20 (1%), sodium dodecyl sulphate (0.4%) and sodium chloride (0.85%) was used. To determine the agent was effective in neutralising any remaining silver ions, 10mg of sample material was added to 1ml of neutralising agent in a sterile Eppendorf tube (10mg/ml) and serially diluted in SBF to 1mg/ml and 0.1mg/ml. 100µl of the solutions of test material, plus the neutraliser with no test material and only SBF as controls, were added to an agar plate, along with 100µl of the 1000cfu solution of harvested organism, which were then thoroughly spread to mix the two solutions. All the plates were incubated at 37^{o}C and counted after 3 days.

2.5.4. Logarithmic reduction

Staphylococcus aureas ATCC 6538, *Pseudomonus aeruginosa* ATCC 15442 and *Escherichia coli* NCTC 10418 were all harvested in the same method as described in section 2.7.1. The principle behind the logarithmic reduction experiment was to add a known number of microorganisms to a material and then count the number of bacteria to survive at set timepoints. The $\log_{10}$ number of bacteria to survive was subtracted

from the number of bacteria in the initial broth to give a quantitative representation of the ability of the material to kill microorganisms.

Quantitative antimicrobial activity was determined using a logarithmic reduction method. In this experiment, 5 mg of sample material was weighed into an Eppendorf tube and the target organism (harvested as in 2.7.1), added in nutrient broth at a concentration of 10^7 cfu, 1 ml of which was then added to the sample. 100 μl samples of the subsequent broth was removed at times of 0, 5, 30, 60, 120 and 240 minutes and added to 1 ml of neutralising agent. This solution was diluted using SBF to give concentrations of 10^{-2}, 10^{-4} and 10^{-6} cfu with the 10^{-2} and 10^{-4} specimen plated onto agar and incubated at 37 ^{o}C for 24 hours. The experiments were all run with positive and negative controls of silver nitrate and the pure organism. Once the growth period was complete, the colonies remaining were counted and dilution factors accounted for and the results normalised to colony count. The bacterial count at time t = 0 min is used to determine the logarithmic reduction of bacteria.

One $\log_{10}$ reduction is a 90% decrease in the number of microorganisms. The minimum target for the materials is a three $\log_{10}$ reduction (99.9%) in the number of bacteria, as this is the industry standard for a material to be classified as antimicrobial. If the $\log_{10}$ reduction in numbers of viable bacteria is approximately zero, this indicates the material is bacteriostatic or not active at all, depending on the growth of the control organisms. A negative $\log_{10}$ value indicates that the organisms are growing in the presence of the material.

The experiments were performed in triplicate and the results geometrically averaged in an effort to ensure minimal error during sample dilution.

2.6. Bulk characterisation

A range of techniques were used to characterise the composition and functional groups present on the synthesised materials which will be summarised below.

2.6.1. Energy dispersive x-ray absorption spectroscopy

Energy dispersive x-ray absorbance spectroscopy (EDAX) is a bulk elemental analytical technique which involves the examination of emitted x-rays following stimulated emission by an x-ray or high energy electron source.

EDAX was performed using Carl Zeiss Evo-40 SEM operating at 10 kV, fit with an Oxford Instruments INCA EDX. Samples were mounted on aluminium stubs using adhesive carbon tape. 5 regions were scanned across the samples and the average elemental compositions taken from these 5 scans.

X-rays which interact with atoms in their ground state can cause emission of core electrons, leaving behind an electron 'hole', which can be filled by an electron in a higher orbital. The difference in energy between the two orbitals is released in the form of x-rays which can be recorded by an x-ray detector and the element determined based on the energy.

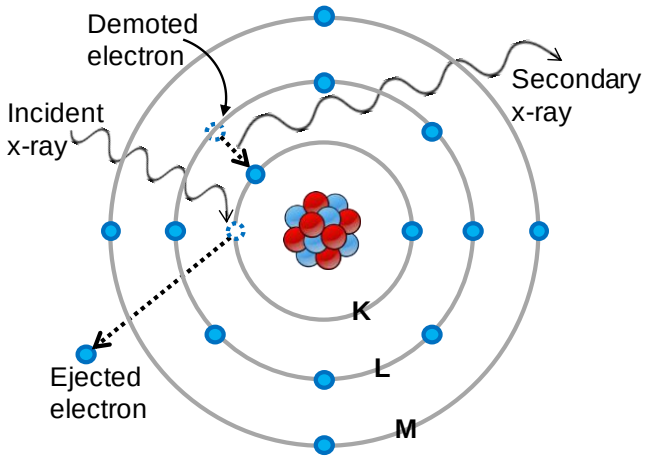

Figure 2.2: EDAX.

These energies are characteristic of elements, allowing for distinction between different elements and bulk quantitative elemental analysis of the sample, in a non-destructive technique.

2.6.2. Inductively coupled plasma mass spectroscopy

ICP-MS was employed to study the dissolution of Ag-nanocomposites as it provided high sensitivity to low levels of silver released from the materials and thus enabled more accurate analysis of silver release rate compared to other possible techniques (e.g. Ion selective electrodes).

ICP-MS was performed using a Varian Vista MPX ICP-MS system. Samples were referenced to a calibration made from a silver nitrate standard (Sigma Aldrich, 1000 ppm) made up to give concentrations of 10, 50, 100, 500 and 1000 ppb.

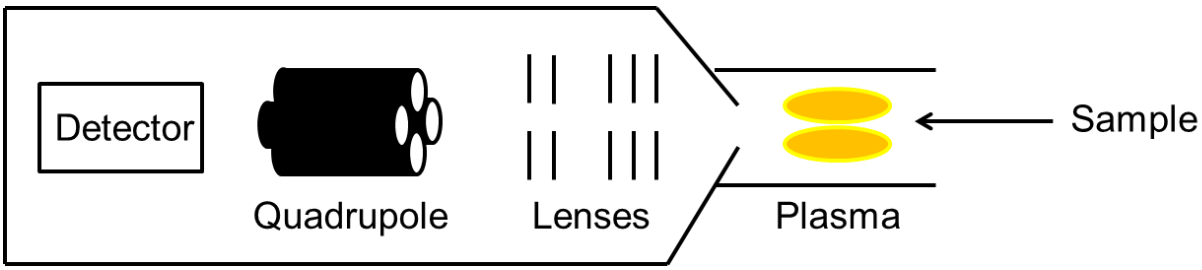

Figure 2.3: ICP schematic.

ICP-MS involves detecting ions within the sample chamber which are distinguished by their mass-to-charge ratio (m/z value, **figure 2.3**). The ions are created using an argon plasma source, which is heated to around 8000 ^{o}C to produce an environment conducive to ion production. The samples, in aqueous solution, are passed through a nebuliser, allowing the sample to enter the plasma torch as an aerosol which is then passed into the analyser as a gaseous, ionized sample, using argon as a carrier gas. The ions are focused using electrostatic lenses into the analyser which then uses a quadrupole mass filter to differentiate the ions present.

2.6.3. Infrared Spectroscopy

Infrared spectroscopy was used to probe the organic moieties encompassed within the nanocomposite architectures.

The analysis of solids by infrared spectroscopy is typically undertaken by using self-supporting wafers of KBr-diluted samples in transmission mode, Diffuse

Reflectance Infrared Fourier Transform Spectroscopy (DRIFTS), or Attenuated total reflectance (ATIR). In this thesis ATIR was employed as it allowed analysis on small sample sizes using a single bounce diamond anvil ATR accessory fitted to a Thermo-Fisher Nicolet IS50 FT-IR spectrometer. ATR is a sampling method which allows IR analysis of a liquid or solid sample by measuring absorption of infrared radiation at the surface of a crystal, commonly comprised of diamond, zinc selenide and germanium.

Infrared spectroscopy measures the absorption of infrared radiation by excitation of vibrational modes of chemical bonds in molecules, the frequency (υ) of which is characteristic of the bond strength (k) and reduced mass of functional groups (μ) according to Hooke's law (**Equation 2.1)**.

$$\upsilon = \frac{1}{2\pi}\sqrt{\frac{k}{\mu}}$$

Equation 2.1: Hooke's law.

The resulting absorptions give rise to characteristic finger print spectra of the target molecule, allowing for functional groups to be assigned and identified.

The vibrational modes must satisfy a selection rule in order for it to absorb infrared radiation, in which the stretch or bend must be associated with a change in dipole moment. Stronger (more intense) absorptions are the result of larger changes to the dipole moment.[10] Detail reviews on the application of IR spectroscopy in the characterisation of materials can be found in the following references.[11-13]

The ATR sampling method utilises total internal reflection to create an evanescent wave, which probes between 0.5 and 2 microns into the sample, before exiting the crystal and being collected by the detector to produce the spectra (**Figure 2.4**).

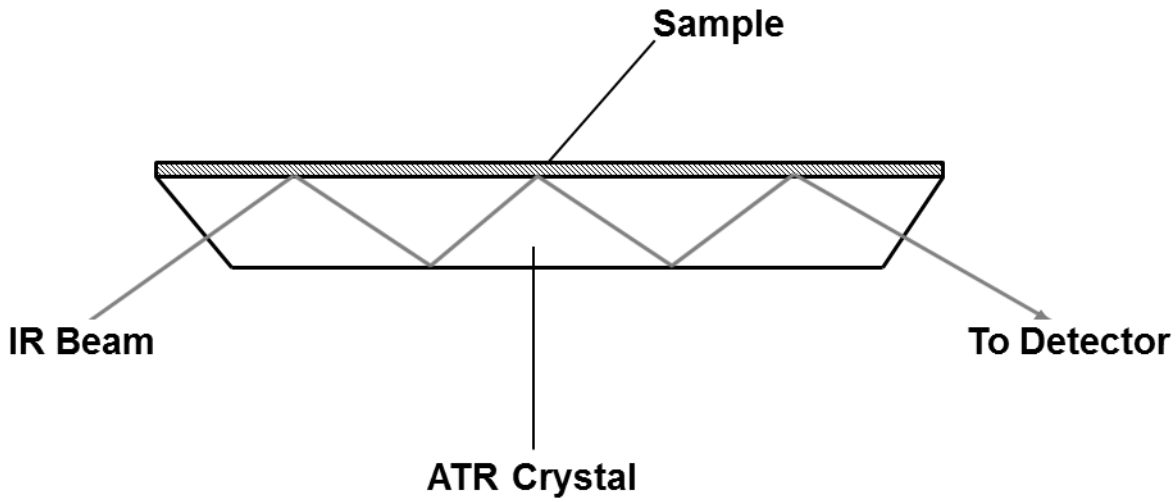

Figure 2.4: ATR crystal schematic.

2.6.4. Nitrogen porosimetry

Porosimetry analysis is used to determine textural physical characteristics of materials such as surface area, pore volumes and pore diameter.

Porosity and surface area were measured using a Quantachrome NOVA 4200e instrument by N_2 adsorption using NovaWin v11.0 analysis software. Samples were degassed under vacuum at 120 ^{o}C for at least 2 hours prior to analysis. Adsorption/desorption isotherms were recorded at -196 °C. BET surface areas were calculated over the relative pressure range 0.05-0.2 where a linear relationship was observed. Microporosity was assessed using the t-plot method, over the relative pressure of 0.2-0.5 which displayed a linear correlation. Mesopore diameters were calculated applying the BJH method to the desorption branch.

Adsorption, at constant temperature and pressure, decreases the entropy of a system, thus enthalpy of adsorption must be negative (exothermic)[14] if they are to occur (Gibbs free energy).[15] Collisions between gas molecules and the surface of the sample can be either elastic (i.e. no interaction), or inelastic. Energy loss from the adsorbate to the adsorbent, during inelastic collisions, make this an exothermic process. If this energy transfer process is substantial enough, spontaneous desorption can be avoided and, provided that no more energy loss occurs through the formation of chemical bonds, this adsorption is classed as physisorption. N_2 adsorption only occurs at temperatures below

the adsorbate boiling point[15], due to the small enthalpy of adsorption. The enthalpy of vaporisation (condensation) from adsorbate-adsorbate interactions is very close in value to the enthalpy of adsorption, which permits multilayer adsorption.[16]

N_2 adsorption and multilayer formation, at liquid nitrogen temperature, results from induced temporary dipoles, arising from variations in electron density, known as London forces.[15] Nitrogen adsorption porosimetry involves dosing N_2 incrementally and recording the amount adsorbed at a known pressure and constant temperature. By plotting the amount of adsorbate against the partial pressure of the system, an isotherm can be constructed, which can provide information regarding the material structure and properties. **Figure 2.5** shows six IUPAC isotherm classifications.

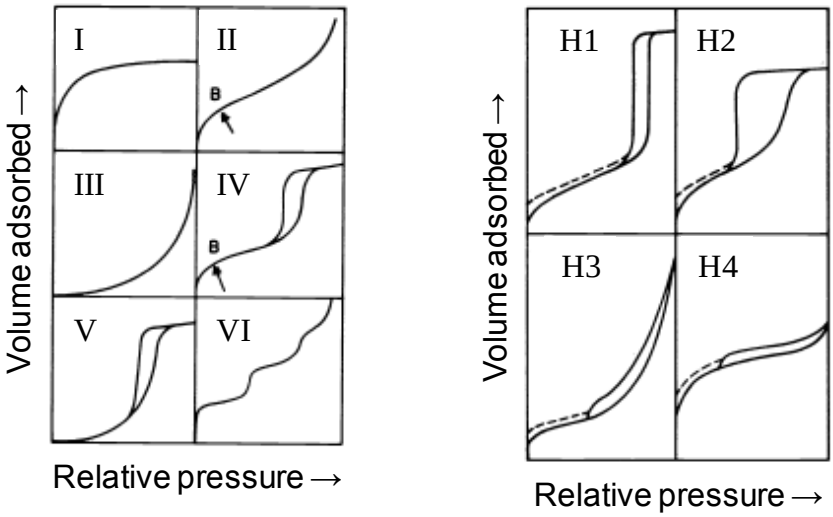

Figure 2.5 : Isotherm and hysteresis types.[17]

Type I represents a microporous material, type II is indicative of a non-porous or macroporous material, type III is the result of stronger adsorbate-adsorbate interactions than adsorbate-adsorbent, type IV and V exhibit a hysteresis loop, which is the result of capillary condensation within mesoporous materials and type VI exhibits a stepwise profile from consecutive adsorbate layers forming, due to a highly uniform surface.[18] Hysteresis loops can also translate information regarding the mesopore environment. Hystereses occur due to differences in the adsorption and desorption processes. Adsorption occurs via a capillary condensation mechanism, from the pore walls inwards, whereas desorption occurs at the liquid surface, at the pore opening. Evaporation occurs at a lower pressure relative to condensation due to the stronger

interactions involved in this mechanism, which produces the hysteresis.[16] The hysteresis shape is dictated by the pore shapes, H1 is from uniform pore sizes, whereas H2 occurs from non-uniform pores with ink-bottle type structures. H3 and H4 are the result of slit type pores.[18]

The Brunauer, Emmett and Teller (BET) isotherm for physisorption of gases onto solids by intermolecular forces can be used to calculate the surface area of the adsorbate. The BET isotherm is an extension of the Langmuir isotherm, which describes monolayer molecular adsorption and can be used to calculate surface areas based on certain assumptions; gas molecules adsorb are distributed onto a solid in infinite layers, no interactions occur between the layers and that each layer can be expressed by the Langmuir theory. The resultant equation forms a $y = mx + c$ format, as shown in **equation 2.2**.

$$\frac{1}{V\frac{P}{P_0}} = \frac{C-1}{V_m C}.\frac{P}{P_0} + \frac{1}{V_m C}$$

Equation 2.2: BET equation.

$$V_m = \frac{1}{(Gradient + Intercept)}$$

$$C = \frac{Gradient}{Intercept} + 1$$

P = pressure; P_0 = saturation pressure; V = volume adsorbed; V_m = monolayer volume; C = multilayer adsorption parameter

Surface areas are calculated from **equation 2.3** Using the monolayer volume, and assume N_2 molecules close pack and occupy 0.162 nm^2.[18]

$$sa = \frac{V_m \sigma N_A}{mv}$$

Equation 2.3: Surface area via BET analysis.

For analysis of pore size, the Barrett-Joyner-Halenda adsorption model is employed, up to $P/P_0 = 0.95$. This method involves the area of the isotherm above the pressures involved in the BET analysis as it models the formation of multilayers and parallel capillary condensation within the pore structure of the material. Capillary condensation is described by the Kelvin equation, which describes the relationship between pore radius and the pressure required to fill said pore radius (**Equation 2.4**).

$$Ln\frac{P}{P_0} = \frac{-2\gamma V_m}{RTr_m}$$

Equation 2.4: The Kelvin equation.

2.6.5. Powder X-ray diffraction

Powder XRD was employed to study the crystal structures of synthesised materials, to confirm the identity of prepared nanoparticles and measure the volume averaged crystallite size.

XRD patterns were recorded on either a Panalytical X'pertPro diffractometer fitted with an X'celerator detector, or a Bruker D8 Advance diffractometer fitted with a LynxEye high-speed strip detector, both using Cu Kα (1.54Å) sources with a nickel filter, calibrated against either Si (Panalytical) or SiO2 (Bruker) standards. Low angle patterns were recorded over a range of 2θ = 0.3-8° (step size 0.01°, scan speed 0.014 ° s^{-1}) and wide angle patterns over a range of 2θ = 25-75° (step size 0.02°, scan speed 0.020 ° s^{-1}).

X-rays were discovered in 1895, by Wilhelm Roentgen[19], then in 1912, experiments undertaken by Max vin Laue determined the wave characteristics of X-rays from studies on a single crystal[20] which lead to the field of X-ray crystallography.

In 1919, A.W Hull published his work on the interaction of x-rays with crystalline substances, which involved probing the arrangement of the materials in question, rather than the electronic configuration of the atoms involved. Monochromatic x-rays were fired through a powdered sample, and the diffraction

pattern recorded on photographic film over the period of an hour.[21] The diffraction pattern was noted to correspond to different planes in the material, and that different structures with different planes would produce different patterns, with chemically similar structures forming similar patterns.

Powder X-ray diffraction is incredibly useful for materials and catalysis studies, due to the fact it eliminates the need for a single crystal sample. Instead, a small sample of the material, ground into a fine powder, can be studied, allowing for the likes of nanocomposites, hierarchically porous inorganic structures and metal nanoparticles to be studied with ease.

X-rays striking a polycrystalline sample give rise to a cone of diffraction, from the countless array of orientations/planes. The X-ray detector moves around a set angle, covering the set of 2θ values which are of interest (**Figure 2.6**).

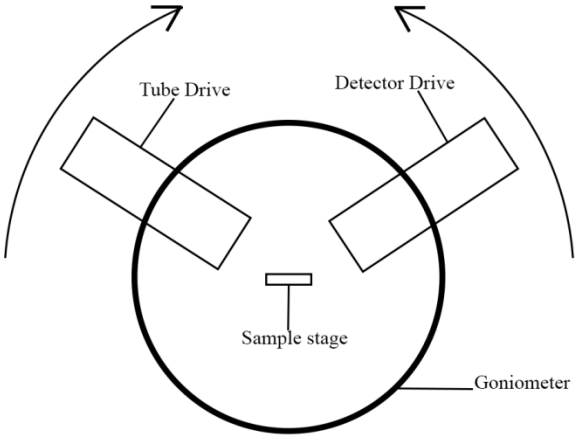

Figure 2.6: Schematic of a powder X-ray diffractometer.

X-ray diffraction patterns result from the constructive and destructive interference of monochromatic X-rays upon scattering within a crystal lattice. The atoms in a crystalline material are arranged in a regular motif, resulting in planes of atoms which will scatter the incoming X-rays by different amounts depending on the

plane spacing. The angle at which the peaks appear in the spectra is related to the *d*-spacing of the plane of the target material's crystal lattice. This relationship is described by Bragg's law (**Equation 2.5**) developed by William H. Bragg and William L. Bragg in 1913, and can be used to determine the lattice dimensions and the crystal structure of the material.

$$n\lambda = 2d\sin\theta$$

Equation 2.5: Bragg's law.

The intensities and occurrences of different peaks are directly related to the unit cell arrangement of the crystal structure or ordered pores . There are seven crystal classes that can be used to describe the structure of crystalline materials which are combined with the basic lattice types (cubic, face-centred cubic, base-centred cubic and body-centred cubic) to form one of 14 unique 'Bravais Lattices'.[22]

In order to determine the lattice spacing of the material in question, a relationship between the Bragg angle obtained from the XRD spectra and the distance between atoms must be derived. Shown in **Figure 2.7** is a representation of two X-rays interacting with a lattice plane.

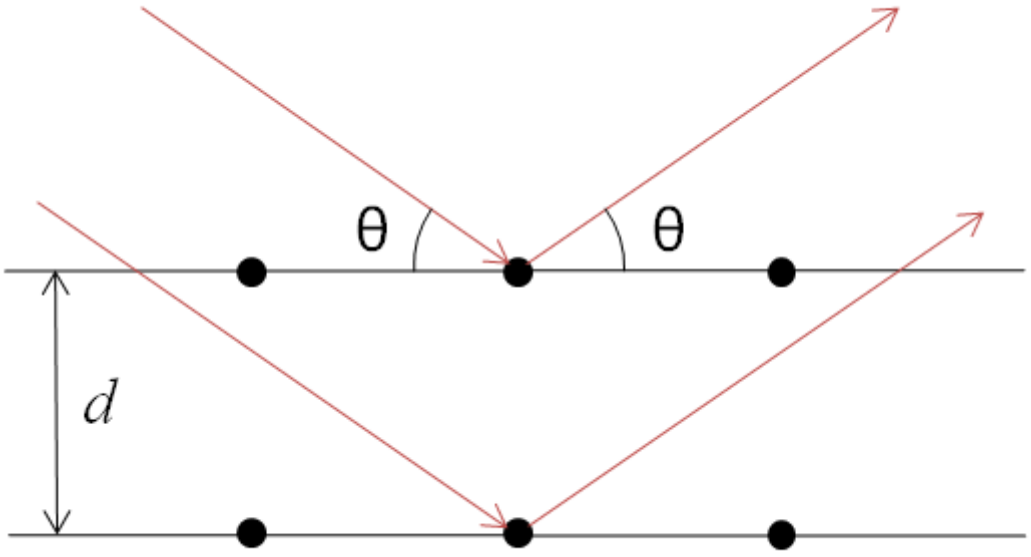

Figure 2.7: Schematic of x-ray interaction with a crystal lattice.

The first X-ray reflects off the outer atomic layer, the angle of reflection equal to the angle of incidence. The second X-ray is parallel to the first and reflects off of the second atomic plane. It must travel a further distance of 2*a* from the first, the angle of incidence and reflection are, of course, equal to that of the first X-ray. If the distance of 2*a* is equal to an integer number of wavelengths (λ), then the X-rays will be in phase after this interaction, leading to constructive interference. If the distance is not an integer of the wavelength, this will cause destructive interference. Using this knowledge, it can be said that for constructive interference to occur, the condition which must be met it;

$$n\lambda = 2a$$

Equation 2.6: Constructive interference.

Combining this with basic trigonometric relationships, it can be determined that the distance between planes, *d*, is equal to;

$$d = a / \sin\theta$$

Equation 2.7: Constructive interference.

This equation can be rewritten as,

$$2a = 2d \sin\theta$$

Equation 2.8: Constructive interference.

And combined with **equation 2.6** to give Bragg's Law (**equation 2.5**)

Using the miller indices of the planes studied, a relation can be observed between the *hkl* values and the *d*-spacing;

$$d = \frac{a}{\sqrt{h^2 + k^2 + l^2}}$$

Equation 2.9

This can then be combined with Bragg's law (**equation 2.5**), to give a modified version of the Bragg law, encompassing the miller indices (**equation 2.10**);[22]

$$(\frac{\lambda}{2a})^2 = \frac{sin^2\theta}{h^2 + k^2 + l^2}$$

Equation 2.10

Bragg's law describes the incoming radiation and the result of the interaction between it and the crystal lattice (as shown in **Figure 2.7**). As radiation of wavelength λ scatters from a lattice with a lattice parameter *d* it will return a peak in the spectra (constructive interference) of θ (reported as 2θ in practise). Since the wavelength is a constant, depending on the X-ray source, rotating the detector will pick up diffracted radiation of different Bragg angles which correspond to individual planes, allowing the full crystal structure to be determined.[23, 24]

Determination of crystallite size is another very useful result of powder X-ray diffraction studies by use of the Scherrer equation (**Equation 2.11**), developed in 1918 by Paul Scherrer.[25] To observe sharp maxima, crystallites must be of a large enough size as to ensure that slightly away from the 2θ maxima, destructive interference occurs. The diffracted waves are only slightly out-of-phase between successive planes, meaning that many planes are needed to completely remove waves either side, but close to, the 2θ maxima. When the crystallites involved are small (in the nanoscale region), the number of planes, and hence degree of destructive interference, is insufficient to completely remove these waves, resulting in a broadening of the diffraction peak. The Scherrer equation relates this peak breadth to particle size.

$$B = \frac{K\lambda}{L\cos\theta}$$

Equation 2.11: The Scherrer equation for particle size analysis by X-ray diffraction, where λ is the wavelength of the monochromatic X-ray beam used for analysis, K is the shape factor, equal to 0.89 for spherical particles, L is the crystallite diameter, B is the FWHM of the observed peak and θ is the Bragg angle.[26]

2.6.6. Transmission electron microscopy

Transmission electron microscopy (TEM) analysis was employed to observe the morphology of the synthesised materials, as well as assess particle and composite dimensions through localised direct imaging of samples.

High resolution TEM (HRTEM) analysis was performed using either a JEOL-2100 LaB_6 TEM fitted with a Gatan 0.2Å camera, or a Phillips CM12 transmission electron microscope operating at 100kV, and images recorded by a SIS MegaView III digital camera. The data was analysed using ImageJ software and Microsoft Excel.

Limitations on the resolution of optical microscopes arise from the wavelengths of visible light (~ 380-750 nm). This is overcome through the use of electrons to image materials on the nanoscale, due to the much shorter wavelength (~12.3 pm at 10 kV decreasing to 2.5 pm at 200 kV), enhancing microscope resolution to an atomic level under high resolution TEM/STEM conditions.[27] Using an electron beam and condensing lenses, a probe can be focused onto a material sample (**figure 2.8**), the interaction (or non-interaction) of which produces a 2d, black and white image, the contrast of which is dependant upon a number of variables, including thickness, atomic mass and density.[27] Electrons are scattered by atomic nuclei (more so by heavier nuclei), allowing determination between different phases within composite materials.

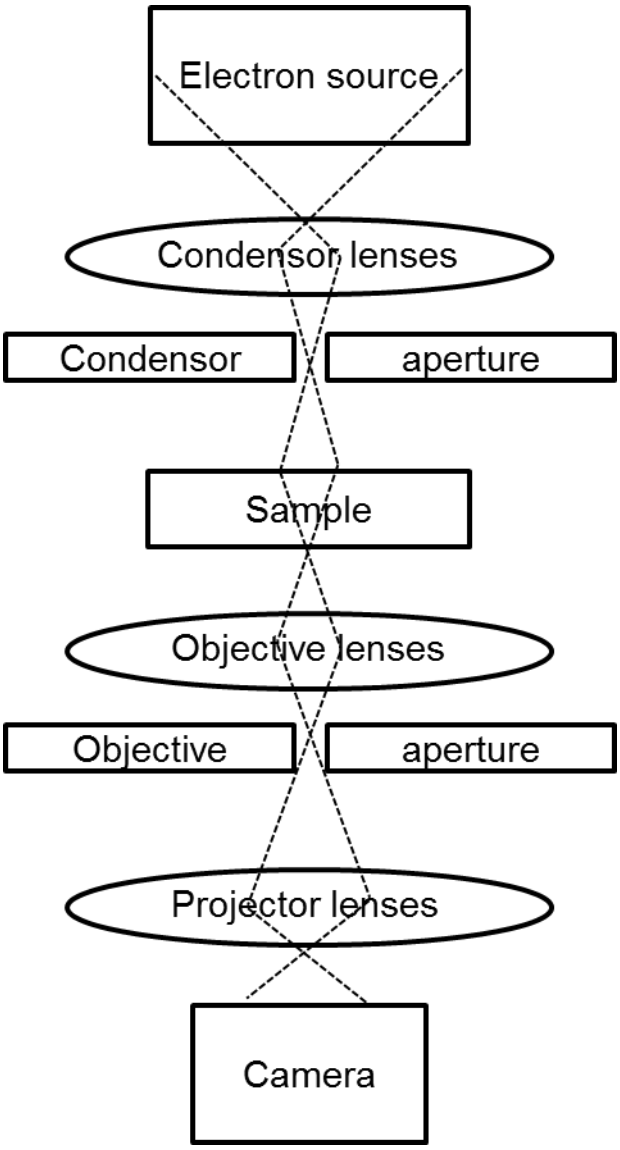

Figure 2.8: Schematic of a TEM.

2.7. Surface characterisation

2.7.1. X-ray photoemission spectroscopy

XPS is a powerful technique for the analysis of surface composition and oxidation state of materials.

XPS measurements in this thesis were collected using a Kratos AXIS HSi instrument, equipped with a charge neutraliser and using a monochromated Al Kα (1486.6 eV) X-ray source. High resolution spectra were recorded using a pass energy of 40 eV with data analysed and fit using CasaXPS Version 2.3.15. All spectra were charged corrected to the adventitious carbon at 284.7 eV with elemental sensitivity factors applied to quantify sample composition. Errors were estimated by varying a Shirley background across reasonable limits.

XPS or as is it also known electron spectroscopy for chemical analysis (ESCA), is a technique used in materials analysis used to probe the elemental composition of surfaces. In addition to elemental analysis, XPS also provides information about oxidation states, chemical environments and coating thicknesses among others. XPS is based on the principles of the photoelectric effect, a famous theorem developed by Albert Einstein, the origins of which can be traced further back to Heinrich Hertz, who first discovered the effect during a study of 'The effect of ultraviolet light on an electrical discharge'.[28] Hertz noticed that in the presence of UV light, sparks are generated more easily by electrodes, this was explained by Einstein in 1905 as the photoelectric effect, and would earn him the Nobel prize.

When X-rays are fired at the material core-level electrons are ejected, which are known as photoelectrons, which are released with different kinetic energies depending on various factors, such as the x-ray energy, element involved, it's orbital and the coordination/oxidation state of the element according to the following energy diagram (**figure 2.9**).

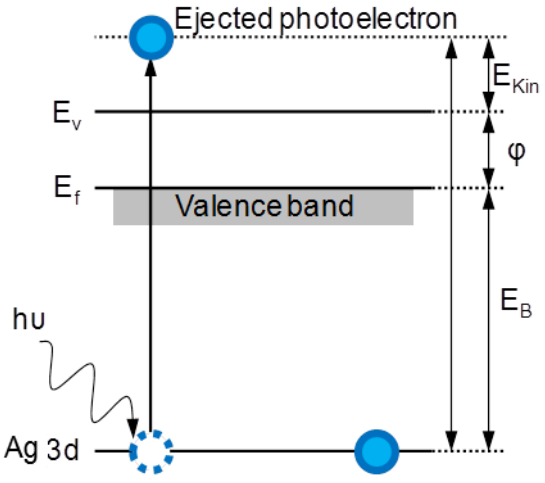

Figure 2.9: Graphical representation of photoelectron ejection.

The kinetic energies of released photoelectrons can be measured and the binding energies calculated using **equation 2.12**.

$$E_{Kin} = h\nu - E_B - \varphi$$

Equation 2.12: Relationship between kinetic energy of released electrons (E_{Kin}), the energy of the incoming X-rays ($h\nu$), the binding energy of the photoelectrons (E_B) and the work function of the spectrometer (φ).

The calculated binding energies can be referenced to a database of standards from the National Institute of Standards and Technology (NIST) photoelectron spectroscopy database to determine chemical identity and garner information regarding chemical environment.[29]

High resolution XPS spectra also show fine structure from spin orbit coupling, which arises from the magnetic moment from the spin (*s*) of the electron which can take value ±½, coupling with the angular momentum of the orbital (*l*) from which it originates. The combination of these two terms gives rise to the total angular momentum (*j*), according to **equation 2.13**, with electrons in orbitals with $l > 0$ giving rise to doublets in XPS spectra due to this coupling effect.

$$j = l + s$$

Equation 2.13: Total angular momentum.

The integrated areas of the two spin orbit split doublets should be in a fixed ratio depending on the degeneracy of the orbital in which the electrons lie. This is easily calculated using the values for the total orbital angular momentum, for example, if observing photoemission from a 2p orbital, for which the orbital angular momentum, *l*, is 1, *j* would be calculated to be either $^3/_2$ or $^1/_2$.. When the atoms in question are light, it is appropriate to use the Russell-Saunders coupling approximation, which works with low spin-orbital couplings as it assumes that the coupling is only effective when all the orbital momenta are operating cooperatively. In such a case all of the electron spins couple to give a total of *S* and all of the orbital angular momenta couple to give *L*

allowing the total angular orbital momentum, *J*, to be calculated using the Clebsch-Gordan series. The multiplicity dictates the ratio of the areas under the peaks for the 2 peaks ($^3/_2$ and $^1/_2$ in the case of p-orbitals), which is calculated using **equation 2.14**;

$$\text{Multiplicity} = 2j + 1$$

Equation 2.14: Multiplicity

For a p-orbital, this returns multiplicities of 4 and 2, which would indicate ratios of the $2p_{3/2}$ and $2p_{1/2}$ component areas of 2:1. The magnitude of the spin orbit coupling will also determine the size of the splitting, which can be measured experimentally and compared to the NIST database. In some cases, this can be further complicated by multiplet splitting, which can be caused by emission of a photoelectron from the core of an atom which has spin itself (unpaired valence electrons) the final states of which can involve coupling between the unpaired valence electrons and unpaired core electrons. Multiplet splitting is most commonly seen in the spectra of first row transition metal elements, from titanium to copper.

Other features of XPS spectra include Auger lines (arising from outer shell electrons 'falling' back into the holes in the core shells left by photoelectron emission and result in peaks of energies independent of exciting energy), satellites (peaks arising from other x-ray components, i.e. $K_{\alpha 2}$ or K_{θ}), ghost peaks (peaks arising from contaminated x-ray sources, though these are rarely seen), shake-up lines (failure of an ion to return to the ground-state following photoemission, mainly an issue with paramagnetic compounds) and energy loss lines (interaction of photoelectron with electrons in the surface region of the sample, which causes metallic species peaks to become asymmetric).

XPS must be done in UHV conditions (typically $<10^{-9}$ bar) as the mean free path of the electrons is not high, such strong attenuation is also the reason why XPS is so surface sensitive. This surface sensitivity can be taken advantage of in calculating coating thicknesses[30] or quantifying dispersion.

By utilising the principles of the photoelectric effect, mainly that altering the energy of the incoming radiation affects the kinetic energy of the released

photoelectrons, shell or coating thicknesses can be determined. Knowledge of the mean free path of the photoelectrons is required for this calculation. Using a dual anode (non-monochromated) X-ray source, which is commonly found in X-ray photoelectron spectrometers), or two monochromated sources of different photon energies (i.e. a silver source and an aluminium source), the analytical depth of XPS can be varied. The escape depth of the photoelectron is dependent on its kinetic energy, varying according to the Universal escape depth curve. By varying the photon energy, the depth from which photoelectrons emergy without undergoing inelastic collisions will be altered. If the escape depth is increased then electrons from deeper layers can be probed, allowing for example material underneath a coating, or inside a shell to be analysed. The mean free path of photoelectrons of many common materials can be calculated from the Universal escape depth curve.[31]

Using this knowledge, the energies of any incoming radiation and **equation 2.15**, final radiation intensity can be calculated;

$$I = I_o e^{-\alpha \chi}$$

Equation 2.15: Attenuation.

Which in this case is written as,

$$I = I_o e^{-d \, l \, P_f \cos \theta}$$

Equation 2.16: Attenuation.

Where d is the shell thickness in nanometres, I is the atomic percentage measured experimentally, I_o is the atomic percentage before attenuation, θ is the detection angle (assumed to be zero) and P_f is the inelastic mean free path (IMFP, reported in nanometres). It is experimentally possible to measure the atomic percentage, and the values for the IMFP are freely available, leaving the initial atomic percentage values and the shell thickness. Rearranging the equations and solving the simultaneous allows d to be calculated, first by taking logs of both sides gives **equation 2.17**.

$$\ln(I) = \ln(I_o e^{-d\, l\, P \cos\theta})$$

Equation 2.17: log attentuation

Expanding out,

$$\ln(I) = \ln(I_o) - d\, l\, P \cos\theta$$

Equation 2.18: Attenuation.

And rearranging, allowing for $\theta = 0^o$,

$$\ln(I_o) = \ln(I) + d / P$$

Equation 2.19: Attenuation.

With $\ln(I_o)$ as the subject, writing out the equations with the two sets of data in mind results in (subscript denotes type of X-ray source);

$$\ln(I_o) = \ln(I_{Mg}) + d / P_{Mg}$$

$$\ln(I_o) = \ln(I_{Al}) + d / P_{Al}$$

Equation 2.20: Simultaneous equations to determine shell thickness.

Combining these and solving for *d*, gives an **equation 2.22** for calculation of shell thickness,

$$\ln(I_{Al}) + d / P_{Al} = \ln(I_{Mg}) + d / P_{Mg}$$

$$\ln(I_{Al}/I_{Mg}) = d(1/P_{Mg} - 1/P_{Al})$$

Equation 2.21

$$d = \ln(I_{Al}/I_{Mg})\ (1/P_{Mg} - 1/P_{Al})$$

Equation 2.22: Determination of shell thickness by XPS.

2.8. References

1. T. Li, J. Moon, A. A. Morrone, J. J. Mecholsky, D. R. Talham and J. H. Adair, *Langmuir*, 1999, **15**, 4328-4334.
2. J. Zhang, Z. Ma, J. Jiao, H. Yin, W. Yan, E. W. Hagaman, J. Yu and S. Dai, *Langmuir : the ACS journal of surfaces and colloids*, 2009, **25**, 12541-12549.
3. Q. Zhang, T. Zhang, J. Ge and Y. Yin, *Nano Letters*, 2008, **8**, 2867-2871.
4. L. Han, H. Wei, B. Tu and D. Y. Zhao, *Chemical Communications*, 2011, **47**, 8536-8538.
5. O. Franke, J. Rathouský, G. Schulz-Ekloff and A. Zukal, in *Studies in Surface Science and Catalysis*, eds. J. M. B. D. P. A. J. G. Poncelet and P. Grange, Elsevier, 1995, vol. Volume 91, pp. 309-318.
6. D. Zhao, J. Feng, Q. Huo, N. Melosh, G. H. Fredrickson, B. F. Chmelka and G. D. Stucky, *Science*, 1998, **279**, 548-552.
7. S. Vaudreuil, M. Bousmina, S. Kaliaguine and L. Bonneviot, *Advanced Materials*, 2001, **13**, 1310-1312.
8. M. V. Landau, E. Dafa, M. L. Kaliya, T. Sen and M. Herskowitz, *Microporous and Mesoporous Materials*, 2001, **49**, 65-81.
9. T. Kokubo, H. Kushitani, S. Sakka, T. Kitsugi and T. Yamamuro, *Journal of biomedical materials research*, 1990, **24**, 721-734.
10. G. Clayden, W. Warren, N. Greeves and P. Wothers, *Organic Chemistry*, Oxford University Press.
11. F. Zaera, *Chemical Society Reviews*, 2014.
12. B. L. Mojet, S. D. Ebbesen and L. Lefferts, *Chemical Society Reviews*, 2010, **39**, 4643-4655.
13. J.-M. Andanson and A. Baiker, *Chemical Society Reviews*, 2010, **39**, 4571-4584.
14. G. A. Somorjai and Y. Li, *Introduction to surface chemistry and catalysis*, John Wiley & Sons, 2010.
15. R. P. H. Gasser and G. Ehrlich, *Physics Today*, 2008, **40**, 128-129.
16. P. A. Webb and C. Orr, *Analytical methods in fine particle technology*, Micromeritics Instrument Corp, 1997.
17. R. Pierotti and J. Rouquerol, *Pure Applied Chemistry*, 1985, **57**, 603-619.
18. J. Rouquerol, F. Rouquerol and K. S. Sing, *Adsorption by powders and porous solids*, Academic press, 1998.
19. W. C. Röntgen, *British Journal of Radiology*, 1931, **4**, 32-33.
20. M. Von Laue, W. Friedrich and P. Knipping, *Annalen der Physik*, 1913, **41**, 971.

21. A. W. Hull, *Journal of the American Chemical Society*, 1919, **41**, 1168-1175.

22. M. T. Weller, *Inorganic materials chemistry*, Oxford University Press Oxford, 1994.

23. R. Jenkins and R. Snyder, *Introduction to X-ray powder diffractometry*, John Wiley & Sons, 2012.

24. B. D. Cullity and S. R. Stock, *Elements of X-ray Diffraction*, Prentice hall Upper Saddle River, NJ, 2001.

25. P. Scherrer, *Nachrichten von der Gesellschaft der Wissenschaften zu Göttingen, mathematisch-physikalische Klasse*, 1918, **1918**, 98-100.

26. A. Patterson, *Physical review*, 1939, **56**, 978.

27. T. G. Rochow and P. A. Tucker, *Introduction to microscopy by means of light, electrons, X rays, or acoustics*, 2nd edn., Springer, New York, 1994.

28. H. Hertz, *Annalen der Physik (Leipzig)*, 1887, **31**, 983-1000.

29. X. Nist, 1997.

30. A. G. Shard, *The Journal of Physical Chemistry C*, 2012, **116**, 16806-16813.

31. *http://www.lasurface.com/xps/imfp.php*.

Chapter 3: Silver-silica core-shell nanocomposites: reverse micelle synthesis

3.1. Introduction

Silver-silica core-shell materials were synthesised using a modified procedure by Adair *et al*[1] as described in **Chapter 2.1**. Reverse micelles containing a silver nitrate precursor in an aqueous phase were formed by dispersing an Igepal co-520 polyoxyethylene nonyl phenyl ether surfactant in an organic cyclohexane phase based on the work by Osseo-Asare *et al*.[2] This methodology has been used to incorporate a variety of metal and metal oxide nanoparticulate cores into silica sphere composite architectures, including Palladium,[3] metallic iron,[4] magnetite[5] and gold.[6] Silver residing within the reverse micelles was subsequently reduced via hydrazine, prior to the addition of ammonium hydroxide as a base catalyst to initiate condensation of an inorganic silica shell from a tetraethyl orthosilicate (TEOS) precursor. These materials were then screened via a range of microbiological assays including the Zone of Inhibition (ZOI) method, the Minimum Inhibitory Concentration (MIC) method, and the Logarithmic Reduction method against *Staphylococcus aureus* and *Pseudomonas aeruginosa* as representative Gram-positive and Gram-negative microorganisms.

3.2. Results and discussion: Silver core size variation

A series of nanocomposites were first synthesised as a function of water concentration by varying the water:surfactant molar ratio (W_o) with a view to producing different core dimensions and thereby assessing the impact of silver core diameter upon antibacterial activity (while maintaining a fixed silica shell thickness). In order to confirm the successful synthesis of the desired core-shell morphology, and determine the silver core size, a variety of bulk and surface sensitive characterisation techniques were employed.

3.2.1. Transmission electron microscopy (TEM)

Direct visualisation of the silver-silica nanocomposites was achieved through high resolution bright-field TEM, enabling accurate measurement of each structural component. **Figure 3.1** shows representative micrographs of the silver-silica

nanocomposites as a function on core size. All materials comprised approximately spherical nanoparticles possessing the desired core-shell morphologies, wherein a darker (denser, high atomic number) shell is apparent associated with a silver containing phase, fully-encapsulated within a lighter (low density) phase indicative of a silica matrix. Particle size distributions and the normal/cumulative distribution for each nanocomposite are shown in **Figure 3.2** and **Figure 3.3**, based upon analysis of >50 particles in every case.

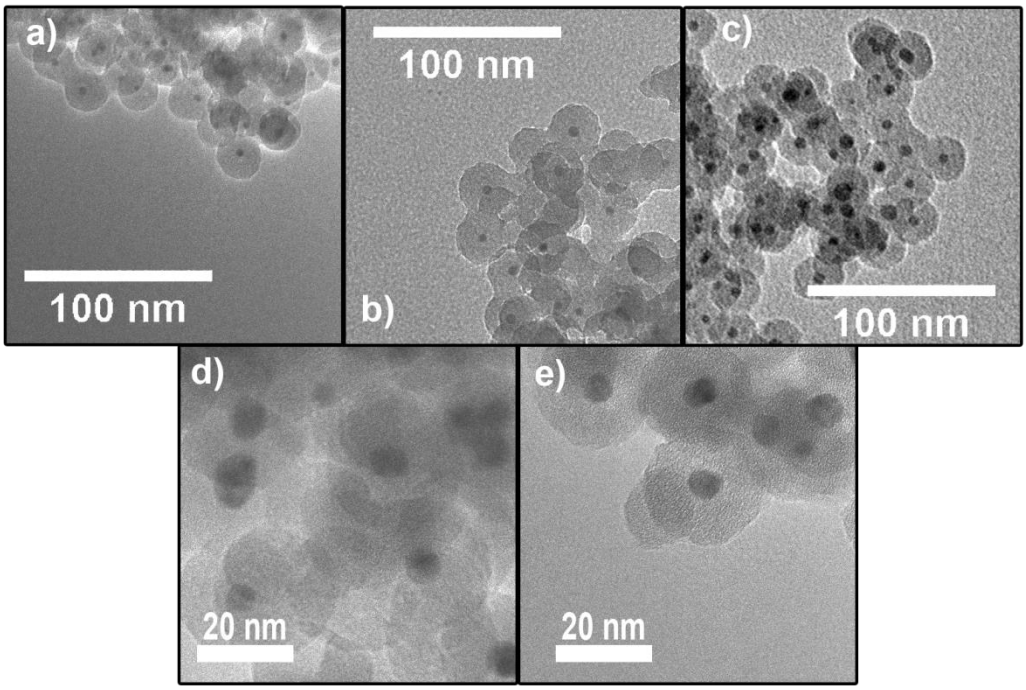

Figure 3.1: Representative bright-field HRTEM images of silver-silica nanocomposites as a function of W_o molar ratio (a) 2, (b) 4, (c) 6, (d) 8, (e) 10. Inset highlights well-defined phase boundary between the silver core and silica shell.

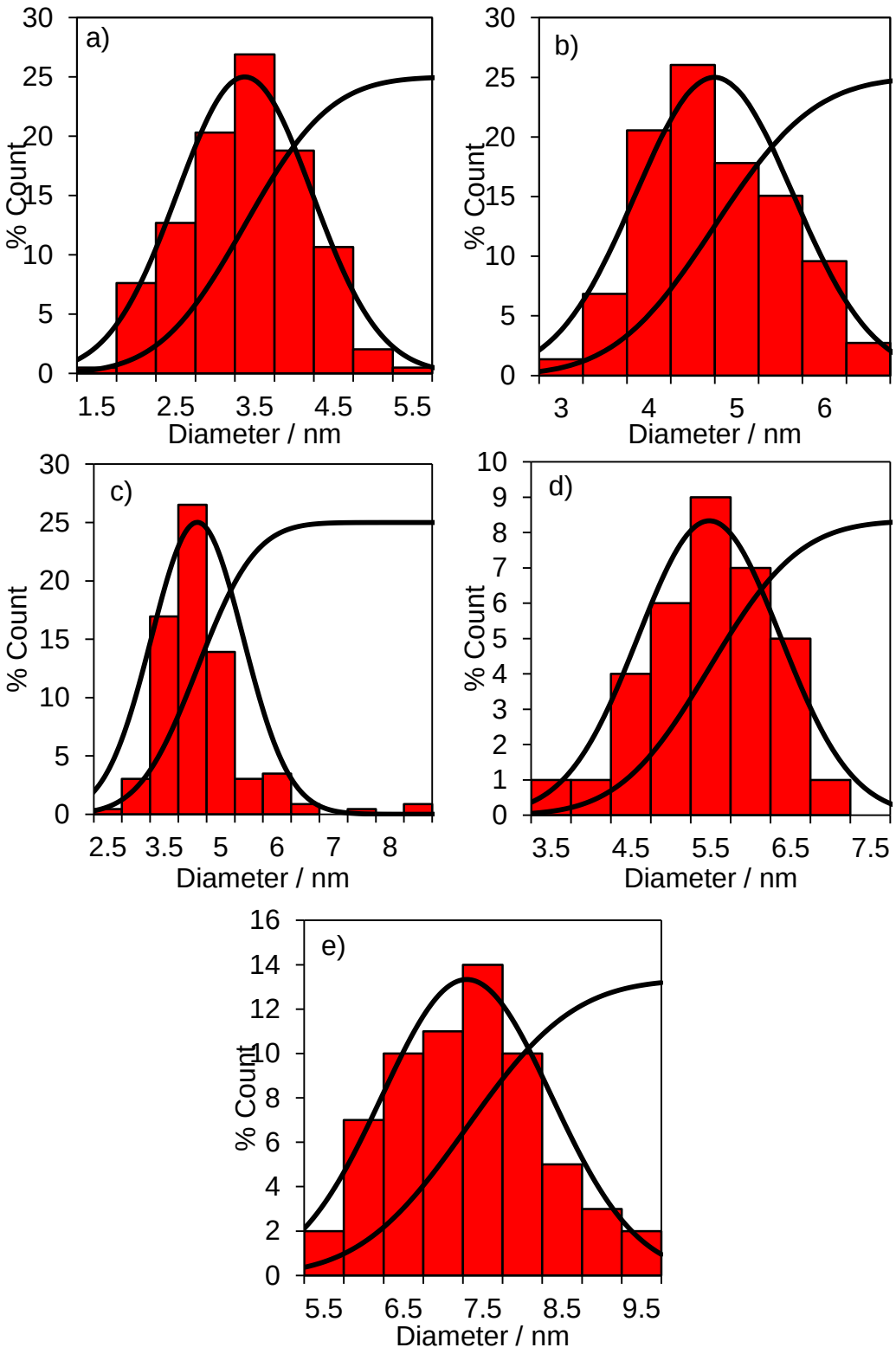

Figure 3.2: Silver core size distributions, normal and cumulative distributions for silver-silica core-shell nanocomposities determined by TEM for W_o ratios of a) 2, b) 4, c) 6, d) 8 and e) 10.

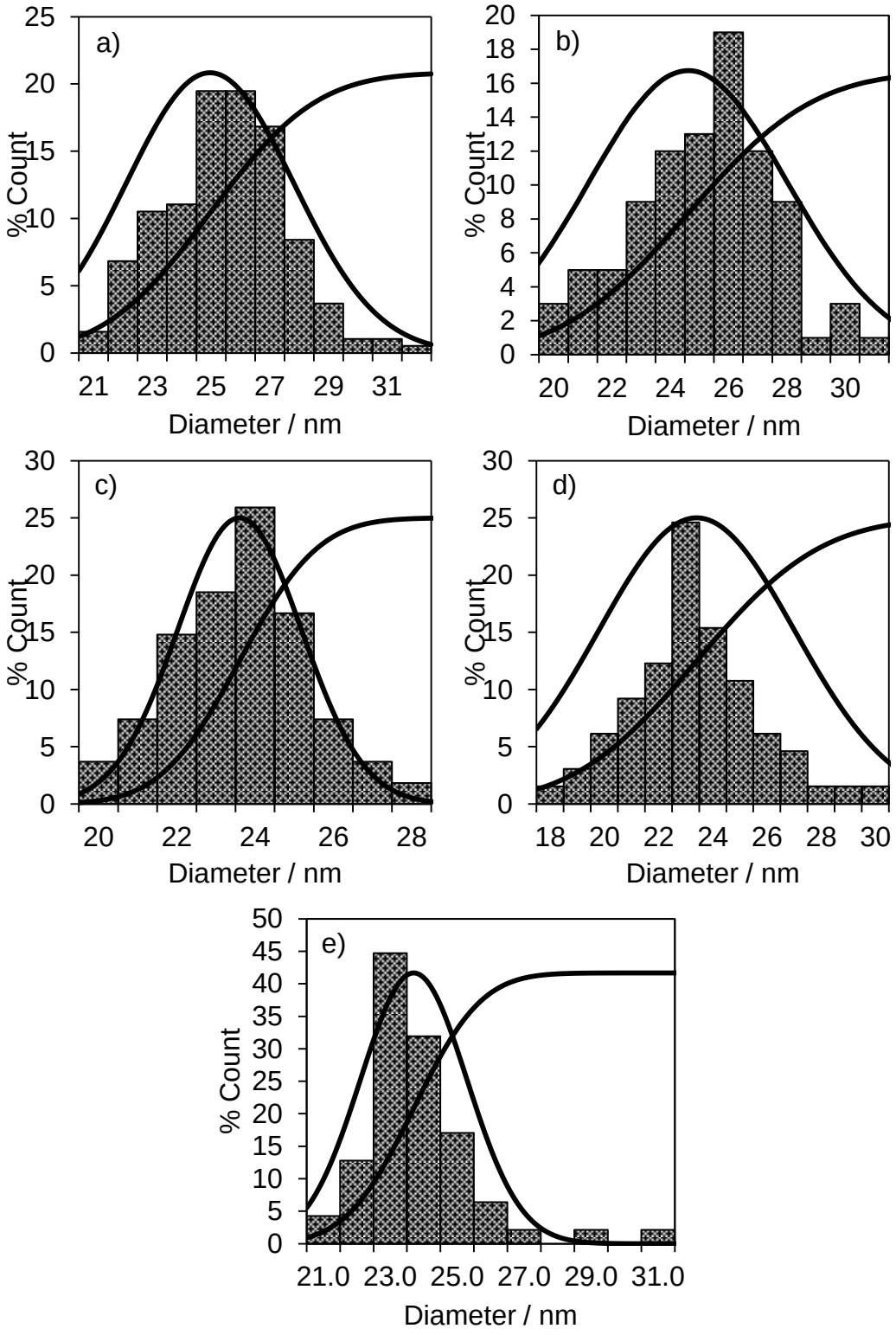

Figure 3.3: Total nanocomposite size distributions, normal and cumulative distributions for silver-silica core-shell nanocomposities determined by TEM for W_o ratios of a) 2, b) 4, c) 6, d) 8 and e) 10.

3. Silver-silica core-shell nanocomposites: Reverse micelle synthesis

The total nanoparticle and silver core diameters determined by TEM are shown in **Figure 3.4**. The total diameter of the silver-silica nanocomposites was approximately 23 nm, independent of W_o, while the silver core diameter increased systematically from 3.4 ±0.8 nm to 7.4 ± 1 nm with increasing water content, confirming successful tuning of the core independent of the nanocomposite dimensions. This equates to a decrease in silica shell thickness from ~10 to 8 nm across the series. This consistency in total particle diameter has been noted previously for similar systems.[7] It has been suggested that the growth kinetics of silica within microemulsions increases as total water content decreases,[8] which could be due to an effective internal increase in pH, caused by tethering of a larger percentage of H_2O molecules to internal hydrophilic groups, leading to a lower particle size for system containing larger water content, which could offset the slight increase caused by core size expansions.

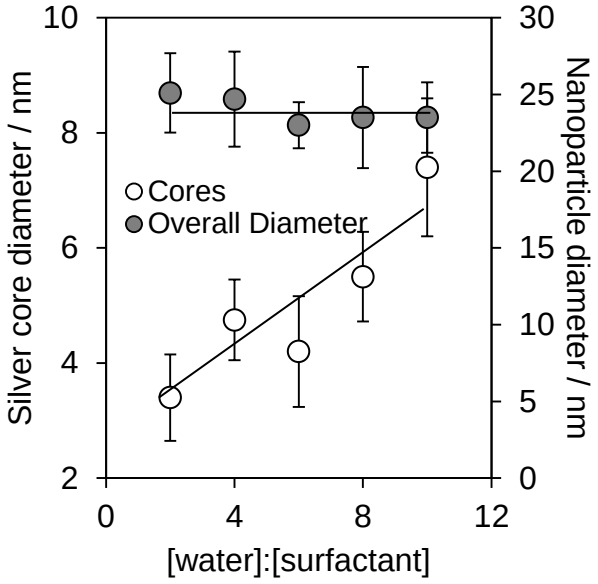

Figure 3.4: Silver-silica core-shell nanocomposite particle dimensions as a function of W_o, determined by TEM.

The mechanism behind the silver core formation is a believed to follow a two-step homogeneous nucleation and growth. The primary step involves complete reduction of the silver precursor to zero valent silver metal, followed by the growth of silver clusters via the exchange of silver atoms between micelles. This occurs via the formation of Ag_4^+ clusters which form quickly through chemical reduction by hydrazine, followed by subsequent agglomeration into larger silver nanoparticles through micellular interactions.[9] The timeframe of chemical reduction of the silver species is larger than

the timeframe of intermicellular exchange processes (4h and milliseconds respectively), the reaction proceeds in a pseudocontinuous phase, with surfactant molecules acting as protecting agents to prevent flocculation.[10] This results in diffusion-controlled silver nanoparticle growth, which is also influenced by factors including the silver precursor concentration within micelles, choice of solvent, and ionic concentration of the water-in-oil micro droplets (**figure 3.5**).

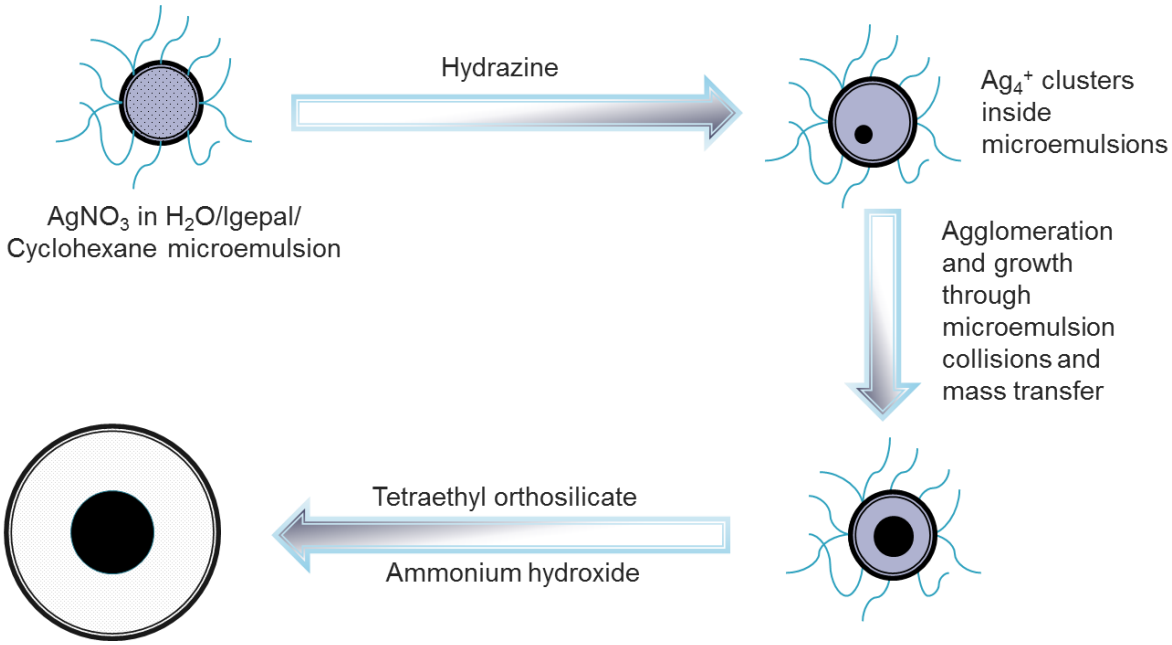

Figure 3.5: Reaction mechanism for the synthesis of silver-silica core-shell nanocomposite materials.

The Ag_4^{2+} clusters are formed by reaction with hydrazine, the proposed reaction scheme for which is outlined in **figure 3.6**.[11]

3. Silver-silica core-shell nanocomposites: Reverse micelle synthesis

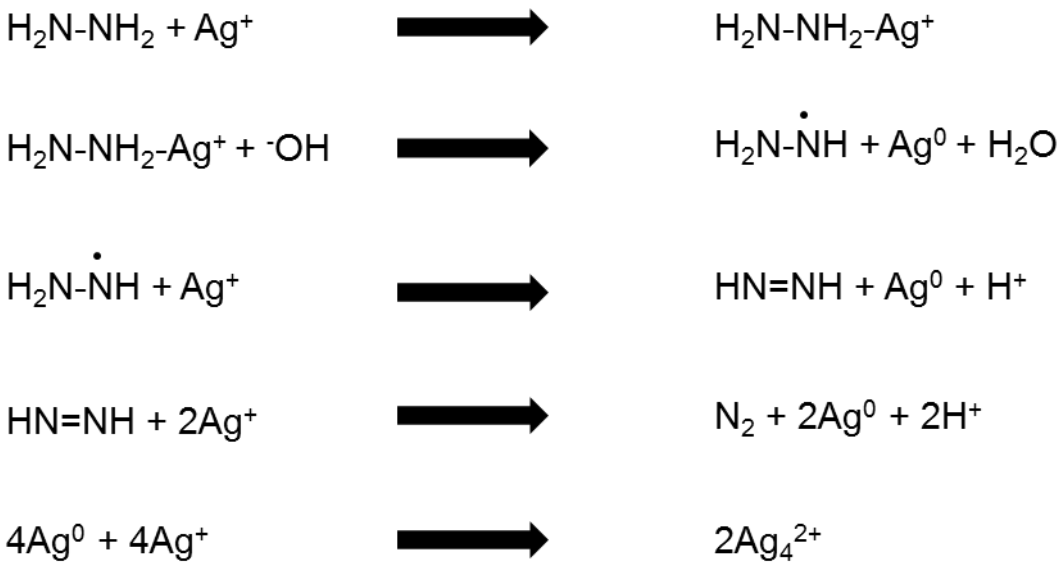

Figure 3.6: Reaction mechanism for the reduction of silver ions to silver clusters.

It is with this mechanism in mind that the increasing size of the water droplets increases the size of the resulting silver nanoparticle cores, whilst the total diameter remains at a constant value. The silica shell forms via a heterogeneous nucleation and growth process and the layer thickness is altered by controlled variation of other parameters.[1]

In addition to the desired single core architecture, a variety of alternative structures were also identified in which a silver core was absent, or a silica shell encapsulated multiple silver cores, as shown in **Figure 3.7**.

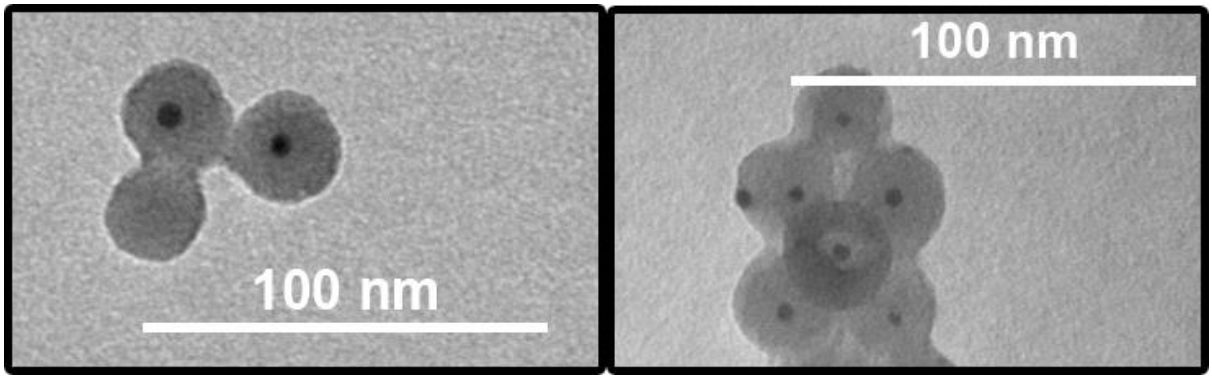

Figure 3.7: Representative bright-field HRTEM images of silver-silica nanocomposites lacking, or possessing multiple, silver cores.

The frequency of these different architectures was quantified by TEM, which is represented in **Figure 3.8**.

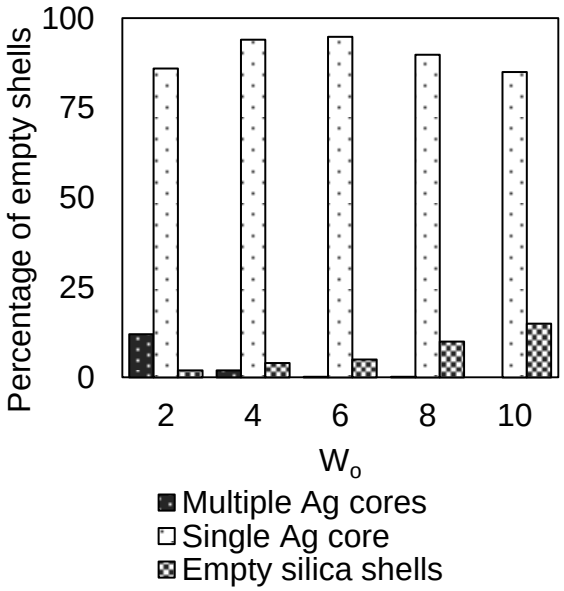

Figure 3.8: Frequency distribution of silver cores within silver-silica core-shell nanocomposites as a function of water:surfactant molar ratio (silver core diameter).

The proportion of empty silica nanoparticles increased monotonically with increasing water content, while nanocomposites possessing multiple silver cores exhibited the opposite trend. In all cases, >85 % of silica nanoparticles contained a single silver core as desired. The presence of empty silica nanospheres likely reflects the formation of a smaller number of larger silver aggregates distributed throughout the water-in-oil microemulsions, resulting in individual micelles devoid of silver species prior to hydrolysis-condensation of the TEOS precursor.

3.2.1. Powder X-ray diffraction

The nature of the silver core was evaluated through powder XRD (**Figure 3.9**), to fingerprint crystalline phases present and their crystallite dimensions. All the nanocomposites only exhibited reflections characteristic of fcc metallic silver at 38.2° (111), 44.3° (200), 66° (220) and 77° (311): Ag_2O and AgO would exhibit reflections at 32.8^o (111) and 38.2° (200) respectively, whilst carbonate produces a reflection at

32°.[12-14] These diffractograms equate to an FCC metallic silver lattice parameter of 2.36 ± 0.05 Å and do not shift to any measureable degree.[15] No reflections were observed for any crystalline silica phase, with a single, strong and broad peak at 20° indicative of amorphous silica. Variations in intensity and signal-to-noise ratios can be explained by differing Ag loadings.

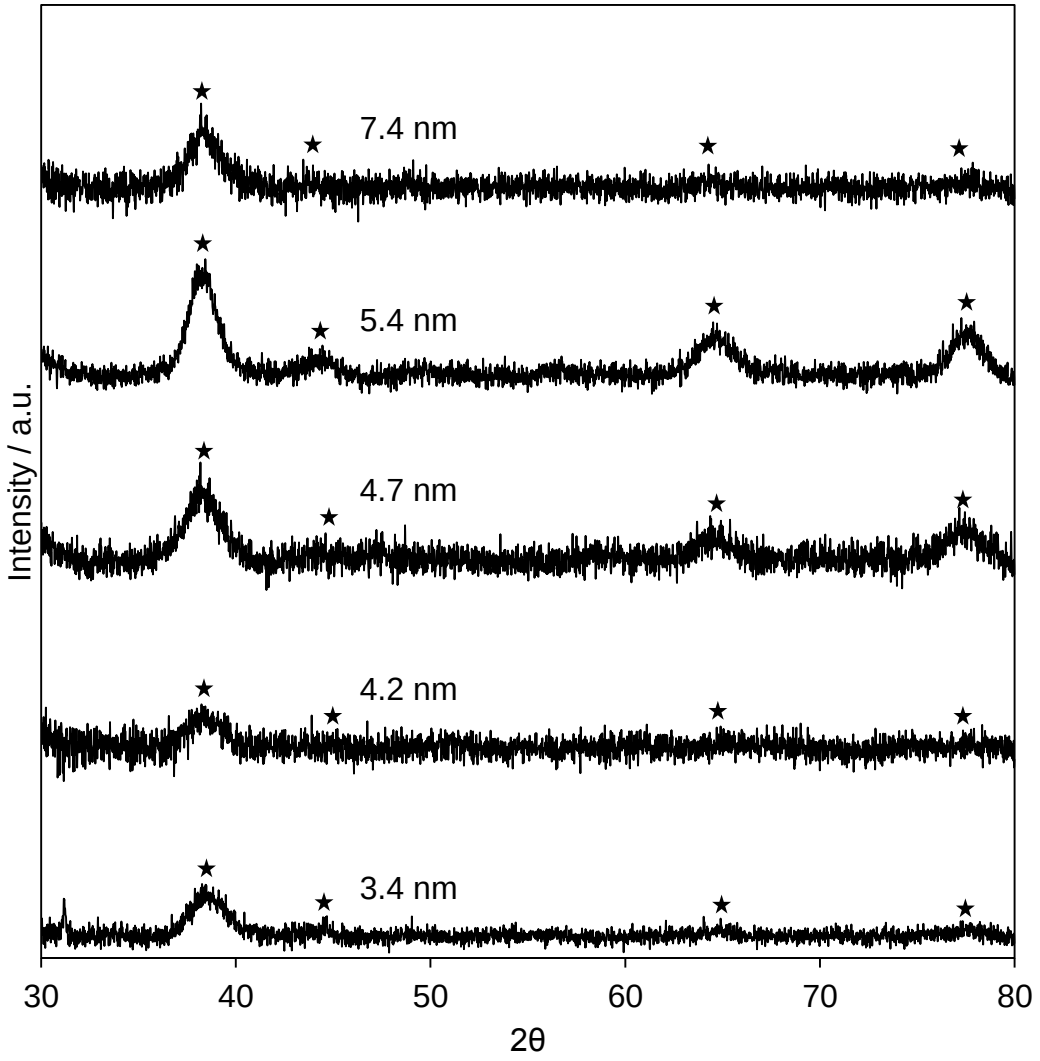

Figure 3.9: Powder XRD patterns of silver-silica core-shell nanocomposites. Ag^0 FCC peaks are labelled with an asterisk.

Volume averaged silver core diameters were determined from the full width half maximum of silver reflections employing the Scherrer equation and are shown in **Figure 3.10**. Mean silver core diameters increased systematically with increasing

water:surfactant molar ratio, in good quantitative agreement with the TEM analysis in **Figure 3.4**.

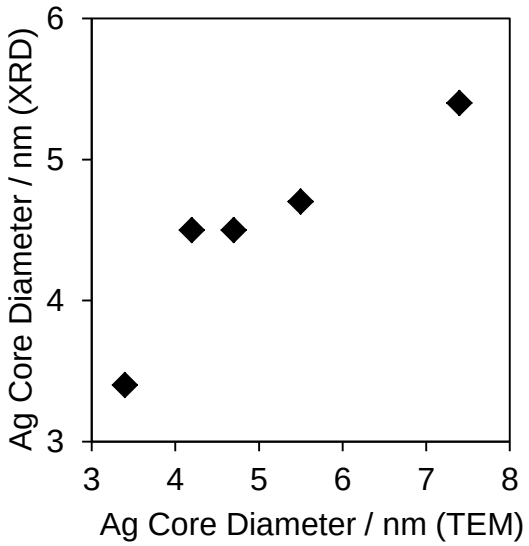

Figure 3.10: Correspondence between silver core diameter of silver-silica core-shell nanocomposites determined by local (TEM) and averaging (XRD) methods.

3.2.3. Elemental analysis

The bulk and surface compositions of the nanocomposite series were evaluated by ICP-AES/EDX and XPS respectively and the results summarised in Table 3.1 below. For each sample the surface silver concentration was significantly lower than the analogous bulk content, consistent with a buried silver core beneath a silica shell which attenuates the signal detectable by the surface sensitive XPS technique. The surface:bulk ratio increased with core size, also consistent with the decrease in silica shell thickness observed by TEM.

Ag core size	Surface Ag wt. %	Bulk Ag wt. %	Surface:Bulk
3.4	0.32	2	0.16
4.2	0.22	0.74	0.30
4.7	0.24	0.83	0.29
5.5	0.5	1.55	0.32
7.4	0.61	0.94	0.65

Table 3.1: Elemental analysis of silver-silica core-shell nanocomposites.

The variation in bulk Ag loading with core size may reflect slight differences in the total amount of TEOS which hydrolysed and condensed to form silica shells during synthesis. Small differences in the final silica yields from TEOS condensation will result in perceivably larger differences in silver yields and therefore final weight percentages. Due to these small differences, the surface to bulk ratio is therefore a more interesting value. This appears to increase in conjunction with silver core size, which is in agreement with the notion that the cores are getting larger, whilst overall diameter remains unchanged. Further to this, although hydrazine is well known to be an effective reductant in this system, ammonium hydroxide can etch silver metal out from the nanoparticulate core, reducing the amount of zero valent silver.[16] A combination of these could lead to the differences is silver content (1.2% Ag ± 0.8%).

The XPS signal is attenuated by the silica shell and, using **equation 3.1**, this can lead to information regarding the silica shell. IMFP was calculated using the method by Seah and Dench.[17]

$$\frac{I}{I_0} = exp^{(\frac{-d}{l\,cos\vartheta})}$$

Equation 3.1: XPS signal attenuation.

***I* = detected intensity, I_0 = initial intensity, *d* = thickness, *l* = inelastic mean free path (IMFP), *cos θ* = analyser acceptance angle (assumed to equal for instrument setup)**

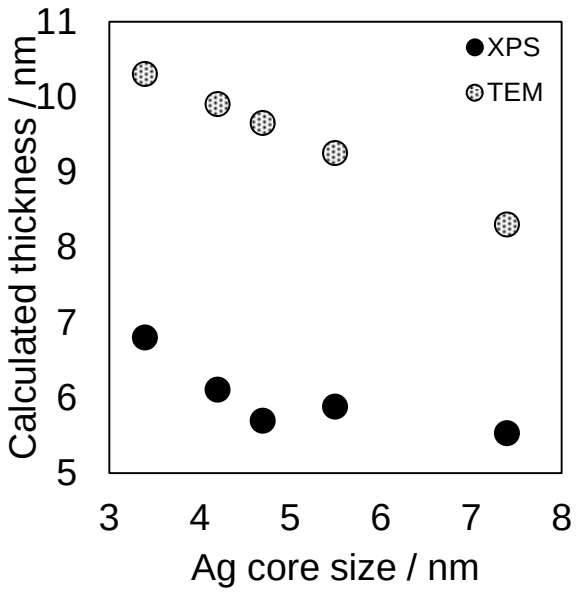

Figure 3.11 : Silica shell thickness from TEM analysis, and calculated from XPS data using **equation 3.1**.

Figure 3.11 shows the calculated silica thickness using this relationship and assuming that I/I_0 = (surface Ag atom%)/(bulk Ag atom%). The values reported are lower that calculated using average particle dimensions form TEM analysis. This could suggest that the silica network is slightly porous, considering that the IMFP is affected by the density of the surrounding media, so if the silica network is not as dense as the value used to obtain IMFP figures (using the method from Dench and Seah, determined based on parameters including density and atomic mass),[17] this will result in a less attenuated silver signal, and silica shells which appear smaller than they are.

By using x-ray sources with different energies (unmonochromated Mg and Al sources), simultaneous equations can be employed to remove the I_0 component of the relationship and rely solely on recorded surface Ag atom% values to calculate values for silica shell thickness. The equations are explained in full in **section 2.7.1**. The calculated shell thicknesses are displayed in **figure 3.**

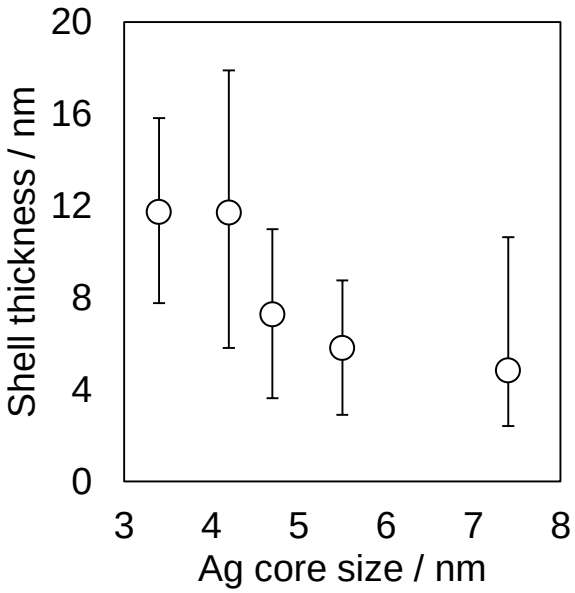

Figure 3.12: Silica shell thicknesses determined by XPS analysis and **equation 2.22**.

A negative trend can be witnessed in the shell size with respect to silver core size. This is in agreement with the results from the monochromated spectra and supports the idea that the average shell thickness decreases as silver core size increases.

The error in this measurement is due to the accuracy with which atomic percentage is measured with the XPS analysis (typically ~0.01 atom %). The silver loadings are highly attenuated by the silica shell, and hence only around 0.01-0.05 atom%, therefore

errors were determined by calculating the shell thickness with ±0.005 atom% for each anode.

3.2.5. X-ray photoelectron spectroscopy

XPS was used to provide additional information regarding the phases of silver detectable in the sample. **Figure 3.13** shows background-subtracted Ag 3d spectra, clearly showing the $3d_{3/2}$ and $3d_{5/2}$ peaks (doublet separation = 6 eV).[18] All spectra were energy referenced to their adventitious C 1s peak at 284.7 eV. The black lines represent the raw data, as collected by the instrument, the red lines represent the envelope fitting of the sum of all component curves and the purple lines represent the individual Ag 3d components.

The peaks were fit using CASA and the FWHM and peak positions locked to identical values for each sample. The binding energy was compared with values from NIST XPS database and were consistent with values reported for silver metal.[18]

The silver species which appears is of only one oxidation state, with no evident shoulders which would give evidence for an oxide layer, from this, it is reasonable to suggest that the silver exists in only one phase. Combining these spectra with the powder XRD patterns in **Figure 3.9** would lead to the conclusion that the single phase of silver in these composites is that of metallic silver, Ag^0.

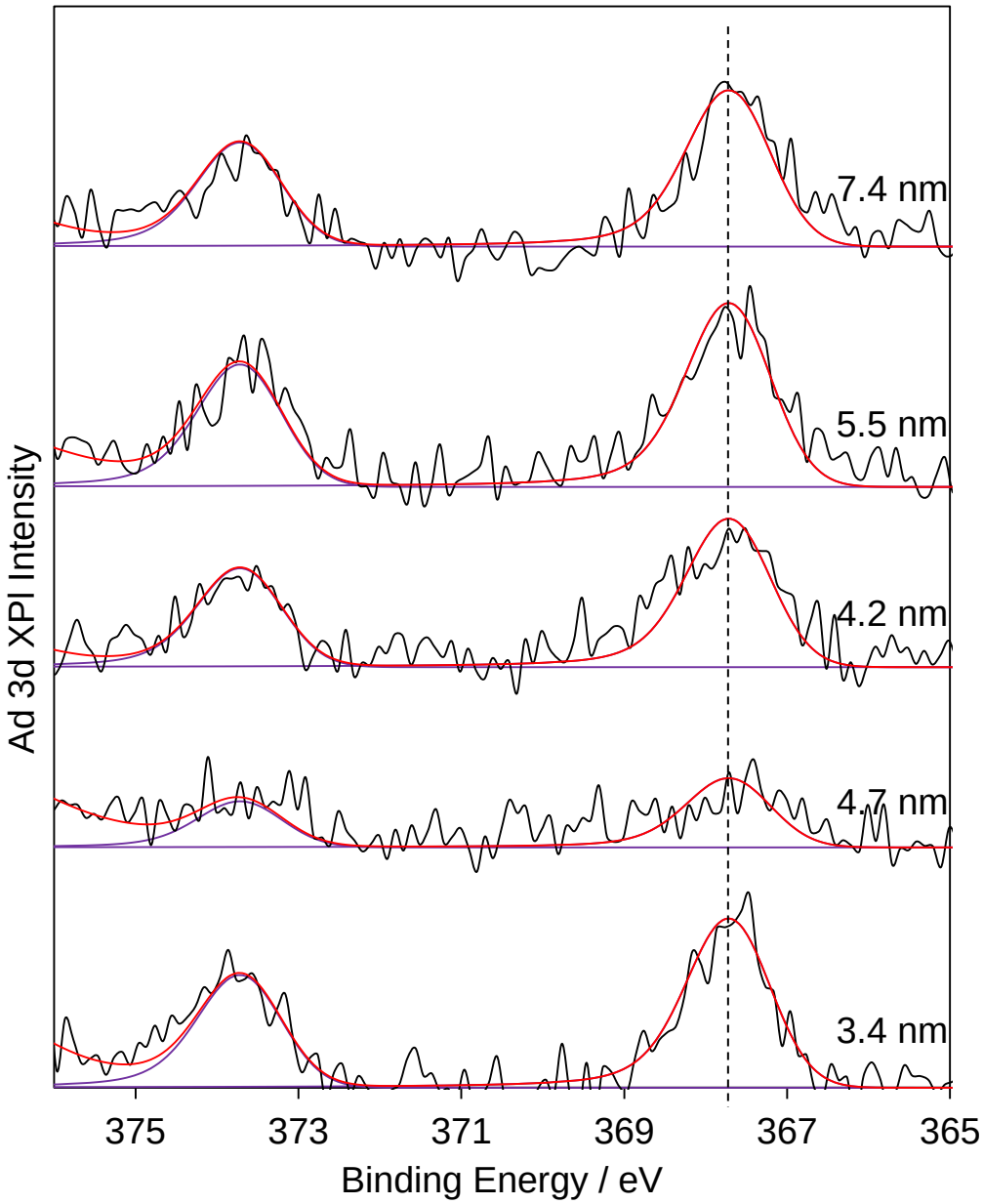

Figure 3.13: Ag 3d XPS stack plot of Ag@SiO_2 core shell nanocomposites.

The silicon regions were investigated, to confirm the identity of the silicon species was in-fact, silicon dioxide. **Figure 3.14** displays a stack plot of the silicon 2p regions, with binding energies consistent with values obtained from the NIST database. A binding energy of 103.4 eV suggests the presence of SiO_2, according to the database, significantly higher than the majority of other silicon species. There is no energy shift observed throughout the series, confirming the silica species remains unaffected by the increasing core size. The doublet separation of the 2p 3/2 and 1/2 peaks was set to 0.6 eV, which was taken from the NIST XPS database, and the peak ratios were set to 2:1.

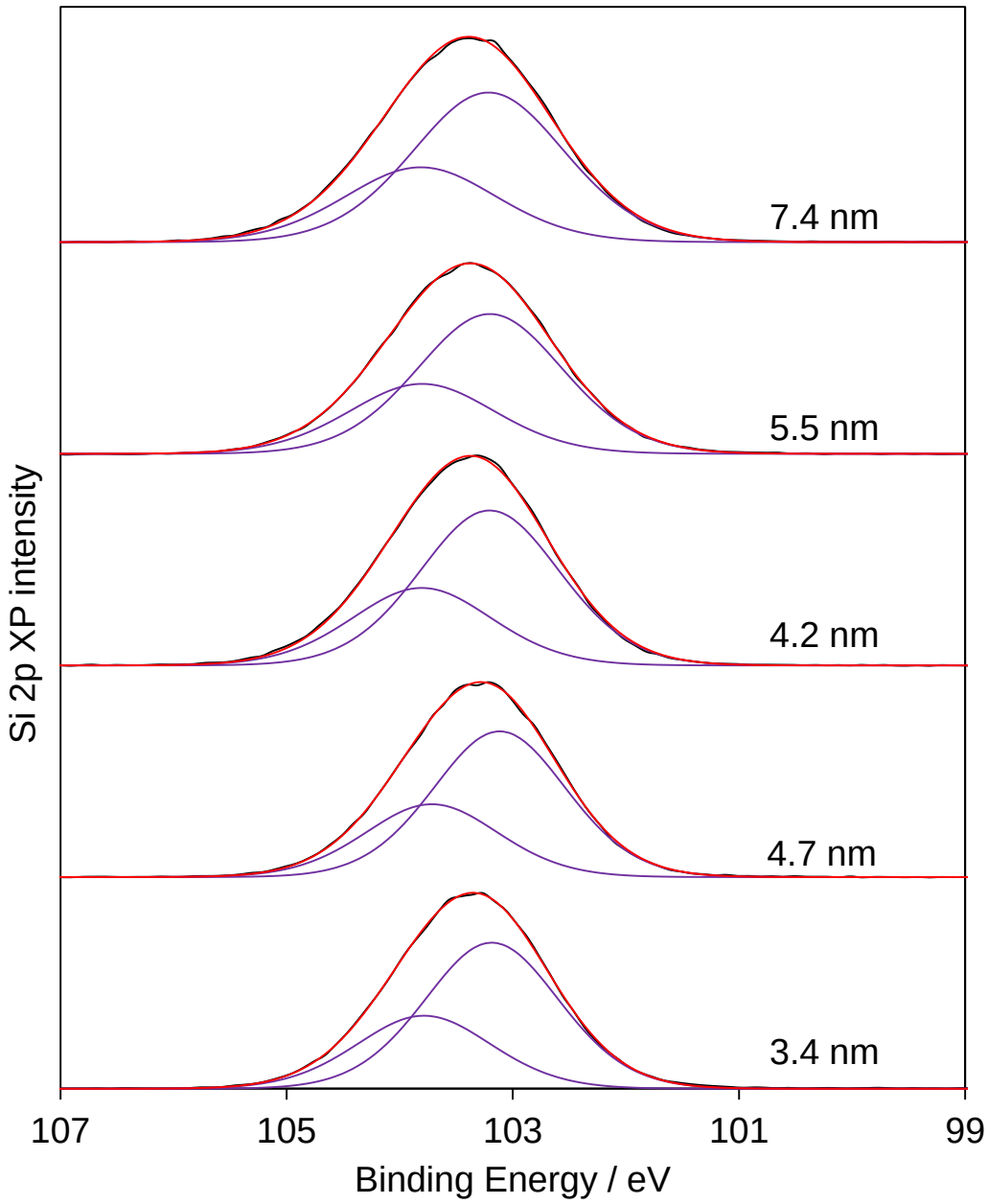

Figure 3.14: Si 2p XPS stack plot of $Ag@SiO_2$ core shell nanocomposites.

The oxygen 1s regions studied by XPS analysis (**Figure 3.15**) displayed a single, broad peak at 532.2 eV, which can be attributed to the Si-O-Si species.[19]

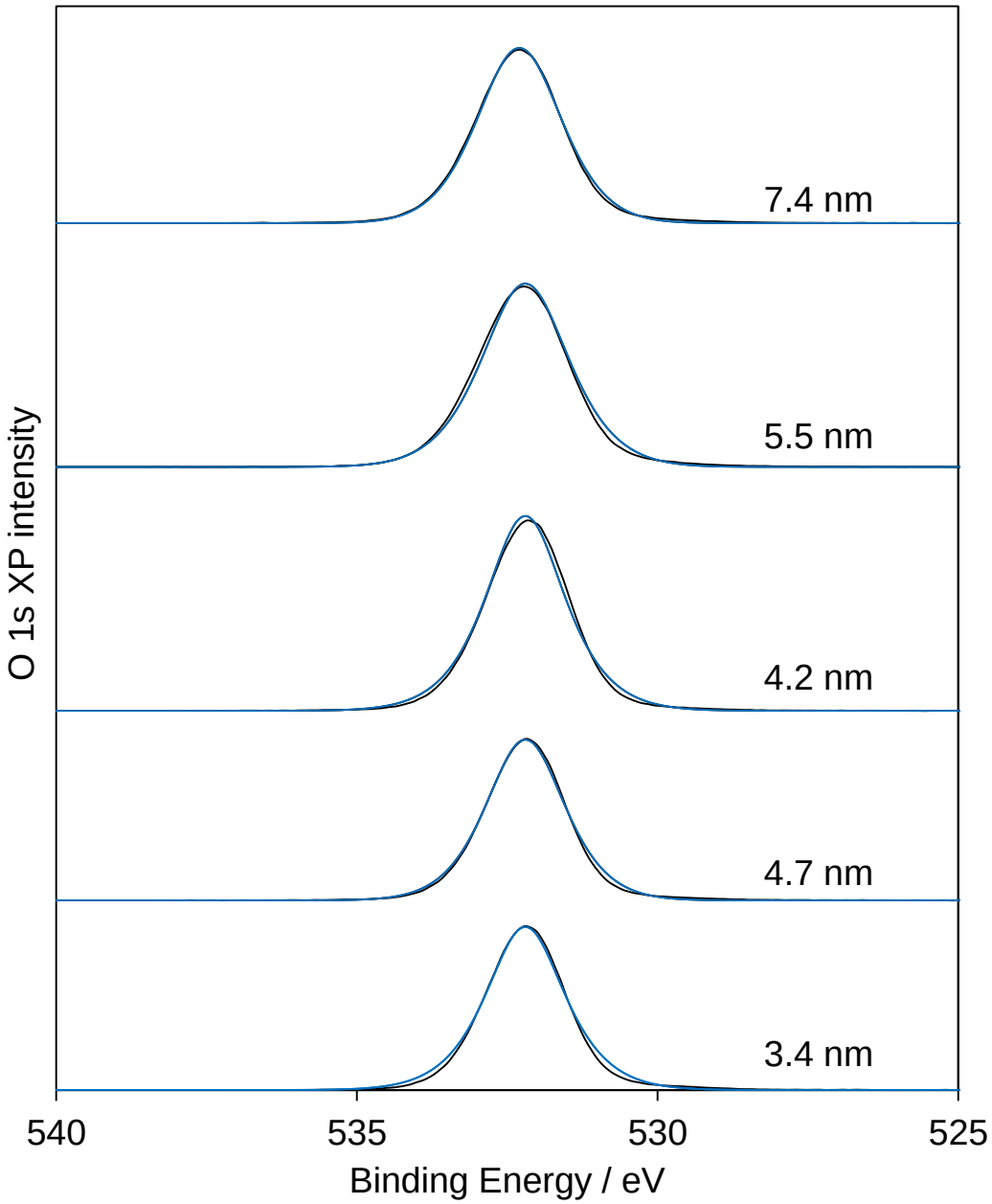

Figure 3.15: O 1s stack plot of Ag@SiO_2 core shell nanocomposites.

3.2.4. Porosimetry

The textural properties of the nanocomposites were studied by nitrogen porosimetry. **Figure 3.16** shows the N_2 adsorption isotherms for the composite materials, with a y-axis offset to aid visualisation. The isotherms vary very little, exhibiting a type IV characteristic complete with a hysteresis loop, indicative of capillary condensation. It is unlikely that this is due to mesoporosity however,

considering the size of the composites. Instead, this feature is likely a result of interparticulate spacings between the composite spheres.

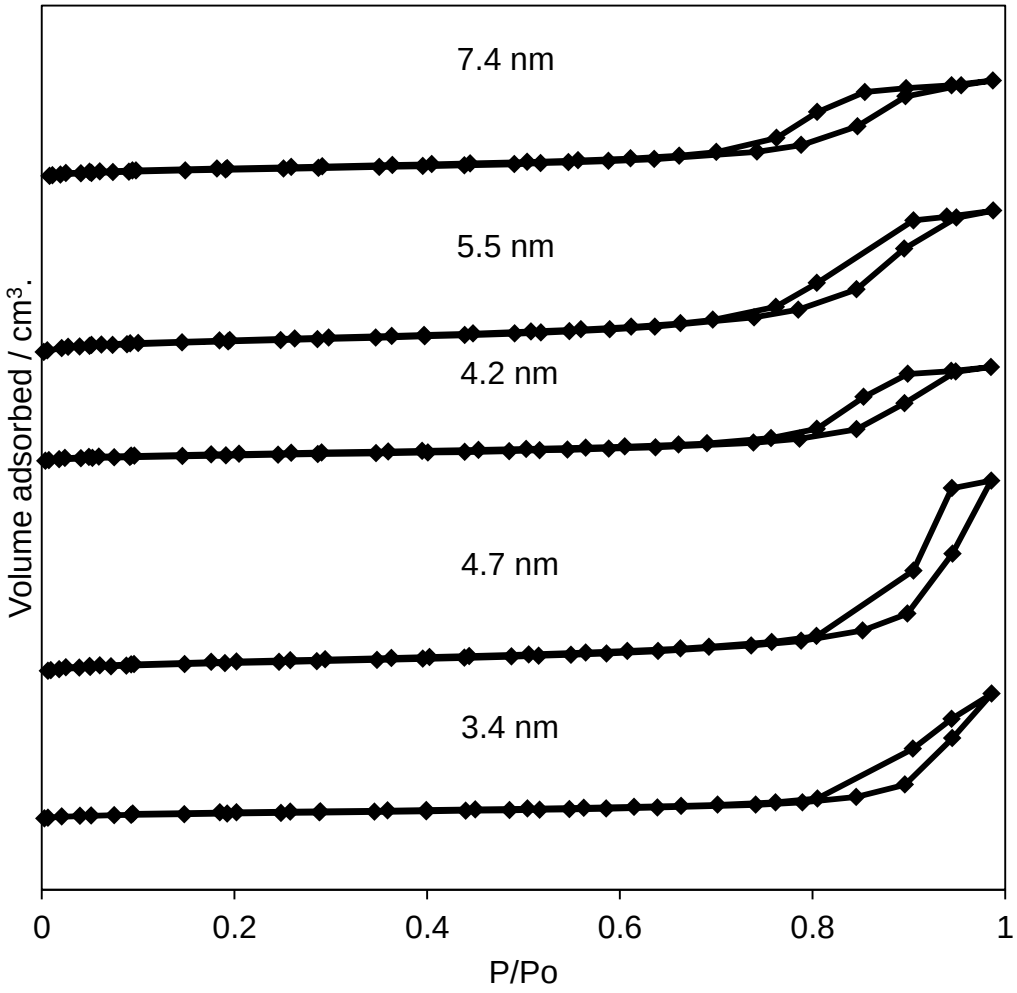

Figure 3.16: Nitrogen porosimetry isotherms for silver-silica core-shell nanocomposites, offset on the y-axis for display purposes.

The BET method was employed to determine the specific surface areas of these materials for $0.15 < P/P_o < 0.35$ shown in **Figure 3.17** as a function of the water:surfactant molar ratio.

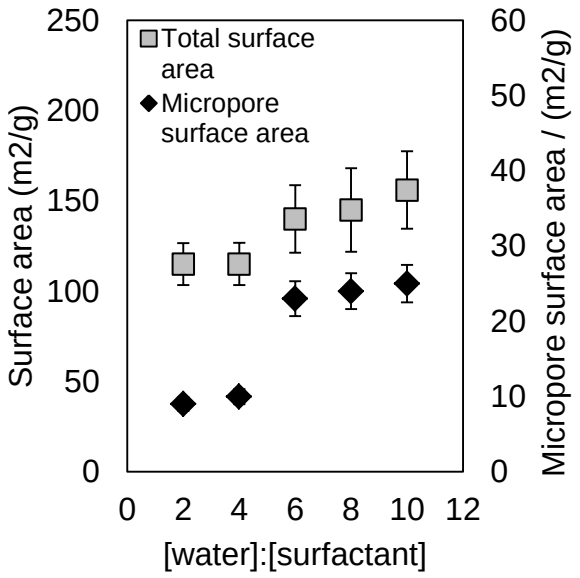

Figure 3.17: BET surface areas for silver-silica core-shell nanocomposites as a function of water:surfactant molar ratio.

The recorded surface areas are slightly higher than the calculated value for these materials (94 m^2 g^{-1}), which could indicate the materials have some microporous character, which is indeed confirmed by analysis of the t-plot treatments, which suggest a small contribution in surface area from microporosity. The increase in surface area could also be attributed to the presence of the empty silica particles which are smaller in size, and would lead to an increase in surface area.

Using the BJH method, applied to all relative pressures on the desorption branch of the recorded isotherm, the porosity of the material could be studied, **Figure 3.18** shows these profiles.

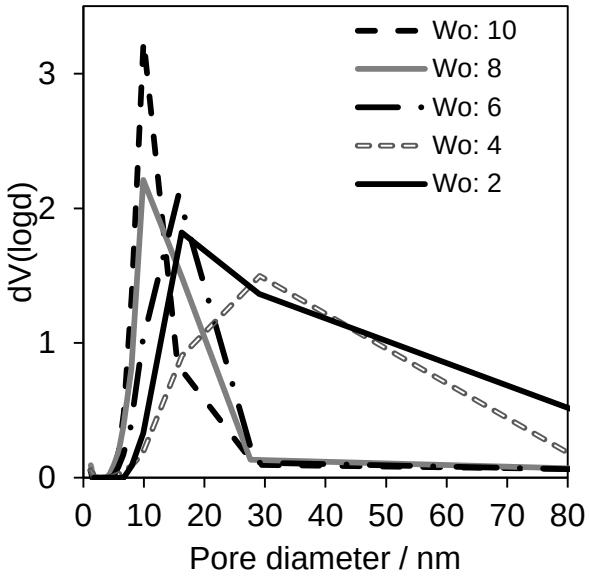

Figure 3.18: Barrett-Joyner-Halenda profiles for composite materials.

The BJH plots indicate a slight increase in gas adsorbed in the region of 7-10 nm, which is too large to be considered intrinsic mesopores as this is larger than the silver core diameter which would inevitably lead to removal of the silver cores through these large voids. Instead, this increase in adsorbed gas can be attributed to the interparticulate spacings between composite materials, with the similar profiles suggesting a similar environment between samples.

3.2.5. Summary of properties of variable core size nanocomposites

Silver-silica core shell architectures with controllable silver core sizes have been developed using a microemulsion reactor based synthesis, utilising water-in-oil droplets to create silver nanoparticles, the size of which can be adjusted through regulation of the water content in the system, and subsequent coating with silica through hydrolysis and condensation of tetraethyl orthosilicate.

TEM analysis indicates a clear core-shell architecture, and was used to determine the increase of silver nanoparticle diameter with water content as well as monitor the silica shell size of the nanocomposites. XRD and XPS studies indicated the silver was present as Ag^0, having been reduced by hydrazine *in situ*.

3.3. Results and discussion: Variation of silica shell thickness

Control over the silica shell thickness was seen as a pathway to controlling silver dissolution and antibacterial activity. The target was to adjust the shell thickness by controlling synthetic parameters without affecting the size of the silver core within. This would lead to silver-silica composites of differing size and silver content which was designed to lead to slower silver species release from the larger silica shells, due to a larger silica network slowing down the release progress of the silver ions into solution.

A range of characterisation techniques was used to determine the physical and chemical properties of the nanocomposites, using a combination of surface and bulk techniques to probe the differences in the silica shell during etching treatment and characterise the state of the silver core.

3.3.1. Transmission electron microscopy

TEM was once again used to examine the structural architecture and monodispersity of the synthesised composites, with representative bright field TEM images exhibited in **figure 3.19**.

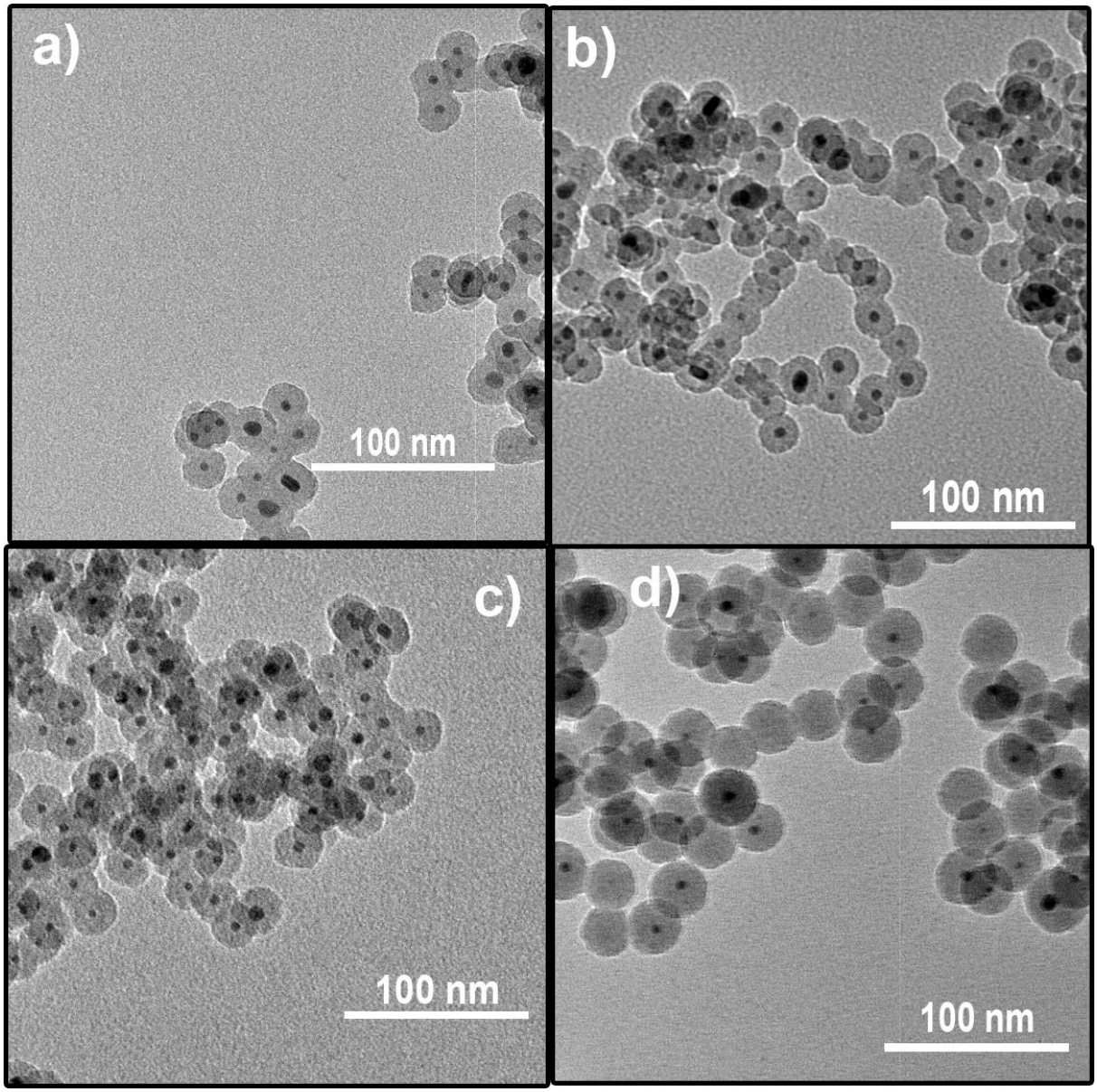

Figure 3.19: Representative bright-field HRTEM images of silver-silica nanocomposites as a function of W_o = 6 and [water]:[TEOS] molar ratio (a) 130, (b) 100, (c) 75, (d) 40.

Consistent core-shell architectures can be seen in the bright field TEM images, confirming that the increase in size has no bearing on the observed particle morphology. The images were analysed using ImageJ software and the particle sizes measured and compiled in **figure 3.20**.

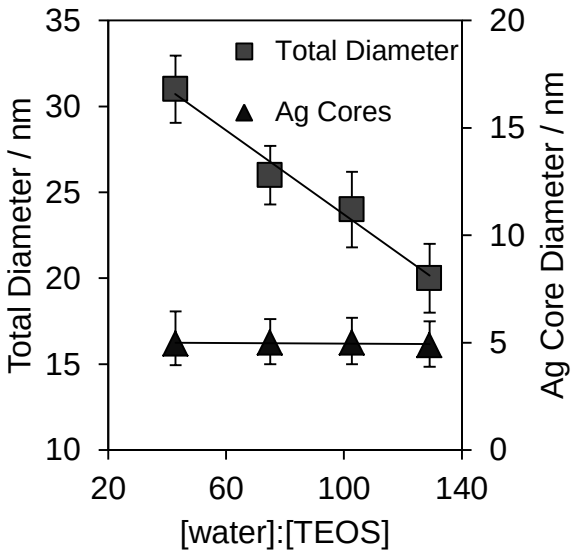

Figure 3.20: Silver-silica nanocomposite dimensions as a function of water to TEOS ratio.

A linear trend can be seen in the plot of total particle diameter versus ratio of water to TEOS. The silver core size remains constant throughout the series, indicating the increase of silica shell size as the concentration of silica precursor increases in the synthesis. The measured pH of the reactant solution is kept at a constant of pH = 11, with $[NH_4OH]$:[TEOS] kept at a constant ratio, so as to ensure the rate of hydrolysis does not change, which would also affect the size of the resultant silica coatings.[1] The ratios of the other reagents are also kept at constant values, to ensure the size of the reverse micelle micro reactors is not altered, as this will alter the size of the silver cores, as shown in **section 3.2**.

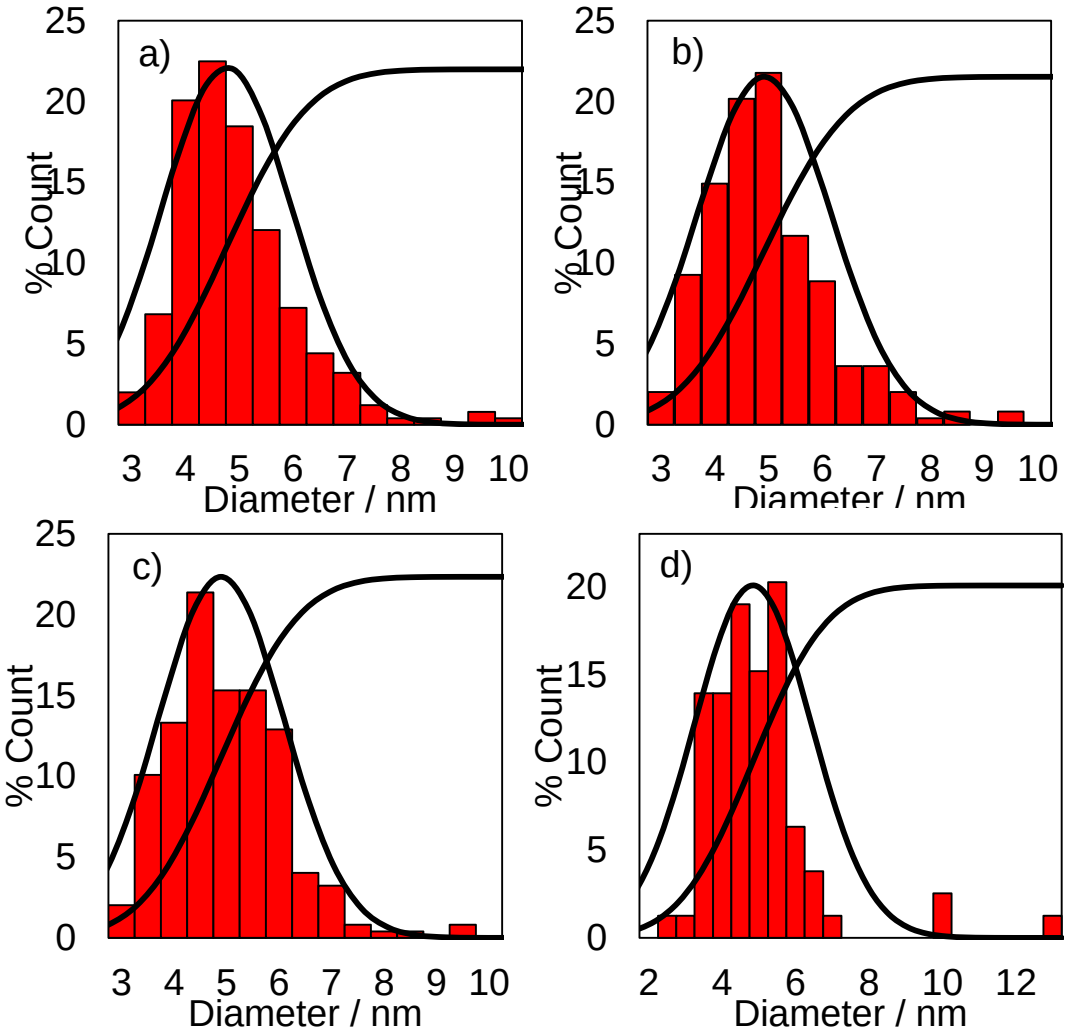

Figure 3.22 : Silver core size distributions, normal and cumulative distributions for silver-silica core-shell nanocomposities determined by TEM for W_o = 6 and [water]:[TEOS] ratios of a) 130, b) 100, c) 75 and d) 40.

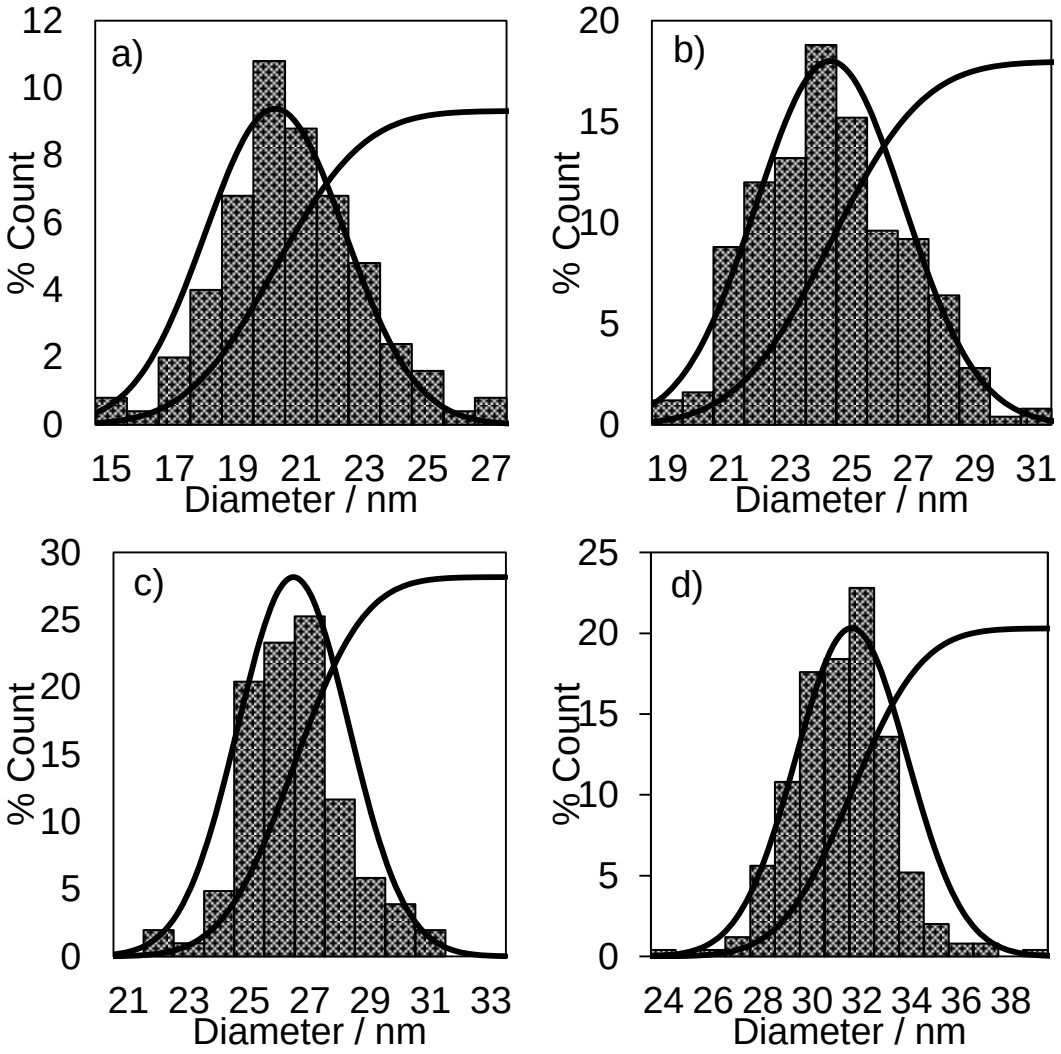

Figure 3.21 : Total size distributions, normal and cumulative distributions for silver-silica core-shell nanocomposities determined by TEM for [water]:[TEOS] ratios of a) 130, b) 100, c) 75 and d) 40.

As the concentration of silica precursor is increased, and with it, silica shell size, the probability of silica particles forming containing no silver cores increases. This ranges from close to zero for the smaller particles, to above 10% of all silica particles which contain no silver for the largest materials (**Figure 3.23**).

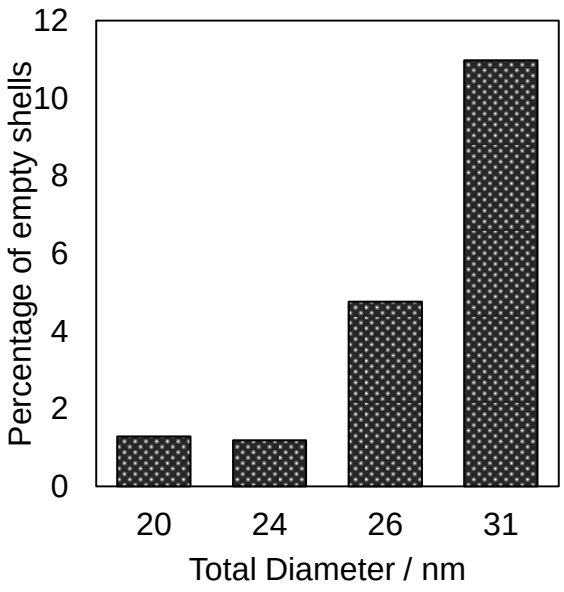

Figure 3.23: Percentage of composite materials containing no silver cores as a function of total composite diameter, as determined by TEM.

No nancomposites with multiple cores were observed in the electron micrographs. This is consistent with the previous series, as with a W_o ratio of 6, no multiple cored materials were witnessed.

3.3.2. Powder X-ray diffraction

Powder x-ray diffraction experiments were performed to identify the silver phase and determine crystallite size of the silver cores. The diffraction patterns are shown in **Figure 3.24**.

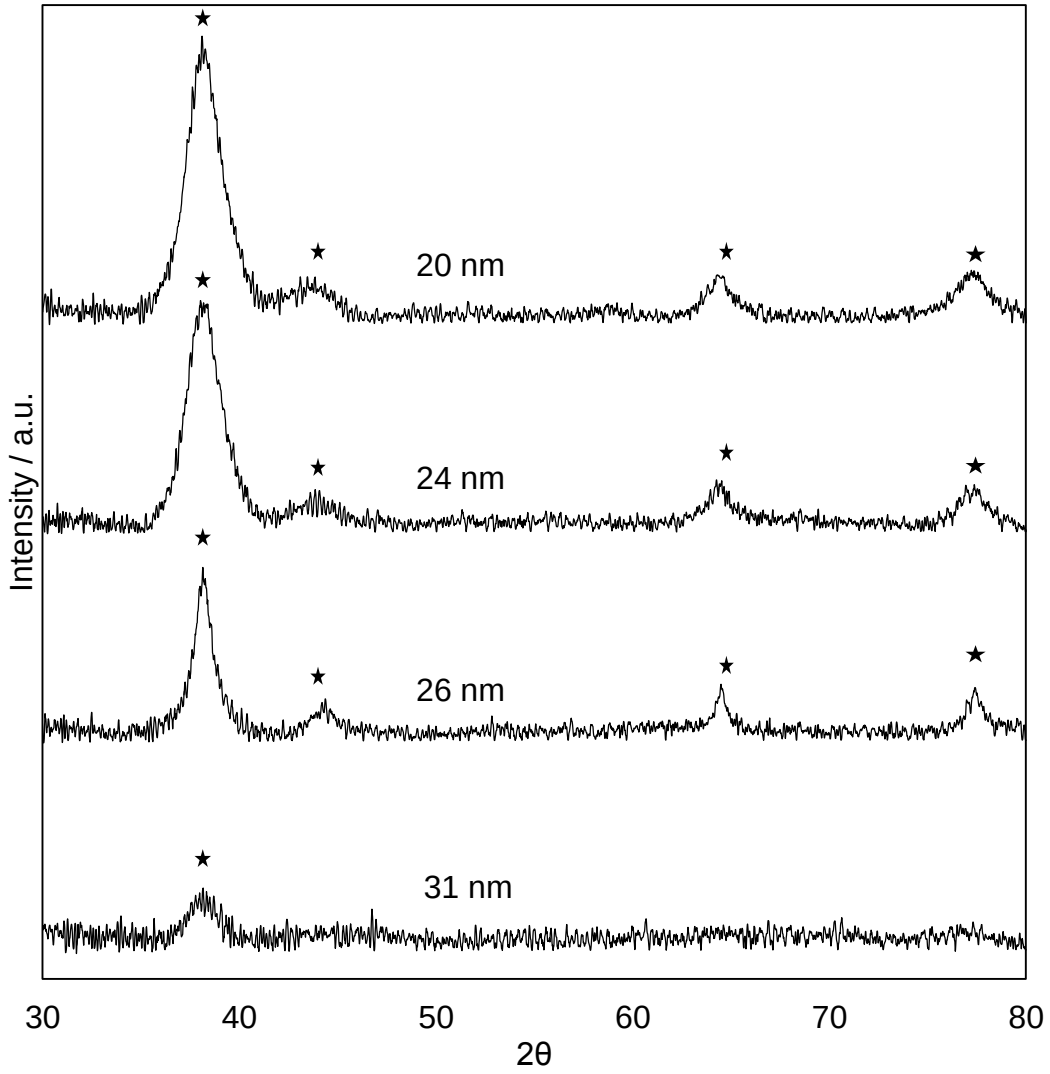

Figure 3.24: Powder XRD diffraction patterns for silver-silica core shell nanocomposite materials with variable shell thicknesses. Ag^0 FCC peaks are labelled with an asterisk.

The powder XRD diffraction patterns for these materials show the characteristic peaks for silver metal (Ag^0), as in the previous series of this type of material, indicating that as before, the silver is completely reduced to silver metal *in situ.*

Particle sizes of the silver cores are also obtained using the Scherrer equation and full width half maxima of the main silver 111 peak (as this was the only peak measureable in all samples). The values for this are shown in **table 3.2**.

Total Diameter / nm	Ag core size (XRD) / nm
20	4.6
24	4.4
26	5.5
31	4.9

Table 3.2: Silver core diameters obtained from the Scherrer equation and powder XRD data for silver-silica core shell nanocomposites with variable shell thicknesses.

The mean particle sizes from the powder XRD diffraction patterns show a consistency in silver core size which agrees with the results from the TEM analysis. This indicates that altering the silica shell size by increasing the concentration of silica precursor has no bearing on the silver nanoparticulate core size.

The intensity of the silver peaks relative to the amorphous silica signal decreases with increasing silica shell size, which is due to the decrease in bulk Ag content.

3.3.3. Elemental analysis

The silver loadings of the synthesised Ag@SiO_2 nanocomposites was determined by ICP and XPS analysis.

Total Diameter / nm	Bulk Ag wt. %	Surface Ag wt. %	Surface:Bulk Ag ratio
20	3.45	1.13	0.33
24	2.14	0.56	0.26
26	1.76	0.40	0.23
31	1.24	0.12	0.10

Table3.3: Surface and bulk silver weight loadings, determined by XPS and ICP respectively.

The surface to bulk ratios decreased as silica shell size increased, which is consistent with the idea that the silver photoelectrons are attenuated throughout the silica shells. The shell thicknesses were calculated using **equation 3.1** and plot with the thicknesses determined by TEM analysis (**figure 3.25**).

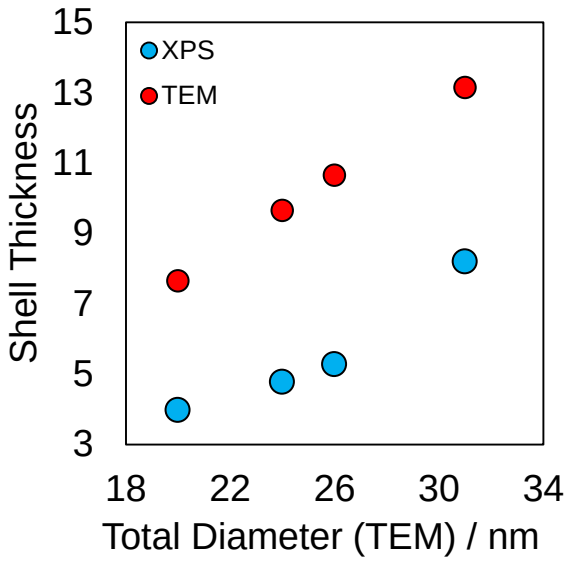

Figure 3.25: Silica shell thicnkesses determined by TEM and XPS analysis.

The shell thicknesses determined by XPS analysis are, again, smaller than those measured by TEM analysis and by the same margin as in the previous section, which would suggest that if the density of the silica shells has decreased due to porosity, it is by the same margin.

3.3.4. X-ray Photoelectron Spectroscopy

XPS spectroscopy was again used to determine the speciation of the silver metal cores in the nanocomposites. To confirm they were identical to the previous materials in **section 3.2**. **Figure 3.26** shows the silver regions recorded by XPS. There is no change in silver position either along the series, or in comparison with the previous materials, with the Ag 5/2 peak centred at 367.5 eV. There is also a noticeable difference in peak area as the size of the silica shell increases, due to greater attenuation of released silver photoelectrons by the silica shell.

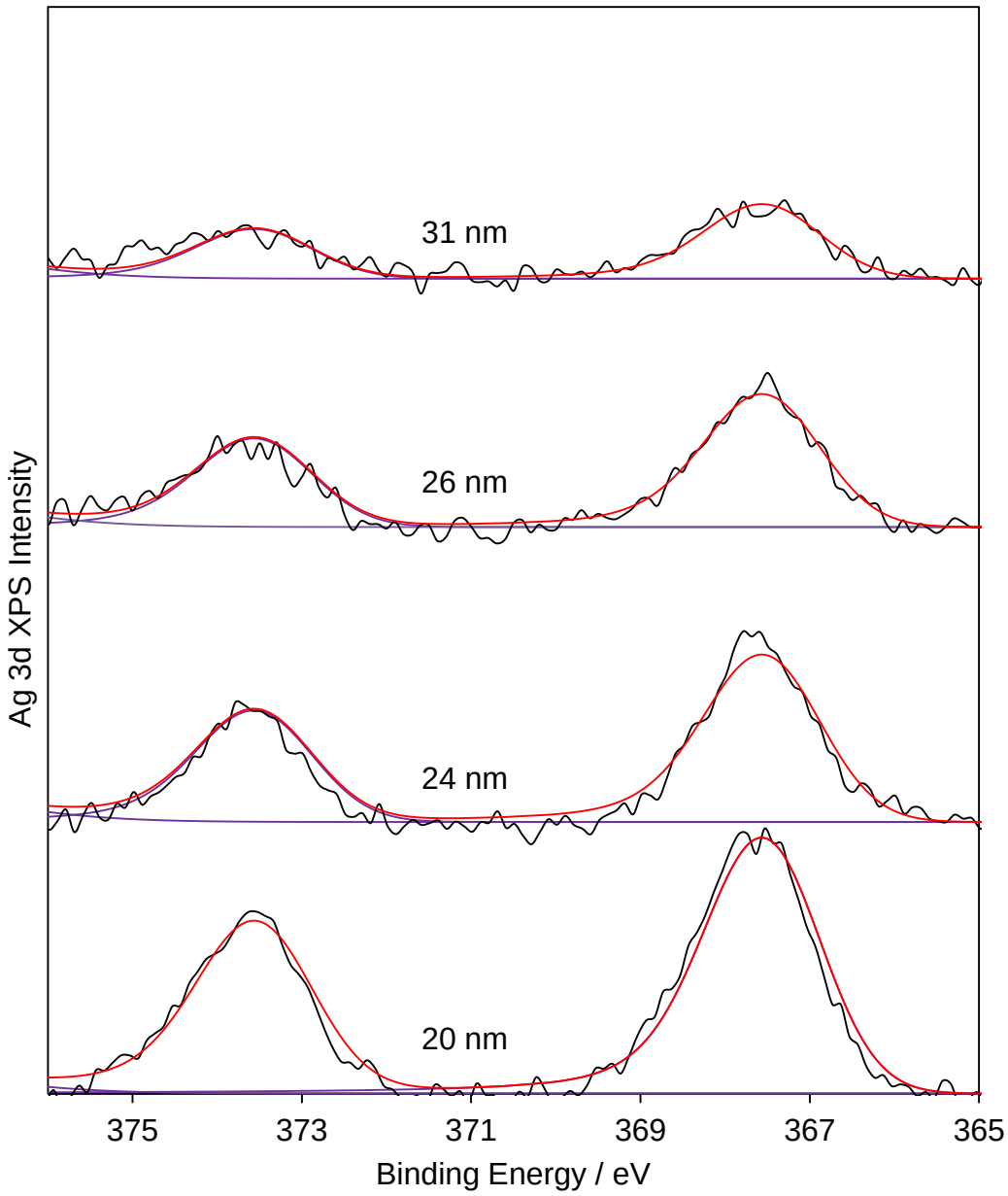

Figure 3.26: Silver regions from XPS analysis of materials with varying total diameters.

The attenuated silver regions can be used to estimate shell thickness and look for differences in shell size by using two sources of different energies and studying the different amounts of attenuation of photoelectrons excited of sources of different energies and hence possessing differing kinetic energies.

The differences in atomic percentages calculated from the XPS peak areas can be used in **equation 2.22**.

Calculated Thickness by XPS / nm	Thickness from TEM / nm
11.8	13.5
10.8	11
9.7	10
7.7	8

Table 3.4: Silica shell thicknesses calculated by XPS.

This method assumes that the silver cores are, on average, central in the composite materials, which becomes less true for larger shells which, combined with the smaller silver regions, could lead to a greater error in the calculation. There is good agreement between the TEM and XPS analysis that the shells do indeed increase in thickness along the series.

The silicon 2p regions were investigated, with a set doublet separation of 0.6 eV and peak area ratios of 2:1. These are shown in **figure 3.27**.

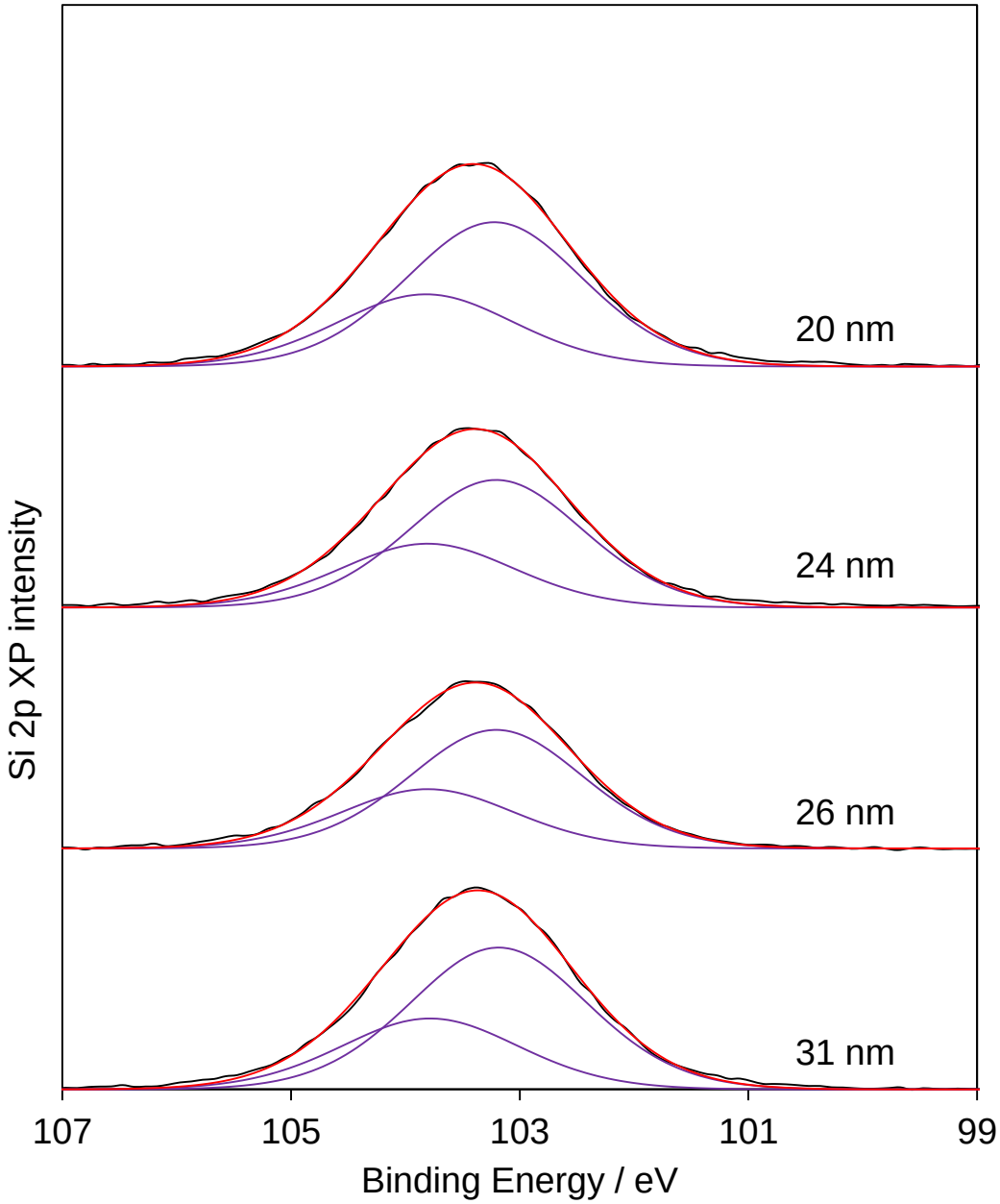

Figure 3.27: Si 2p XPS stack plot from $Ag@SiO_2$ nanocomposites of different total sizes.

The silicon regions are again consistent with silicon dioxide (Si^{4+}), with a binding energy at 103.4 eV (**Figure 3.27**), whilst the oxygen regions retain their position at 532.3 eV (**Figure 3.28**). The constant position of the silicon and oxygen peaks confirms a consistent silica species with increasing shell size.

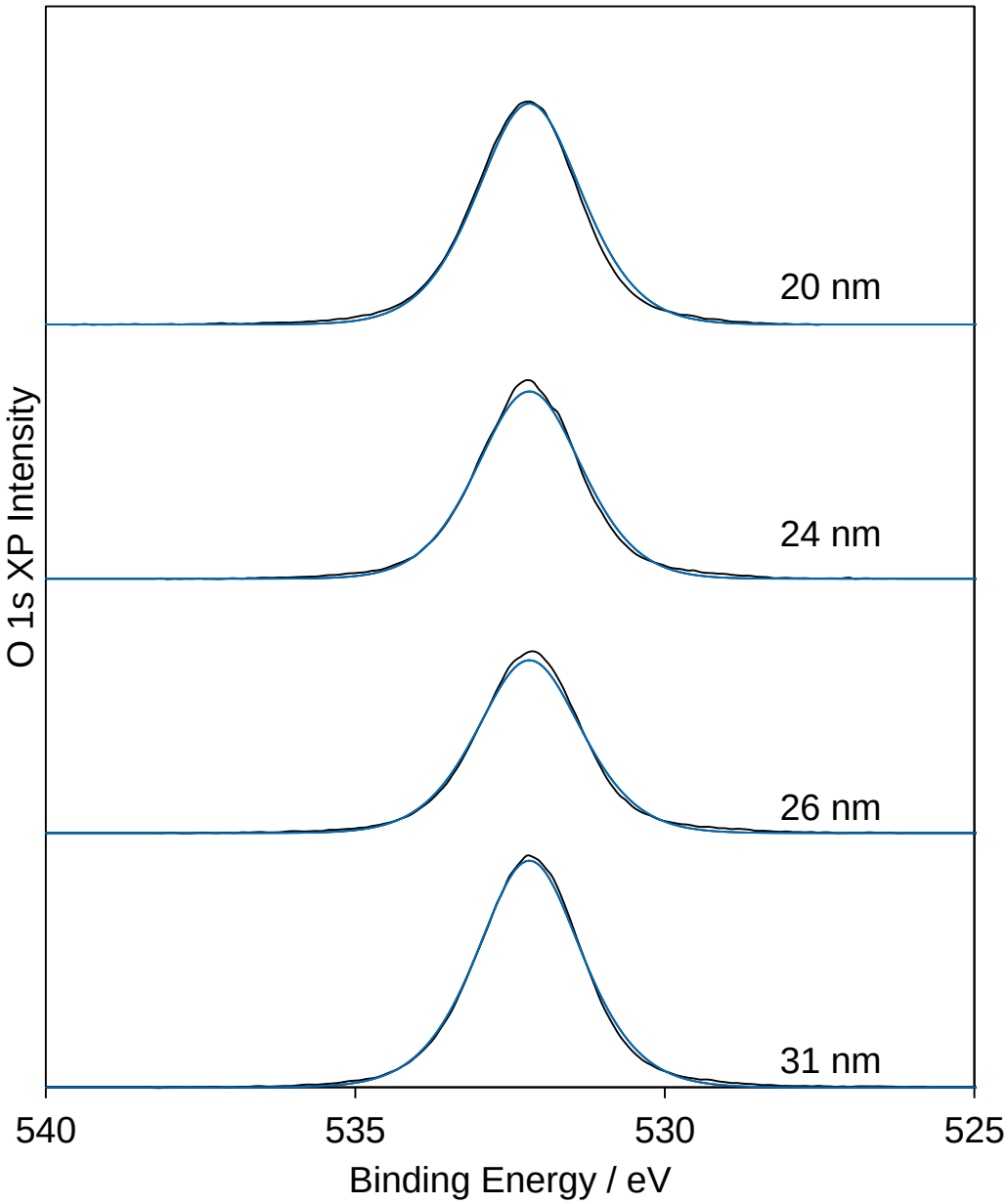

Figure 3.28: O 1s XPS stack plot from Ag@SiO_2 nanocomposites of different total sizes.

3.3.5. Porosimetry

Nitrogen porosimetry indicated a decreasing surface area with increasing particle size, following an expected trend due to the inverse relationship between diameter and specific surface area (**figure 3.29**).

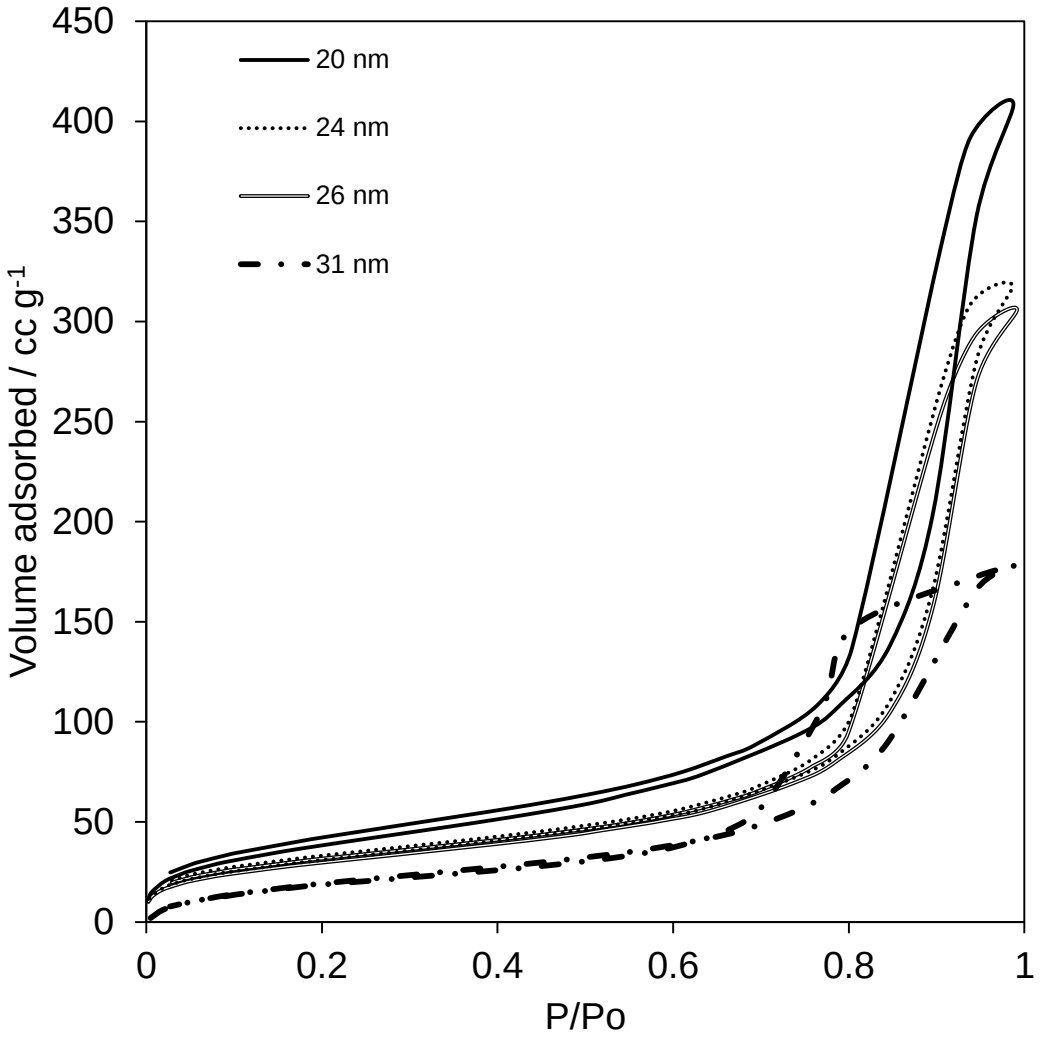

Figure 3.29: Nitrogen porosimetry isotherms for nanocomposite materials of varying total diameter.

The isotherms display a type IV characteristic, indicative of mesoporous materials, as with the previously synthesised materials, however, this is attributed to interparticulate voids causing capillary condensation, as opposed to intrinsic

mesoporosity, as the BJH profile (**figure 3.30**) suggest pores which would be too large for the materials as they exist, and would be evident in TEM images.

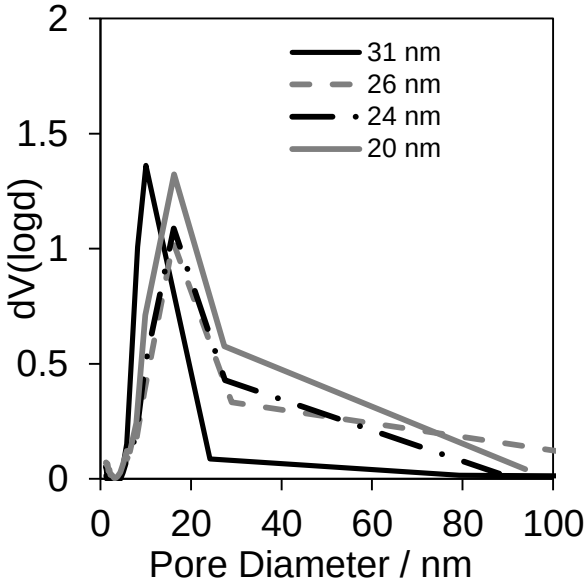

Figure 3.30: BJH profiles for $Ag@SiO_2$ nanocomposite with variable total diameters.

The nanocomposites appear to exhibit no porosity in the mesopore regime, save for that which has been attributed to interparticulate spacings. There is, in fact a slight increase in adsorption below 2nm, as seen in the previous materials, attributed to microporosity caused by removal of organic surfactant

The specific surface areas were assessed via the BET equation, applied to the isotherms between $P/P_0 = 0.05$ and 0.2, where the plot was linear. The surface areas are in line with what was expected, and the increase in surface area was attributed to pores below 2 nm, and confirmed by t-plot analysis.

Total size / nm	BET surface area / $m^2 g^{-1}$	Expected surface area / $m^2 g^{-1}$	Microporous surface area / $m^2 g^{-1}$
20	141 ± 14	113	21
24	113 ± 11	94	17
26	108 ± 11	87	11
31	80 ± 8	73	8

Table 3.5: Specific surface areas from BET analysis of nanocomposite materials of varying total diameter.

3.3.6. Summary of properties of variable shell size nanocomposites

Silica shells with an increasing thickness were coated onto the silver cores prepared by reverse micelle microemulsion as a function of overall tetraethyl orthosilicate concentration. This was confirmed, mainly, by TEM analysis, which reported an increase from 20 nm to 31 nm across the synthesised series. As a complement to TEM analysis, XPS analysis indicated a decrease in silver signal as a function of surface to bulk silver as the thickness increased, suggestive of greater attenuation of the emitted silver photoelectrons.

3.4. Results and discussion: Etching of silica shell

Tuning the properties of the shell was considered a possible mechanism for controlling silver ion release and antibacterial effectiveness. Expanding on the porosity of the silica shell was theorised to increase the ease of release of silver ions due to a more exposed silver surface, able to discharge a greater number of silver ions. To accomplish this, a thermal and base etching treatment route was utilised.

Thermal treatment of the composite materials was achieved using the method described in **section 2.1.2** and involved heating the materials to 100^{o}C in the presence of PVP K10 for one hour with vigorous stirring.[20] Following this, a base etching treatment was performed to enhance the porosity of the silica shells, in which the materials were dispersed in 0.01M sodium hydroxide solution with stirring. Aliquots of the solution were removed at set time intervals and the product isolated by centrifugation.

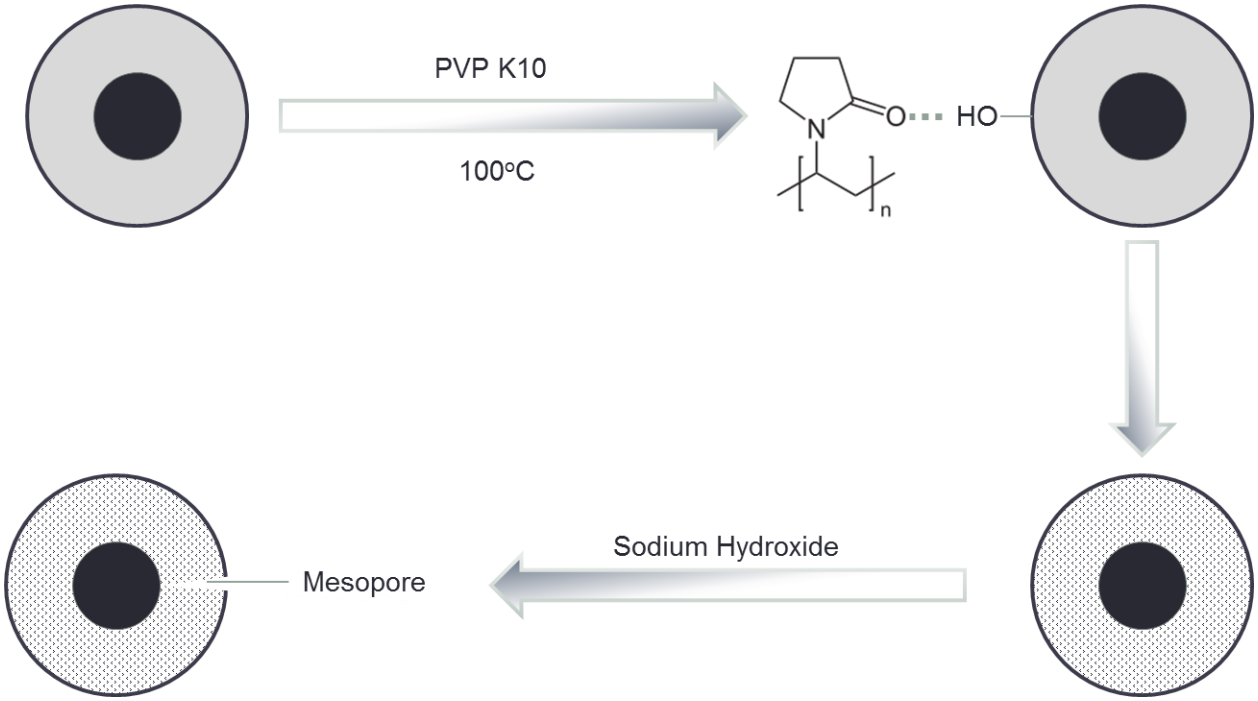

Figure 3.31: Schematic illustration of thermal treatment and base etching procedure.

The dissolution process in water of silica is due to the breaking of Si-O-Si network structures and the formation of monosilicic acid ($Si(OH)_4$)[21] The use of PVP in these systems was intended to aid in the stabilisation of these structures and help prevent agglomeration of the composites, as well as protect the surface from base attack during the second phase of etching.

Sodium hydroxide is a powerful base, and will readily attack and dissolve silica networks.[22, 23] It is for this reason a surface protectant was required and PVP was chosen due to its ability to form strong hydrogen bonds between the surface hydroxyl groups on the silica and the carbonyl groups of the PVP.[24, 25]

A variety of bulk and surface techniques were employed to analyse the materials and study the effect of the etching treatment on the properties of the silver-silica composite materials.

3.4.1. Transmission electron microscopy

The effect of thermal and base etching on the structural integrity and morphology of the parent nanocomposites material was investigated by TEM analysis. This method

allowed observation of possible changes to the nanocomposites dimensions during the post-synthetic treatment procedure. Representative images of the parent and processed materials are evidenced in **figure 3.32**.

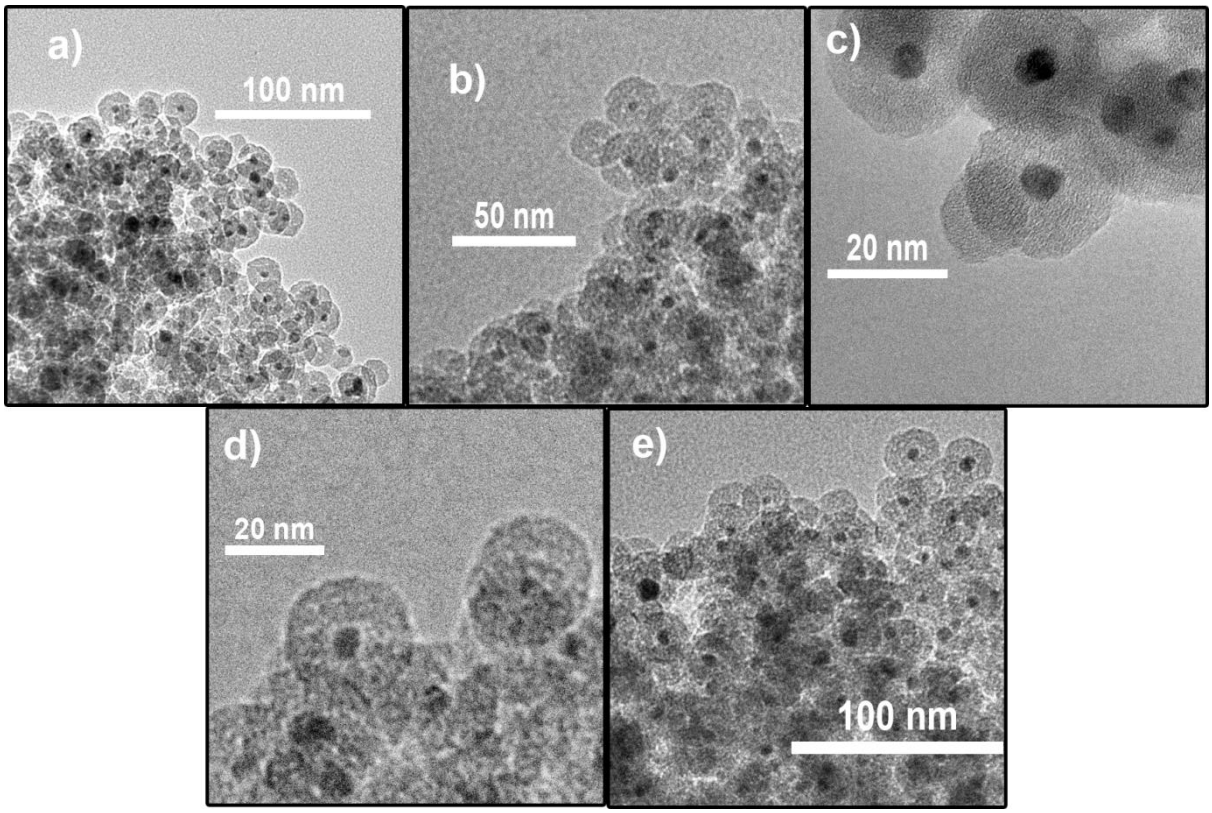

Figure 3.32: Representative bright-field HRTEM images of silver-silica nanocomposites as a function of post-synthetic treatment (a) parent material, (b) heat-treated, (c) 30 minute base etching, (d) 60 minute base etching, (e) 120 minute base etching.

As with previous materials, the clear boundary between silver core and silica shell can be witnessed easily, allowing for facile identification of the core-shell architecture. In all cases, the materials appear to retain the original structure. A summary of the measured particle sizes is displayed in **figure 3.33** From the size analysis, it can be seen that the effect of the base treatment has no impact on the average dimensions of either the silver core or the silica shell.

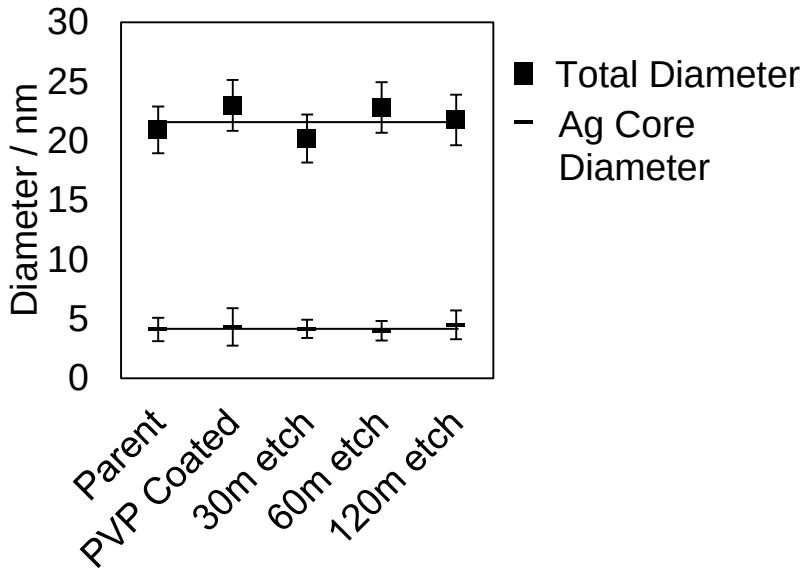

Figure 3.33: Particle dimensions of the two components of the core-shell nanostructure, determined by TEM analysis.

The particle sizing histograms for silver core size and silica shell size are presented in **figure 3.34** and **figure 3.35** respectively.

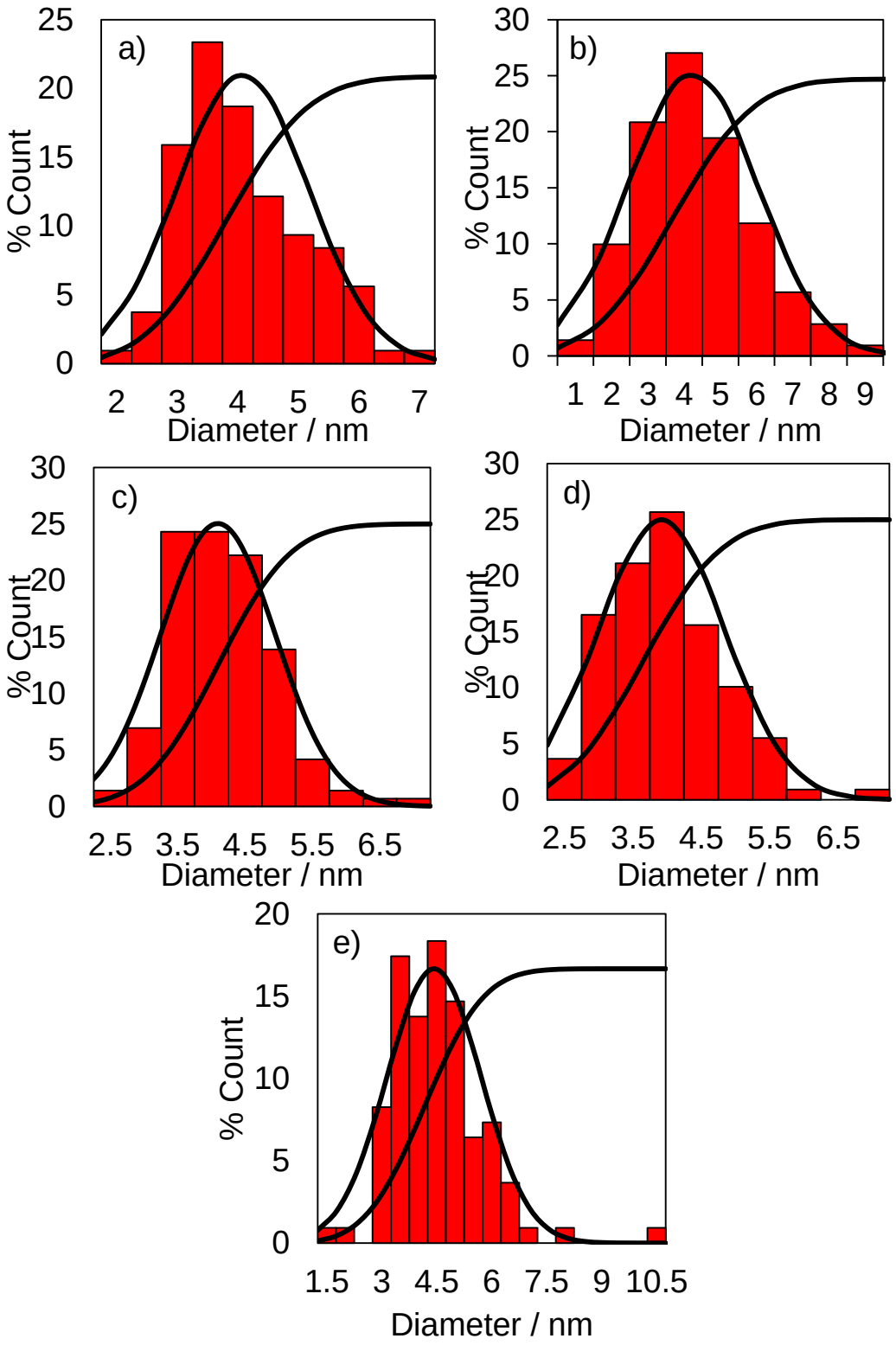

Figure 3.34: Silver core size distributions, normal and cumulative distributions for silver-silica core-shell nanocomposities determined by TEM for post-synthetic treatments of a) parent material, b) heat-treated, c) 30 minute base etching, d) 60 minute base etching and e) 120 minute base etching.

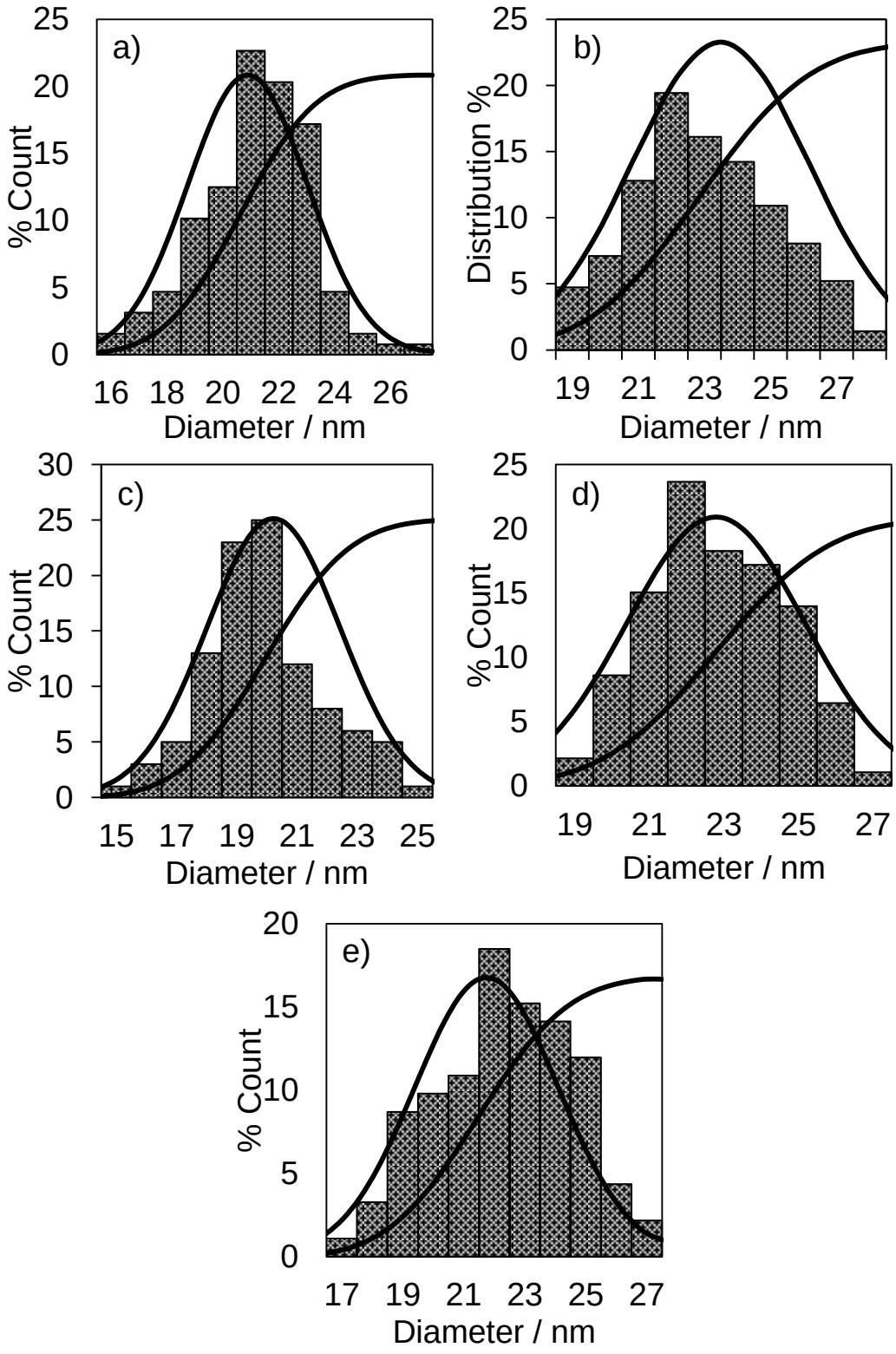

Figure 3.35: Silica shell size distributions, normal and cumulative distributions for silver-silica core-shell nanocomposities determined by TEM for post-synthetic treatments of a) parent material, b) heat-treated, c) 30 minute base etching, d) 60 minute base etching and e) 120 minute base etching.

The silver cores are, on average, unaffected by the etching treatment, with the size remaining at around a constant 5 nm and within error. After longer treatment periods, however, some silver cores appear to have been removed from their silica shell. This is evident by the appearance of a light halo in the centre of the silica shell in the TEM. The number of cores which are removed from the composite materials increases as the length of etching treatment increases. As the silver cores which remain encapsulated inside the silica shells do not decrease in diameter on average, it is likely that the silver cores are removed as a whole, i.e. a pore appears which is large enough to cause migration of the silver core to outside of the composite material and is allowed to form an agglomerate elsewhere.

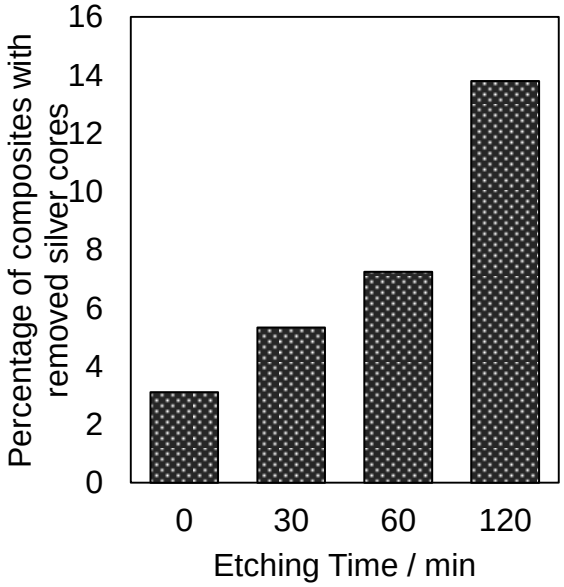

Figure 3.36: Percentage of composite materials to have 'lost' a silver core during the etching treatment, as a function of etching time

Figure 3.36 indicates the percentage of composite particles to have had a silver core removed during the base etching treatment, as a function of etching time. The 'zero' minute etching material has undergone the thermal treatment, which is the reason for the loss of some cores, as the composite materials which have not undergone any kind of treatments do not exhibit any hollow shells in TEM analysis.

Following the longer etching treatments, some silver agglomerations can be seen in the TEM as the silver cores removed by sodium hydroxide treatment are unstable at

such small sizes, and seek to form lower energy, more stable agglomerations of larger silver particles.

3.4.2. Powder x-ray diffraction

The XRD diffraction patterns (**figure 3.37**) show that the silver is in the metallic state in the untreated material once again, and remaining unchanged in both size and oxidation state throughout the duration of the treatment.

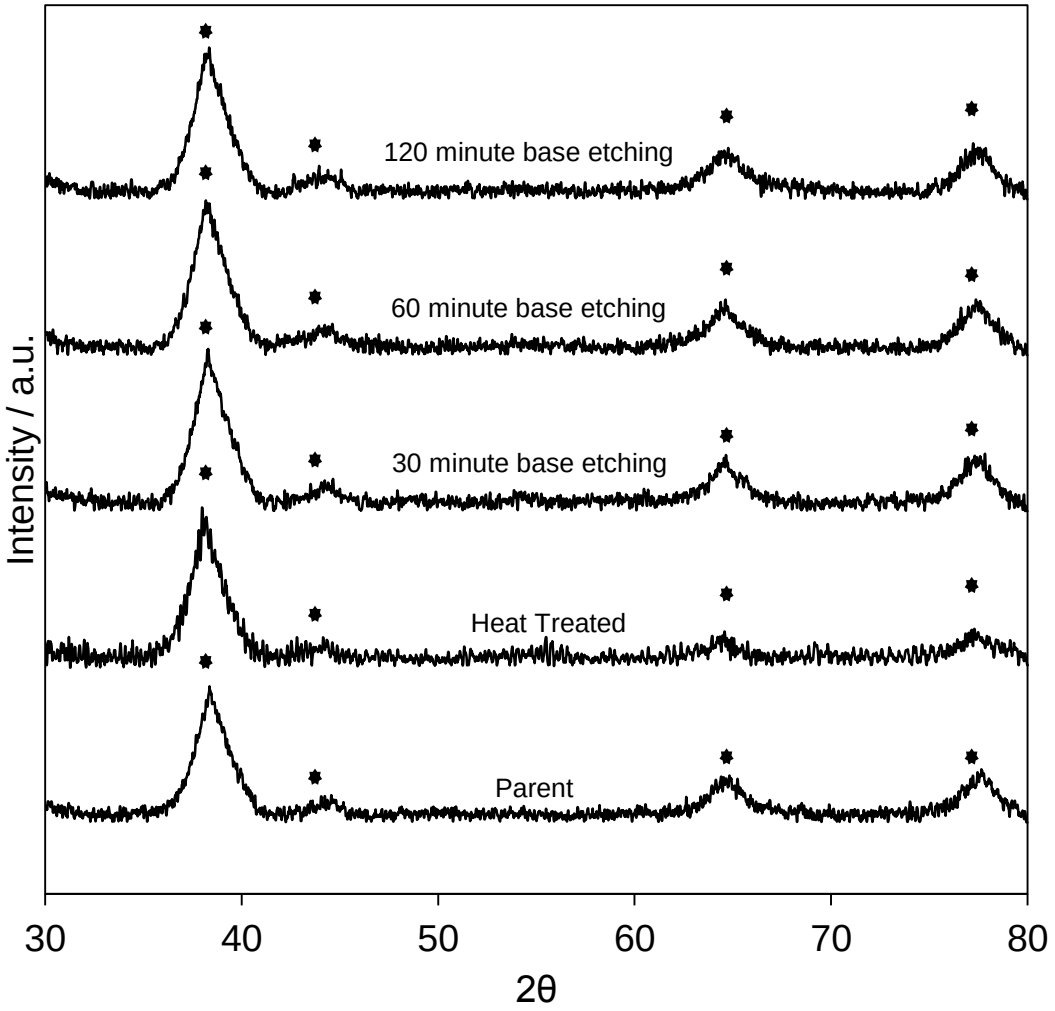

Figure 3.37: Powder XRD diffraction patterns for etched $Ag@SiO_2$ nanocomposite materials. (*) indicated Ag^0 FCC reflections.

Particle sizing using the Scherrer equation (**Table 3.6**) indicates the consistency in silver core size during the etching procedure. This complies with the particle sizing from TEM analysis, confirming that the silver cores are largely unaffected by the treatment. Particle sizing was performed using by fitting curves using CASA software to the raw data and obtaining values to FWHM.

Material	Ag Core Diameter (XRD) / nm
Parent	4.7 ± 0.2
Heat Treated	5 ± 0.2
30m base etch	4.6 ± 0.2
60m base etch	4.8 ± 0.2
120m base etch	4.9 ± 0.2

Table 3.6: Silver core particle sizes from Scherrer equation.

3.4.3. Elemental analysis

The silver bulk loading was determined using ICP-MS, following HF digestion of the material samples. Tese values were compared with the values for surface Ag, determined by XPS analysis. These are tabulated in **table 3.7**.

Sample	Bulk Ag wt. %	Surface Ag wt. %	Surface:Bulk Ag ratio
Parent	2.05	1.24	0.60
Heat Treated	1.83	0.88	0.48
30 min etch	1.89	1.39	0.74
60 min etch	1.84	1.42	0.77
120 min etch	1.78	1.67	0.94

Table 3.7: Bulk and surface Ag wt. % values for etched Ag@SiO_2 nanocomposites.

The silver loading is seen to decrease post thermal treatment, which is consistent with the adsorbing of PVP onto the surface of the silica shells, lowering the overall silver percentage. After this decrease from the silver content in the parent material, there is no further significant decrease in silver content. This could suggest that silica which is removed during the etching treatment is either not in a significant enough amount to affect the silver loading to any large extent, or, that the silica species which

is removed is simply moved to a different form and not removed from the solution during the centrifugation and washing step. The increase in surface to bulk Ag wt. % is represented graphically in **figure 3.38**.

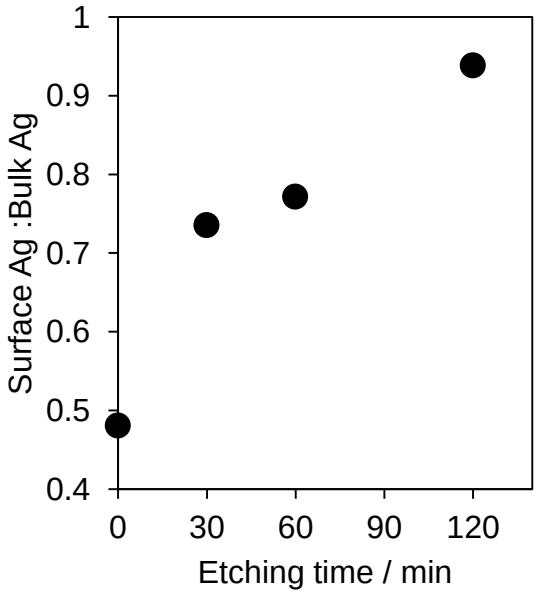

Figure 3.38: Ratio of surface (determined by XPS) to bulk (determined by ICP-AES) silver content as a function of etching time.

Figure 3.39 represents the increase in surface silver to silver bulk in the composite materials during the etching process. This increase is unaffected by any potential decreases in silica content and is a pure comparison between surface available silver, and absolute silver content. The ratio shows a dramatic increase during the etching procedure, which lends support to the idea that the silica shells are becoming more porous.

Some evidence of amorphous silica can be seen in the TEM images for the etched materials, which could support this theory. Post etching, small regions of amorphous, non-structured material appears in the surrounding areas, which are not present in the parent material (**figure 3.39**).

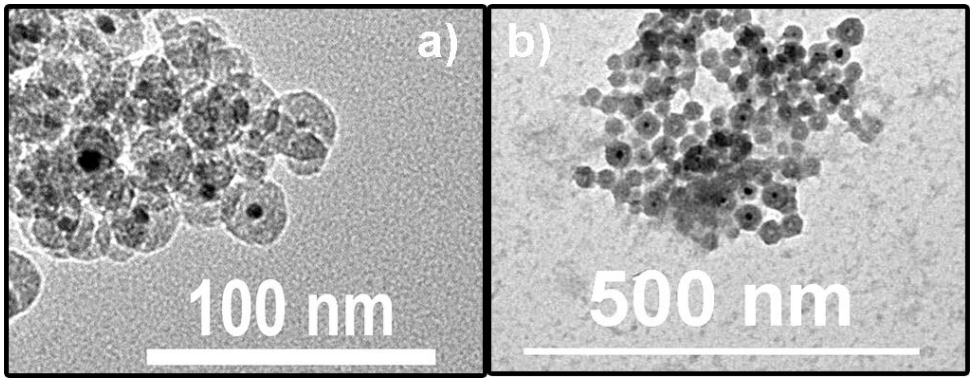

Figure 3.39: Bright field TEM images of (a) parent Ag@SiO_2 material and (b) 120 minute etched nanocomposites material, highlighting a particularly heavy region of 'excess amorphous silica'.

The increase in surface:bulk ratio of detectable silver in the etched materials, despite the consistent overall bulk loading, is a promising indicator that the silica shells are indeed being etched. It has been observed by TEM that the particle sizes remain unchanged throughout the prodecure, however the surface available silver increases, which is suggestive of a less dense silica network surrounding the metallic silver cores, imparting a lower degree of attenuation upon the released silver photoelectrons.

3.4.4. X-ray photoelectron spectroscopy

XPS was used to quantify the silver present in the etched materials, and to look at how that value changed over the etching period. **Figure 3.40** represents the increase of the silver signal detected by XPS, relative to the silica signal.

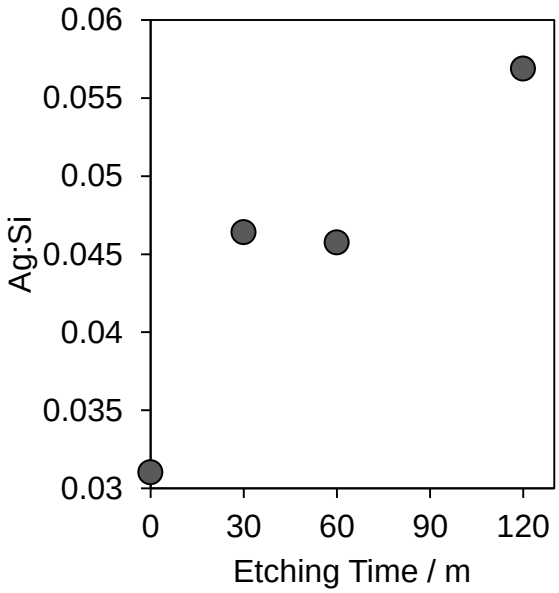

Figure 3.40: Surface silver to silica ratios in the nanocomposites as a function of etching time.

The reasons behind this increase could include the removal of silver cores and formation of agglomerate particles, increasing the amount of silver at the surface of the particles, however these large particles would also suffer from reduced penetration depth due to the high density of silver metal decreasing the mean free path of released photoelectrons, thus a large increase in the silver region is unlikely. A second reason behind this increase could be due to the removal of silicate species by the base etching treatment. Finally, as **figure 3.41** exhibits, the particle dimensions are unaffected by the etching process, so the increase in silver availability at the surface of these composites could suggest less attenuation of the photoelectrons through the silica shell, due to a lower density throughout the shell due to the presence of pores.

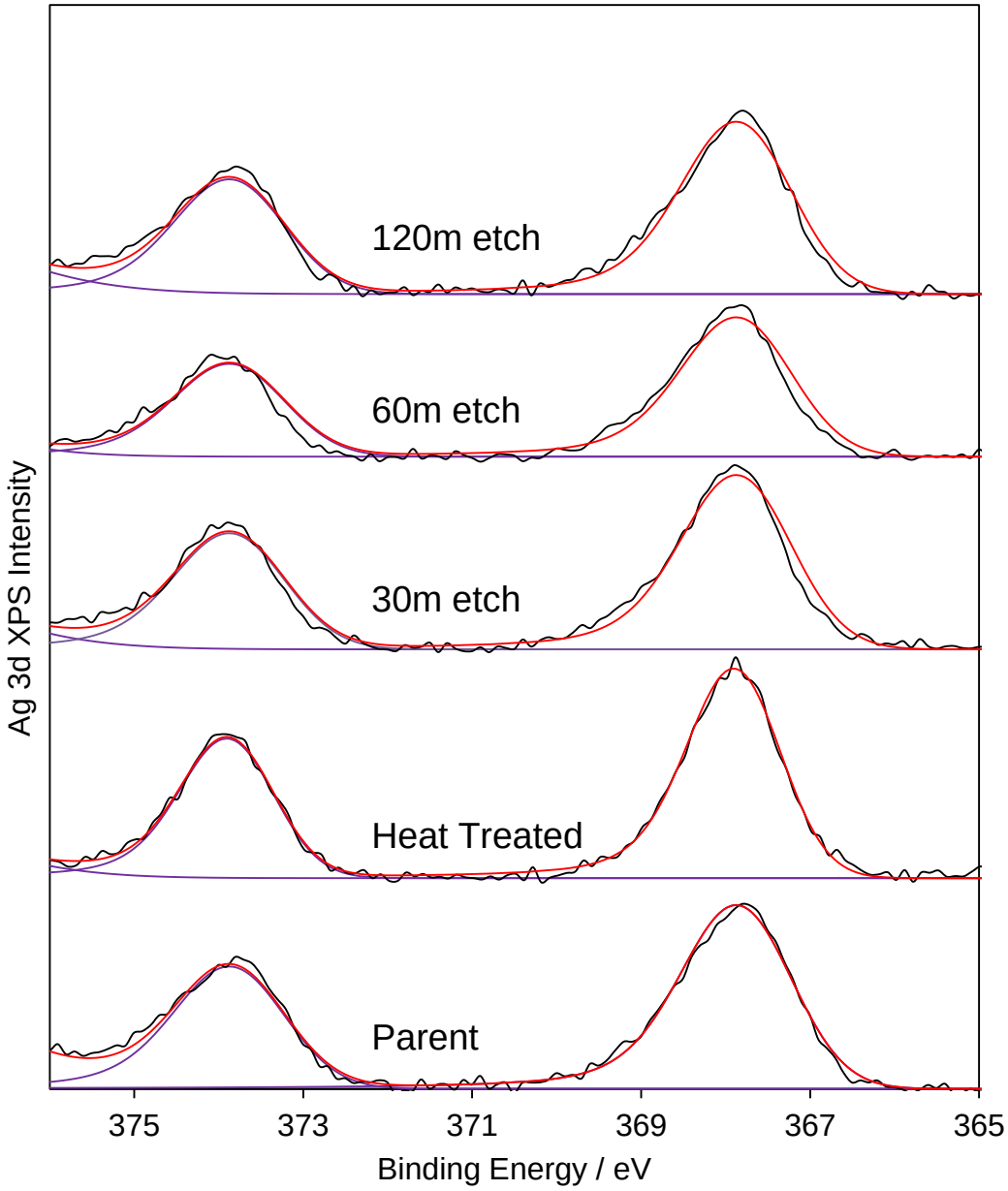

Figure 3.41: Ag 3d XPS stack plot of etched Ag@SiO_2 nanocomposites.

The binding energy of the silver regions was consistent with previous materials, recording a peak for Ag 3d 5/2 at 367.9 eV suggesting the presence of silver metal, with no visible shoulders indicative of the presence of additional oxidation states.

The nitrogen regions were studied using XPS to measure changes in PVP content adsorbed onto the surface of these composites during the base etching treatment (**Figure 3.42**).

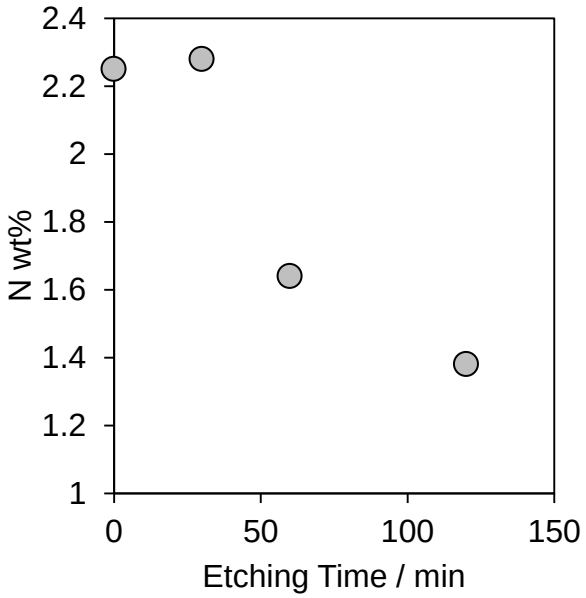

Figure 3.42: Surface nitrogen content as a function of etching time.

A steady decrease in nitrogen amount can be seen by XPS analysis, a resultant peak from adsorbed PVP, which proposes that some PVP suffers removal during the base etching treatment.

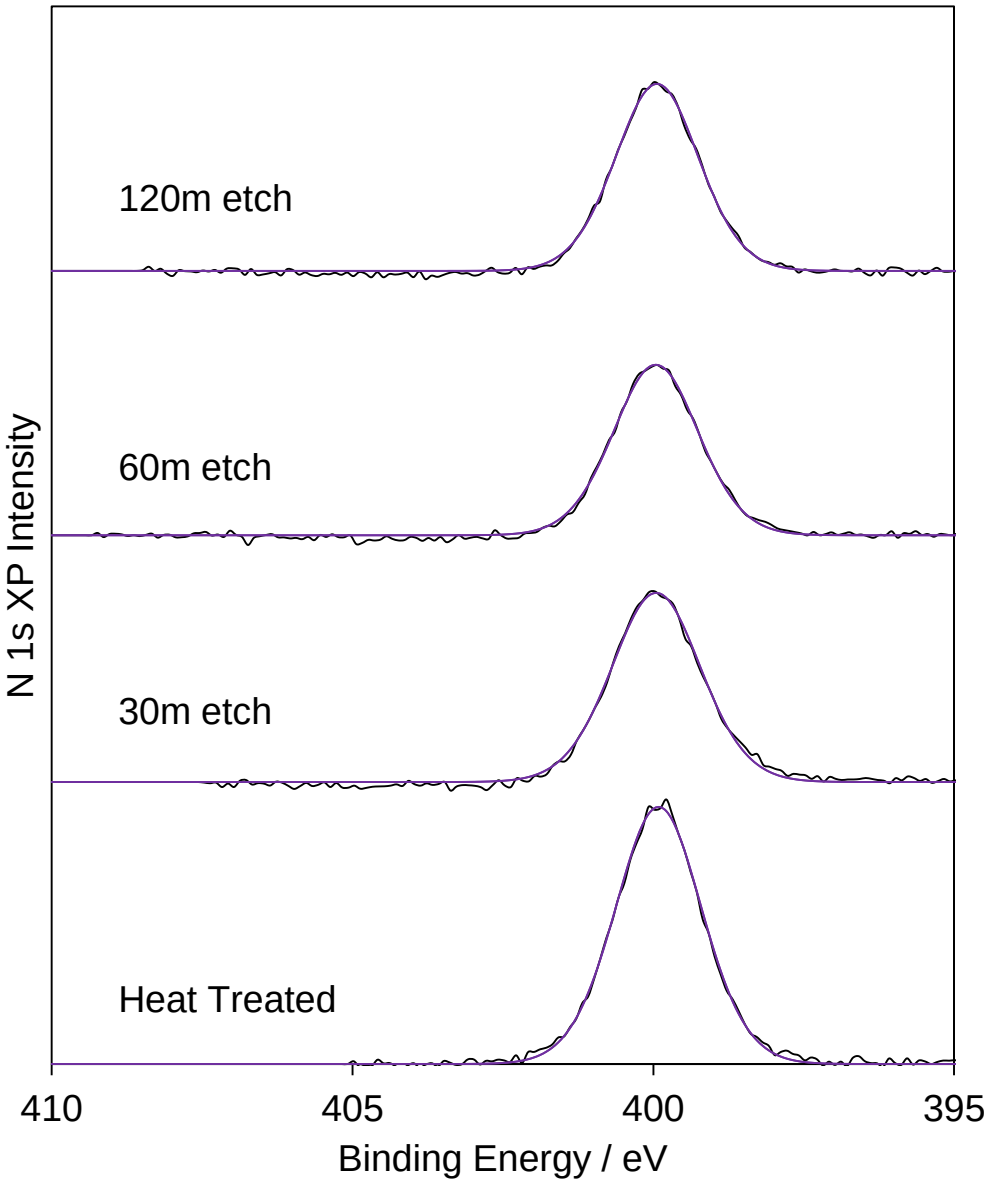

Figure 3.439: N 1s XPS stack plot of etched Ag@SiO_2 nanocomposites

It can be seen from the XPS data that some PVP is removed from the surface of these materials during the base etching treatment. It is also possible that as pores are opened up in the silica, the PVP molecules are desorbing and readsorbing inside the pores of the structures, which would decrease their visibility in the XPS.

The N 1s peaks in **figure 3.43** appear at 399.9 eV, higher than the recorded value for PVP (399 eV). This could be due to interactions between polymeric nitrogen and surface silanols.[26]

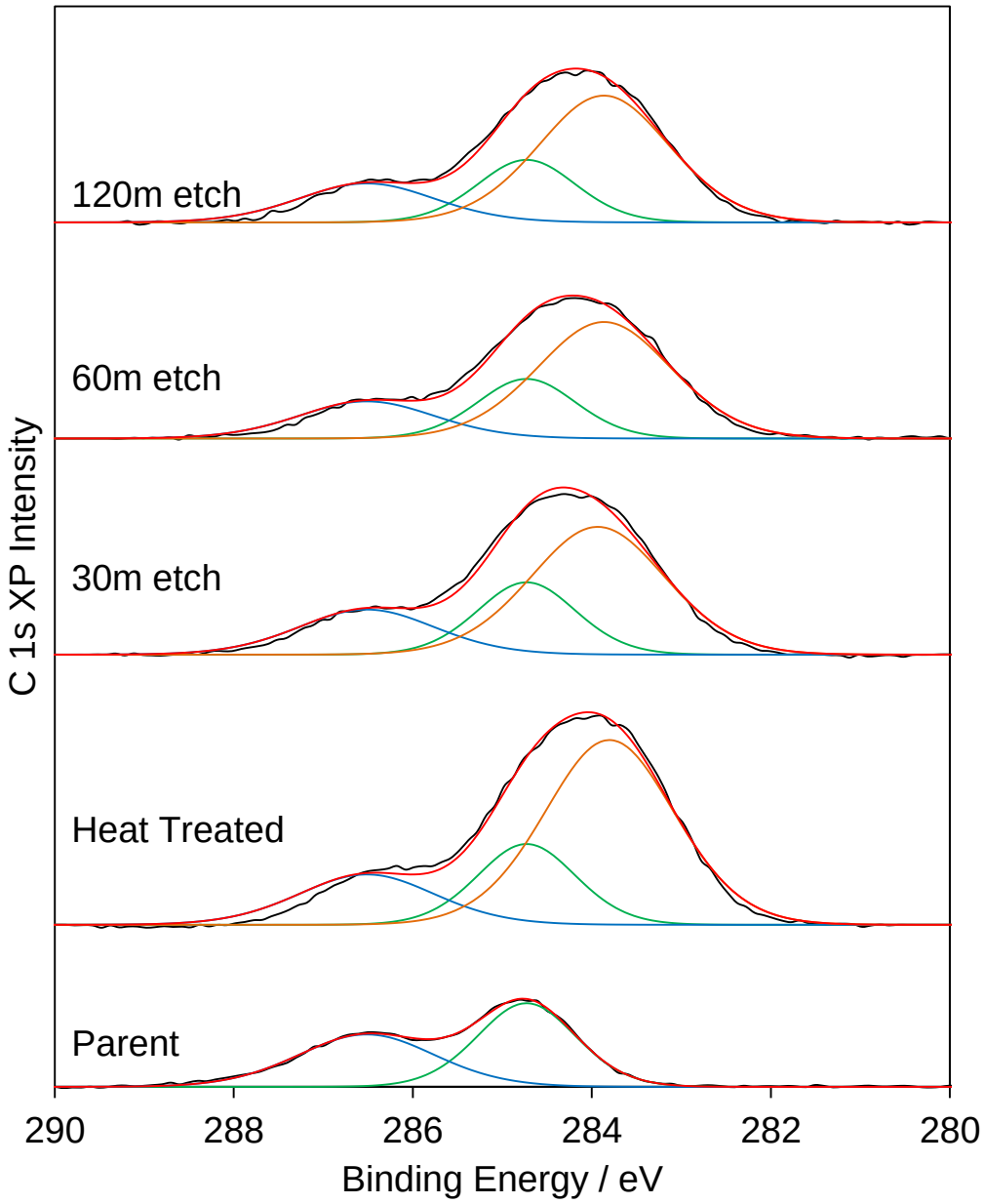

Figure 3.44: C 1s XPS stack plot of etched Ag@SiO_2 nanocomposites.

The carbon regions identified by XPS analysis are exhibited in **figure 3.44**. There is a strong increase in carbon signal, post PVP adsorption, with the carbon region associated with the PVP molecules appearing at 283.6 eV.

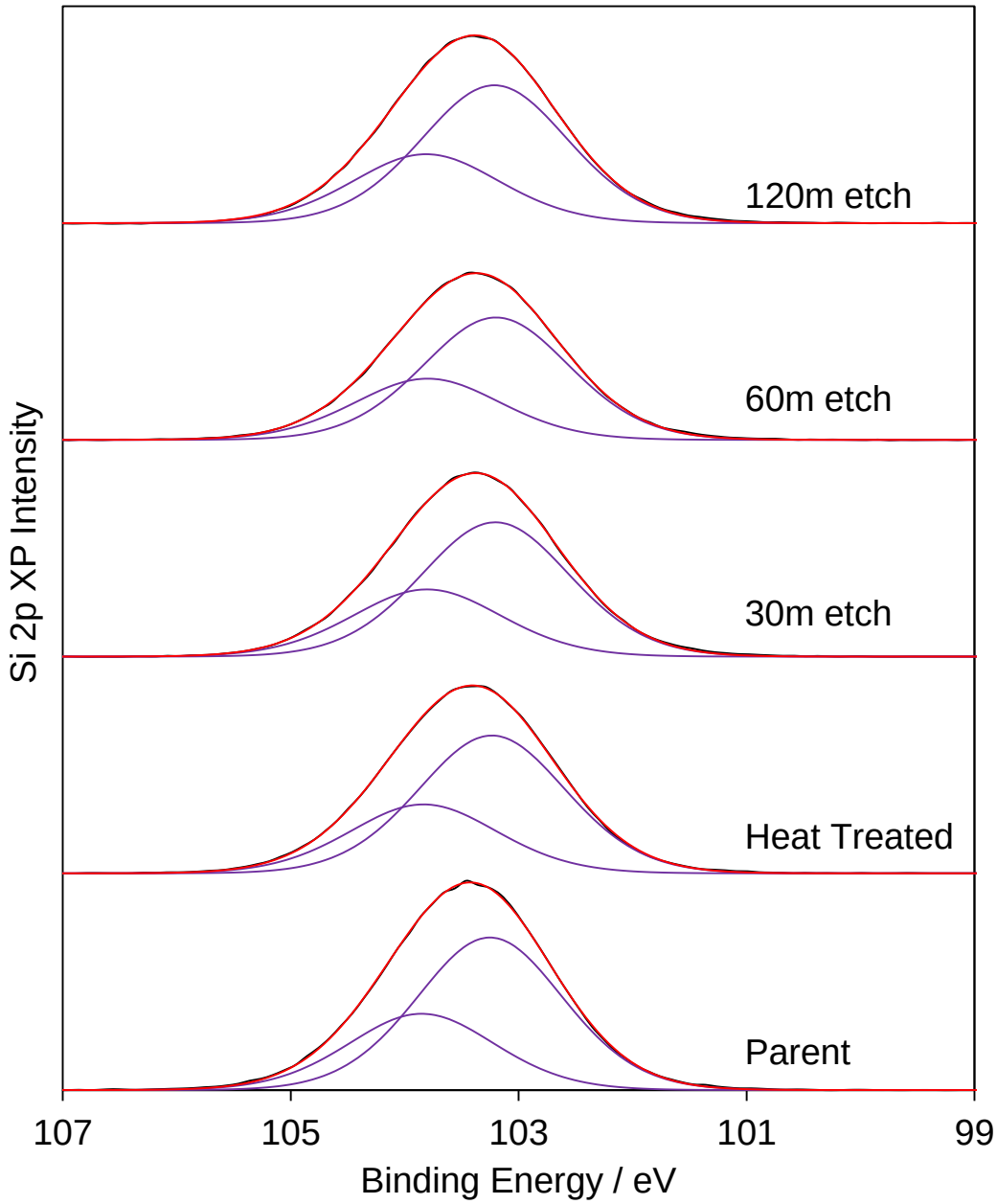

Figure 3.45: Si 2p XPS stack plot of etched Ag@SiO_2 nanocomposites.

Figure 3.45 displays the recorded silicon regions, which corroborate with previous studies, recording a maxima at a binding energy of 103.4 eV. The doublet separation was set at 0.6 eV, with peak areas set to a 2:1 ratio for the 2p 3/2 and 1/2 components, according to values obtained from the NIST database.[27]

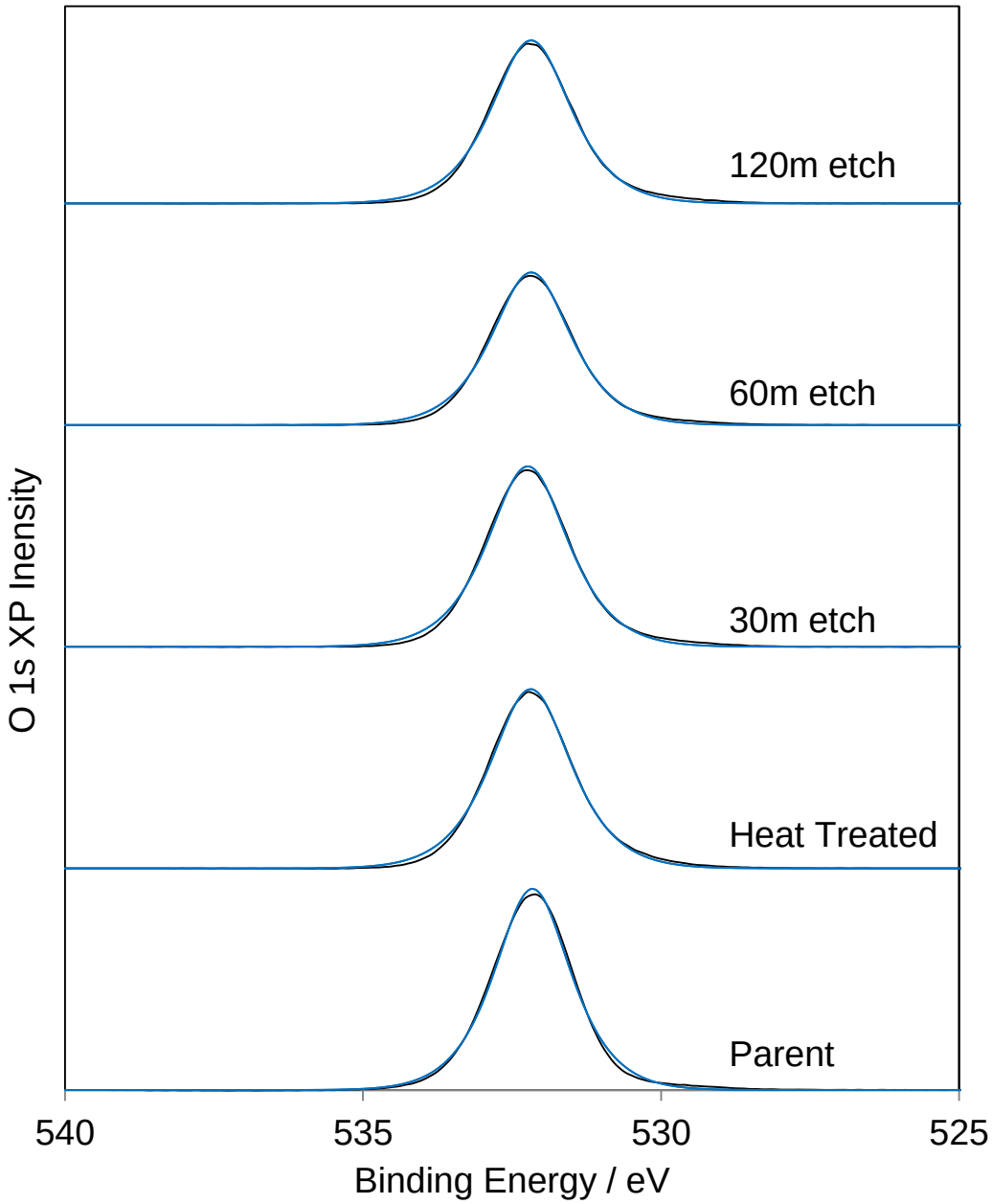

Figure 3.46: O 1s XPS stack plot of etched Ag@SiO_2 nanocomposites**.**

Figure 3.46 shows the oxygen regions, recorded by XPS measurements. The oxygen region is seen to remain constant throughout the post-synthetic treatment. No contribution from the oxygen in PVP can be seen, this is likely due to the relative insignificance of this moiety with regards to the oxygen signal from the silica.

3.4.5. Porosimetry

Following the etching procedure, the samples are analysed using nitrogen adsorption porosimetry, to determine any change to the surface areas of the etched materials. The recorded isotherms are presented in **figure 3.31**.

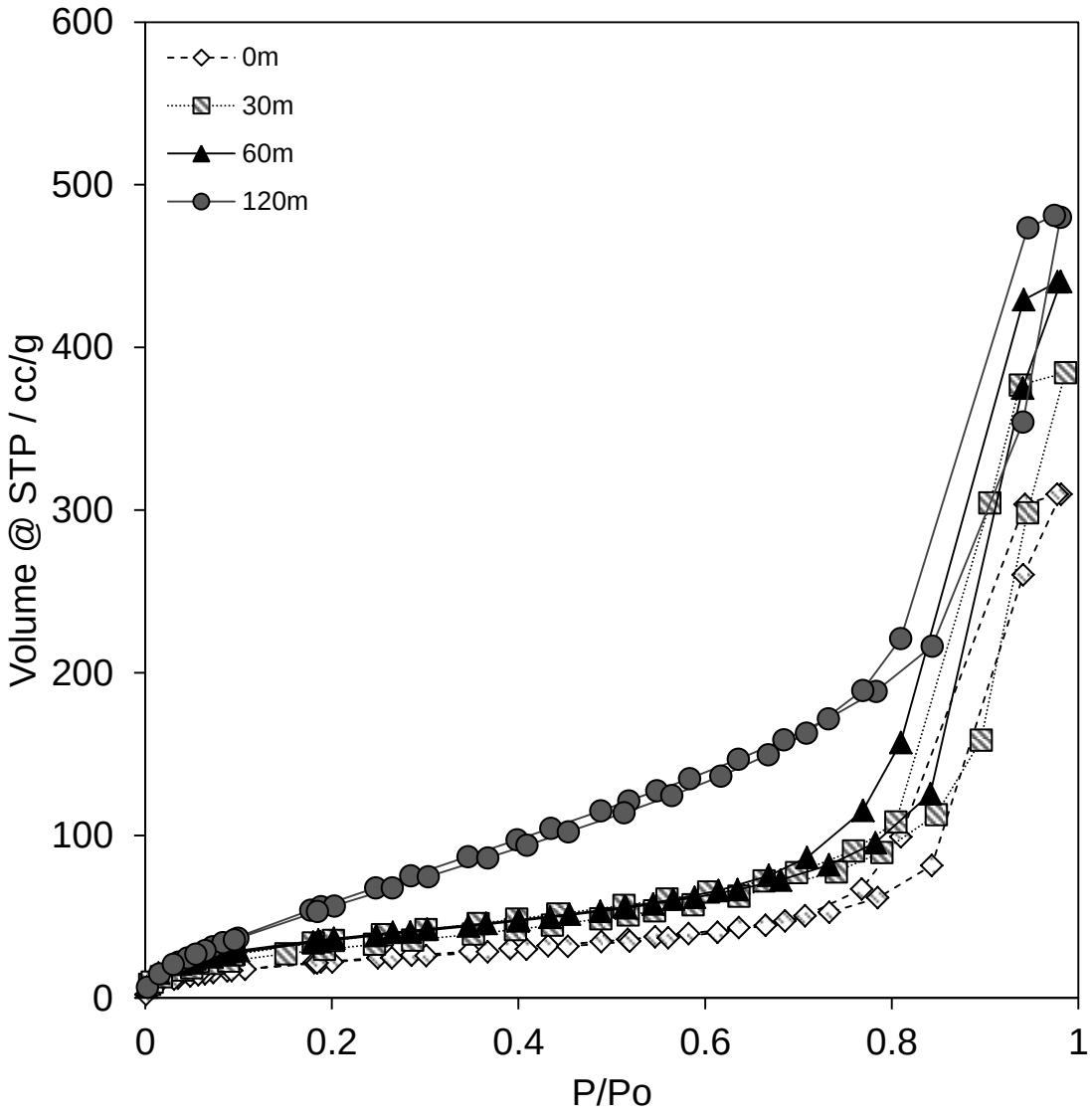

Figure 3.47: Nitrogen adsorption isotherms for etched Ag@SiO_2 nanocomposite materials.

Using the BET equation, the surface areas were determined and an increase was noted which correlated with the increase in etching time (**Figure 3.48**).

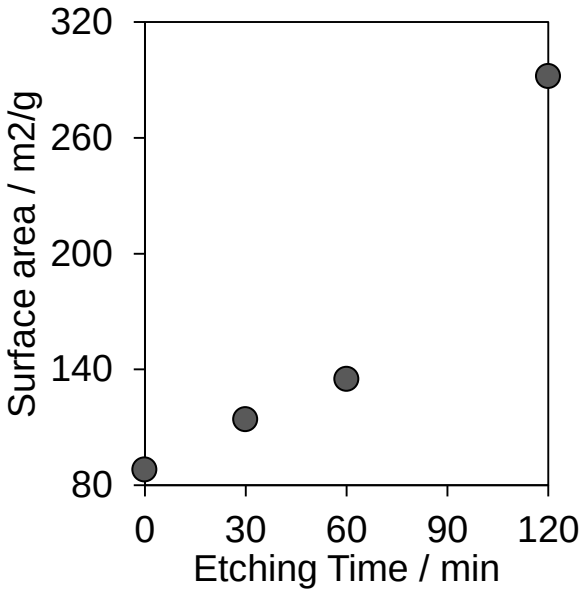

Figure 3.48: Increase in Ag@SiO_2 nanocomposite surface area during etching treatment.

.

To look in more detail at the porous nature of these materials, a Barret-Joyner-Halenda method was applied to the adsorption data. This allows for a representation of pore size and pore size distribution of the prepared materials (**Figure 3.49**).

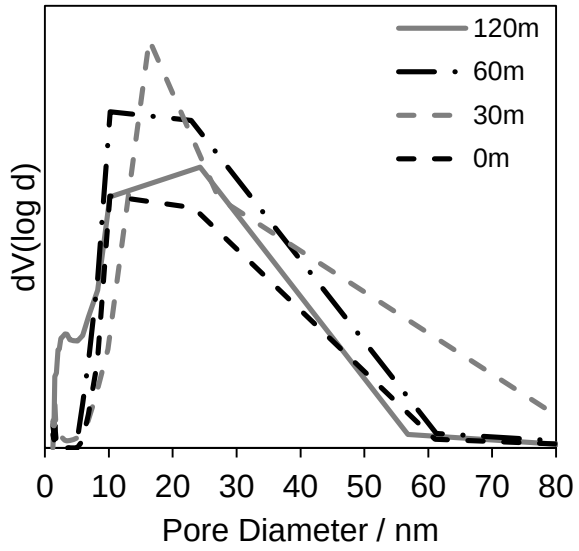

Figure 3.49: Barrett-Joyner-Halenda profiles from etched Ag@SiO_2 nanocomposite materials.

From the BJH plot, it is evident that the pores etched into these materials cover a wide range of sizes. The large increase in adsorbed gas at around 10nm and above is likely due to interparticle spacings, rather than intraparticle voids.

It would appear that the pores do not appear in large numbers until 2 hours in the presence of sodium hydroxide, which is consistent with the recorded increase in surface area and isotherms. After 1 hour, there is an increase in pore volume for pores between 5-10 nm, which would account for the increase in surface area for this material. After 30 minutes of etching, the surface area increases, although there is actually a slight increase in recorded pore sizes (attributed to interparticle spacings), which could be due to removal of some surface PVP before the particles have a chance to develop any pores.

Incidentally, the microporous surface area of all materials, with the exception of the parent material (17 m^2/g), is zero, according to the t-plot method. This could be attributed to blocking of the pore openings by PVP molecules adsorbed onto the surface.

3.4.6. Attenuated total reflectance Fourier transform spectroscopy

ATR FT-IR was used to identify the adsorption of polyvinylpyrrolidone onto the surface of the silver-silica nanocomposites and has the advantage of being more specific to PVP molecules than analysis of the nitrogen regions with XPS. Polyvinylpyrrolidone exhibits a characteristic fingerprint in the FT-IR spectra which is clearly evident upon the adsorption of PVP to the particle surface during the heat treatment stage of the etching (**Figure 3.50**). There is a strong absorption at 1630 cm^{-1} which can be easily used to identify adsorbed PVP onto the silica surface, as it is free from any interfering absorptions form other moieties.

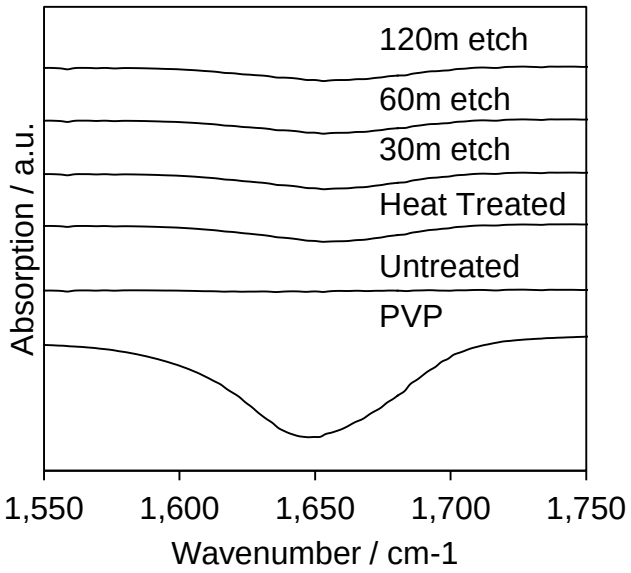

Figure 3.50: FT-IR spectra of adsorbed PVP to composites, before and during etching treatment.

The peak areas of these spectra can be calculated to form a quantitative analysis of the amount of PVP adsorbed onto the surface which can be used to compare between samples (**Figure 3.51**).

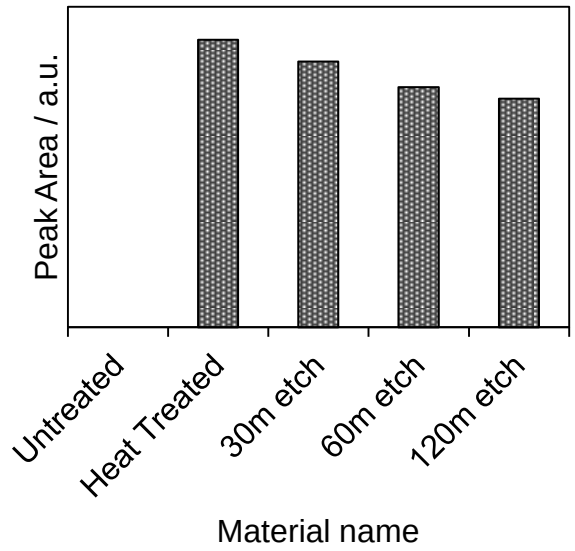

Figure 3.51: Peak areas of PVP adsorption of etched materials.

These areas can also be normalised to the area for the heat/PVP treated composite material, allowing for a quantitative plot representing PVP removed from the materials

during the base etching treatment. **Figure 3.52** plots the removal of PVP with etching time.

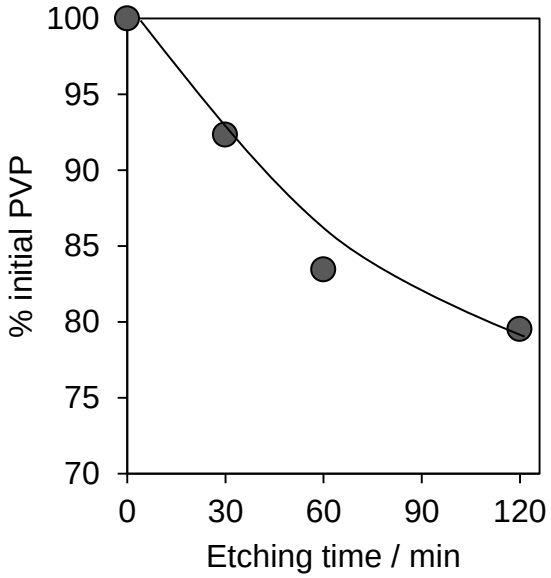

Figure 3.52: Loss of adsorbed PVP as a function of etching time.

This data is consistent with the XPS spectra for nitrogen regions in **section 3.4.4**. As the PVP materials are exposed to longer periods in the presence of nitrogen, some PVP is removed, although this amounts to a total of 20% at the maximum etching time, so the vast majority of PVP remains adsorbed onto the surface of the composites.

3.4.7. Summary of properties of etched nanocomposites

To further functionalise the Ag@SiO_2 nanocomposite materials, a combination treatment was employed, comprising of a thermal treatment, simultaneously adsorbing polyvinyl pyrollidone molecules onto the surface of the silica shells, to act as a protecting agent for the second stage of post synthetic treatment. The second stage involved a dilute base etching methodology to further interact with the silica species and expand the pores present in the sample.

The resultant materials retained the core-shell architecture with which they were created, and absolute particle dimensions were uncompromised throughout the treatment. This was confirmed by TEM analysis, which also saw that some silver cores were, in-fact, removed from the shells during base etching. The silver detectable at the

surface of the materials increased with etching time, whilst the bulk Ag amount remained steady, which has been attributed to a decrease in silica shell density as a result of the etching. This effect was also monitored by nitrogen porosimetry, which resulted in an increase in overall surface area of the materials, as well as an increase in volume adsorbed in the region of 1-10 nm, which is within the targeted range for pore introduction.

3.5. Performance Assays

In order to determine the suitability of these materials as antibacterial agents, and to study how changes to the silver core size affect the activity of these materials, performance assays were undertaken, as described in **Chapter 2**.

3.5.1. Silver dissolution

As the active species thought to be responsible for the antibacterial activity of silver is Ag^{+}, the release of silver ions into solutions was monitored, in order to correlate activity with silver ion release rates. The dissolution was monitored using ICP-MS to study the concentration of solutions taken from a stock at set time points as described in **section 2.4**. These concentrations were then normalised to bulk silver content, so as to determine a release as a function of total silver percentage released.

Silver is known to dissolve into aqueous media via an oxidative process by which solid silver, in the form of nanoparticles, undergoes a redox reaction in the presence of dissolved oxygen and hydrogen species in water, to release silver ions into solution (**figure 3.53**). It is for this reason that the reaction is highly dependent on pH.[28]

$$2\,Ag_{(s)} + {}^{1}/_{2}O_{2(aq)} + 2H^{+}_{(aq)} \longrightarrow 2\,Ag^{+}_{(aq)} + H_2O_{(l)}$$

Figure 3.53: Oxidative dissolution of silver into aqueous media.[29]

3. Silver-silica core-shell nanocomposites: Reverse micelle synthesis

The target dissolution profile for the synthesised materials was a slow release of ionic silver from the bulk particulate form. Silver compounds which have been utilised within the fields of antibacterials and medicine include silver nitrate, which was used to treat burn victims[30] and eye infections in children.[31] The problem with silver nitrate for these applications, is the fast release profile, which is unsuitable for sustained release and long term appications. Silver sulfadiazine has a much slower release profile, and has been in use for many years, however recent reviews have brought into question the benefits of this compound on wound healing.[32]

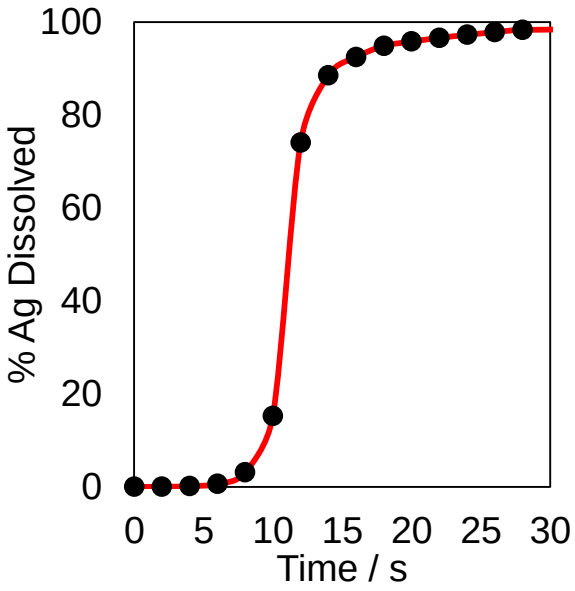

Figure 3.54: $AgNO_3$ dissolution profile determined using a Ag^+/SO_4^{2-} ion-selective electrode.

The release profile for silver ions from nitrate is essentially instantaneous dissolution into aqueous media (**figure 3.54**). Such kinetics are wholly inappropriate for the purposes of this work, and dissolution profiles with more in character with more insoluble silver salts, such as AgO and Ag_2CO_3 are required. A range of silver containing compounds were studied to observe the difference between quick ($AgNO_3$), medium (silver acetylacetonoate) and slow (AgO/Ag_2CO_3) release profiles (**figure 3.55**).

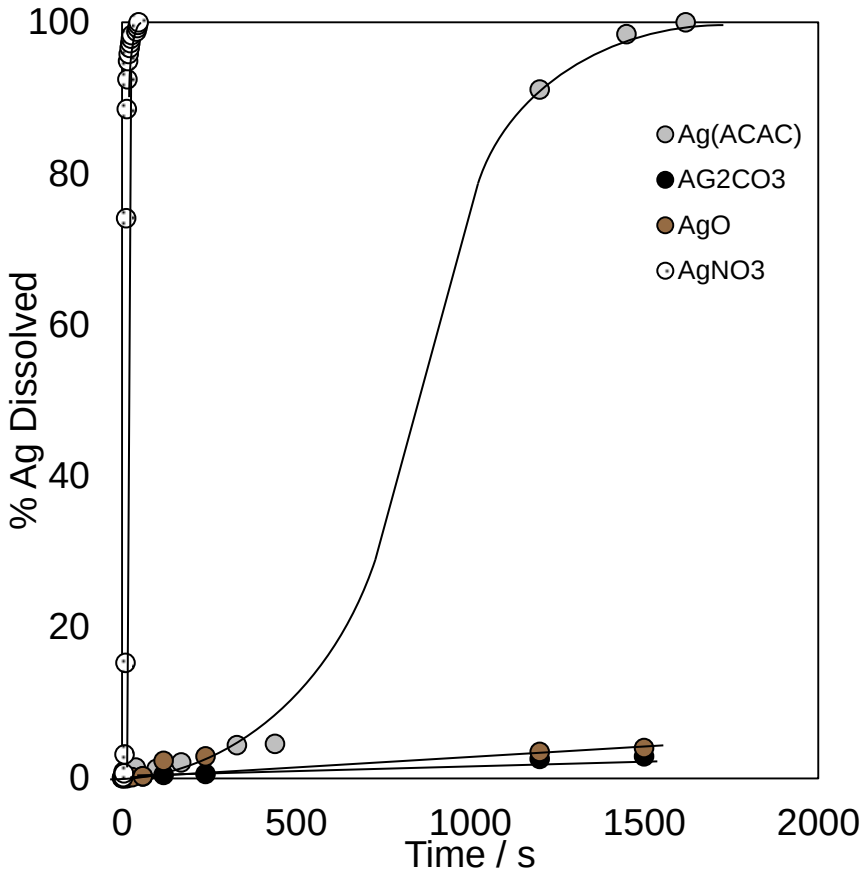

Figure 3.55: Silver ion dissolution profiles from a range of silver containing compounds.

The ideal dissolution range is in the slow region, allowing for the materials to release silver of a long period of time, preferably with rates similar to those observed for AgO/Ag_2CO_3.

Due to the limitations of ionic salts which can be passed through the ICP-MS system, the measurements were performed in a solution of 0.5M sodium nitrate, rather than a complex solution of simulated body fluid, which contains anions, such as sulphates and chlorides, which can damage the instrument.

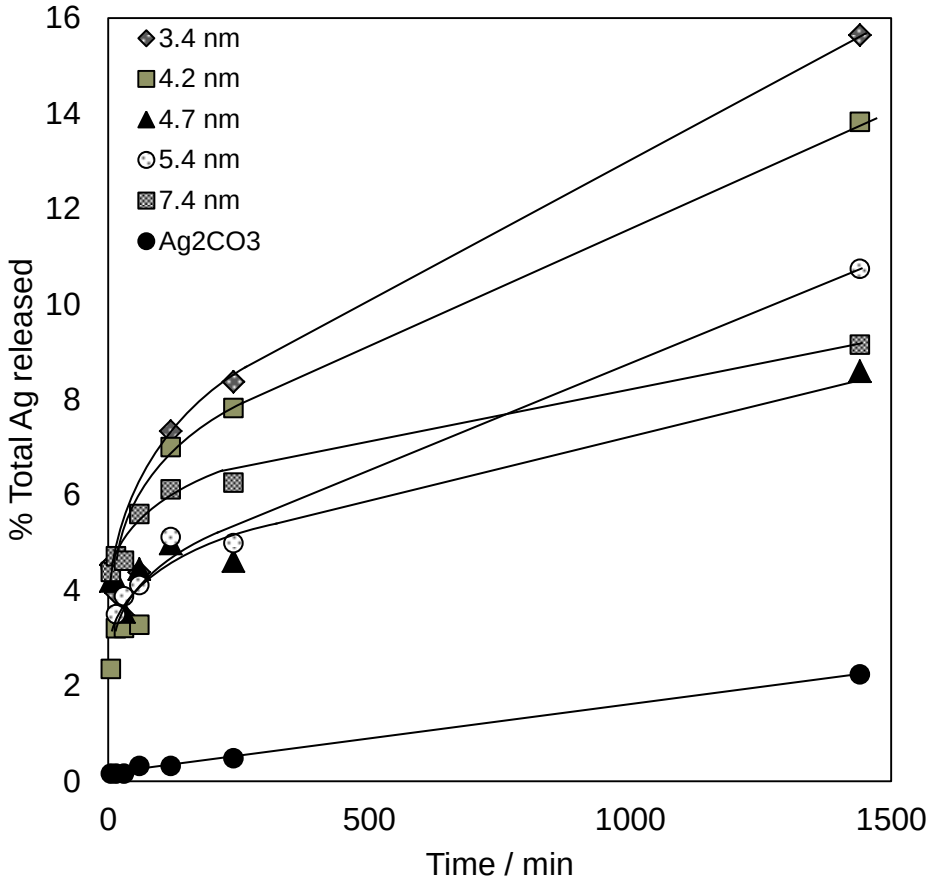

Figure 3.56: Dissolution profiles for silver-silica core-shell nanocomposite materials, normalised to Ag content.

Figure 3.56 plots the dissolution of silver ions into a solution of sodium nitrate as a percentage of the total silver available in the system over a 24 hour period. Whilst there does not appear to be much difference between the larger silver cores, the smaller cores release Ag ions at a faster rate than their larger counterparts. This could be attributed to lower surface areas for the larger cores resulting in lower dissolution rates, as there is less surface contact with aqueous fluid solution, whilst the smaller cores with larger specific metal surface areas have greater contact areas, and hence opportunities for silver ions to be released into solution.

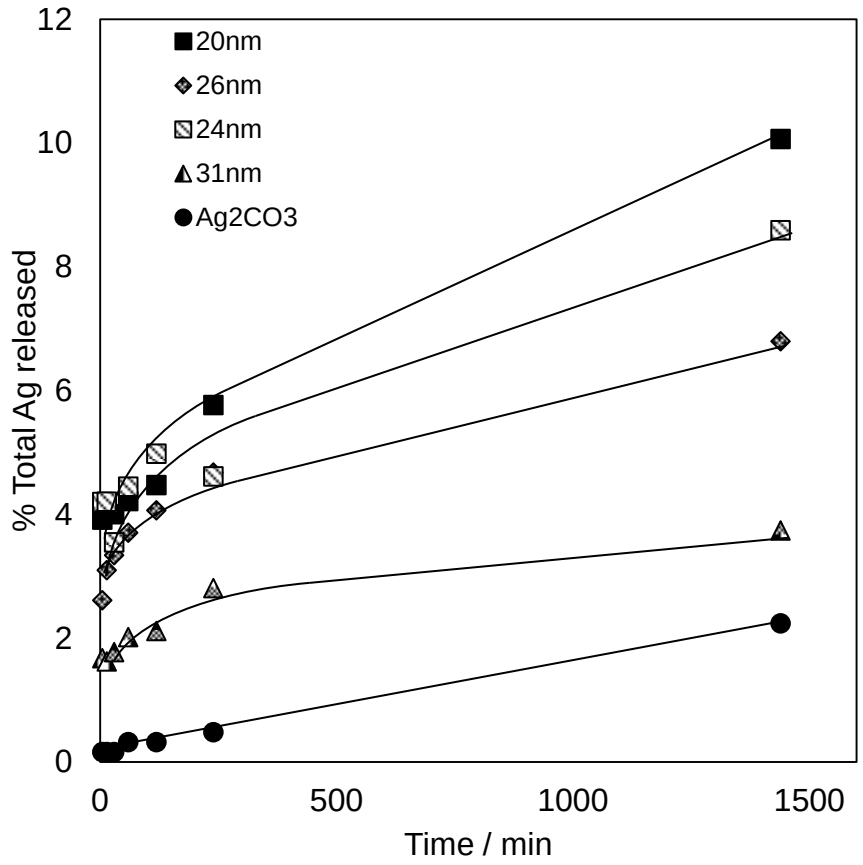

Figure 3.57: Dissolution of silver ions from nanocomposite materials with variable shells, normalised to Ag content.

Figure 3.57 shows how the silver release rate is affected by increasing silica shell sizes over a 24 hour period. The larger shelled materials exhibit the slowest release profile, which could be attributed to a larger silica network surrounding the silver cores slowing the transport of dissolved silver moieties into free solution through interactions with surface hydroxyls.

With such a slow dissolution rate, such materials could be an ideal candidate for sustained release materials, as a very small amount of the total silver is released over a 24 hour period. Provided the materials can display antibacterial activity at such release concentrations, then this increase in shell size could be an intriguing method to increasing the lifetime of these antibacterial additives.

Figure 3.58 displays the dissolution profiles for the etched nanocomposite materials.

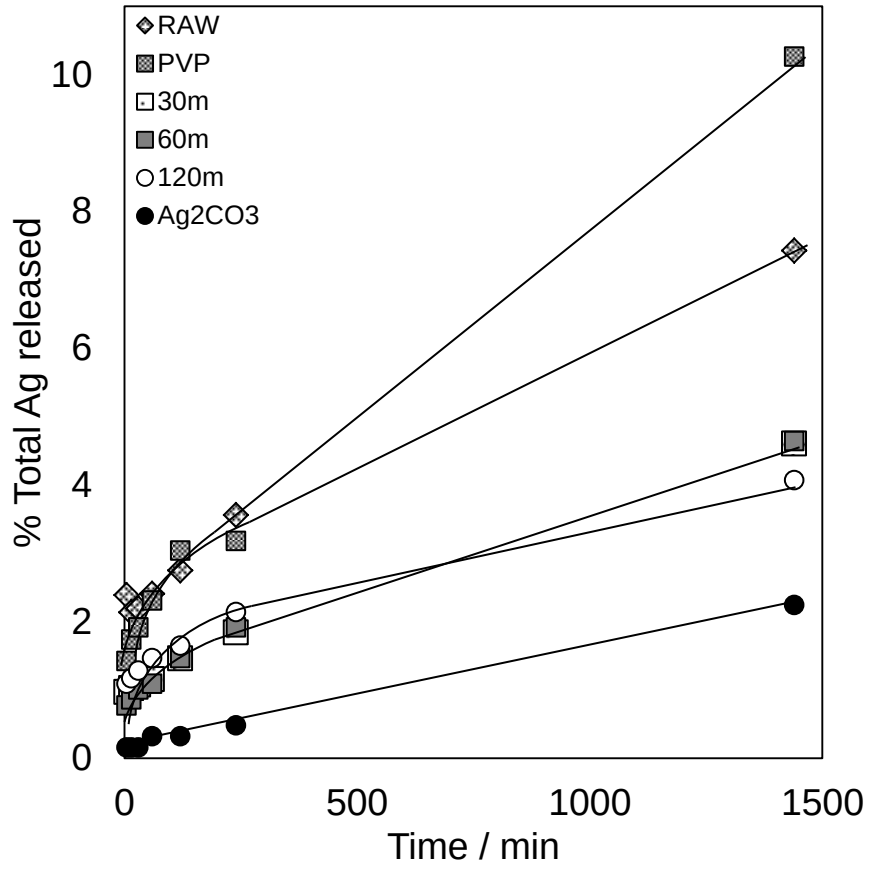

Figure 3.58: Dissolution of silver ions from etched nanocomposite materials, normalised to Ag content.

The heat treatment of the composite materials appears to expedite the delivery of silver ions into aqueous media over a 24 hour period. The subsequent base etching treatment, however, reduces the amount of free silver species released, despite the apparent increase in porosity of the silica shells. The reason for this decrease could be ascribed to blocking of silver surface sites by either redeposited silicate species or PVP molecules decelerating silver ion release.

The composites exhibit attractive dissolution rates for the outlined applications, releasing slowly into aqueous media, with total dissolutions after 24 hours at around 10% of silver content, it is probable that these materials would have far improved lifetimes to silver compounds.

3.5.2. Microbiological assays

To study the effectiveness of the prepared materials as antibacterials, a variety of antibacterial assays were performed as described in **section 2.5**. Inhibition, minimum bactericidal concentration and time kill assays were collected for all samples and silver standards to determine antibacterial activity as a function of silver core size.

3.5.2.1. Zone of inhibition

Zone of inhibition testing was performed, allowing for a quick determination of the presence of antibacterial activity and a semi-quantitative analysis of bactericidal strength. The zone of inhibition test involves spreading a bacterial inoculum onto an agar plate, boring holes into the agar, inserting the material to be testing into the resulting wells and incubating. After 24 hours at 37^{o}C, the wells will have a clear zone around them where bacteria have not been allowed to grow. This zone can be measured and used as an indicator of antibacterial activity and comparative strength, although this test is heavily limited by diffusion through the agar itself. The zones are reported in millimetres and normalised to total silver content. These zone of inhibition tests give a good indicator of the presence of antibacterial activity, but do not give information about kill rates, which is an important factor in the antibacterial industry.

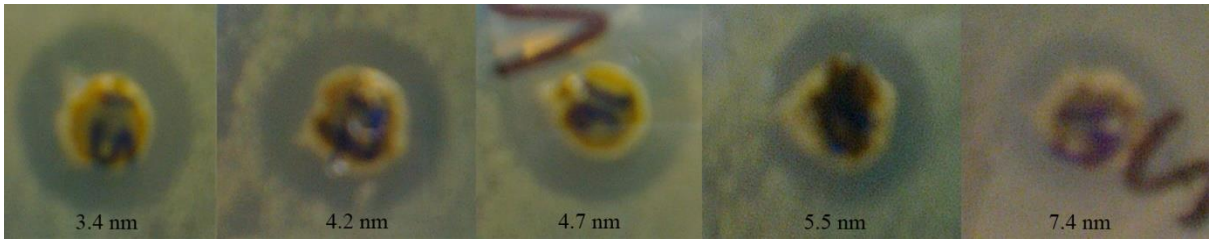

Figure 3.59: Zones of inhibition for silver-silica core shell nanocomposite materials with variable silver core sizes against *Staphylococcus aureus.*

Figure 3.59 is a composite picture of the zones of inhibition obtained from the nanocomposite materials against *Staphylococcus aureus*, along with a positive control (silver oxide) and a negative control (silica nanoparticles, made using the same method as the nanocomposites, which do not contain any silver). The clear areas visible around the wells are the inhibited bacterial regions which are a representative measure of

antibacterial efficacy, assuming diffusion rates are constant between samples. The zones of inhibition against *Pseudomonas aeruginosa* are presented in **figure 3.60**.

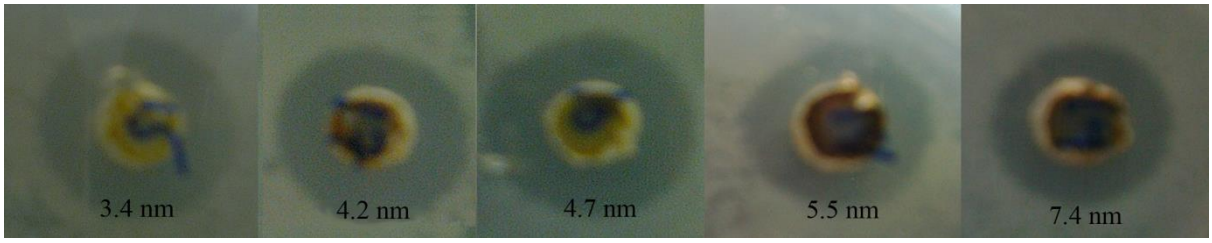

Figure 3.60: Zones of inhibition for silver-silica core shell nanocomposite materials with variable silver core sizes against *Pseudomonas aeruginosa*

The materials were tested in triplicate and averaged, all on the same plate along with a control to ensure consistency in measurements. The zones were measured using image J software, which was calibrated using a steel rule.

Along with the silver containing species, a pure silica sphere material was prepared and tested for antibacterial activity to ensure that the zones were created by the evolved silver species alone. This material created no zones of action around the wells, which suggests that any zone recorded from the composite materials is due to silver ion release (**Figure 3.61**).

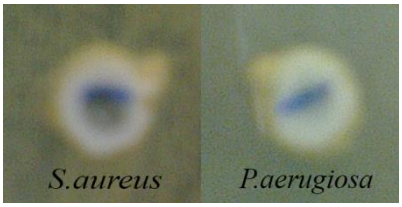

Figure 3.61: Zones of inhibition for pure silica spheres versus *Staphylococcus aureus and Pseudomonas aeruginosa.*

There is no real trend noted in the zone size of the materials, normalised to silver content, against *S.aureus*, MRSA, *E.Coli* or *P. aeruginosa* with respect to the size of the silver core size. This is likely due to the difference in silver ion release being small enough that the limiting factor is diffusion through the agar, resulting in very similar sized zones, and hence the observed antibacterial efficacy of these materials remaining largely similar (**Figure 3.62**).

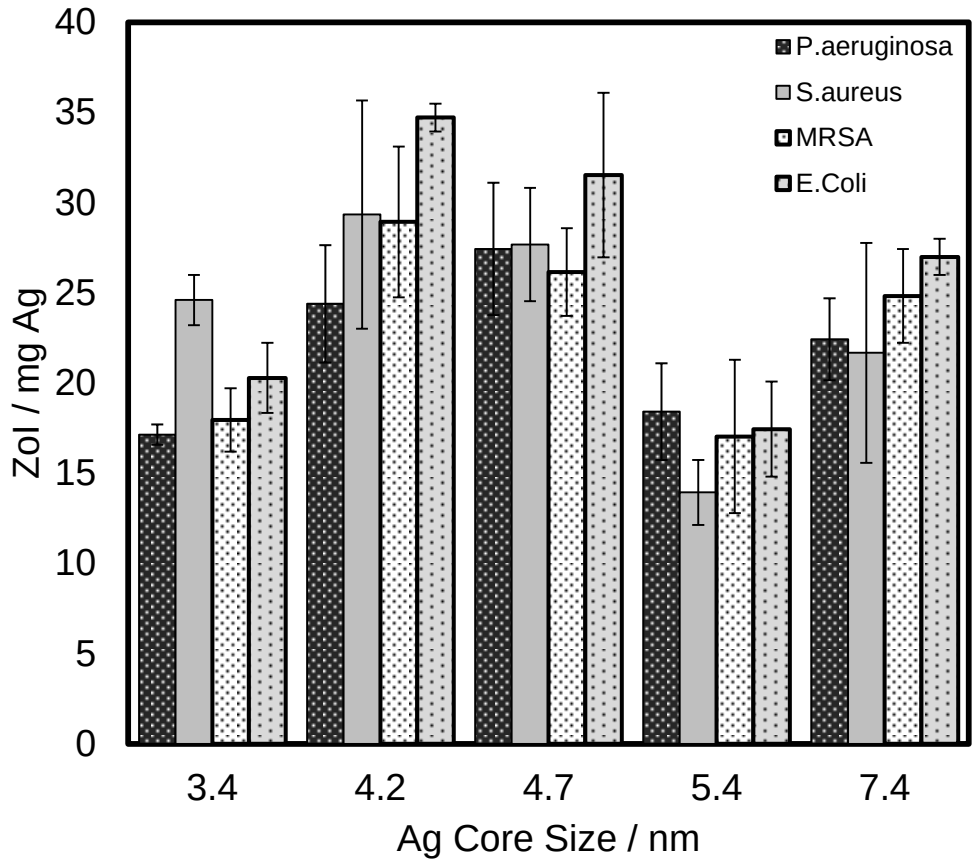

Figure 3.62: ZoI plots for silver silica core shell materials with variable core sizes normalised to Ag content.

It is important to remember when looking at the normalised plots, that the ZoI analysis is not a fully quantitative measurement, merely a tool for determining the presence of antibacterial activity, for a test material.

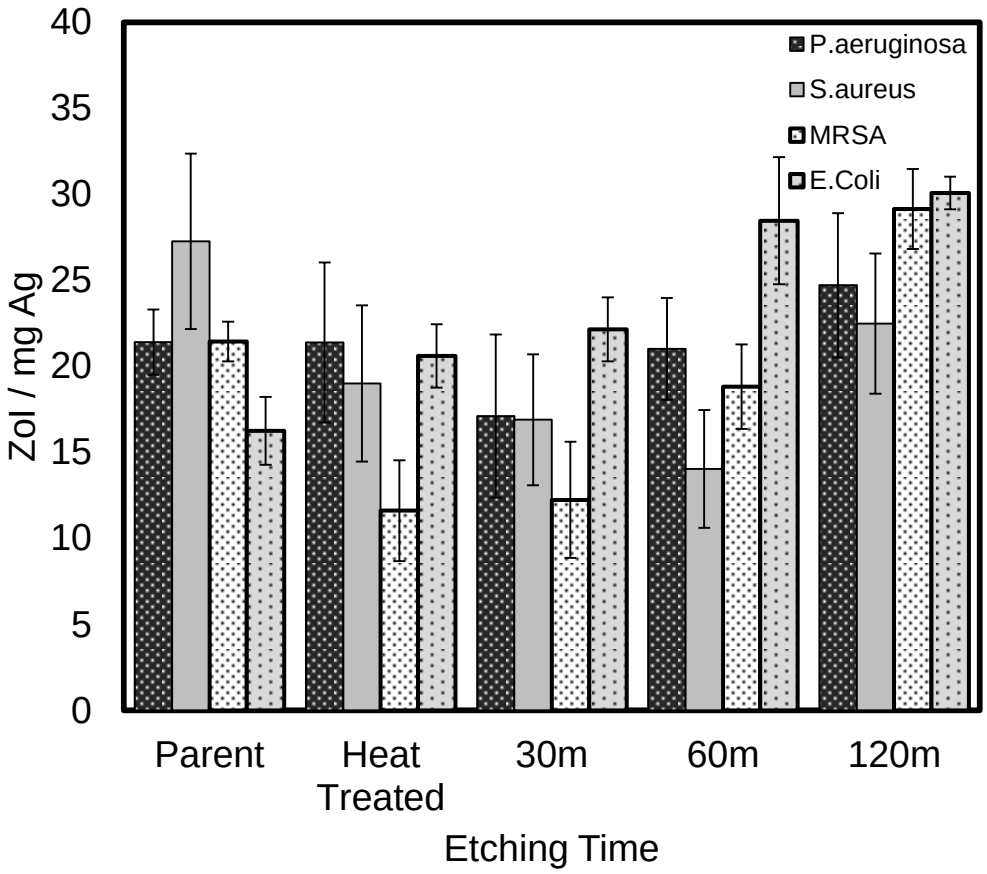

Figure 3.63: ZoI plots for etched silver silica core shell materials normalised to Ag content.

Figure 3.63 displays the recorded inhibited zone sizes for the etched materials normalised to overall silver content, displaying antibacterial activity against all strains tested. There is little difference in the normalised plots, as the materials have similar silver contents and the differences in silver release rates are likely too small to affect the zone size in any measurable way. The results do, however, indicate the release of silver and confirm the antibacterial activity of the composite materials against a broad range of bacteria types. Furthermore, the silver composite materials are as active against MRSA in most cases as they are against non-methicillin resistant *S.aureus*.

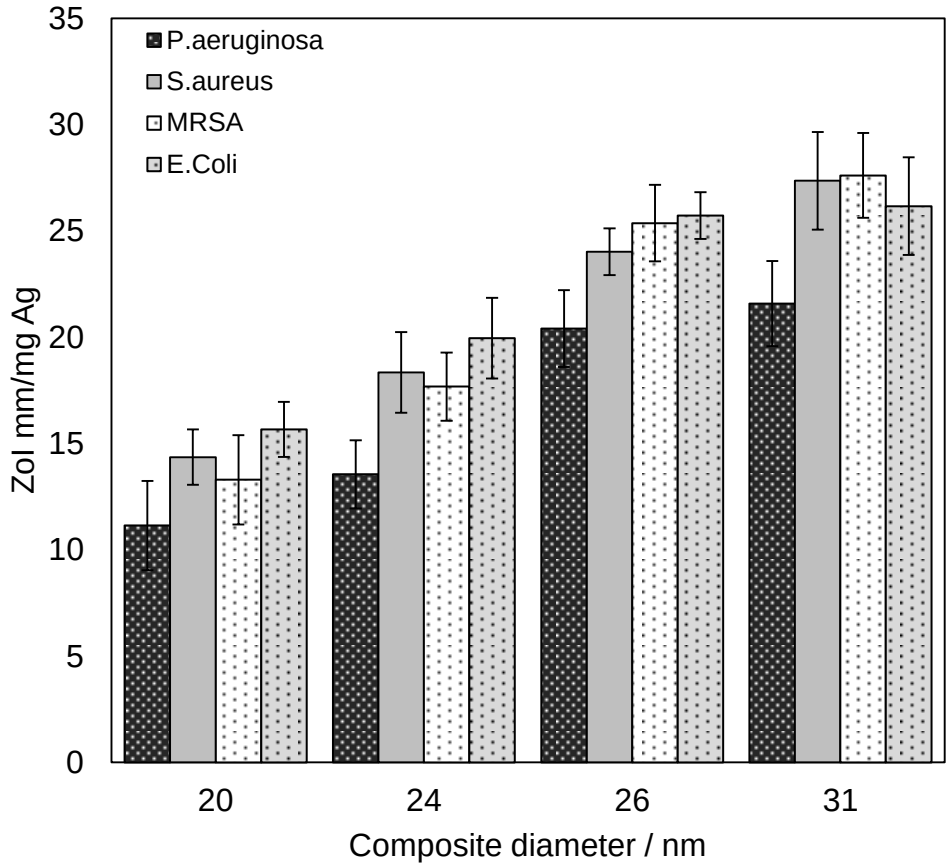

Figure 3.64: ZoI plots for silver silica core shell materials with varying silica shell sizes normalised to Ag content.

The materials of varying silica shell sizes exhibited the largest differences in recorded zones (**figure 3.64**), with the larger shells appearing more effective than the smaller shells. This is despite larger absolute recorded values for zones created by smaller shells (and hence higher wt% of Ag), similarly, if the zones are limited in size by factors outside of total silver release, then upon normalisation to Ag content, the lower weight % materials appear more effective.

3.5.2.2. Minimum bactericidal concentrations

In order to ensure that the concentration of materials tested by the logarithmic reduction method was sufficient to eliminate bacterial cultures, a minimum bactericidal concentration experiment was performed. This allowed to work with concentrations which would give a sensible and measurable kill rate.

The minimum bactericidal concentration for these materials was studied using the methodology described in **section 2.5.2**. This testing involved preparing solutions containing the target organism at a known concentration, along with the test material at a variety of concentrations to determine a break point, below which the material was not considered antibacterial. These solutions were incubated with agitation at 37^{o}C for 24 hours, before being plated out and the bacterial colonies counted.

The solutions were made using a serial dilution technique and the materials were dispersed into a solution of microorganisms in the following concentrations; 10, 1, 0.1, 0.01, 0.001, 0.0001 mg/ml. The materials were allowed to exhibit their antibacterial effects over a 24 hour time frame, at which point a sample of the solution was taken and spread onto an agar plate before being incubated at 37^{o}C prior to counting the viable organisms.

The material tested was a representative sample from the series, with a core size of 4.7 nm and shell size of 24 nm. Following the testing and incubation period, it was observed that the composite was effective at concentrations above 0.01 mg/ml, at which point the material failed to reduce the viable count of bacteria by a factor of 1000, the industry standard.

Considering accuracy of weight measurements and time scales, a concentration of 10 mg/ml was chosen for further testing.

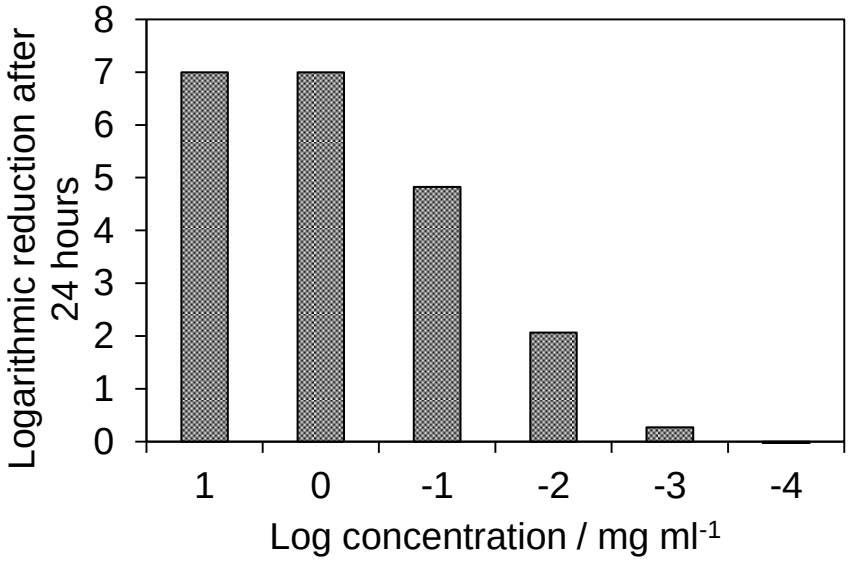

Figure 3.65: Bacterial colonies for the lowest concentration of material against *S.aureus* following a 24 hour assay.

Although there was visible growth witnessed for the lowest concentrations of materials tested, the logarithmic reduction of these colonies was still at 4.2, which is above the kill requirement for a material to be considered antibacterial.

3.5.2.3. Validity of neutralisation

In order to asses quantitatively the antibacterial activity of these materials as a function of time and correlate this to silver core size, a logarithmic reduction assay was required. This is a commonly used technique, involving adding a known number of microorganisms to the target material and determining the number of bacteria which are exterminated by plating out serial dilutions of the test solution at set time intervals. Due to the low concentrations of colonies required for counting purposes, serial dilution is required which can lead to possible inaccuracies during the process. It is for this reason that the samples are tested at least three times, for each time point.

Prior to performing a quantitative logarithmic reduction assay on these materials, a neutraliser was required which was able to render the silver materials incapable of killing the target organisms, allowing for a snapshot of antibacterial activity at the desired time points. For this, a solution of STS was tested as described in **section 2.5.3**.

STS is a solution of 1% Tween20, 0.85% sodium chloride and 0.4% sodium thioglycolate. Sodium thioglycolate is known to neutralise silver due to the high affinity of silver for thiol moieties.[33, 34] The mechanism behind the antibacterial activity of silver is known to be connected with the interaction with thiol groups; silver ions and thiol groups in enzymes and proteins are a large part of the inactivation of said enzymes and proteins, leading to cell death.

The STS agent was effective in neutralising the antibacterial effects of the silver-silica materials, following 24 hours of contact, plus an incubation period, against both *P.aeruginosa* and *S.aureus*. The solution was therefore considered a viable option for the logarithmic reduction experiments.

3.5.2.4. Logarithmic reduction

Logarithmic reduction experiments allowed for a more quantitative representation of the synthesised materials. The materials were agitated in a solution of simulated body fluid and the target organism and samples taken out at set intervals in order to determine the viable count of living organisms at that point and obtain the reduction of bacteria as a function of time. **Figure 3.66** and **figure 3.67** show the logarithmic reduction in the viable count of *Staphylococcus aureus and Pseudomonas aeruginosa* respectively against silver-silica materials of varying silver core size, a silver carbonate standard and a control.

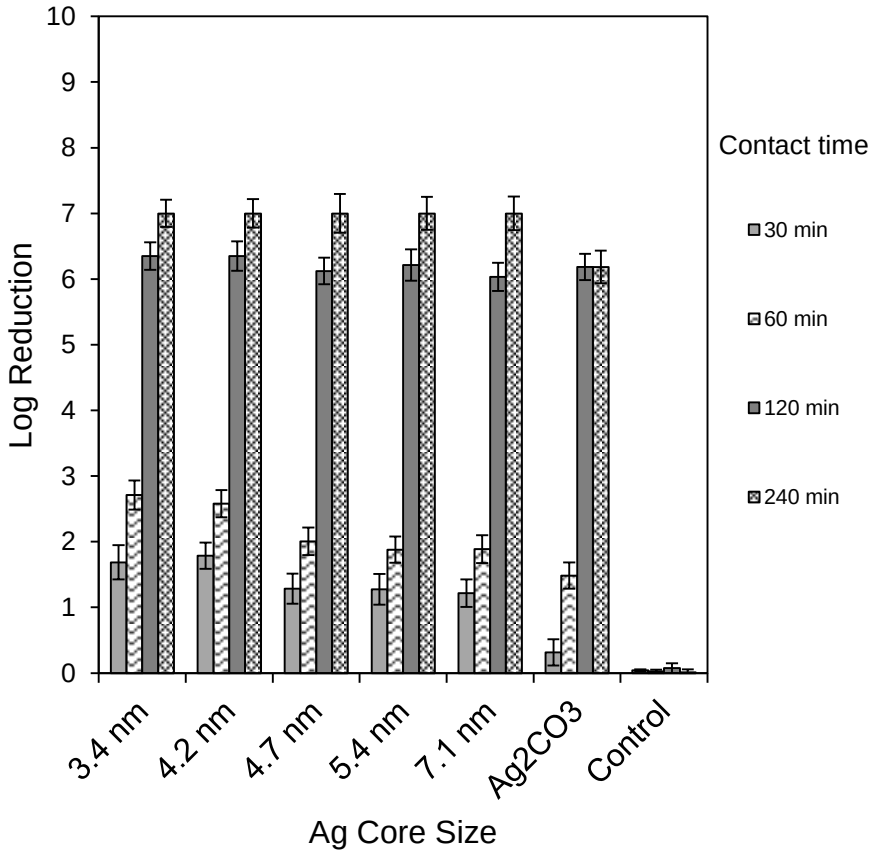

Figure 3.66: Logarithmic reduction of *Staphylococcus aureus* ATCC 6538 as a function of time in the presence of silver-silica core shell materials with variable silver core sizes, normalised to total silver content present.

Against the Gram positive representative organism, *Staphylococcus aureus*, the materials were highly effective, with no bacteria remaining after a 4 hour time period. The raw rate of bacterial mortality was quite similar for these materials and the silver carbonate standard, although when normalised to total silver content, the composite

materials outshine the silver carbonate, as they are more effective per unit mass of silver.

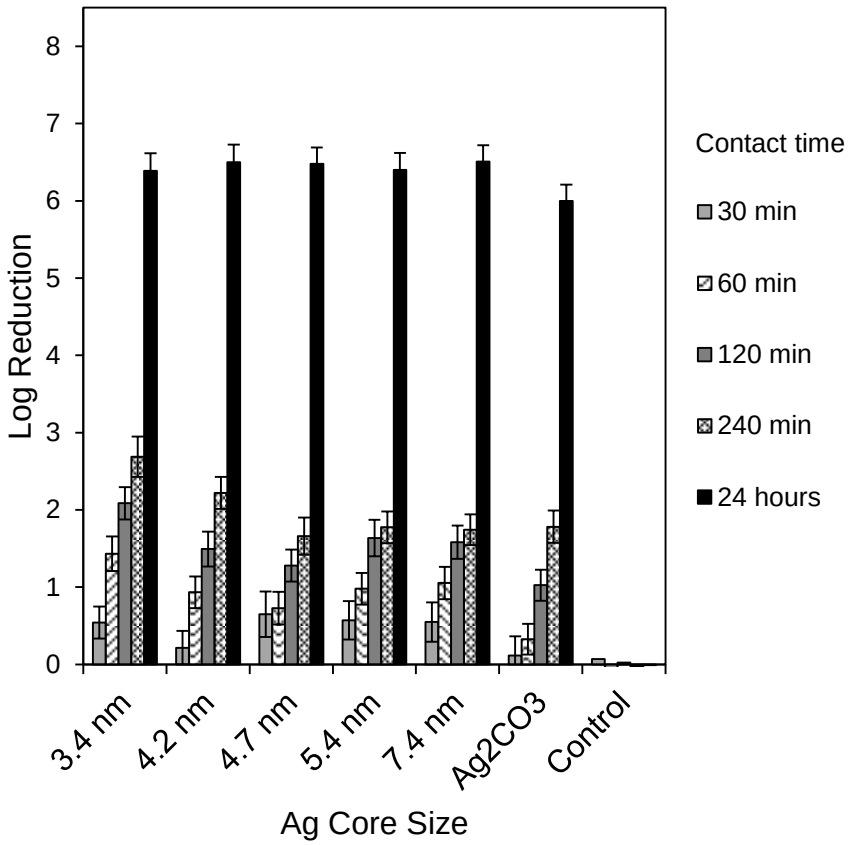

Figure 3.67: Logarithmic reduction of *Pseudomonas aeruginosa ATCC 15442* as a function of time in the presence of silver-silica core shell materials with variable silver core sizes, normalised to silver content.

There is a trend, consistent with the silver ion dissolution data, which indicates that the kill rate is faster for the smaller cores, this can be attributed to the active phase being silver (I) species in solution, hence the smaller cores possessing faster dissolution kinetics allows for faster bacteria mortality rates.

The materials are display faster action against *S.aureus* compared to *P.aeruginosa*, which can be attributed to the lower permeability of the cell wall and membrane of this species,[35] which has shown to render this strain (ATCC 15442) more resistant than the *Staphylococcus aureus* ATCC 6538 strain to silver toxicity.[36]

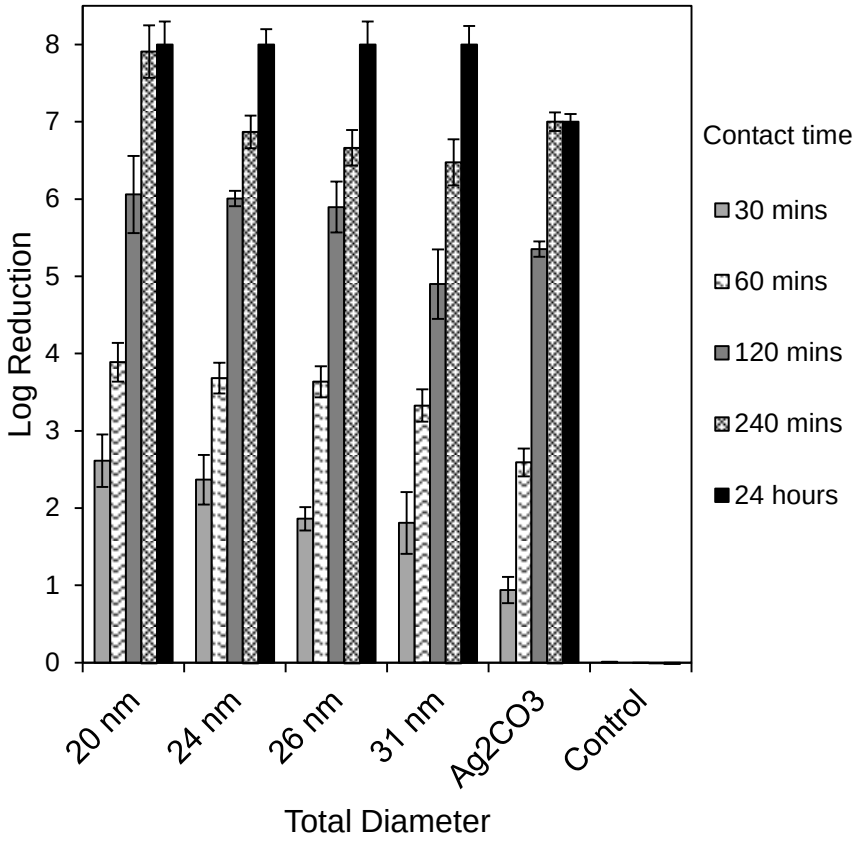

Figure 3.68: Logarithmic reduction of *Staphylococcus aureus* ATCC 6538 as a function of time in the presence of silver-silica core shell materials with variable total diameters, normalised to silver content.

Figure 3.58 shows the antibacterial efficacy of materials with varying diameters against *S.aureus*, indicating that as silica shell size increases, the rate at which the bacteria reduce is diminished, which is consistent with the dissolution profiles observed for these materials.

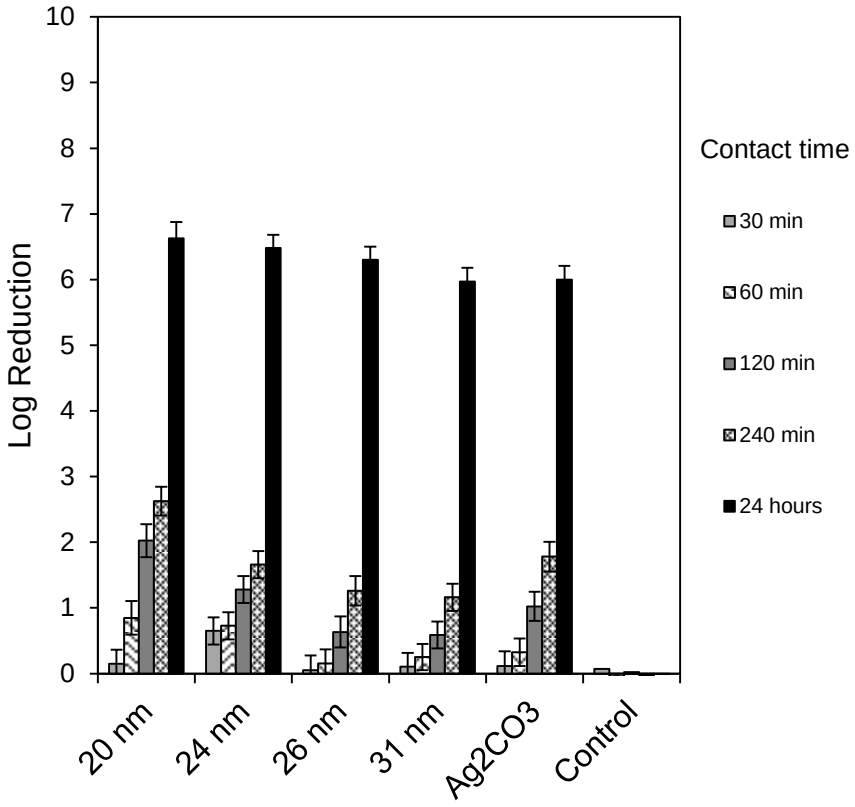

Figure 3.69: Logarithmic reduction of *Pseudomonas aeruginosa* as a function of time in the presence of silver-silica core shell materials with variable total diameters, normalised to total silver content.

The smaller shells consistently exhibit favourable kill rates against both bacterial strains, swifter than the materials with larger surrounding silica matrices. This may indicate that the smaller materials would be more effective swift action materials, killing bacteria quickly, whilst the larger shelled materials would be useful longer action materials, delivering a steady release of silver to produce a slower but longer lasting antibacterial effect.

The etched materials were studied for antibacterial efficacy via the same method.

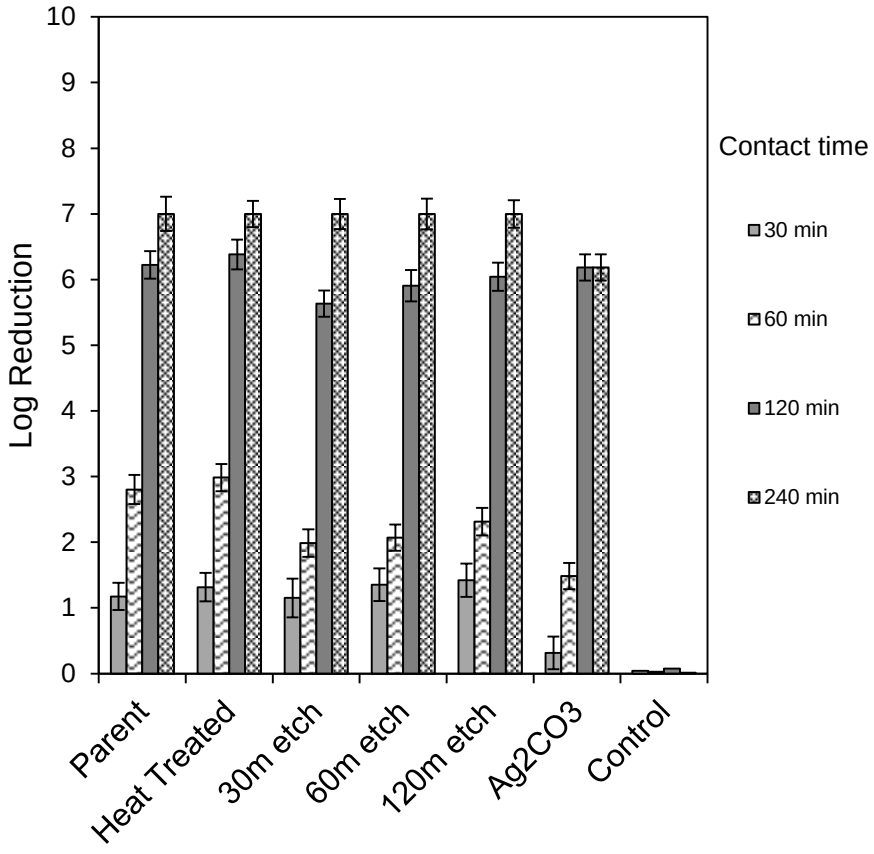

Figure 3.70: Logarithmic reduction of *Staphylococcus aureus* ATCC 6538 as a function of time in the presence of etched silver-silica core shell materials, normalised to total silver content.

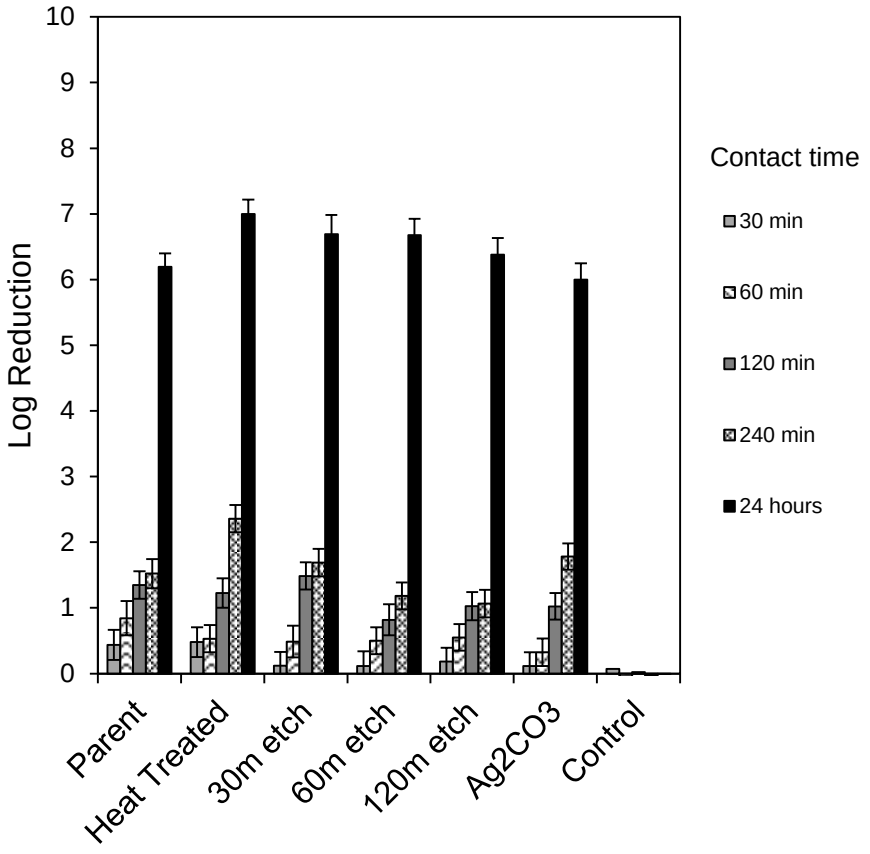

Figure 3.71: Logarithmic reduction of *Pseudomonas aeruginosa* as a function of time in the presence of etched silver-silica core shell materials, normalised to total silver content.

Against *S.aureus*, the materials have reduced the bacterial colony count over a threefold reduction after 2 hours in contact, with the heat treated material acting fastest, followed by the untreated material, which mirrors the trend observed in the silver ion dissolution study. The nanocomposites are again met with greater resistance from the *P.aeruginosa*, taking 24 hours to record a three-fold log reduction. The heat treated material exhibited superior antibacterial activity compared to the other samples, marginally better than the silver carbonate standard per unit mass of silver.

That the etched materials are outperformed by their unetched equivalents is no doubt disappointing, although the improved performance of the heat treated material suggests that perhaps tuning this heat treatment would be a good alternative to base etching to provide a route to increased antibacterial performance.

3.5. Conclusions

Silver based antibacterial additives are coming to the forefront of technology with the rise of resistant strains of bacteria and the advent of nanotechnology allowing for fine control over material properties. The applications to have been developed include dental care,[37] catheter coatings,[38] antibacterial textile materials,[39] in wound and burn care[40] and water treatment.[41] Silver based materials are already in use in the wound management industry, with materials such as Acticoat™ and Actisorb® using nanocrystalline and silver polymer based technologies,[42, 43] whilst silver sulphadiazene has been a common treatment for burns since the middle of the last century.[44]

The fine control over the physical properties and characteristics of nanodevices allows for, in theory, antibacterial agents with high degree of control over their eventual potency and lifetime.[45] The core-shell architecture lends not only a stabilising effect to the silver nanoparticles, of the equivalent to an inorganic support, but also a barrier to silver dissolution which slows the release of active species and thus increases the lifetime.

In this work it has been demonstrated that the physical dimensions of core shell architectures, developed using a reverse micelle microreactor emulsion synthesis, can be highly tuned to suit the purpose. The silver core size increases linearly with the water concentration inside the reverse micelles and subsequent increase in micelle diameter, whilst retaining a high degree of monodispersity resulting in a series of silver particles of increasing size. Whilst there is no great difference in overall performance of these materials, the smaller cores do indeed release silver species into solution faster than their larger counterparts, leading to slightly improved kill rates. All things considered, it may infact be more advantageous from an antibacterial additive point of view to use larger silver cores, within this size range, for these applications, as the kill rates against *S.aureus* and *P.aeruginosa* are sufficiently high that the retarded silver release could lend itself to composite materials with a longer shelf life, whilst maintaining the same high degree of antibacterial efficacy.

Silica shell sizes are a secondary parameter which can be tuned to affect performance, with increased concentrations of silica precursor tending towards increased shell dimensions. With larger shell sizes comes diminished silver release and hence activity, although the kill rate remains at a reasonably high value with a 3-fold

reduction in bacterial count after 2-4 hours of contact with the materials. The slow release profiles of larger shelled materials would suggest longer potential lifetimes for these materials, whilst remaining active at a fast enough rate to be considered effective bactericidal agents.

Enhancement of the silver dissolution via a surface protected etching route yielded unexpected results, as whilst the characterisation of the materials suggested materials of increased porosity, the release rate of silver suffered negatively upon base etching treatment. A possible explanation for this has been provided, in that stabilisation of the silver surface by free PVP molecules could be hindering the release of silver species into solution, as a greater number can access the silver core with increased porosity. Further to this, some removal and agglomeration of silver cores into larger particles could lead to supressed silver release and activity. A milder, high temperature treatment, however, did infact demonstrate superior silver release.

Potential longevity of these antibacterials was assessed through consecutive logarithmic reduction experiments, performed daily for 14 days by virtue of removal of bacterial solution after a 24 hour period, filtration and washing of composite materials and resuspension in a a fresh solution of 10^7 cfu of the target organism (*S.aureus*). Materials tested included 3.4 nm and 7.4 nm silver cored composites, and 31 nm silica shelled materials. All composites exhibited no decrease in activity over a 14 day period (**figure 3.72**), indicating stability and long lasting activity. The smaller composites actually outlasted expected lifetime based upon silver dissolution profiles. This is possibly due to formation and redeposition of silver chloride species, which are themselves antimicrobially active.

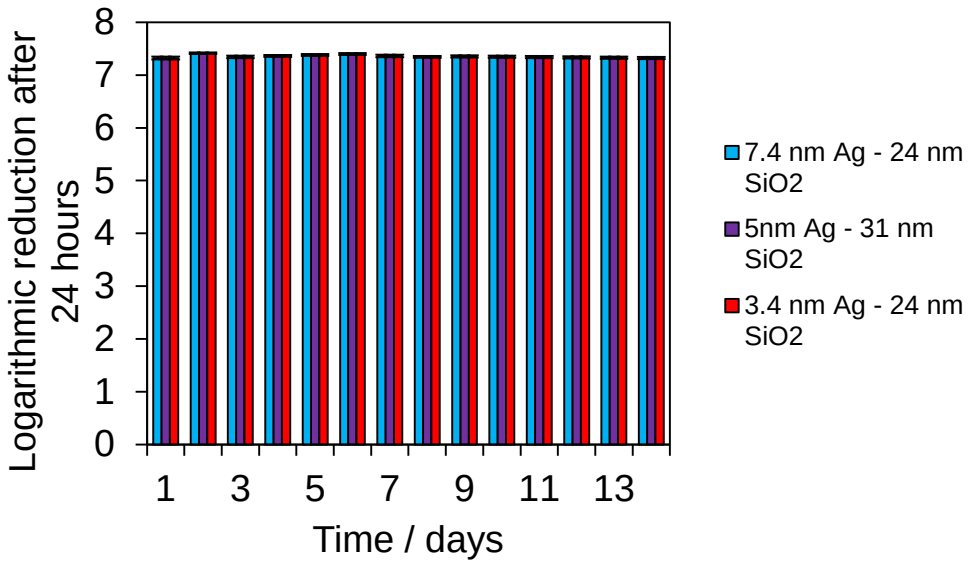

Figure 3.72: Antimicrobial lifetime assays.

Overall, the composites exhibited excellent antibacterial properties and swift action against the test organisms, both *S.aureus* and *P.aeruginosa* and tuning them to release as slow as possible, whilst retaining their antibacterial ability, has great potential as a bactericidal material with an extended lifetime of action. Ultimately, however, whilst these materials provide excellent properties, the cost and scalability of the synthesis, as well as high levels of waste chemicals, renders their use in industrial or commercial applications less desirable. Nonetheless, they provide a valuable template, highlighting the advantages of core-shell materials and how the properties can affect performance, with small silver particles with smaller, heat treated shells preferential for fast acting materials, and larger core and shells more suited for longer, sustained release.

3.6. References

1. T. Li, J. Moon, A. A. Morrone, J. J. Mecholsky, D. R. Talham and J. H. Adair, *Langmuir : the ACS journal of surfaces and colloids*, 1999, **15**, 4328-4334.
2. K. Osseo-Asare and F. J. Arriagada, *Colloids and Surfaces*, 1990, **50**, 321-339.
3. J.-N. Park, A. J. Forman, W. Tang, J. Cheng, Y.-S. Hu, H. Lin and E. W. McFarland, *Small*, 2008, **4**, 1694-1697.

4. P. Tartaj and C. J. Serna, *Journal of the American Chemical Society*, 2003, **125**, 15754-15755.

5. M. Zhang, B. L. Cushing and C. J. O'Connor, *Nanotechnology*, 2008, **19**, 085601.

6. Y. Han, J. Jiang, S. S. Lee and J. Y. Ying, *Langmuir : the ACS journal of surfaces and colloids*, 2008, **24**, 5842-5848.

7. D.-S. Bae, K.-S. Han and J. H. Adair, *Journal of Materials Chemistry*, 2002, **12**, 3117-3120.

8. S.-Y. Chang, L. Liu and S. A. Asher, *Journal of the American Chemical Society*, 1994, **116**, 6739-6744.

9. W. Zhang, X. Qiao and J. Chen, *Materials Chemistry and Physics*, 2008, **109**, 411-416.

10. C. Petit, P. Lixon and M. P. Pileni, *The Journal of Physical Chemistry*, 1993, **97**, 12974-12983.

11. Z. Khan, S. A. Al-Thabaiti, E. El-Mossalamy and A. Y. Obaid, *Colloids and Surfaces B: Biointerfaces*, 2009, **73**, 284-288.

12. X.-Y. Gao, S.-Y. Wang, J. Li, Y.-X. Zheng, R.-J. Zhang, P. Zhou, Y.-M. Yang and L.-Y. Chen, *Thin Solid Films*, 2004, **455–456**, 438-442.

13. G. I. Waterhouse, G. A. Bowmaker and J. B. Metson, *Physical Chemistry Chemical Physics*, 2001, **3**, 3838-3845.

14. Y. Sawada, N. Mizutani and M. Kato, *Thermochimica Acta*, 1989, **146**, 177-185.

15. R. Xu, D. Wang, J. Zhang and Y. Li, *Chemistry – An Asian Journal*, 2006, **1**, 888-893.

16. M. Priebe and K. M. Fromm, *Particle & Particle Systems Characterization*, 2014.

17. M. Seah and W. Dench, *Surface and interface analysis*, 1979, **1**, 2-11.

18. C. D. Wagner, A. V. Naumkin, A. Kraut-Vass, J. W. Allison, C. J. Powell and J. R. Rumble Jr, *NIST XPS (Web Version)*, 2003, **3**.

19. Y. H. Kim, D. K. Lee, H. G. Cha, C. W. Kim and Y. S. Kang, *The Journal of Physical Chemistry C*, 2007, **111**, 3629-3635.

20. Y. Hu, Q. Zhang, J. Goebl, T. Zhang and Y. Yin, *Phys Chem Chem Phys*, 2010, **12**, 11836-11842.

21. G. B. Alexander, W. M. Heston and R. K. Iler, *The Journal of Physical Chemistry*, 1954, **58**, 453-455.

22. Q. Zhang, J. Ge, J. Goebl, Y. Hu, Z. Lu and Y. Yin, *Nano Res.*, 2009, **2**, 583-591.

23. Q. Zhang, T. Zhang, J. Ge and Y. Yin, *Nano Letters*, 2008, **8**, 2867-2871.

24. A. Nelson, K. S. Jack, T. Cosgrove and D. Kozak, *Langmuir : the ACS journal of surfaces and colloids*, 2002, **18**, 2750-2755.

25. M. A. Cohen Stuart, G. J. Fleer and B. H. Bijsterbosch, *Journal of Colloid and Interface Science*, 1982, **90**, 321-334.

26. A. Gniewek, A. M. Trzeciak, J. J. Ziółkowski, L. Kępiński, J. Wrzyszcz and W. Tylus, *Journal of Catalysis*, 2005, **229**, 332-343.

27. X. Nist, 1997.

28. J. Liu and R. H. Hurt, *Environmental Science & Technology*, 2010, **44**, 2169-2175.

29. Y.-J. Lee, J. Kim, J. Oh, S. Bae, S. Lee, I. S. Hong and S.-H. Kim, *Environmental Toxicology and Chemistry*, 2012, **31**, 155-159.

30. C. A. Moyer, L. BRENTANO, D. L. GRAVENS, H. W. MARGRAF and W. W. MONAFO, *Archives of surgery*, 1965, **90**, 812-867.

31. G. B. Forbes and G. M. Forbes, *Archives of Pediatrics & Adolescent Medicine*, 1971, **121**, 1.

32. J. Wasiak, H. Cleland and F. Campbell, *Cochrane Database Syst Rev*, 2008, **4**.

33. S. Y. Liau, D. C. Read, W. J. Pugh, J. R. Furr and A. D. Russell, *Letters in Applied Microbiology*, 1997, **25**, 279-283.

34. J. R. Furr, A. D. Russell, T. D. Turner and A. Andrews, *Journal of Hospital Infection*, 1994, **27**, 201-208.

35. K. I. Batarseh, *Journal of Antibacterial Chemotherapy*, 2004, **54**, 546-548.

36. M. J. Brady, C. M. Lisay, A. V. Yurkovetskiy and S. P. Sawan, *American journal of infection control*, 2003, **31**, 208-214.

37. S. Ohashi, S. Saku and K. Yamamoto, *Journal of oral rehabilitation*, 2004, **31**, 364-367.

38. M. E. Rupp, T. Fitzgerald, N. Marion, V. Helget, S. Puumala, J. R. Anderson and P. D. Fey, *American journal of infection control*, 2004, **32**, 445-450.

39. K. Nischala, T. N. Rao and N. Hebalkar, *Colloids and Surfaces B-Biointerfaces*, 2011, **82**, 203-208.

40. E. Ulkur, O. Oncul, H. Karagoz, E. Yeniz and B. Celikoz, *Burns : journal of the International Society for Burn Injuries*, 2005, **31**, 874-877.

41. P. Jain and T. Pradeep, *Biotechnology and Bioengineering*, 2005, **90**, 59-63.

42. K. Dunn and V. Edwards-Jones, *Burns : journal of the International Society for Burn Injuries*, 2004, **30**, S1-S9.

43. J. Furr, A. Russell, T. Turner and A. Andrews, *journal of Hospital Infection*, 1994, **27**, 201-208.

44. S. Silver, L. Phung and G. Silver, *J IND MICROBIOL BIOTECHNOL*, 2006, **33**, 627-634.

45. N. Hagura, W. Widiyastuti, F. Iskandar and K. Okuyama, *Chemical Engineering Journal*, 2010, **156**, 200-205.

Chapter 4: Mesoporous silver-silica core-shell nanocomposites

4.1. Introduction

In **Chapter 3**, it was observed that silver-silica core-shell materials afforded potent antimicrobial performance, and exhibited high stability in aqueous solution. The expected lifetime of these materials, based on silver dissolution studies, increased for larger silver nanoparticles due to lower total silver % release over a 24 hour period (**Chapter 3.5.1**), whilst effects on antimicrobial efficacy were relatively small, compared to the possible advantages in an increased timeframe of continuous action.

In this chapter, a micellular organic templating methodology was developed with a view to introducing intrinsic mesopores into the inorganic shell of silver-silica core-shell nanocomposites, with a view to synthesising larger diameter silver nanoparticles accompanied by increased routes for silver dissolution via a highly porous shell.

4.2. Results and discussion

Mesoporous silver-silica core-shell nanocomposites (MP-Ag@SiO_2) were prepared and characterised by a range of experimental techniques, including thermogravimetric analysis, FT-IR, TEM, XPS, XRD and porosimetry, in order to identify the silver species present and properties of the silica shell.

4.2.1. Synthesis of silver-silica core-shell nanocomposites

The synthesis of nanocomposites was adapted from a method by Zhao *et al* as described in **Chapter 2.2**,[1] involving the dissolution of CTAB in water to form micelles, followed by sodium hydroxide addition in the presence of a hydrazine reductant, heated to 80 ^{o}C under vigorous stirring (900 rpm). Following a 30 min equilibration period, $AgNO_3$ was added and the solution aged for 5 min prior to addition of the TEOS silica precursor as illustrated in **Figure 4.1**.

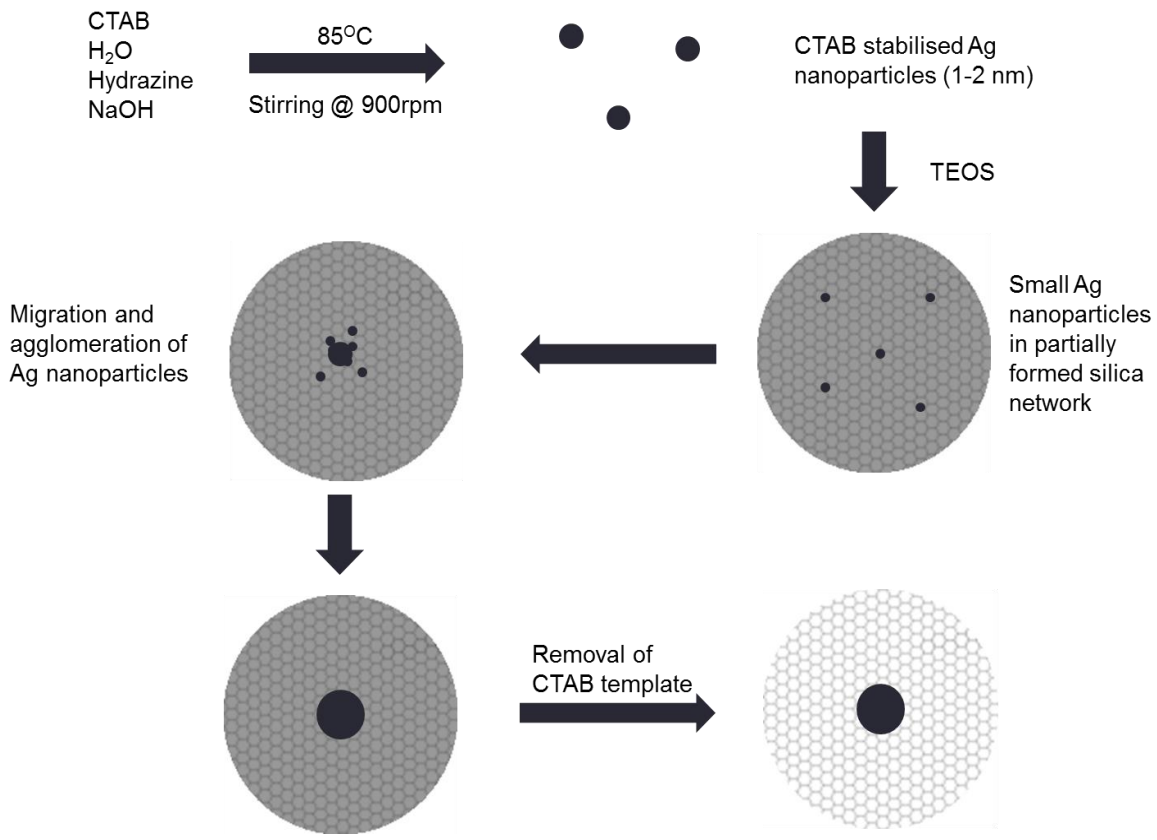

Figure 4.1: Schematic representation of mesoporous silver-silica core-shell nanocomposites formation.

Sodium hydroxide fulfils a double purpose, acting as a base catalyst for the hydrolysis and condensation of TEOS to form silica, while also preventing the formation of $H_2N\text{-}NH_3^+$ species through equilibration of hydrazine in water; displacing the equilibrium to maintain a high level of molecular hydrazine in solution, increasing the silver reduction rate.[2]

CTAB present at a concentration of 5.5 x 10^{-3} M (i.e. above the critical micelle concentration of 9 x 10^{-4})[3] self-assembles with hydrolysed silicate oligomers to form silicate micelles comprising S^+/I^- components (S = surfactant, I = inorganic oligomer). The packing and condensation of these promotes agglomeration of the self-assembled micelles and subsequent removal of the organic template through calcination results in a mesoporous silicate.

The combination of silicate oligomers in the Gouy-Chapman region (region of diffuse, solvated ions surrounding micelles) is weaker in aqueous sodium hydroxide than in ammonium hydroxide, resulting in shorter self-assembled structures and

promoting the growth of spherical particles, compared with the longer rod-like micelles preferred by ammonium hydroxide base catalysed materials.[4]

Hydrazine was chosen as a reducing agent as it has been employed extensively in the literature for the formation of metallic silver nanoparticles. The proposed mechanism for hydrazine reduction of Ag^{+} to stable Ag_4^{2+} clusters is outlined in **Figure 4.2**.[2] The resulting cationic silver clusters agglomerate and undergo further reduction to Ag^0 nanoparticles.

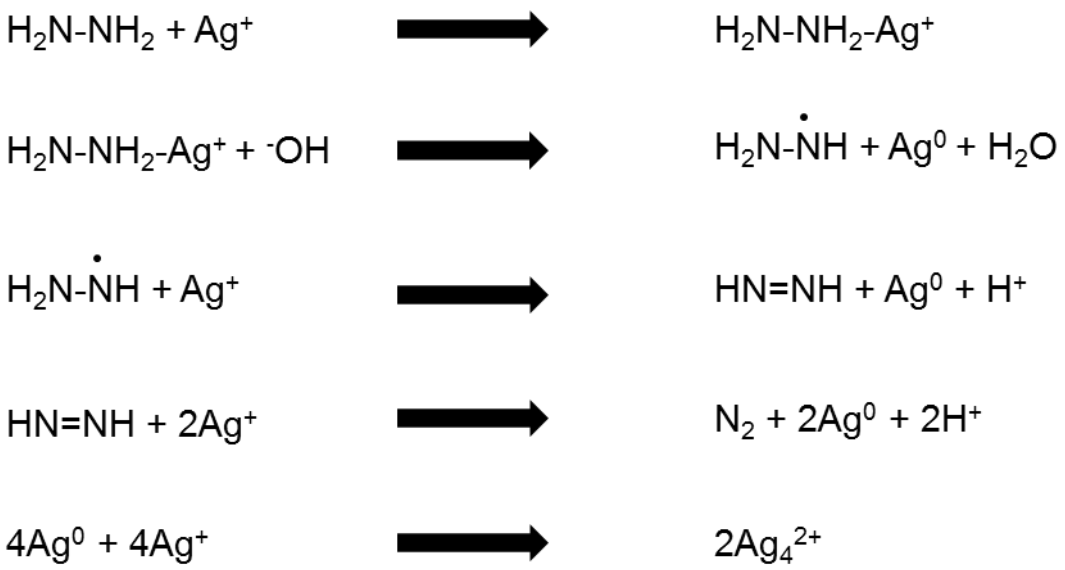

Figure 4.2: Reaction mechanism for the reduction of silver ions to silver clusters.[2]

Powder X-ray diffraction was utilised to determine the nature of the silver species present. The desired silver nanoparticles were Ag^0, and silver nanoparticles were produced and compared with those formed using alternate reducing agents in order to produce silver metal nanoparticles and prevent the formation of stable silver bromide species, formed from interactions between silver nitrate and the bromide counterions in CTAB.

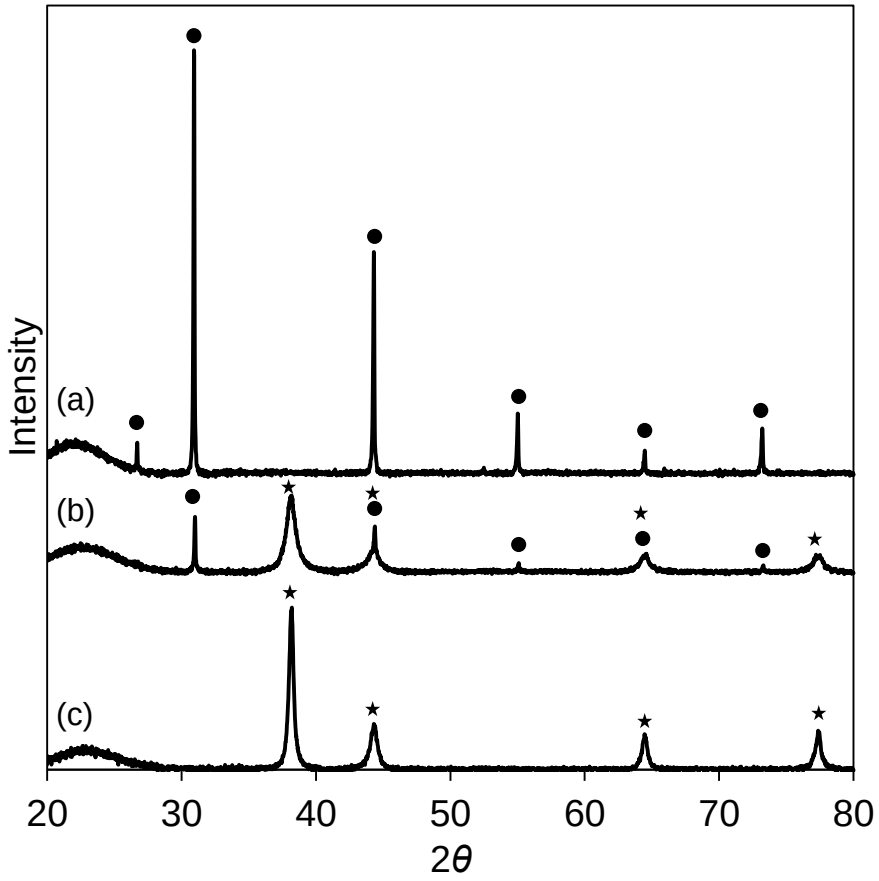

Figure 4.3: Powder XRD patterns from MP-Ag@SiO_2 nanocomposites using (a) aniline, (b) formaldehyde, (c) hydrazine as a reducing agent (6.54 % Ag). (★) indicates Ag^0 FCC structure, (●) indicates AgBr FCC structure.

Figure 4.3 shows the powder XRD patterns for these composite materials using three different reducing agents, all of which have been reported to reduce silver ions to silver metal nanoparticles.[1, 5, 6] The aniline and formaldehyde were unable to prevent the formation of silver bromide within the nanoparticles, with the aniline producing solely large (60 nm) silver bromide particles and the formaldehyde leading to a mixture of large particles of AgBr (54 nm) and small crystallites of silver metal (10 nm), whilst when in the presence of hydrazine, the silver was fully reduced, forming zero valent silver metal particles of 20 nm in diameter. The AgBr peaks were identified as 2θ = 26.6 (111), 30.9 (200), 44.31 (220), 55 (222), 64.35 (400), 73.17 (420).[7] The Ag^0 FCC pattern was identified as 2θ = 38.1 (111), 44.15 (200), 64.3 (220) and 77.2 (311).[8] As the goal was to produce silver metal nanoparticles, hydrazine was chosen as the reducing agent for the synthesis.

Following confirmation of the silver species and formation of silver metal nanoparticles, TEM analysis was used to confirm the core-shell nanoarchitecture.

Figure 4.4 shows a representative example of the initial nanocomposites formation post-synthesis. There are clearly defined phase boundaries between the silver metal cores and mesoporous silica shells.

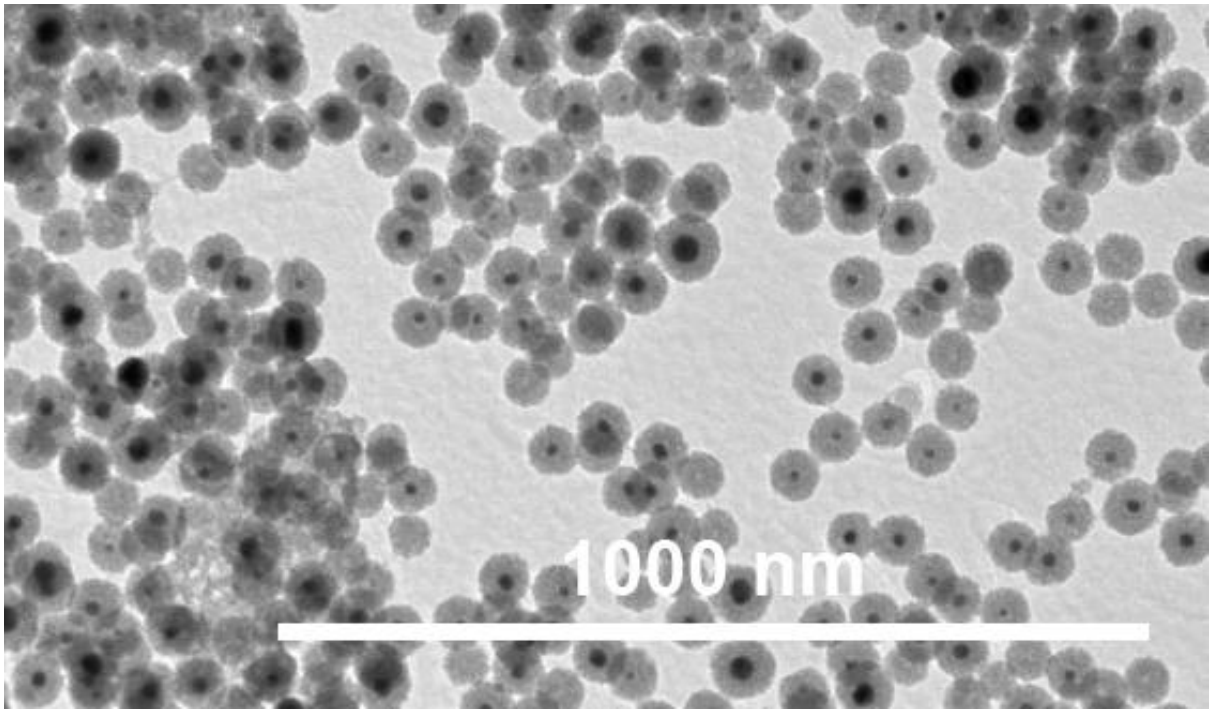

Figure 4.4: Representative bright field TEM image of synthesised MP-Ag@SiO_2 nanoarchitectures.

Removal of the organic template was required in order to introduce the mesoporous network into the silica framework, and for this a thermal treatment was used. The decomposition temperature of CTAB is 237-243 °C, which was confirmed by TGA analysis (**figure 4.5**).

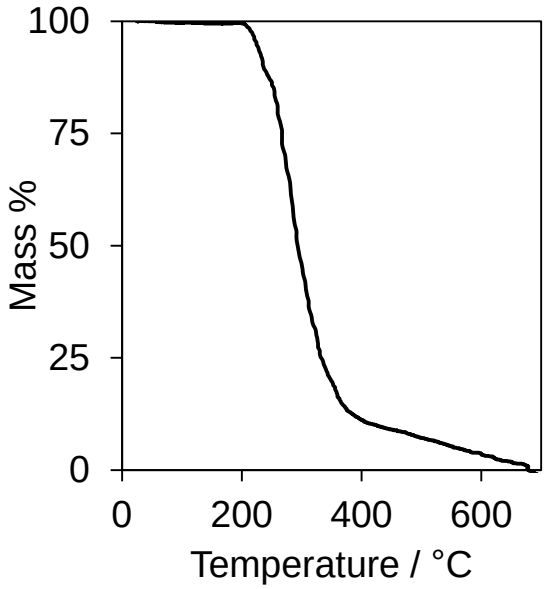

Figure 4.5: Thermogravimetric analysis of cetyltriammonium bromide.

A calcination temperature of 400 °C was used to remove the organic template. During calcination however, silver bromide species were formed, as evidenced in **Figure 4.6**, which shows powder XRD patterns from calcined and uncalcined nanocomposites, before removal of residual bromide species.

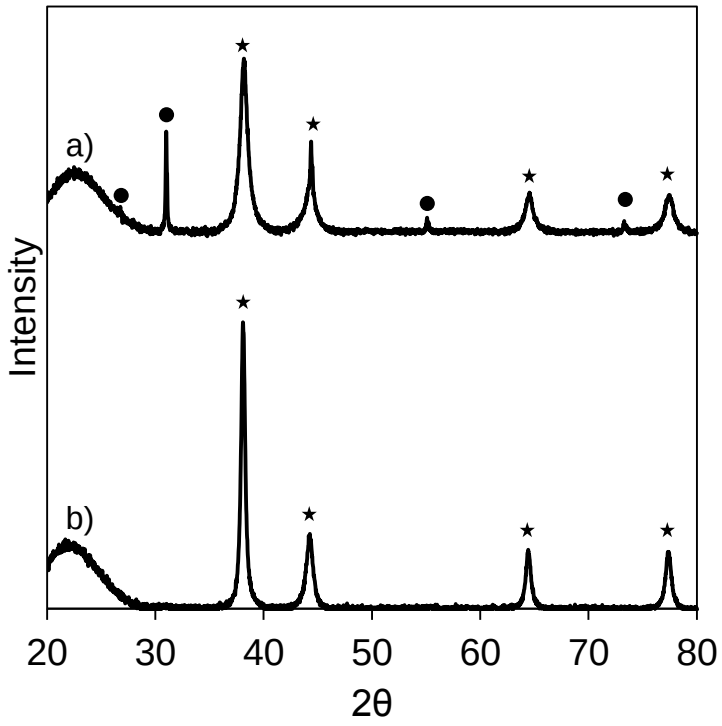

Figure 4.6: Powder XRD patterns for (a) calcined and (b) uncalcined 6.54% Ag MP-Ag@SiO_2 nanocomposites, prior to bromide removal. (★) indicates Ag^0 FCC structure, (●) indicates AgBr FCC structure.

Silver bromide species of 53 nm are evident in the XRD patterns alongside silver metal particles of 10 nm, indicating their formation during the thermal treatment. To remove these bromides, the materials were washed three times in ethanol and ammonium carbonate, before being washed in water. The powder XRD patterns for the calcined and uncalcined nanocomposites after removal of the bromide species are shown in **figure 4.7**. These show that after the bromide species are removed, the materials can be calcined in air and retain the silver metal identity. Particle sizing from the Scherrer equation reports negligible particle growth, reporting silver crystallites of 18.5, 18.9 and 19.6 nm respectively for the parent, washed and calcined materials respectively.

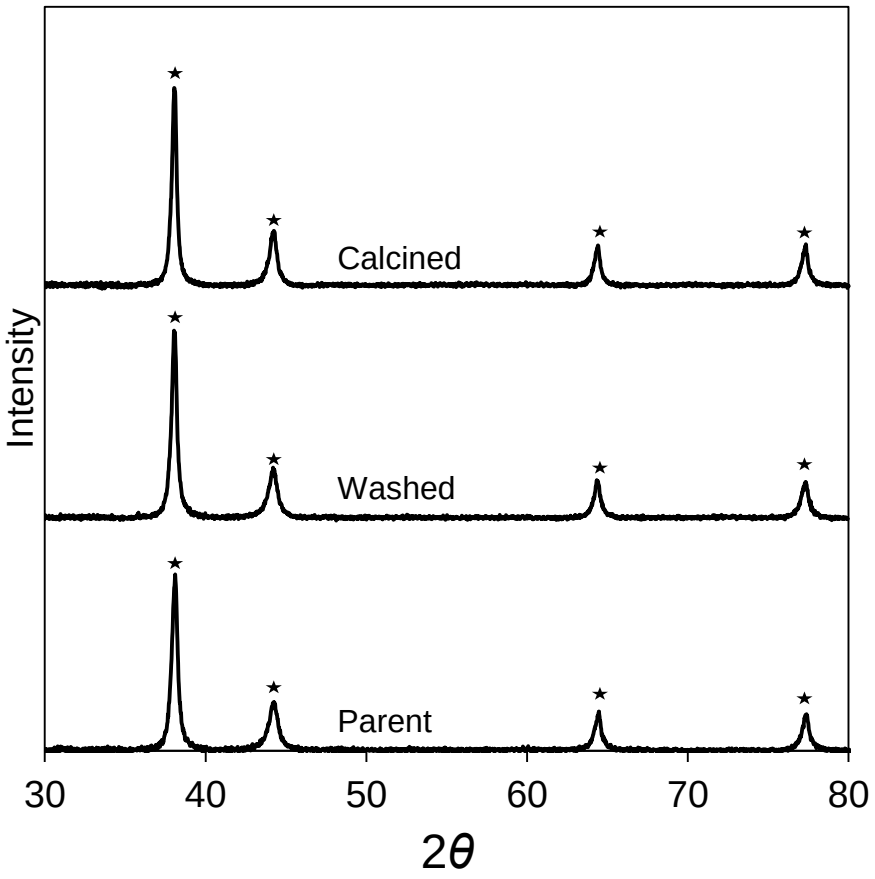

Figure 4.7: Powder XRD patterns for calcined ammonium carbonate/ethanol washed and parent MP-Ag@SiO_2 nanocomposites. (★) indicates Ag^0 FCC structure.

Confirmation of the removal of bromide species was also obtained using XPS analysis, which indicated the disappearance of the Br 3d moiety post-washing (**Figure 4.7**).

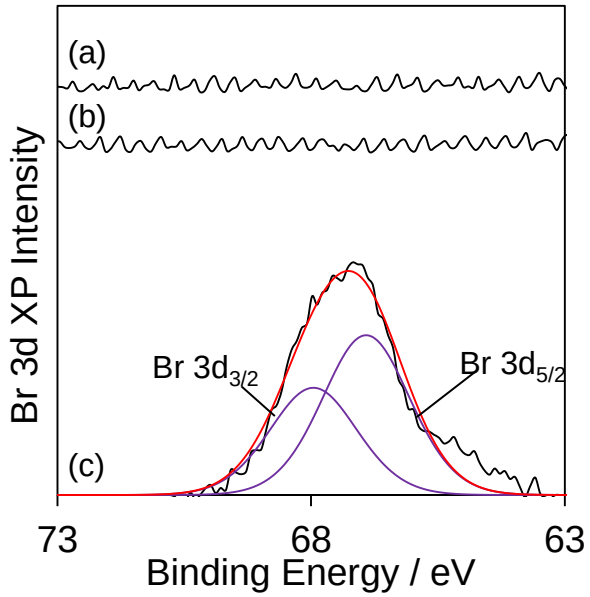

Figure 4.8: Br 3d XPS stack plot of (a) calcined, (b), washed and (c) parent 6.54% Ag MP-Ag@SiO_2 nanocomposites.

The N 1s regions were studied for evidence of remaining cetyl triammonium species. **Figure 4.9** shows the N 1s regions for CTAB, the washed and unwashed samples. This indicates that whilst the bromide is removed by ethanol/ammonium carbonate washing, that the CTAB may well remain in the pores of the nanocomposites.

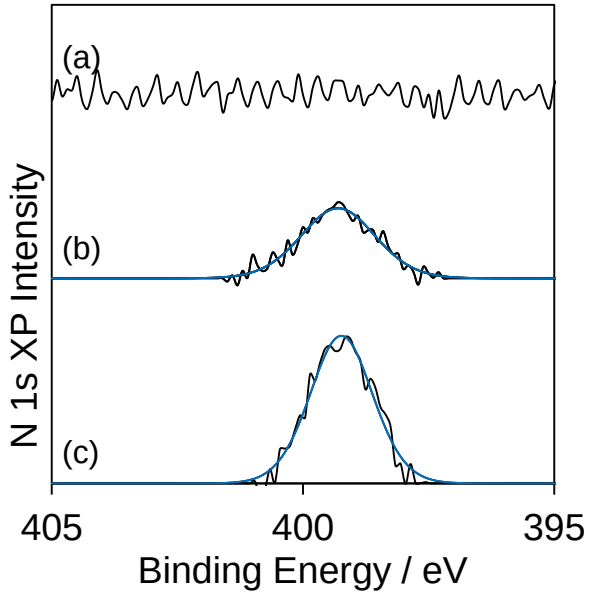

Figure 4.9: N 1s stack plot of (a) calcined, (b) washed and (c) parent 6.54% Ag MP-Ag@SiO_2 nanocomposites.

The presence of remaining organic residuals not removed during the washing procedure was studied using ATR FT-IR, between 4000 cm^{-1} and 1300 cm^{-1}, in which

region a strong signal is observed for cetyl moieties. **Figure 4.10** shows the infrared spectrum in this range and confirms that the organic material is not removed from the pores during the washing treatment. The calcined sample exhibited no stretches in the expected region, which is evidence of removal of the organic template.

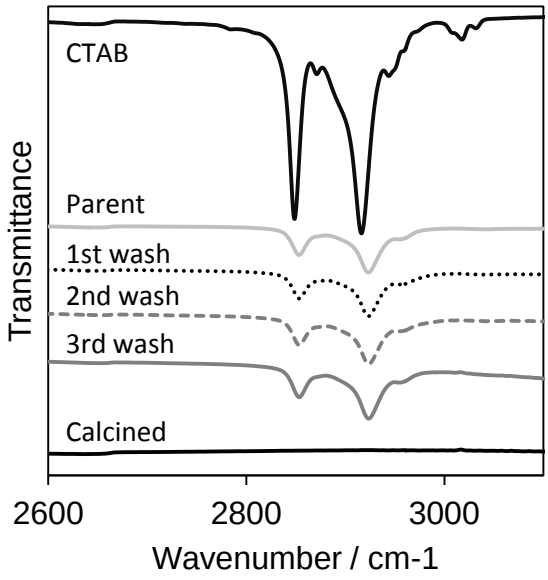

Figure 4.10: ATR FT-IR spectra of CTAB, washed, unwashed and calcined 6.54 wt. % MP-Ag@SiO_2 nanocomposites.

This was also observed by thermogravimetric analysis, which is shown in **figure 4.11**. CTAB decomposes at 237-243 °C, and there is a large decrease in mass in this range for the uncalcined materials, which can be attributed to the decomposition and removal of this material.

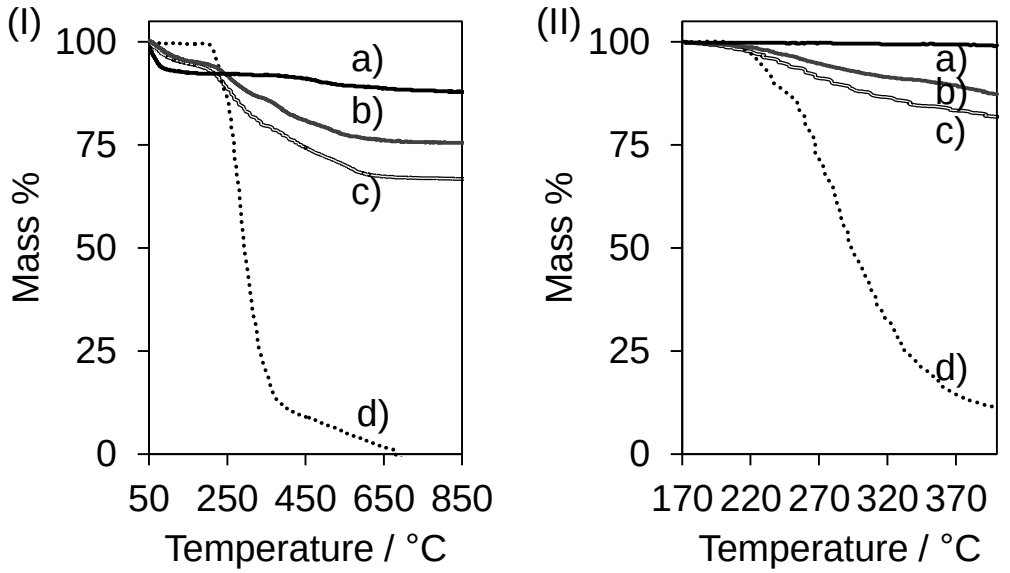

Figure 4.11: Thermogravimetric analysis of (I) total mass % loss, (II) % mass loss over the temperature range of CTAB decomposition for 6.54 wt. % Ag (a) calcined MP-Ag@SiO_2, (b) uncalcined, washed MP-Ag@SiO_2, (c) uncalcined, unwashed MP-Ag@SiO_2 and (d) CTAB.

By looking at the regions between 170 and 400 °C, it can be estimated how much CTAB is removed by the calcination and washing treatments. The raw material loses 18% of its mass over this region, so assuming this is all through the removal of CTAB, this can be considered the starting %mass of CTAB and decreases in organic content calculated by measuring the mass loss in this region.

Post washing, the CTAB content drops from 18% to 12.7%, a roughly 30% decrease. This indicates that washing the materials to remove the bromide species does also remove some of the alkyl chains from the pore networks. After calcination, the % mass loss in this region is effectively zero, as it should be after heat treatment at 400 °C for 5 hours.

Nitrogen porosimetry was employed to study the resulting pore network. **Figure 4.12** shows the isotherms for the calcined and uncalcined samples. The calcined material exhibits a type IV isotherm with a capillary condensation step at around 0.4-0.6 P/P_0. The uncalcined and unwashed parent materials possess a much lower surface area of 600 m^2/g and 512 m^2/g respectively compared to 860 m^2/g, which is consistent with the removal of organic template.

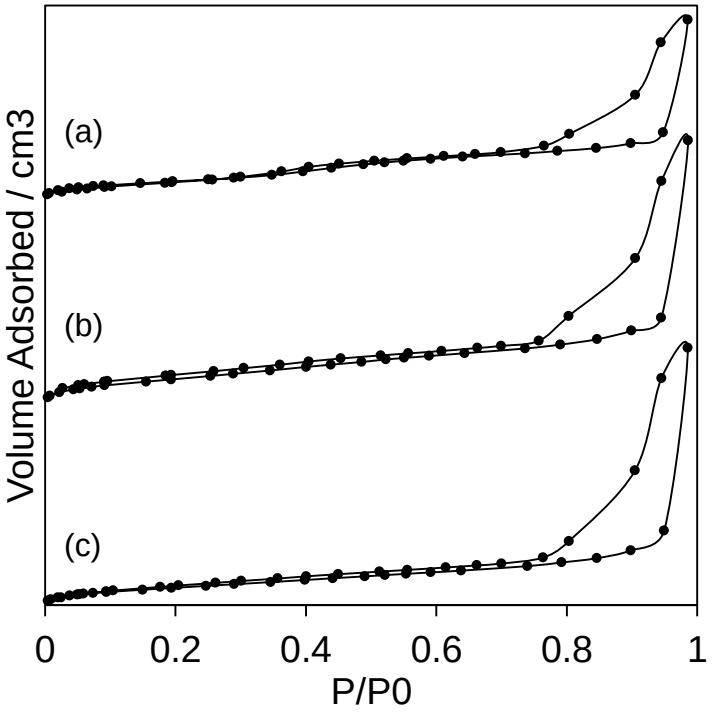

Figure 4.12: N_2 adsorption isotherms for (a) calcined and (b) ethanol/ammonium carbonate washed and (c) parent 6.54 wt % Ag MP-Ag@SiO_2 nanocomposites.

The pore size within these materials was studied by applying the BJH method to this isotherm, and resulted in an average pore size of 2.5 nm. **Figure 4.13** shows the BJH plot, whilst inset is the BET plot, which recorded and specific surface area of 700 cm^3/g. Micropore analysis via the t-plot method recorded a micropore volume of 0 cm^3/g for all materials.

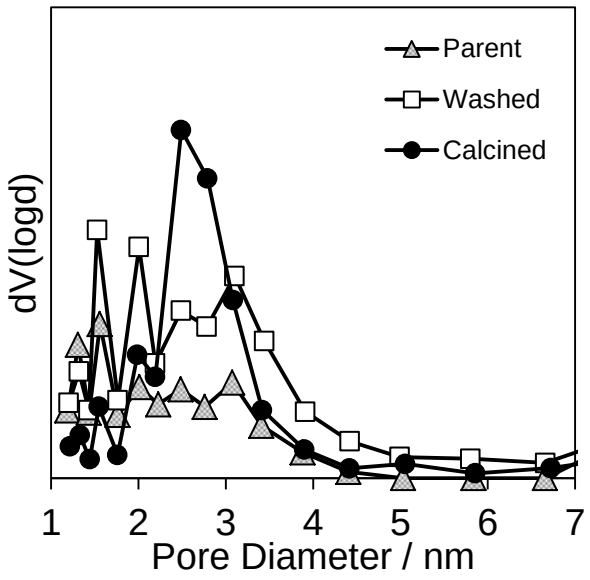

Figure 4.13: BJH profile of calcined and uncalcined 6.54 wt. % Ag MP-Ag@SiO_2 nanostructured materials. Inset displays BET plot.

Post calcination the material reports a clear and monodisperse pore size distribution at 2.5 nm in diameter, which is consistent with similar materials using a CTAB templating agent.[9] The BJH plot for the material after ethanol/ammonium carbonate washing indicates some template removal is occurring, with porous regions beginning to appear in the identical region to the calcined material, as well as smaller pores, indicating partial removal of some template.

4.2.2. Silver loading

With a methodology for producing silver nanoparticles encased in mesoporous silica shells in place, the total silver loading was investigated, in order to determine how silver content affected parameters such as particle size, antimicrobial efficacy and expected lifetime of the composite structures.

The total silver loading of these materials was adjusted by varying silver nitrate concentration during the synthetic procedure in the reaction mixture from 2 μM to 6 μM. The materials were processed as described previously in this chapter, to remove the organic template and produce silver metal nanoparticles encased in mesoporous silica shells. The bulk and surface loadings of the materials, determined by XPS and EDX, are listed in **table 4.1**.

Bulk Ag wt. %	Surface Ag wt. %	Surface:Bulk
3.38	0.45	0.13
6.54	0.85	0.13
9.5	1.15	0.12

Table 4.1: Bulk and surface Ag content for MP-Ag@SiO_2 nanocomposites.

The recorded values for silver surface to bulk silver implies a great deal of attenuation, and in this regard, porosity of the silica shell can be implied due to a lower degree of attenuation than expected. Surface to bulk ratios, based on calculations using particle diameters determined by TEM analysis, are expected to be of the order of 0.02. These higher than expected recorded values, would imply a lower silica density, which would decrease the observed photoelectron attenuation.

4.2.2.1. Transmission electron microscopy

TEM analysis was employed to confirm that the structural integrity of the nanocomposites materials was not compromised by increasing or decreasing silver loadings, and to evaluate any subsequent changes to the particle size as a result of this variation. Figure 4.13 shows an electron micrograph image of the synthesised materials.

There is clear contrast between the dark silver cores and lighter silica shells which, furthermore, exhibit apparent intrinsic porosity.

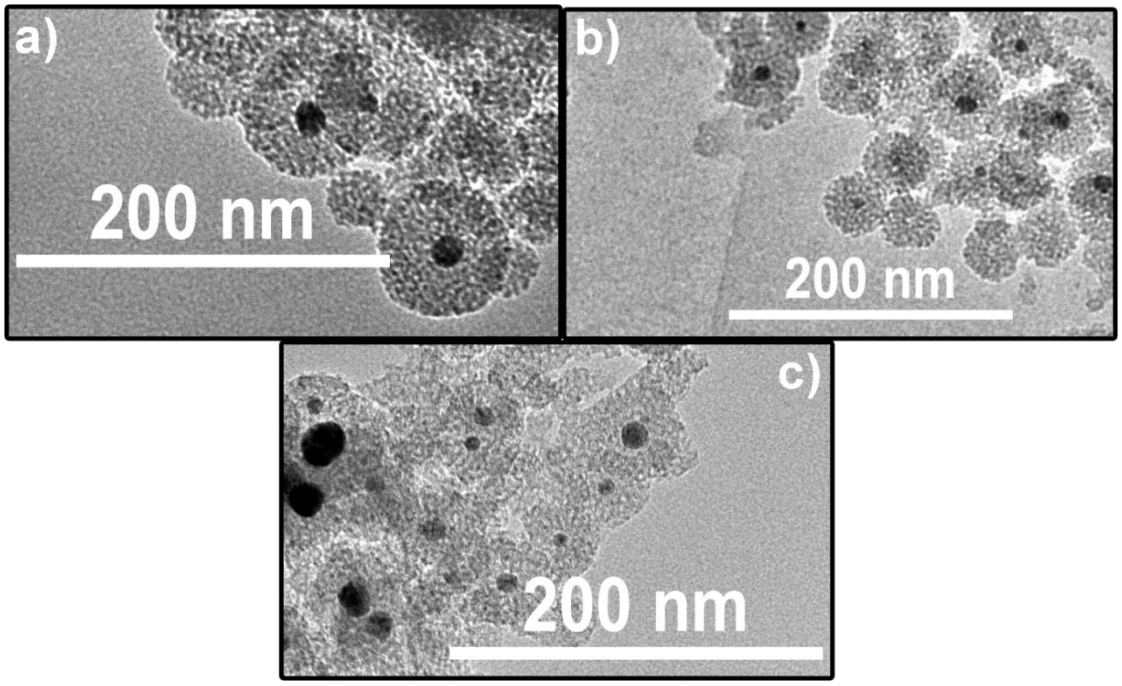

Figure 4.14: Representative bright-field HRTEM images of MP-Ag@SiO_2 nanocomposites at silver loadings of (a) 3.38%, (b) 6.54% and (c) 9.5%.

The average particle size of these nanostructures was unaffected by silver loading content, remaining constant across the series. **Figure 4.15** shows the particle size distributions for each loading of silver and the total diameter of the nanocomposites materials, which also remained largely unaffected by increasing silver content.

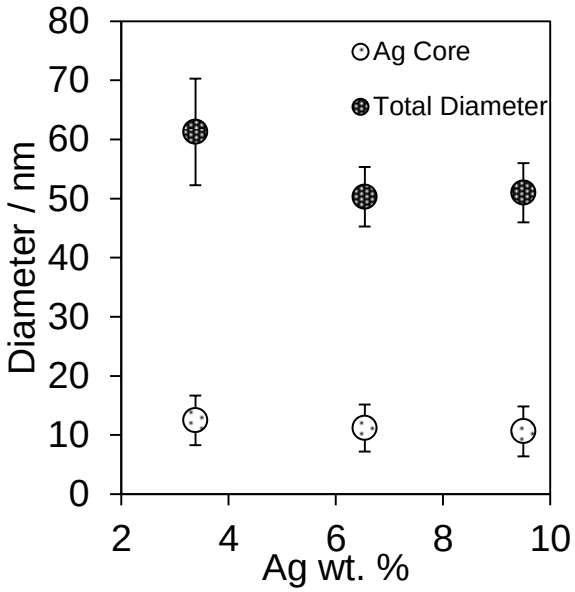

Figure 4.15: Summary of particle dimensions for different silver loadings in MP-Ag@SiO_2 nanocomposites.

The absolute size histograms for the silver cores are displayed in **figure 4.16** and total composite diameter in **figure 4.17**.

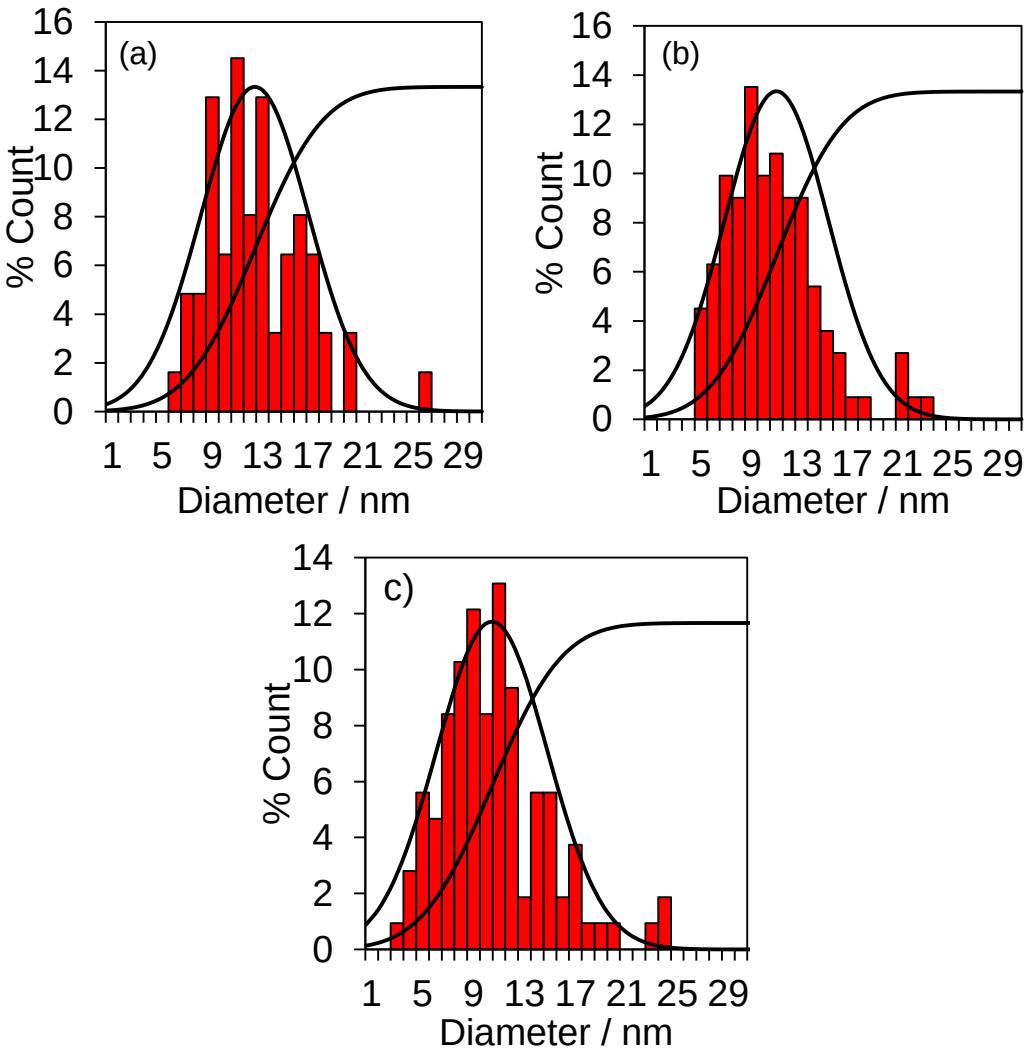

Figure 4.16: Silver core size distributions, normal and cumulative distributions for MP-Ag@SiO_2 nanocomposites at silver loadings of a) 3.38%, b) 6.54%, c) 9.5%.

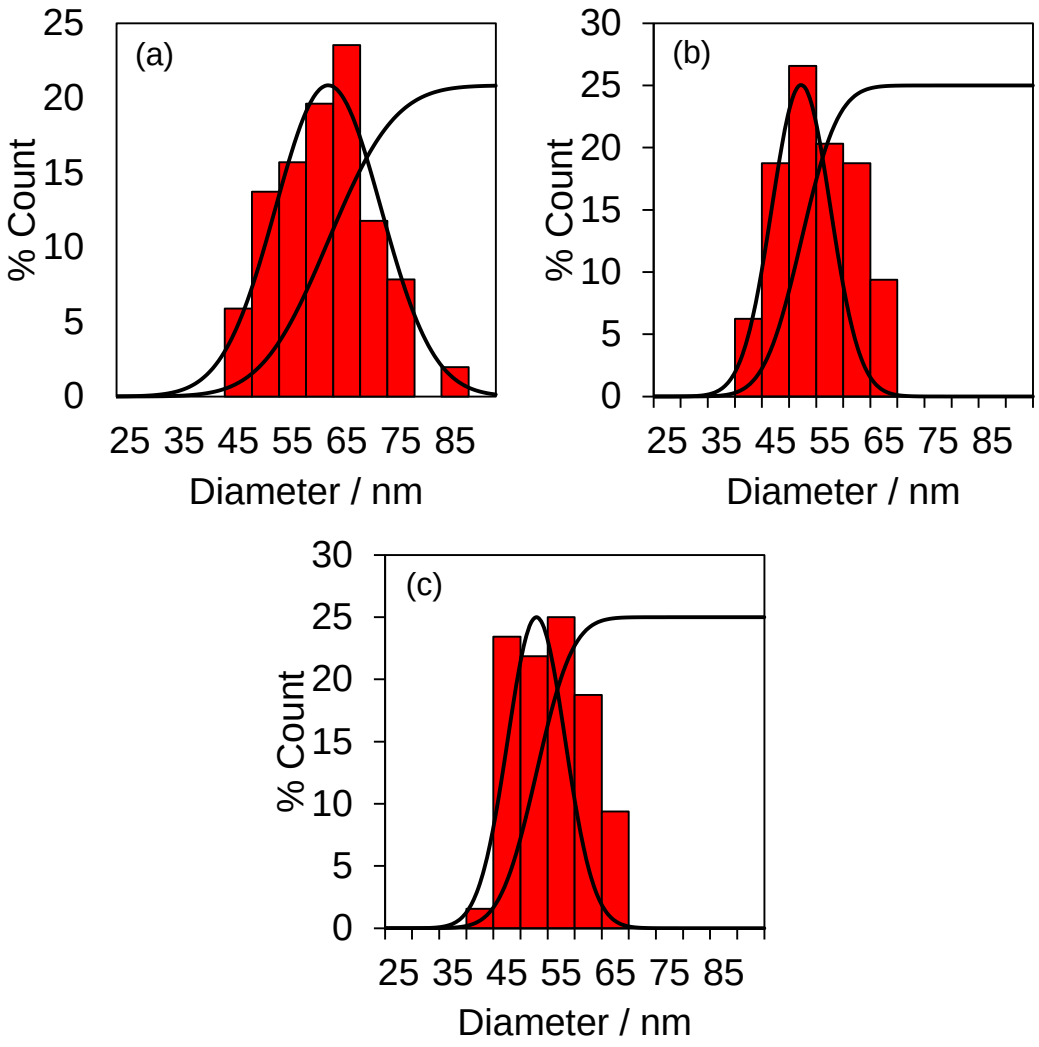

Figure 4.17: Total particle size distributions, normal and cumulative distributions for MP-Ag@SiO_2 nanocomposites at silver loadings of a) 3.38%, b) 6.54%, c) 9.5%.

Whilst silver nanoparticle diameter was not affected by the increase in silver loading, the number of silver species per silica particle was determined by loading. For the composites of lowest loading, the percentage of silver nanoparticles per silica mesoporous particle was 25%, whereas this increased to nearly 100% for the highest loading. **Figure 4.18** represents the increase in number of silver particles per silica particle.

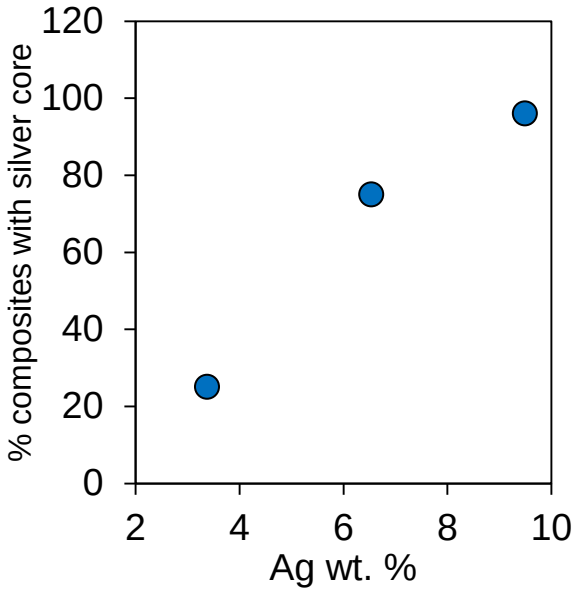

Figure 4.18: Number of silver nanoparticulate cores per mesoporous silica particle.

4.2.2.2. Powder X-ray Diffraction

The nature of the silver core was evaluated through powder XRD (**Figure 4.19**), to fingerprint crystalline phases present and their crystallite dimensions. All the nanocomposites only exhibited reflections characteristic of FCC metallic silver at 38.1° (111), 44.3° (200), 66° (220) and 77° (311), denoted by an asterisk in the figure (*). These diffractograms equate to an FCC metallic silver lattice parameter of 4.1, which is in line with the literature value.[10] No reflections were observed for any crystalline silica phase, with a single, strong and broad peak at 20° indicative of amorphous silica. The intensities of the silver peaks increase with silver loading due to the greater number of crystalline planes for samples of higher loading.

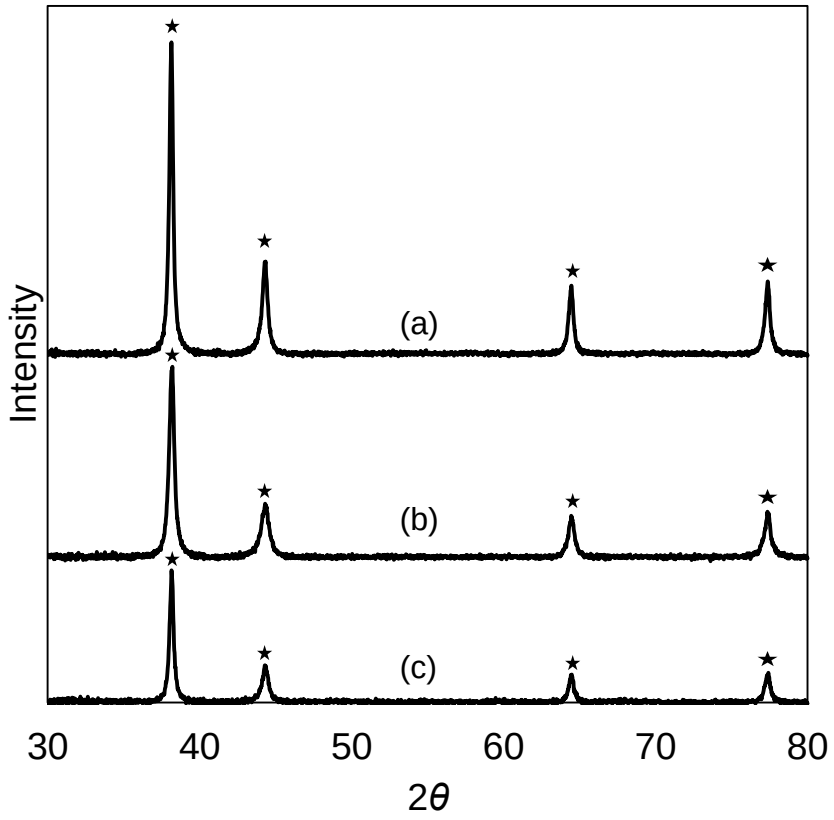

Figure 4.19: Powder XRD patterns of MP-Ag@SiO_2 nanocomposites for (a) 9.5%, (b) 6.54% and (c) 3.38% Ag Wt. %.

The silver FCC peaks were analysed using the Scherrer method to obtain average particle sizes for the silver cores using CASA software to fit peaks to the raw data and obtain values for the FWHM. The average particle sizes are displayed in **figure 4.20**, along with the values obtained by TEM analysis for comparison. Errors were determined using the standard deviation of the dual particle dimensions for TEM analysis, and the standard deviation of the calculated particle sizes for the four Ag^0 FCC peak FWHM values for XRD analysis.

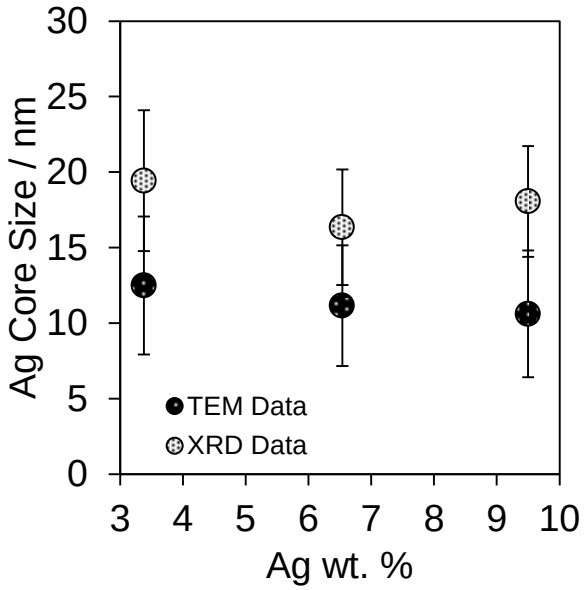

Figure 4.20: Average silver particle sizes for MP-Ag@SiO_2 nanocomposites determined by TEM and XRD analysis.

Low angle XRD was employed, to assess the pore structure, and determine order and arrangement. These are displayed in **figure 4.21**.

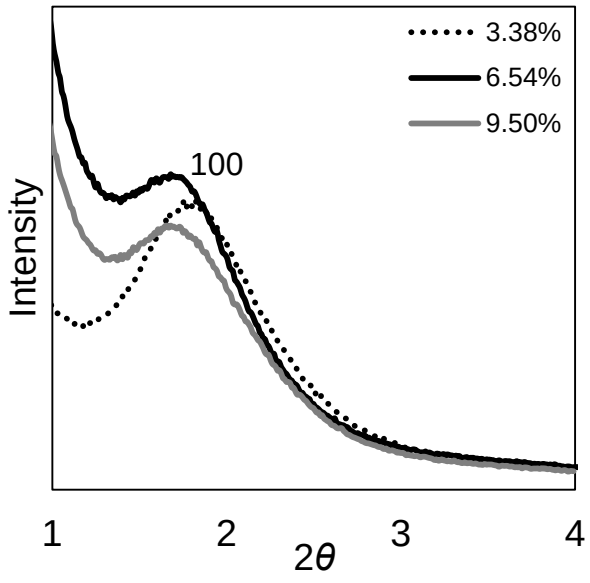

Figure 4.21: Low angle XRD patterns of MP-Ag@SiO_2 nanocomposites for different loadings of silver.

Recorded low angle patterns are consistent with similar materials, which have been reported to exhibit a hexagonally arranged pore structure, with the space group *P*6*mm*.[9] The visible peak is attributed to the 100 facet, whilst the expected 110 and 200 peaks at 2θ = 3.5 and 4 respectively are not well resolved in the diffraction pattern, and are not

visible, possibly due to a shorter range ordering of the mesopores caused by the central silver metal core. There is a slight increase in 2θ value as the loading decreases, signifying a decrease in pore spacing. This can be explained by the effect that increasing the concentration of ionic species has on micelle size, due to interactions between the free electrolytes and ionic head groups.[11] The peak is also the most well resolved in the lowest silver wt. % sample, presumably due to the greater number of empty silica particles and hence, larger regions of longer range order within the pore structures. Using the measured 2θ value from the XRD pattern, pore spacing can be calculated using the Bragg equation (**equation 2.5**) and the relationship between d-spacing and pore spacing (denoted **a** in **Figure 4.22)**.

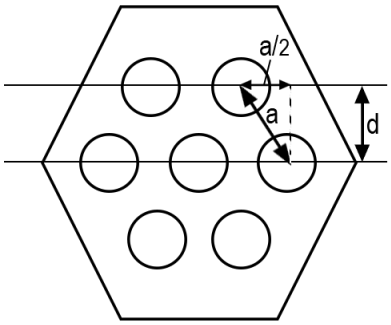

Figure 4.22: Inter-pore distances in hexagonally structured mesoporous silica.

Using Pythagoras theorem, it can be known that;

$$a^2 = (\frac{a}{2})^2 + d^2$$

Equation 4.1: Pythagoras theorem.

The square of **a** is equal to the square of a half **a** plus the square of the d-spacing, calculated by XRD. Re-arranging this equation results in:

$$a = \frac{2}{\sqrt{3}} d$$

Equation 4.2: Pore spacing.

The calculated pore spacings are shown in **table 4.2**.

Ag wt. %	2θ / °	d-spacing / nm	Pore spacing / nm
3.38	1.7	5.3	6.11

6.54	1.67	5.38	6.22
9.5	1.63	5.52	6.37

Table 4.2: Pore spacings for MP-Ag@SiO_2.

There is a minor increase in pore spacing with silver loading, potentially arising from an increasing concentration of free nitrate counterions, which are known to perturb CTAB micelle size to a small degree at high temperatures.[12] Addition and regulation of ionic salts into CTAB micelle-containing solutions causes a decrease in charge density of the micelle surface, leading to destabilisation and micelle swelling.[13]

4.2.2.3. X-ray Photoelectron Spectroscopy

XPS was used to probe the detectable oxidation states of materials**. Figure 4.23** shows background-subtracted Ag 3d spectra, clearly showing the $3d_{3/2}$ and $3d_{5/2}$ peaks (doublet separation = 6 eV).[14] All spectra were energy referenced to their adventitious C 1s peak at 284.7 eV. The black lines represent the raw data, as collected by the instrument, the red lines represent the envelope fitting of the sum of all component curves and the purple lines represent the individual Ag 3d components.

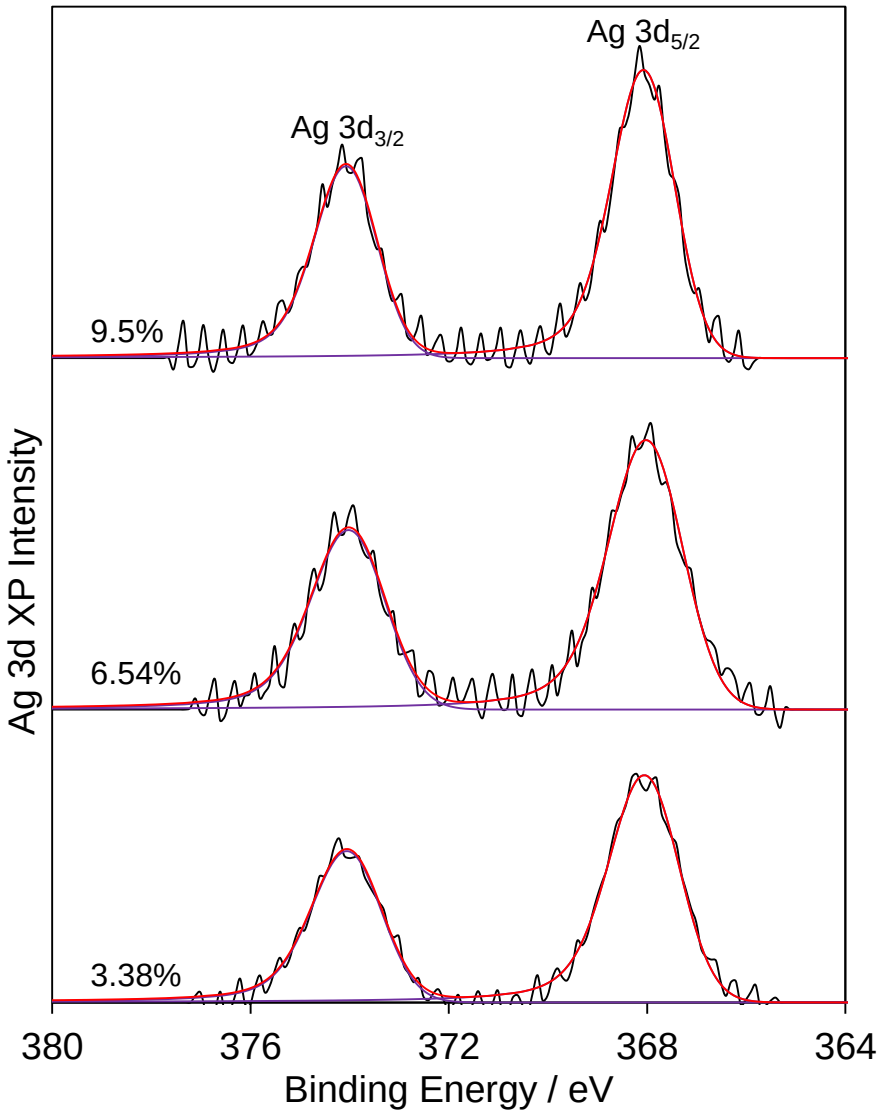

Figure 4.23: Ag 3d XPS stack plot of MP-Ag@SiO_2 nanocomposites.

The silver is identified to exist in a singular oxidation state, with a binding energy that suggests it is in the zero valent silver metal form , which corroborates with the powder XRD results.

The silicon regions were studied, to identify the silicon species as silicon dioxide. **Figure 4.24** displays a stack plot of the silicon 2p regions, with binding energies consistent with values obtained from the NIST database. A binding energy of 103.4 suggests the presence of SiO_2, according to the database, significantly higher than the majority of other silicon species. There is no energy shift observed throughout the series, confirming the silica species remains unaffected by the increasing silver loading.

The doublet separation of the $2p_{3/2}$ and $2p_{1/2}$ peaks was set to 0.6 eV, which was taken from the NIST XPS database, and the peak ratios were set to 2:1.

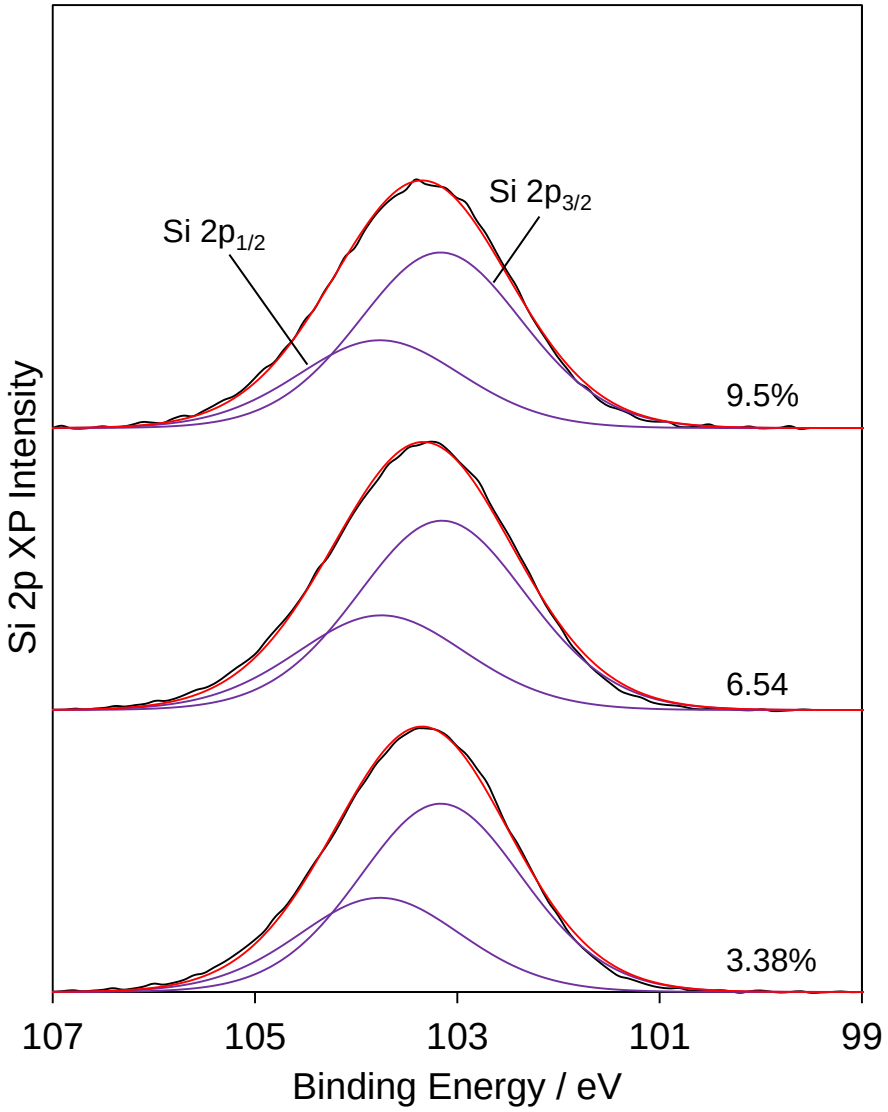

Figure 4.24: Si 2p XPS stack plot of MP-Ag@SiO_2 nanocomposites.

Analysis of the oxygen 1s regions (**figure 4.25**) confirmed the presence of a single species of oxygen which remained unaffected by increasing silver loading. The position of the peak was at a constant 532.2 eV throughout the series, which can be attributed to the Si-O-Si species.[15]

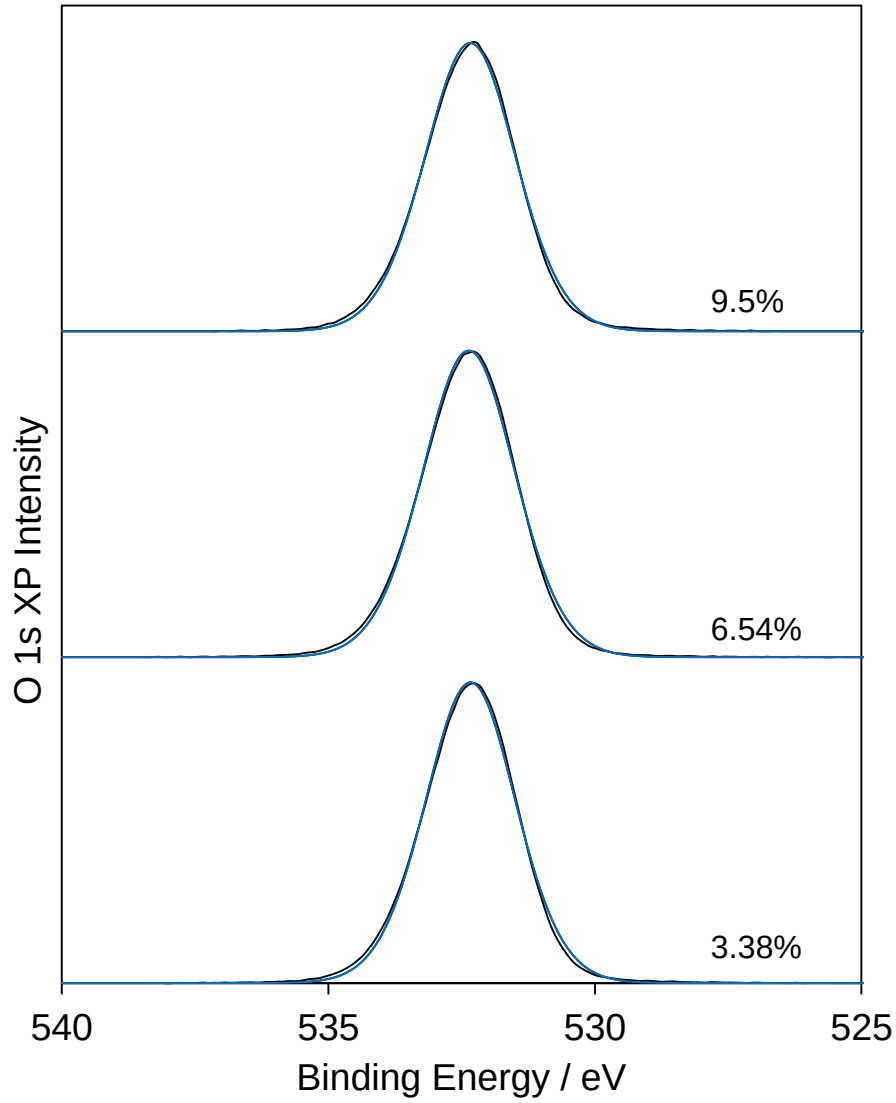

Figure 4.25: O 1s XPS stack plot of MP-Ag@SiO_2 nanocomposites.

Analysis of the nitrogen 1s and bromine 3d regions confirmed the absence of any remaining species resulting from the CTAB template, confirming its removal, as seen in **Chapter 4.2.1**. A summary of the elemental analysis by XPS is presented in **table 4.3**.

Bulk Ag wt. %	Surface Ag wt. %	Surface:Bulk (Ag)	Si wt. %	O wt. %	N wt. %	Br wt. %
3.38	0.45	0.13	50.29	49.26	0	0
6.54	0.85	0.13	50.23	48.92	0	0
9.5	1.15	0.12	49.96	48.89	0	0

Table 4.3: Elemental compositions of MP-Ag@SiO_2 by XPS analysis.

The surface to bulk silver ratio is unaffected by the increase in silver loading, which corroborates the idea that silver core size and silica matrix thickness are unperturbed by increasing silver loadings.

4.2.2.4. Porosimetry

The porosity of the synthesised nanocomposites was investigated by N_2 porosimetry, the isotherms of which are exhibited in **figure 4.26**.

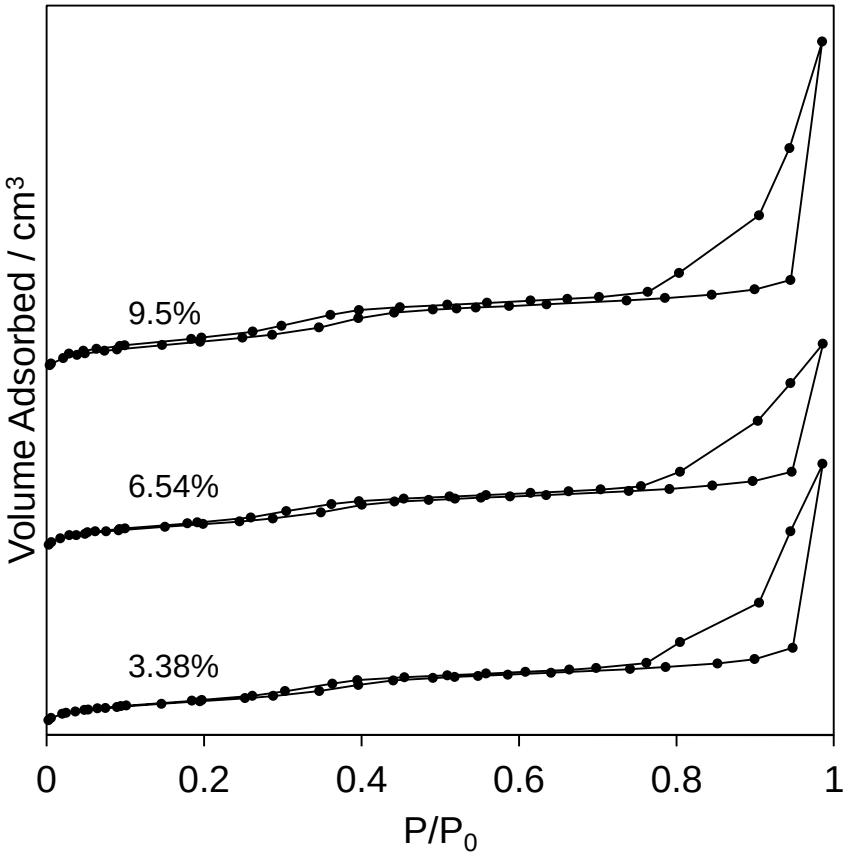

Figure 4.26: N_2 adsorption isotherms for MP-Ag@SiO_2 nanocomposites.

A clear type IV isotherm shape was observed, complete with hysteresis loop typical of mesoporous materials. The recorded surface areas were very high, solely due to the intrinsic mesoporosity, as t-plot analysis of the isotherm suggested there was no microporosity in the materlals. Full pore analysis is displayed in table 4.3, with microporosity information gained by t-plot analysis and mesopore information from BJH analysis of the isotherm.

Ag loading (wt. %)	Surface Area (cm^2/g)	Mesopore Volume (cm^3/g)	Pore Diameter / nm	Micropore Volume (cm^3/g)
3.38	710 ± 70	0.39	2.8 ± 0.15	0
6.54	770 ± 75	0.44	2.8 ± 0.15	0
9.5	660 ± 65	0.38	2.8 ± 0.15	0

Table 4.3: Structural properties of MP-Ag@SiO_2 nanocomposites.

The BJH profiles for the synthesised materials (**figure 4.27**) indicated monodisperse pores of 2.8 ± 0.15 nm.

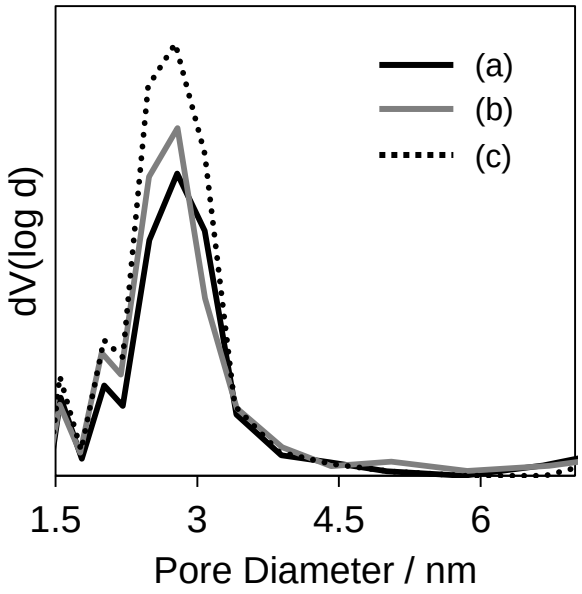

Figure 4.27: BJH profiles for (a) 3.38%, (b) 6.54% and (c) 9.5% Ag in MP-Ag@SiO_2 nanocomposites.

Coupling mean pore size with pore spacing from low angle XRD allows for calculation of mean silica wall thickness (**table 4.4**). As the pore diameters are found to be constant, within error, the silica wall thicknesses calculated are seen to alter. It is, however, given the hypothesised nature behind pore spacing increases, likely that the pore sizes are incrementally larger as weight loading increases, but below a detectable increase with the methodology implemented.

Ag wt. %	Pore spacing / nm	Pore diameter / nm	Silica wall thickness / nm
3.38	6.11	2.8 ± 0.15	3.31 ± 0.15
6.54	6.22	2.8 ± 0.15	3.42 ± 0.15
9.5	6.37	2.8 ± 0.15	3.57 ± 0.15

Table 4.4 Pore dimensions for MP-Ag@SiO_2

4.2.2.5. Summary of silver loading variation in MP-Ag@SiO_2 nanocomposites

Silver nanoparticles encased in a mesoporous shell were prepared using an organic micelle templating methodology, in which hydrazine was used to reduce the ionic silver nitrate salt reagent to silver metal nanoparticles via the mechanism outlined in **Chapter 4.2**. The silica condensed around the surfactant micelles via hydrolysis and condensation of tetraethyl orthosilicate.

The organic template was removed from the material using a thermal treatment method, following a removal of the bromide counterions associated with the organic template by washing with a mixture of ethanol and ammonium carbonate, to prevent the formation of silver bromide during the thermal treatment procedure. The removal of bromide ions was followed by XPS, whilst organic molecule content was observed using infrared spectroscopy. The bromide was successfully removed before the calcination and heating to 350 ^{O}C removed the surfactant to leave monodisperse pores within the silica framework, which was confirmed via infrared spectroscopy and nitrogen porosimetry.

XPS and XRD analysis identified the silver species and zero valent silver metal, signifying that the silver was completely reduced during the chemical reduction treatment via hydrazine.

4.2.3. Pore size

Utilising an intrinsic mesoporous structure as a coating for silver nanocomposites allows for stabilisation of the silver nanoparticles, whilst maintaining a fully accessible site for silver ion dissolution and antimicrobial activity.

Mesoporous silicas have been the subject of much interest and research into the tuning of pore sizes for use in multiple fields. This has been achieved through utilisation of organic additives to swell templating micelles, adjustments in synthetic parameters such as temperature or through the use of templating surfactants of differing chain lengths and cosurfactants.[16-19]

It is thought that variations in pore size could lead to more exposed silver surfaces, and hence an increase in ionic silver release rates. The nanocomposites prepared in this section are a combination of larger silver nanoparticulate cores (which should have, in principle, slower dissolution speeds than the small, monodisperse particles prepared in **chapter 3)** with a more exposed surface area as a result of increased porosity. It was hoped that the inclusion of a porogen, such as mesitylene, could increase the diameter of mesopores relative to that of conventionally prepared silica shell as for ordered MCM-41[20] and hence result in nanoarchitectures with good release rates and long lifetimes (due to the greater pool of available silver), while maintaining the high structural integrity associated with core-shell nanomaterials.

Determined bulk and surface silver loadings, from EDX and XPS analysis are displayed in **table 4.5**. The elemental analysis confirmed addition of mesitylene bore no effect upon silver loading.

[Mesitylene] / mM	Bulk Ag wt. %	Surface Ag wt. %	Surface:Bulk
0	6.54	0.85	0.13
8.5	6.48	0.8	0.12
17	6.57	0.84	0.13

Table 4.5: Bulk and surface Ag content for MP-Ag@SiO_2 nanocomposites.

4.2.3.1. Transmission electron microscopy

TEM analysis was utilised to confirm that the integrity of the mesoporous core-shell architecture was not compromised during the pore expansion procedure. **Figure 4.28** displays representative bright field TEM images of the nanocomposites synthesised.

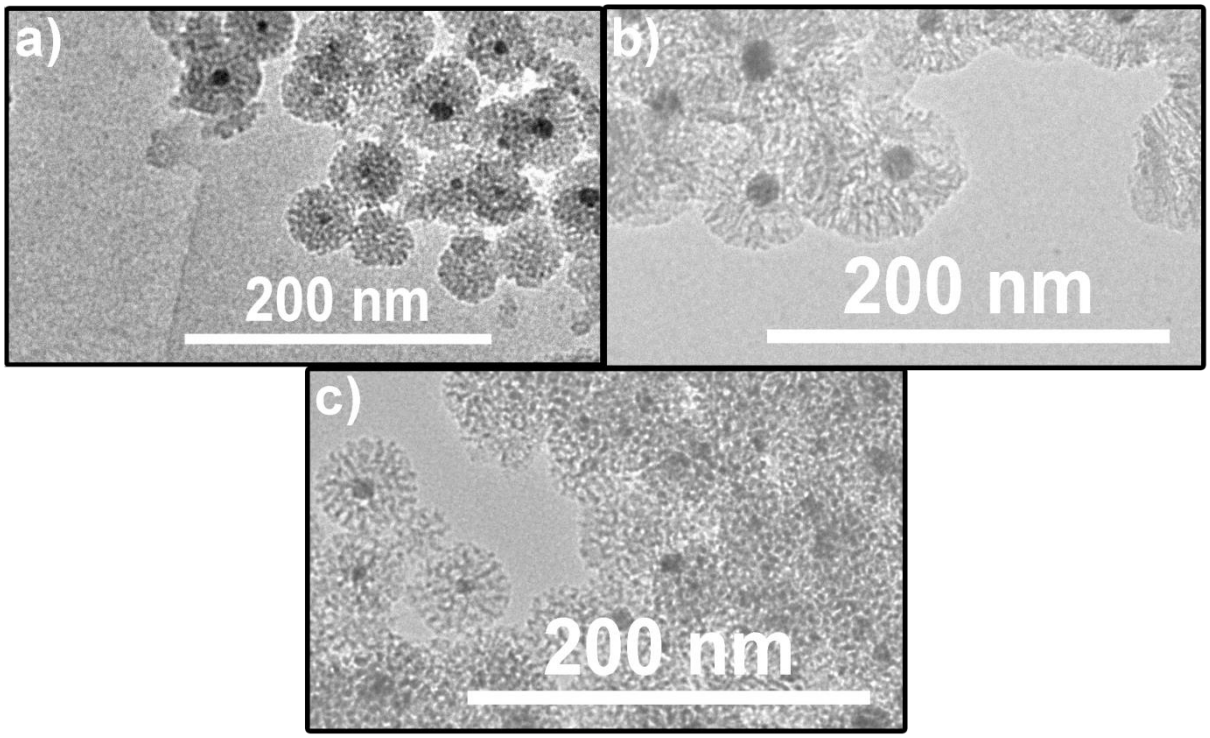

Figure 4.28: Representative bright field TEM images of (a)

The particles display the characteristic dark silver core, surrounded by a light grey halo, with noticeable mesoporous percolating through the silica shells. The porosity is evident across all three samples, although a fully ordered region of mesopores, as seen in mesoporous silicas such as MCM-type structures[21] or SBA-type materials,[22] although these materials, being smaller and spherical in morphology, would likely not have many regions of long range order, which can be imaged using electron microscopy.

The particle dimensions were recorded using imageJ software and the mean and standard deviation calculated and plot in **figure 4.29**.

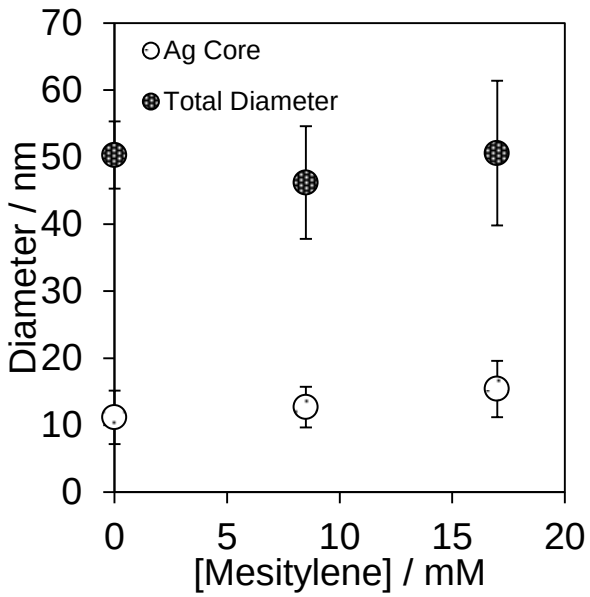

Figure 4.29: Particle dimensions for MP-Ag@SiO_2 determined by TEM analysis.

The silver core size and total composite diameter remain unaffected by the inclusion of mesitylene in the reaction, with the silver core size measured at 13.1 ± 2.3 nm and the total particle diameter at 49 ± 3 nm. The dispersities are relatively large, as with the previous series of materials, and the full composite dimensions histograms are displayed in **figure 4.30** and **figure 4.31** for the silver cores and silica shells respectively, along with the normal and cumulative size distributions based on mean and standard deviation from the measured particles (>50 in each case).

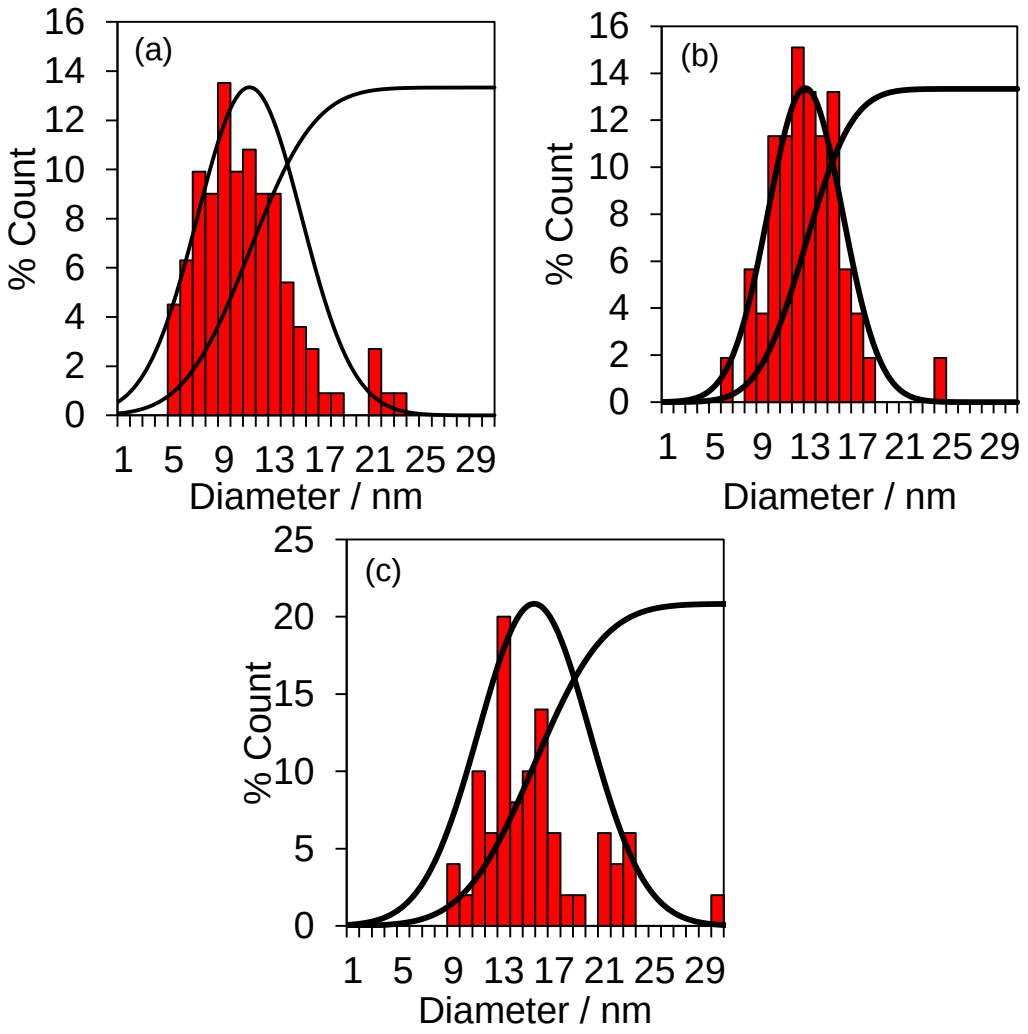

Figure 4.30: Silver core size distributions, normal and cumulative distributions for MP-Ag@SiO_2 nanocomposites synthesised with (a) 0 mM mesitylene, (b) 8.5 mM mesitylene and (c) 17 mM mesitylene.

As can be seen in the particle size distribution plots, there is a wide range of particle sizes for the silver cores, fitting with previously observed results. The dispersity, however, appears to be unaffected by the introduction of mesitylene to the reaction and, barring one or two outliers, the particle size histograms appear invariable.

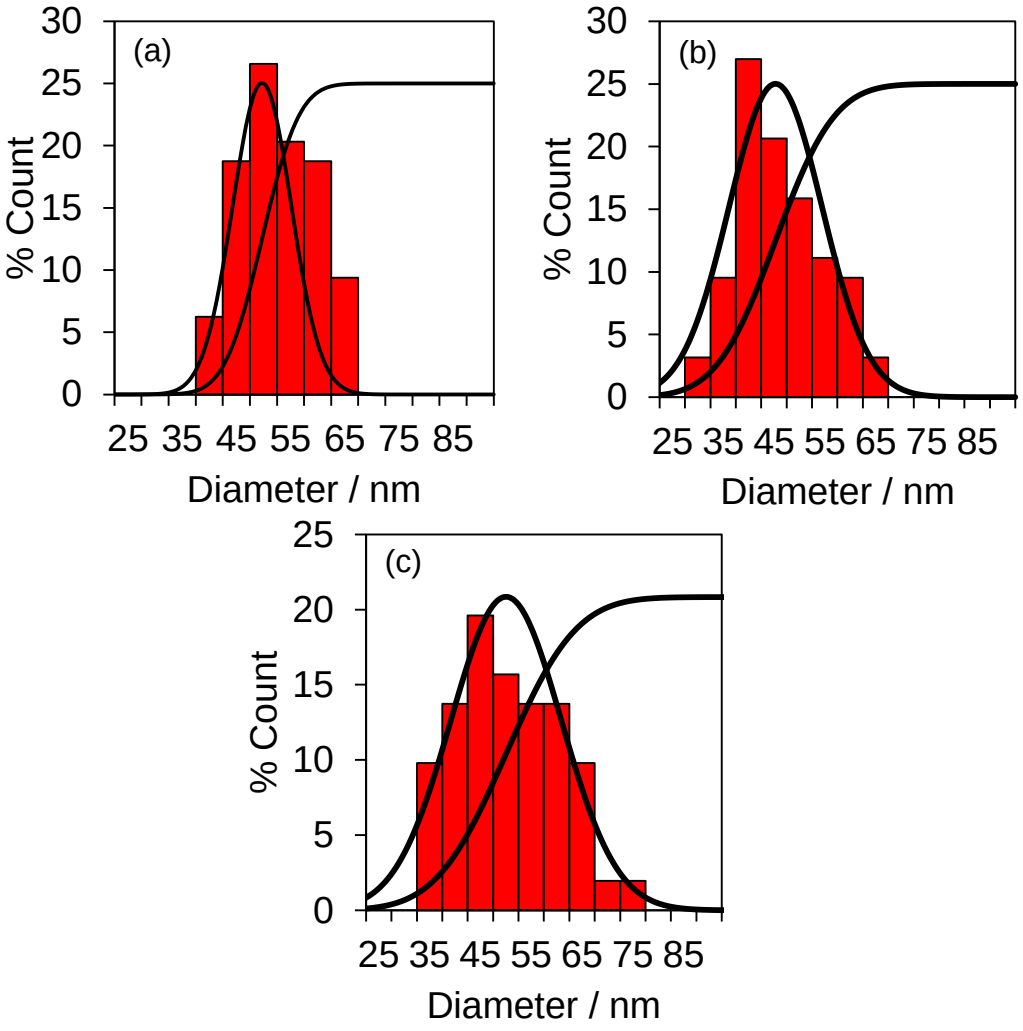

Figure 4.31: Silica shell size distributions, normal and cumulative distributions for MP-Ag@SiO_2 nanocomposites synthesised with (a) 0 mM mesitylene, (b) 8.5 mM mesitylene and (c) 17 mM mesitylene.

The total diameters of the silver-silica nanocomposites also appear unperturbed by the organic additive during synthesis. This is fitting with expectations, as the overall particle diameters for silicas in these kinds of systems are affected by the growth kinetics and, hence, condensation rates and reaction times.[1]

4.2.3.2. Powder X-ray diffraction

Powder XRD was used to analyse changes to the silver crystallites as a result of mesitylene addition to swell the pores. **Figure 4.32** shows the diffraction patterns for these samples, indicating that there was no change to the silver speciation during the pore expansion.

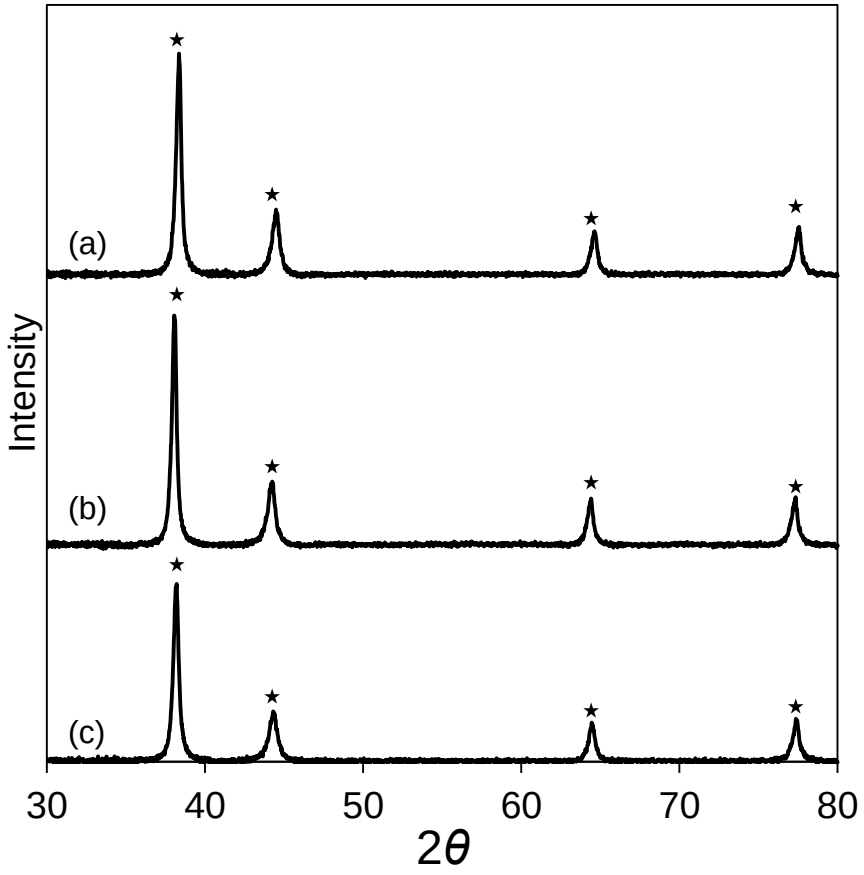

Figure 4.32: XRD patterns for (a) 0 mM, (b) 8.5 mM and (c) 17 mM of mesitylene in synthesis of MP-Ag@SiO_2 nanocomposites.

The XRD patterns indicate the silver retains the speciation of Ag^0 with an FCC structure, with the 111 reflections appearing at 38.08 ± 0.1 ^{o}, a lattice parameter of 2.45 ± 0.05 Å, which indicates the formation of metallic silver. From the 4 reflections exhibited in the XRD patterns, silver particle size was determined using the Scherrer equation (**figure 4.33**).

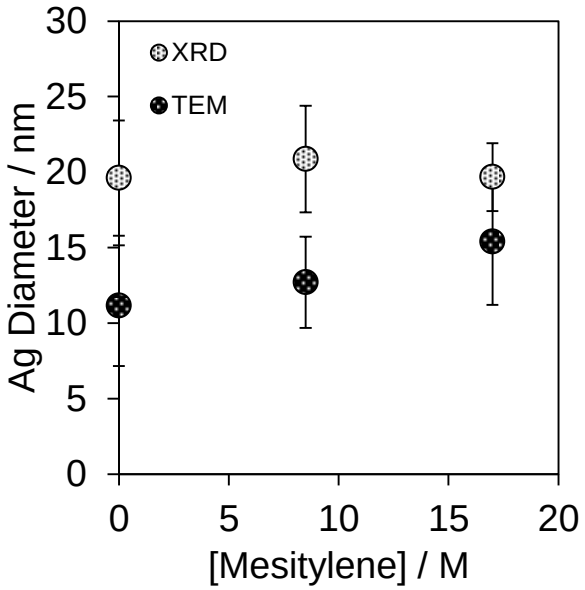

Figure 4.33: Average silver particle sizes for MP-Ag@SiO_2 nanocomposites with addition of mesitylene, determined by TEM and XRD analysis.

The particle sizes determined from TEM and XRD analysis are relatively consistent within error, however XRD particle sizing suggests a slightly larger average particle size than that measured from TEM analysis. A potential cause for this discrepancy could be regions of agglomerates increasing average crystallite size, which are not observed within localised electron micrography analysis.

XRD analysis of these materials was performed at low angles to characterise the quasi-ordered mespore structure (**figure 4.34**).

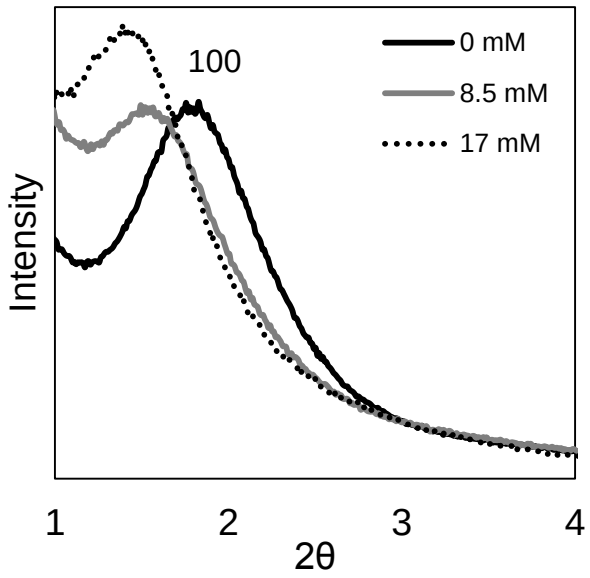

Figure 4.34: Low angle XRD patterns for MP-Ag@SiO_2 nanocomposites prepared using differing concentrations of auxillary organics.

As with the previous materials, calculation of pore spacing can be performed using the 2θ value from the (100) peak in the low angle XRD patterns. These are tabulated in **table 4.6**. In this table, a clear increase in pore spacing is observed, rising with mesitylene concentration, due to incorporation of the hydrophobic additive within the CTAB micelles, and subsequent micelle swelling.

[Mesitylene] / mM	2θ / °	d-spacing / nm	Pore spacing / nm
0	1.67	5.38	6.21
0.6	1.46	6.16	7.11
1.2	1.35	6.66	7.69

Table 4.6:Pore spacings for MP-Ag@SiO_2 with mesitylene addition.

4.2.3.3. X-ray photoelectron spectroscopy

Analysis of the silver oxidation state and surface silver content was achieved through XPS analysis (**figure 4.35**). All spectra were calibrated to adventitious carbon at 284.7 eV and the data analysed using CASA software.

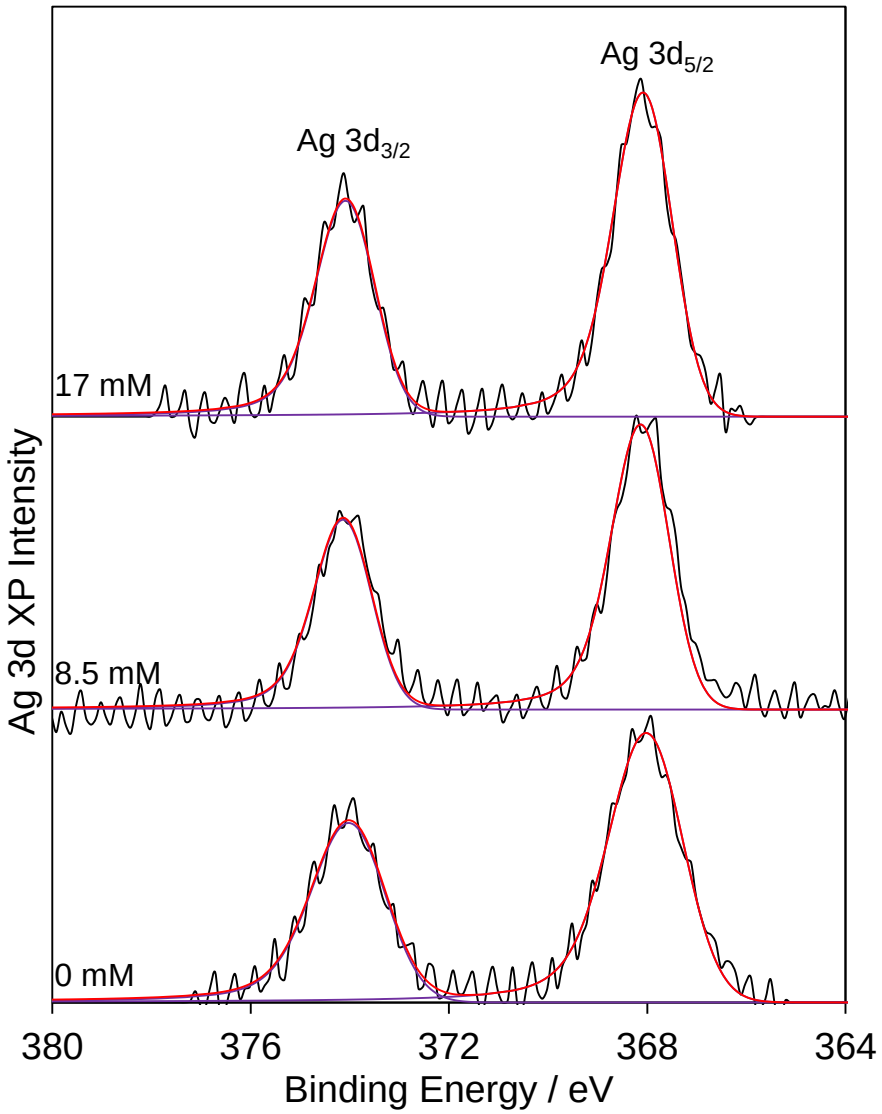

Figure 4.35: Ag 3d XPS stack plot of MP-Ag@SiO_2 nanocomposites synthesised with additional mesitylene (concentrations listed are that of mesitylene in synthesis).

The Ag 3d regions were fit using a doublet separation of 6 eV and peak area ratios of 3:2 for the $^5/_2$:$^3/_2$[23] Ag 3d components and a hybrid peak shape of Gaussian-Lorentz and Doniach-Sunjic was employed to account for the asymmetry of metal XPS spectra. A singular silver species was observed at 368 eV, with no evident shoulders or secondary components. No peak shift can be observed as concentration of mesitylene increases, which lends support to the theory that the silver cores themselves are unaffected by the micelle swelling process.

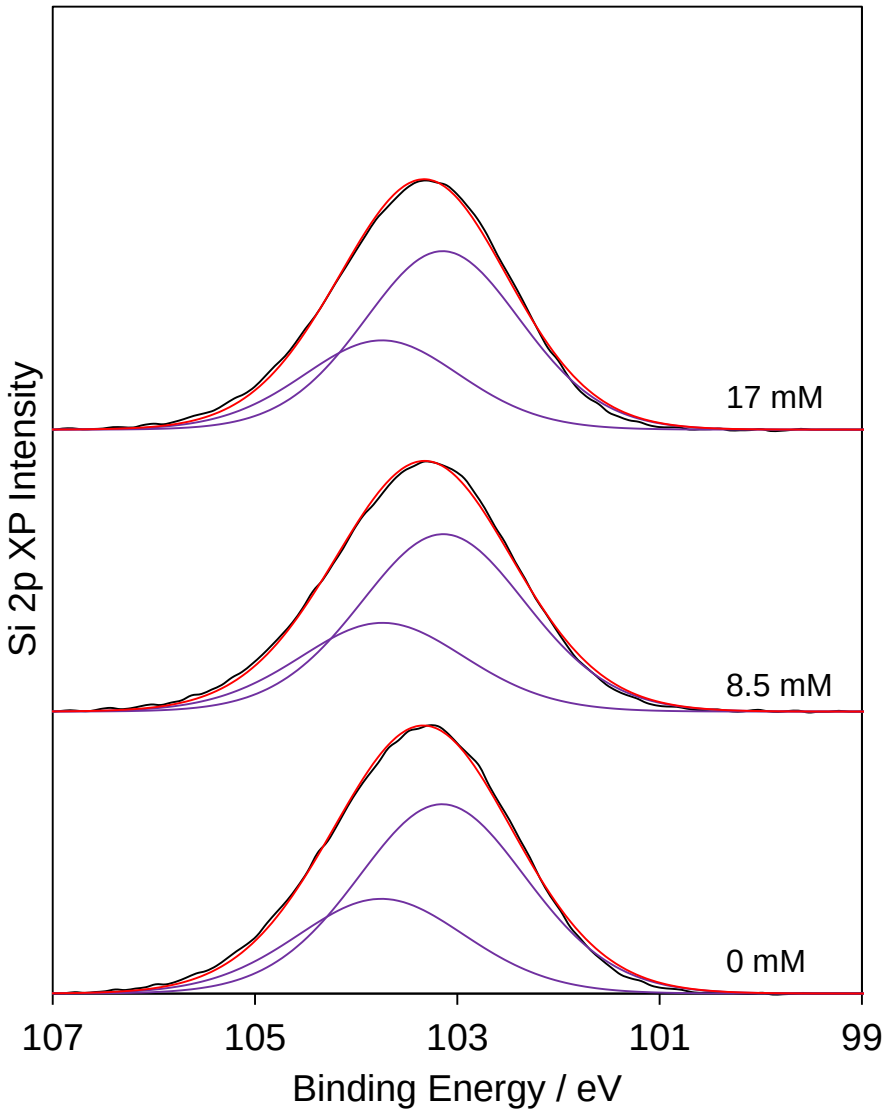

Figure 4.36: Si 2p XPS stack plot of MP-Ag@SiO_2 nanocomposites synthesised with additional mesitylene.

Si 2p regions were fit using a doublet of Si $2p_{3/2}$ and $2p_{1/2}$ with a doublet separation of 0.6 eV. Si $2p_{3/2}$ peaks record a position of 103.3 eV, which is correct for SiO_2 species (**figure 4.36**).

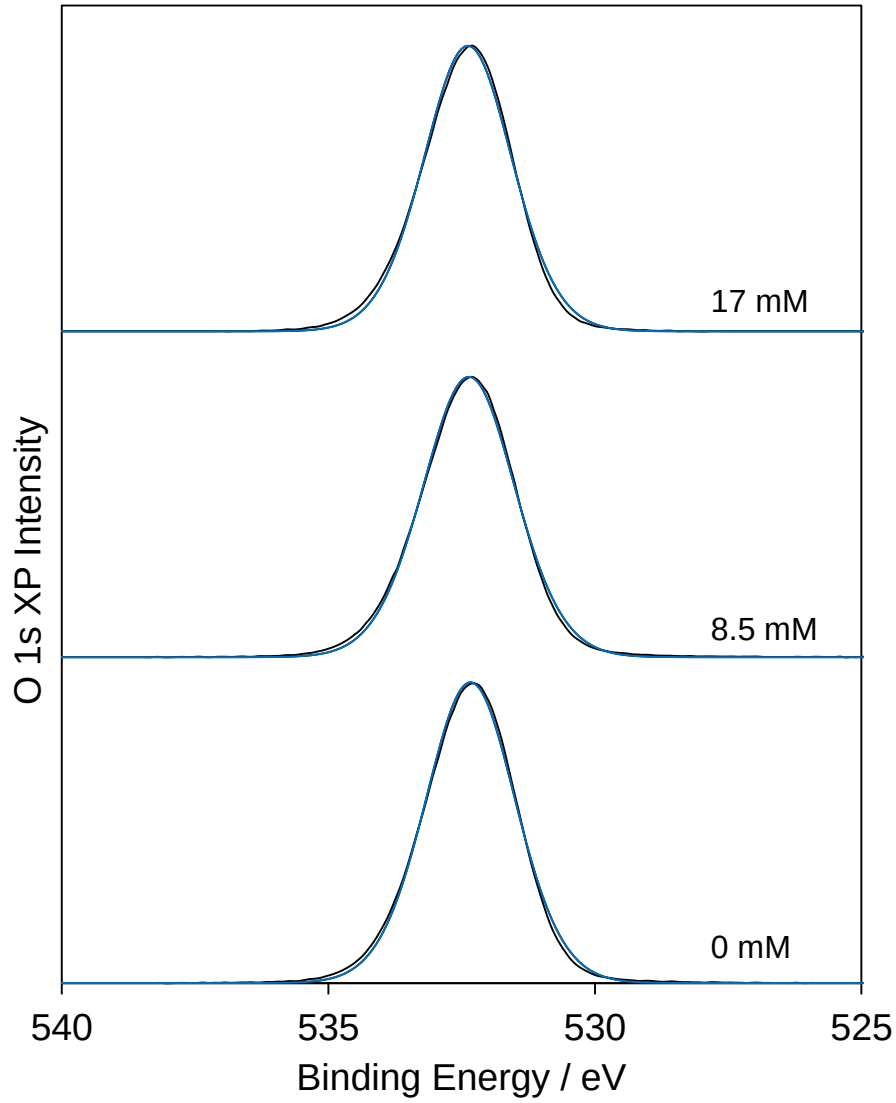

Figure 4.37: O 1s XPS stack plot of MP-Ag@SiO_2 nanocomposites synthesised with additional mesitylene.

Study of the O 1s regions reports no change to the oxygen species (**figure 4.37**), which exists at the binding energy of 532.3 eV, indicative of SiO_2. Overall elemental compositions determined by XPS analysis are tabulated in **table 4.7**.

[Mesitylene] / mM	Bulk Ag wt. %	Surface Ag wt. %	Surface:Bulk	Si wt. %	O wt. %	N wt. %	Br wt. %
0	6.54	0.85	0.13	50.23	48.92	0	0
8.5	6.54	0.8	0.12	48	52.2	0	0
17	6.54	0.84	0.13	49.71	49.45	0	0

Table 4.7: Elemental compositions of MP-Ag@SiO_2 with mesitylene addition by XPS analysis.

The silver loadings and available surface silver display a steady, constant trend with the addition of mesitylene.

4.2.3.4. Porosimetry

Expansion of the pores was determined by performing nitrogen porosimetry to probe the external, exposed surface of the synthesised materials and confirm the influence of organic swelling agent on the product materials.

The recorded isotherms (**Figure 4.38**) exhibit a type IV characteristic with a mesostructural material. There is a large volume increase at high partial pressure, which can usually be attributed to the presence of macropores in a type II isotherm, however consultation of the electron micrographs confirms that at no point does the material display any sort of intrinsic macroporous structure, and the presence of this feature is likely the result of interparticular voids, resulting in capillary condensation in the 10-90 nm regime, as determined by BJH analysis.

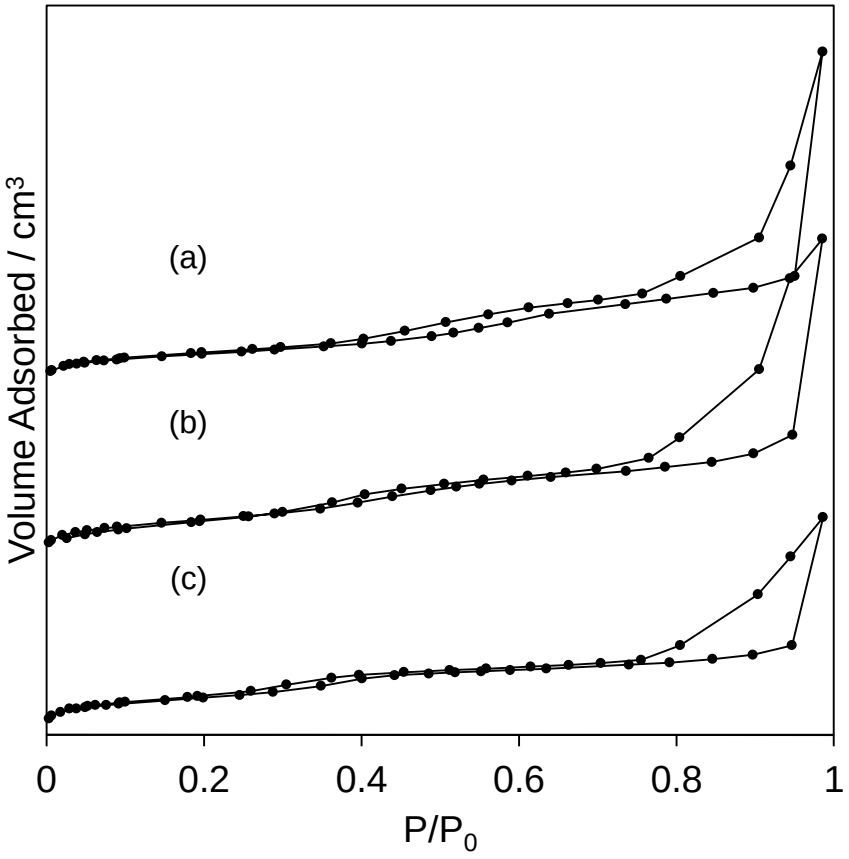

Figure 4.38: Nitrogen adsorption isotherms for (a) 0 mM, (b) 8.5 mM and (c) 17 mM of mesitylene in synthesis of MP-Ag@SiO_2 nanocomposites.

Analysis of the structural properties of the prepared materials determined through porosimetry analysis are tabulated in **table 4.8**. The materials display typically high surface areas associated with these mesostructural nanocomposites, as witnessed previously although no trend is evident for increasing or decreasing total surface area nor mesopore volume. The pore diameter from BJH analysis

[Mesitylene] / mM	Surface Area (cm^2/g)	Mesopore Volume (cm^3/g)	Pore Diameter / nm	Micropore Volume (cm^3/g)
0	768 ± 75	0.386	2.49 ± 0.15	0
8.5	868 ± 85	0.444	3.11 ± 0.18	0
17	695 ± 70	0.376	3.88 ± 0.24	0

Table 4.8: Structural properties of MP-Ag@SiO_2 nanocomposites with addition of mesitylene.

Applying the BJH method to these isotherms allows for analysis of the average pore size of these materials, a summary of which is presented in **figure 4.38**. It can be seen from this figure that the average pore diameter of the synthesised materials increases linearly with concentration of mesitylene over the range studied.

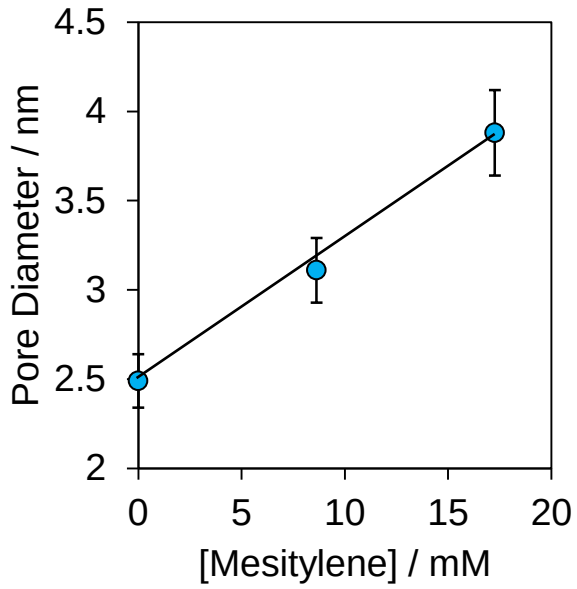

Figure 4.39: Pore size (as determined by BJH analysis) increase with mesitylene concentration.

Subtraction of average pore diameter measured from BJH analysis from pore spacing, determined from low angle XRD patterns, allows for average silica wall thickness to be calculated (**table 4.9**).

[Mesitylene] / mM	Pore spacing / nm	Pore diameter / nm	Silica wall thickness / nm
0	6.21	2.49	3.72
0.6	7.11	3.11	4
1.2	7.69	3.88	3.81

Table 4.9: Pore dimensions for MP-Ag@SiO_2 with addition of mesitylene.

Further analysis of the BJH profiles (**figure 4.40(I)**) indicates that, whilst the mean pore size does increase with time, larger pores suffer from more polydisperse distributions, which could explain the noted discrepancies in silica wall thickness determined from low angle XRD pore spacings. Geometric means and standard deviations for pore diameters were calculated and plotted as normal and cumulative

distributions, which are displayed in **figure 4.40(II)** and further display evidence of increasing pore size.

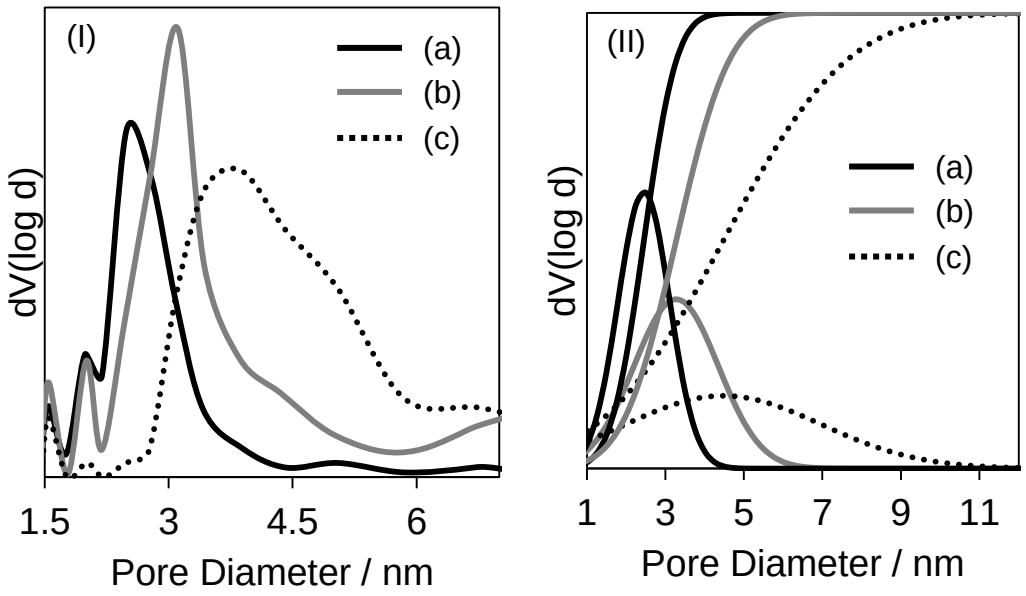

Figure 4.40: (I) BJH profiles and (II) normal and cumulative pore size distributions for (a) 0 mM, (b) 8.5 mM and (c) 17 mM of mesitylene in synthesis of MP-Ag@SiO_2 nanocomposites.

4.2.3.5. Summary of pore diameter variation in MP-Ag@SiO_2 nanocomposites

Silver metal nanoparticles encased in a mesoporous silica shell were synthesised and the pore size in the silica shell was tuned between 2.5 ± 0.15 nm and 3.9 ± 0.24 nm by using an organic substance, in the form of mesitylene to swell the micelles during formation. This variation in pore size was monitored by nitrogen adsorption porosimetry, using the BJH methodology applied to the desorption branch of the isotherm. The swelling of the micelles caused an increase in the mean pore size, however also increase the polydispersity, resulting in a larger range of pores sizes. The pore structure was also studied by low angle XRD analysis, which reported a small, broad peak, suggesting a low degree of order, which shifted to lower angles as pore size increased.

The silver metal core was found to remain unchanged as pore size was altered. This was studied by XPS and XRD analysis, as well as verifying the core-shell architecture by TEM analysis. The mean silver core size and silica shell size was unchanged by the addition of the auxiliary organics, and the silver core was determined

to consist of zero valent silver metal, with an FCC structure and lattice spacing consistent with silver metal, having been completely reduced by hydrazine.

4.2.4. Performance assays

To determine the suitability of the prepared materials for use as antimicrobial agents, they were screened, to determine the ionic silver release rates and bacterial mortality rates. The correlation between silver ion release rates and bacterial efficacy can then be observed, and assessments made regarding the optimal nanocomposites properties, in terms of loadings and pore size.

4.2.4.1. Silver dissolution

As the active species thought to be responsible for the antimicrobial activity of silver is Ag^{+}, the release of silver ions into solutions was monitored, in order to correlate activity with silver ion release rates. The dissolution was monitored using ICP-MS to study the concentration of solutions taken from a stock at set time points as described in **Chapter 2.4**. These concentrations were then normalised to bulk silver content, so as to determine a release as a function of total silver percentage released.

The target dissolution profiles for the synthesised materials was a slow steady release of ionic silver from the bulk particulate form, similar to that observed by silver carbonate and silver oxide, two fairly insoluble silver compounds. Silver carbonate is used as a standard by which to measure the performance of the materials synthesised in this section.

The dissolution profiles of the prepared MP-Ag@SiO_2 nanocomposite materials with varying silver loadings is reported in **figure 4.41**.

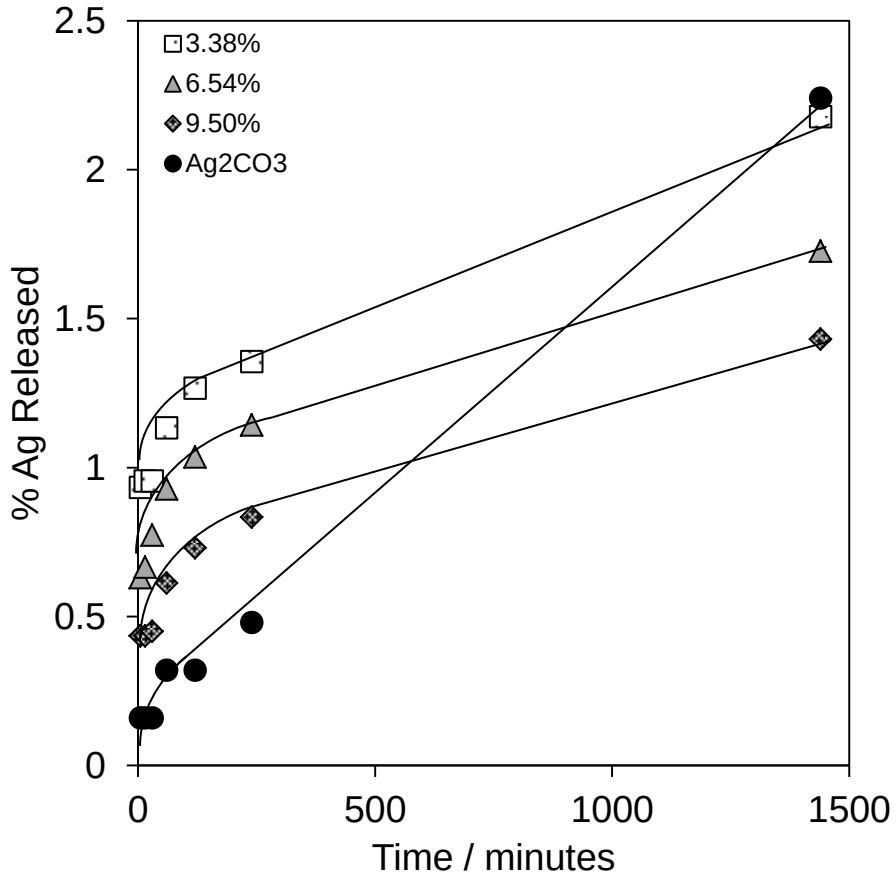

Figure 4.41: Dissolution profiles for MP-Ag@SiO_2 nanocomposites with varying silver loadings.

Upon normalisation to bulk silver content, the MP-Ag@SiO_2 nanocomposites exhibit a slight dependence towards bulk silver content upon the silver ion release rates. The silver nanoparticles exist in the same form in all three examples, with consistent particle sizes and silica shell environments. This would suggest that there is a trend for silver nanoparticles to release more slowly when in solutions of higher concentration. This has been reported in previous literature, which suggests that higher concentrations of silver nanoparticles exhibit reduced silver ion release rates due to the existing equilibrium between solid nanoparticulate and free ionic silver, which can exit solution via agglomeration or by rejoining existing nanoparticles.[24] These materials exhibit an extremely slow release rate, which, when considering the relatively large reserve pool of bulk silver, suggests they are excellent potential long-term antimicrobial agents.

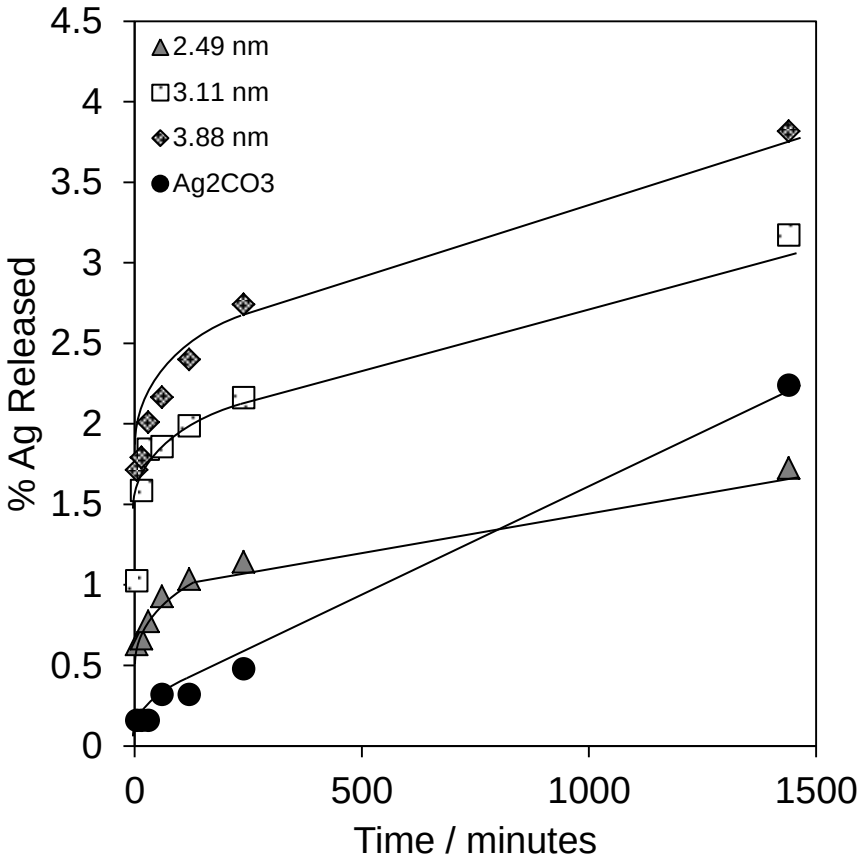

Figure 4.42: Dissolution profiles for MP-Ag@SiO_2 nanocomposites with varying silver pore sizes from mesitylene addition.

Figure 4.42 displays the silver ion release profiles for MP-Ag@SiO_2 nanocomposites with enlarged pore sizes. There is a noticeable increase in silver ion release percentage upon increase of mesopore diameter. It is likely a result of an increase in available silver surface area, caused by a more open silica shell network. Silver dissolution rates from bulk nanoparticles have been reported to increase in correlation to available surface area before, due to the oxidative release process in silver metal to silver ion process which occurs at the surface of silver nanoparticles (**figure 4.43**).[25]

$$2\,Ag_{(s)} + {}^{1}/_{2}O_{2(aq)} + 2H^{+}_{(aq)} \longrightarrow 2\,Ag^{+}_{(aq)} + H_2O_{(l)}$$

Figure 4.43: Silver ion release process in aqueous media.

This increase in silver ion release could possibly be combined with larger pools of bulk silver, attained through increase of silver weight loading, to produce a material with optimal silver release and an increased lifetime.

4.2.4.2. Microbiological assays

Testing for antimicrobial activity began with zone of inhibition tests, which is a standard test for determining antimicrobial activity, involving the test material being placed into a well bored into an agar plate loaded with microorganisms. Following this, time based kill rates were reported by logarithmic reduction method, alongside minimum bactericidal concentration tests and validity of neutralisation tests, which are performed to ensure the neutralising agent employed in the logarithmic reduction and MBC tests sufficiently retards the bactericidal action of the released silver.

4.2.4.2.1. Zone of Inhibition tests

Zone of inhibition testing was performed, allowing for a quick determination of the presence of antimicrobial activity and a semi-quantitative analysis of bactericidal strength. The zone of inhibition test involves spreading a bacterial inoculum onto an agar plate, boring holes into the agar, inserting the material to be tested into the resulting wells and incubating. After 24 hours at 37^{o}C, the wells will have a clear zone around them where bacteria have not been allowed to grow. This zone can be measured and used as an indicator of antimicrobial activity and comparative strength, although this test is heavily limited by diffusion through the agar itself. The zones are reported in millimetres and normalised to total silver content. These zone of inhibition tests give a good indicator of the presence of antibacterial activity, but do not give information about kill rates, which is an important factor in the antimicrobial industry.

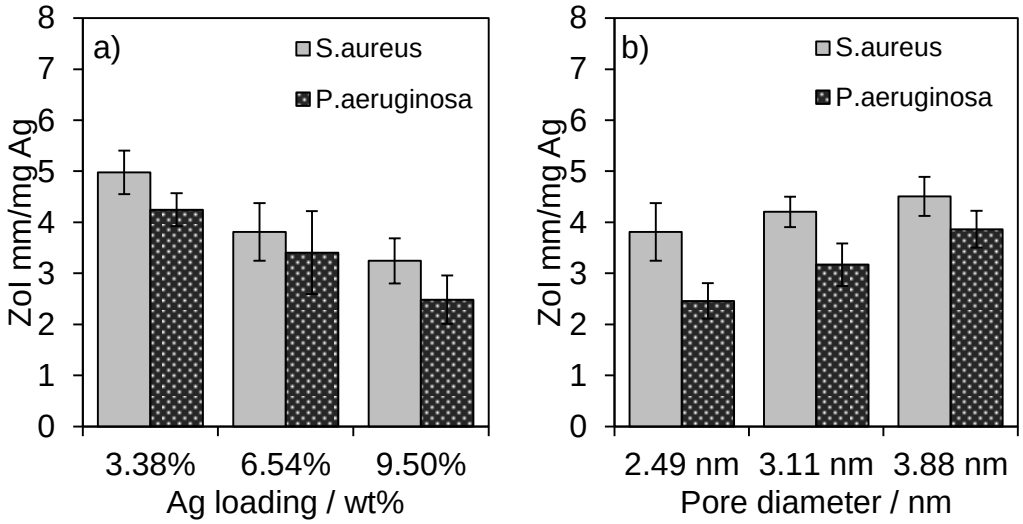

Figure 4.44: Zones of inhibition for MP-Ag@SiO_2 nanocomposite materials for (a) different loadings and (b) different pore sizes against *Staphylococcus aureus* and *Pseudomonas aeruginosa* normalised to bulk silver content.

The zone of inhibition experiments reveal clear antimicrobial activity of the nanocomposites materials (**figure 4.44**). There appears to be a slight dependence on bulk silver loading on zone size, and hence antimicrobial strength. This is, however, likely a result of limiting factors resulting from silver ion diffusion rates throughout the agar media, giving the appearance of a higher activity per unit mass of silver. These experiments are not a fully quantitative display of antimicrobial activity, which is better observed through the use of logarithmic reduction methods employed in a later section. That these materials display a clear zone of inhibition is the first step in determining antimicrobial efficacy, which evidences the suitability for further investigation.

4.2.4.2.1. Minimum bactericidal concentration

The minimum bactericidal concentration was determined by serial dilution of a solution of 1 mg/ml of MP-Ag@SiO_2 in simulated body fluid solution and dosed with a known concentration of the target organism (10^7) cultures. The samples were agitated at 37^{o}C for 24 hours, before the a sample of the solution was removed, neutralised, diluted and plated onto an agar dish and incubated at 37^{o}C overnight, in order to count the number of viable colony forming units which remained.

Figure 4.45 displays bacterial kill counts for concentrations of nanocomposites of 1, 0.1, 0.01, 0.001 and 0.0001 mg/ml.

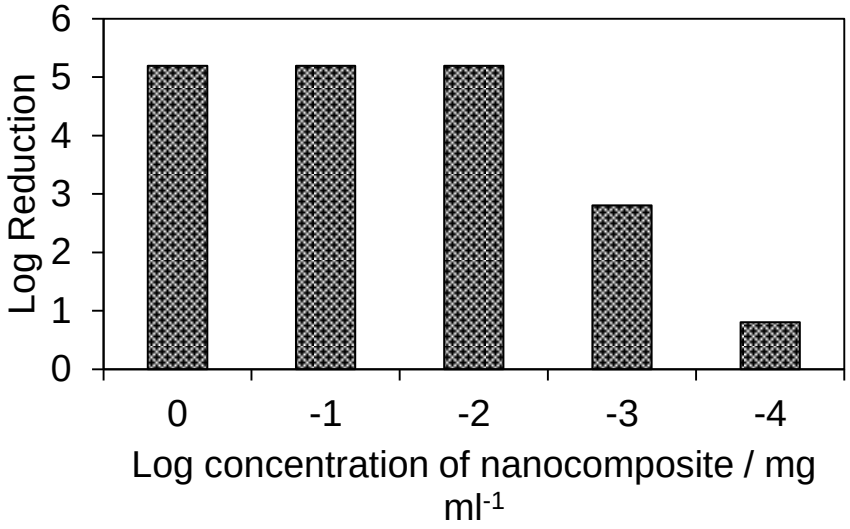

Figure 4.45: Logarithmic reductions of MP-Ag@SiO_2 nanocomposite (6.54% Ag) against *Staphylococcus aureus*.

The results of the MBC testing were that the nanocomposites material reduced the number of bacteria by a factor of at least 5 for concentrations of nanocomposites of 1, 0.1 and 0.01 mg/ml. At a concentration of 0.001 mg/ml, the logarithmic reduction was very slightly below a factor of 3, which is the requirement to be considered an antimicrobial, and it can therefore be proposed that the minimum bactericidal concentration for these materials is somewhere between 0.001 and 0.01 mg/ml.

4.2.4.2.2. Logarithmic reduction

Logarithmic reduction was performed in order to determine the killing potential of these materials as a function of time, and determine the length of time required in order to complete a log-3 reduction in the viable count of the target organism.

Into 1 ml of a known concentration of the target organism in simulated body fluid was dispersed 10 mg of the MP-Ag@SiO_2 nanocomposite materials, prior to agitation at 37^{o}C. At intervals of 30, 60, 120, 240 minutes and 24 hours, samples were taken and neutralised to stop further inhibition by the silver species. The neutralised samples were

diluted and plated onto agar dishes and incubated at 37°C overnight, to allow cultures to grow. The number of viable colonies was counted and the decrease in bacterial colony forming units calculated and plot as a logarithmic function against time.

Figure 4.46 displays the logarithmic reduction profiles for the MP-Ag@SiO_2 nanocomposites with a series of silver loadings.

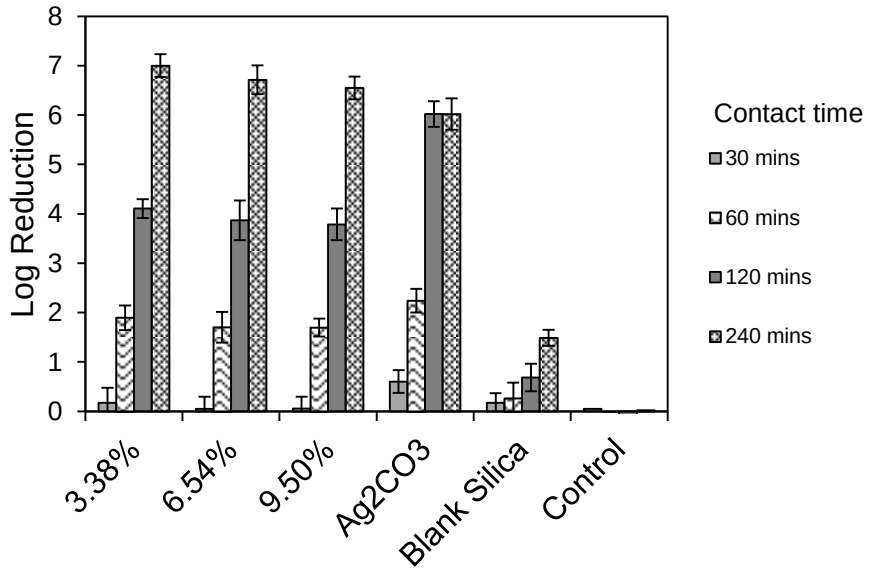

Figure 4.46: Logarithmic reduction profiles for MP-Ag@SiO_2 nanocomposites normalised to Ag weight loadings against *Staphylococcus aureus*.

It is evident from the normalised logarithmic reductions vs. *Staphylococcus aureus* that the weight loadings of the MP-Ag@SiO_2 materials bear some significance over the end result, in the form of a more effective antimicrobial material at lower concentrations, when normalised to silver content. This can be related to silver ion release, as seen in the previous section, which displayed a slight increase in effective silver release upon decreasing silver content. The materials exhibit a 3-fold log reduction for all three materials following the two hour mark, however, which would suggest that the advantage of improved performance is insignificant when balanced against the potential increase in activity lifetime attained through increased bulk loading.

A control material was prepared and studied in the form of mesoporous silica shells with no added silver (BET surface area 850 m^2/g). That this species report antimicrobial activity is attributed to surface generation of reactive oxygen species

(ROS) by the surface silica.[26] Reactive oxygen species can cause oxidative damage to DNA[27] and arises from surface silicate radicals forming hydroxide, superoxide, singlet oxygen and peroxide radicals in aqueous solution (**figure 4.47**).[28] The contribution from ROS generation within these tests is small, however it is widely reported that these species may have detrimental effects to human health, as they can be very damaging to human cells through DNA oxidation and membrane and enzyme attack, and reduction of ROS generation, if required, can be achieved using surface modifications, such as PVP adsorption, to block surface silica sites.[28]

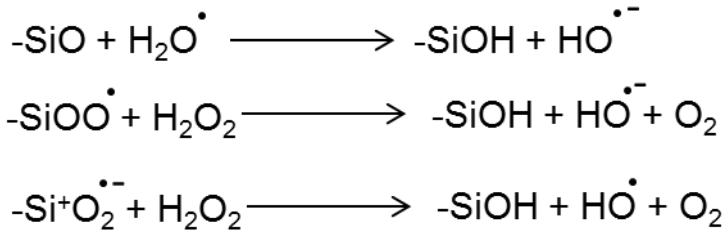

Figure 4.47: Generation of hydroxide radicals by surface silicate species.

The activity against the two microorganisms as a function of mean pore size was determined via the same method. The profile of which is displayed in **figure 4.48**.

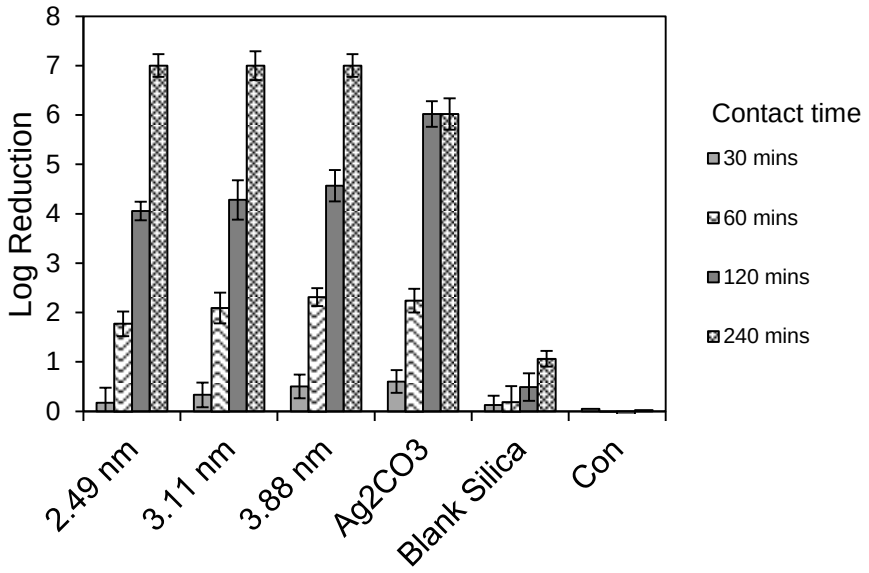

Figure 4.48: Logarithmic reduction profiles for MP-Ag@SiO_2 nanocomposites with different pore sizes normalised to Ag weight loadings against *Staphylococcus aureus*.

The larger pore sized materials display an improved activity in the 120 minute mark, once again, supporting the dissolution profiles in corroborating silver ion release with antimicrobial efficacy. There is an almost 10-fold increase in viable cell count upon increase of pore diameters to 3.88 nm, which is a considerable improvement. After 4 hours in contact with the solution of simulated body fluid and *Staphylococcus aureus*, a complete reduction of 10^7 viable cells is recorded, which represents the maximum possible reduction. This point remains constant when normalised to silver content of course, due to consistent silver loadings.

4.3. Conclusions

The materials synthesised in this chapter have been shown to be entirely silver metal nanoparticles of roughly 15-20 nm, encased within a silica shell. In order to prevent the formation of silver bromide species, a strong reducing agent in hydrazine was required, as the synthesis using alternate reducing agents such as aniline and formaldehyde could not prevent the formation of this species, despite literature suggesting this is the case.[1] Silver loading bears no effect on the resultant silver particle diameter, the silica shell diameter or the morphology of the produced materials, although the percentage of 'filled' silica shells (i.e., those present containing a silver core) increased with loading.

The structural templating agent, cetyl trimethylammonium bromide, was successfully removed by a combination of ethanol and ammonium carbonate washings, and subsequent thermal treatment. This was studied and confirmed by a combination of thermogravimetric analysis, nitrogen porosimetry, infrared spectroscopy and x-ray photoelectron spectroscopy. The procedure of removal of the organic templating agent was confirmed to not alter the structure or speciation of the silver core nanoparticles by a combination of XRD and XPS. Removal of the bromide counterions prior to heat treatment prevented the formation of silver bromide species, resulting in uniform silver metal cores.

The pore size distributions of the resultant silver-silica nanocomposites materials were found to be tuneable through the addition of mesitylene to act as a swelling agent

within the micelle region of the reaction solution. Nitrogen porosimetry provided confirmation of this increase in pore size, accompanied, however, by an increase in the overall polydispersity of the pore size distribution. The addition of mesitylene as a swelling agent bore no effect on the produced silver nanoparticle species, in either resulting dimensions, or the metal speciation. Additionally, the overall size of the nanocomposites was not affected to a significant degree by the inclusion of the auxiliary organic moieties within the synthetic procedure, confirming that the only structural or chemical change to the produced materials was the dimensions of the porous network.

The dissolution profiles for these materials indicated that the release of silver occurs very slowly, attributed to the relatively small surface areas for these particles in comparison to the previous chapter. The mesoporous silica shell allows for free transmission of the silver ions and soluble silver compounds into the surrounding media, and so whilst the normalised rates indicate that the material release a very small fraction of the bulk silver into solution, the recorded level of 'free' silver reaches approximately 2.5 ppm after 24 hours, roughly 5 times that of the core-shell materials prepared via the method in chapter 3. This increase in silver release efficiency, combined with a more cost effective synthetic procedure, outline these materials as antimicrobial additives with an extremely large potential.

When determining antimicrobial activity, the materials were subjected to zone of inhibition tests, which confirmed the antimicrobial nature of the composite particles, before a more quantitative method was involved. Performing a minimum bactericidal concentration test on the prepared composites indicated that they exhibited a high degree of antimicrobial activity in concentrations as low as 0.01-0.001 mg/ml, which amounts to approximate silver contents in the region of 1-0.03 μg/ml. It is highly likely that the extremely low concentrations reported in the MBC tests are a result of not only silver ion release, but high areas of exposed silver surface and silica surface area, leading to generation of reactive oxygen species, which in turn can cause cell degradation and death.[26] The logarithmic reduction experiments, performed as a function of time represented a similar trend to that observed by the dissolution experiments, suggesting that any antimicrobial effects as a result of surface generated ROS is consistent across the series, and differences in the time kill rates arise from the silver ionic species release rates.

These materials exhibit as great deal of potential as antimicrobial agents, as high surface areas and tuneable pore sizes are ideal for additional functionalization, either to further control silver release rates, retard ROS generation or to incorporate additional antimicrobial functionality (surface modification/coatings, secondary antimicrobials). The larger silver core particles, along with the large silver loadings possible, allow for a great pool of silver, which is released at a slow and steady rate, suggesting that the lifetime of the particles may well extend those of the current commercial dressings available on the market.

4.4. References

1. L. Han, H. Wei, B. Tu and D. Zhao, *Chemical Communications*, 2011, **47**, 8536-8538.
2. Z. Khan, S. A. Al-Thabaiti, E. El-Mossalamy and A. Y. Obaid, *Colloids and Surfaces B: Biointerfaces*, 2009, **73**, 284-288.
3. L. K. Patterson and E. Vieil, *The Journal of Physical Chemistry*, 1973, **77**, 1191-1192.
4. Q. Cai, Z.-S. Luo, W.-Q. Pang, Y.-W. Fan, X.-H. Chen and F.-Z. Cui, *Chemistry of Materials*, 2001, **13**, 258-263.
5. J. Yang, H. Yin, J. Jia and Y. Wei, *Langmuir*, 2011, **28**, 5047-5053.
6. T. Li, J. Moon, A. A. Morrone, J. J. Mecholsky, D. R. Talham and J. H. Adair, *Langmuir : the ACS journal of surfaces and colloids*, 1999, **15**, 4328-4334.
7. X.-H. Liu, X.-H. Luo, S.-X. Lu, J.-C. Zhang and W.-L. Cao, *Journal of colloid and interface science*, 2007, **307**, 94-100.
8. X.-Y. Gao, S.-Y. Wang, J. Li, Y.-X. Zheng, R.-J. Zhang, P. Zhou, Y.-M. Yang and L.-Y. Chen, *Thin Solid Films*, 2004, **455–456**, 438-442.
9. L. Han, H. Wei, B. Tu and D. Y. Zhao, *Chemical Communications*, 2011, **47**, 8536-8538.
10. H. W. Lu, S. H. Liu, X. L. Wang, X. F. Qian, J. Yin and Z. K. Zhu, *Materials Chemistry and Physics*, 2003, **81**, 104-107.
11. V. K. Aswal and P. S. Goyal, *Physical Review E*, 2000, **61**, 2947-2953.
12. K. Kuperkar, L. Abezgauz, D. Danino, G. Verma, P. A. Hassan, V. K. Aswal, D. Varade and P. Bahadur, *Journal of Colloid and Interface Science*, 2008, **323**, 403-409.

13. J. W. Larsen and L. J. Magid, *Journal of the American Chemical Society*, 1974, **96**, 5774-5782.

14. C. D. Wagner, A. V. Naumkin, A. Kraut-Vass, J. W. Allison, C. J. Powell and J. R. Rumble Jr, *NIST XPS (Web Version)*, 2003, **3**.

15. Y. H. Kim, D. K. Lee, H. G. Cha, C. W. Kim and Y. S. Kang, *The Journal of Physical Chemistry C*, 2007, **111**, 3629-3635.

16. P. Horcajada, A. Rámila, J. Pérez-Pariente, R. Vallet, amp, x and M., *Microporous and Mesoporous Materials*, 2004, **68**, 105-109.

17. A. Corma, Q. Kan, M. T. Navarro, J. Pérez-Pariente and F. Rey, *Chemistry of Materials*, 1997, **9**, 2123-2126.

18. M. V. Landau, E. Dafa, M. L. Kaliya, T. Sen and M. Herskowitz, *Microporous and Mesoporous Materials*, 2001, **49**, 65-81.

19. A. Galarneau, H. Cambon, F. Di Renzo and F. Fajula, *Langmuir : the ACS journal of surfaces and colloids*, 2001, **17**, 8328-8335.

20. J. S. Beck, J. C. Vartuli, W. J. Roth, M. E. Leonowicz, C. T. Kresge, K. D. Schmitt, C. T. W. Chu, D. H. Olson and E. W. Sheppard, *Journal of the American Chemical Society*, 1992, **114**, 10834-10843.

21. R. Schmidt, E. W. Hansen, M. Stoecker, D. Akporiaye and O. H. Ellestad, *Journal of the American Chemical Society*, 1995, **117**, 4049-4056.

22. D. Zhao, Q. Huo, J. Feng, B. F. Chmelka and G. D. Stucky, *Journal of the American Chemical Society*, 1998, **120**, 6024-6036.

23. Nist XPS Database, 1997, http://srdata.nist.gov/xps/.

24. Y.-J. Lee, J. Kim, J. Oh, S. Bae, S. Lee, I. S. Hong and S.-H. Kim, *Environmental Toxicology and Chemistry*, 2012, **31**, 155-159.

25. W. Zhang, Y. Yao, N. Sullivan and Y. Chen, *Environmental Science & Technology*, 2011, **45**, 4422-4428.

26. C. Carlson, S. Hussain, A. Schrand, L. K. Braydich-Stolle, K. Hess, R. Jones and J. Schlager, *The Journal of Physical Chemistry B*, 2008, **112**, 13608-13619.

27. C. Gong, G. Tao, L. Yang, J. Liu, H. He and Z. Zhuang, *Mol Biol Rep*, 2012, **39**, 4915-4925.

28. B. Fubini and A. Hubbard, *Free Radical Biology and Medicine*, 2003, **34**, 1507-1516.

Chapter 5: Titania Grafted Mesoporous Silica Materials

5.1 Introduction

Chapters 3 and 4 have shown the strong antibacterial function exhibited by silver nanocomposites devices. Ag potency is linked with dispersion, which has been shown in previous studies by Buckley *et al.*[1, 2] Utilisation of chemical reduction methods involving reverse micelles and surfactant stabilisers have been shown to provide silver nanoparticles of small size and low polydispersity. Another method to increase Ag dispersity is through the use of porous support materials. Mesoporous silicas, whilst biologically inert[3] can be used to impart this high degree of dispersity of silver nanoparticles. Furthermore, implementing a surface coating which can itself impart antibacterial functionality may lead to an effective dual-acting material.

Mesoporous silicas are a well understood and versatile material, for which advances in control over their pore structure and surface properties[4] have made them an ideal choice as supports for metal nanoparticles for a variety of applications, including catalytic materials,[5-7] vessels for photocatalytic processes[8-10] and drug delivery systems.[11-13] Further to this, the added ability of surface functionalization lends them even more numerous and exciting applications such as carbon capture,[14] drug delivery systems[15] and acid catalysis.[16]

Wet impregnation of porous supports with silver nitrate is a facile process for the deposition of silver nanoparticles which readily form upon thermal decomposition of the salt precursor occurs at 444 ^{o}C. Unlike many other transition metals this approach forms silver metal particles directly due to the low decomposition temperatures of silver oxide and carbonate salts. The fact this method does not rely on sophisticated chemical systems may render it more attractive for mass production in wound dressings, with loading used to control particle size and associated dissolution and antibacterial action.

Mesoporous titania supported silver has proven a useful combination in the generation of photocatalytically activated antibacterial additives and coatings,[17, 18] attributed to the synergistic effect of silver nanoparticles stabilising electron core-hole species generated from photo-excitation of electrons across the bandgap of the semiconducting TiO_2 support.[19] It is this effect, plus the intrinsic antibacterial nature of

the silver ion releasing particles which suggests potential in these nano-composite materials.

Silver and titania nanocomposites have been shown to promote bacterial cell death previously, however studies into these material have been limited to either thin film growth methods,[20, 21] which are unsuitable for these applications, materials with low surface areas[22] or complicated synthetic routes[23]. Titania has been shown to exhibit antibacterial activity in a similar manner to its photocatalytic activity. As a semiconductor, it can excite electrons across the band gap from the valence band into the conduction band, which leaves a free electron in the conduction band and electron-hole in the valence band. This system can cause oxidation of Coenzyme-A, inhibiting cell respiration and causing cell death.[24]

It is hypothesised that combining a high surface area support material in the form of mesoporous SBA-15 with a surface coating of titania will allow for a high surface area support which can provide silver nanoparticles of high dispersity, important due to the effect of increased antibacterial performance as a function of silver particle size. Furthermore, such composites may provide a secondary antibacterial functionality, resulting in a more potent, dual functioning material. Introducing macroporosity into the support material is thought to overcome potential issues regarding diffusion. A hierarchical support increases the accessibility of the mesopore network, which is hoped to further increase dispersity and external surface area, increasing the proportion of titania available for processes responsible for antibacterial activity.

5.2. Results and discussion

The synthesis of mesoporous and hierarchical macro-mesoporous SBA-15, along with the TiO_2 grafted analogues and subsequent preparation of silver loaded materials is described in **section 2.3**. This chapter will discuss the characterisation and performance assessments including dissolution rates and antibacterial assaying of these materials.

5.2.1. Synthesis and characterisation

The successful synthesis of SBA-15 based support materials, nature of grafted of titania films and nature of deposited silver nanoparticles was characterised by a range of analytical techniques including transmission electron microscopy analysis, to determine material morphology and pore arrangement, x-ray diffraction to detect the presence of ordered pore structures and quantify pore-spacing as well as determine bulk crystalline phases. X-ray photoelectron spectroscopy was employed to study surface elemental composition and determine present oxidation states. Nitrogen adsorption porosimetry was used to probe the material textural properties and analyse pore structures.

5.2.1.1. SBA-15

SBA-15 is a mesostructured, ordered silica material which has found many applications in fields such as catalysis[25-28], drug delivery,[15, 29], ion-exchange[30] and CO_2 capture[31] owing to its high surface area and mesopores of monodisperse diameter. The synthesis of this material is widely known and understood[32-34] and the properties readily controlled by adjustments of synthetic parameters,[4] rendering it a useful and popular support material.

SBA-15 is prepared using the non-ionic triblock polymer Pluronic 123 ($HO(CH_2CH_2O)_{20}(CH_2CH(CH_3)O)_{70}(CH_2CH_2O)_{20}H$ in water (2.6 wt. %, cmc = 0.03 wt. % at room temperature)[35] and HCl, which, upon addition of alkoxy silicate precursor, forms cationic hydrolysed silicate oligomers which associate with the PEO chains via hydrogen bonding and electrostatic interactions (**Figure 5.1**).[36]

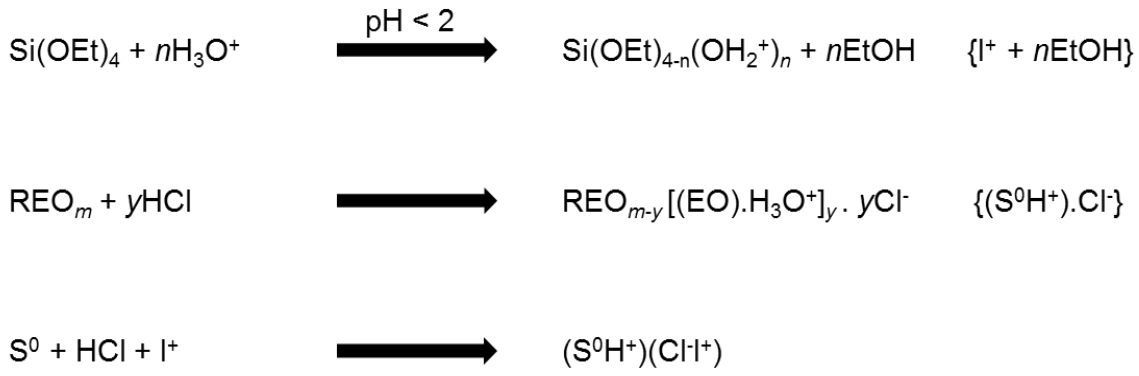

Figure 5.1: Hydrolysis and association to PEO chains of alkoxy silicate species.

Following this hydrolysis and association, the spherical P123 micelles become more rod-like with increasing silicate network condensation, before flocculation and precipitation occurs, forming hexagonally packed aggregates of self-assembled silicate micelles.[32] Removal of the organic template by calcination in air (500 ºC for 6 hours), introduces hexagonally arranged mesopores with *p6mm* symmetry, as well as microporosity within the pore-walls, due to removal of PEO chains, around which silicate species condense (**Figure 5.2**).[33, 34]

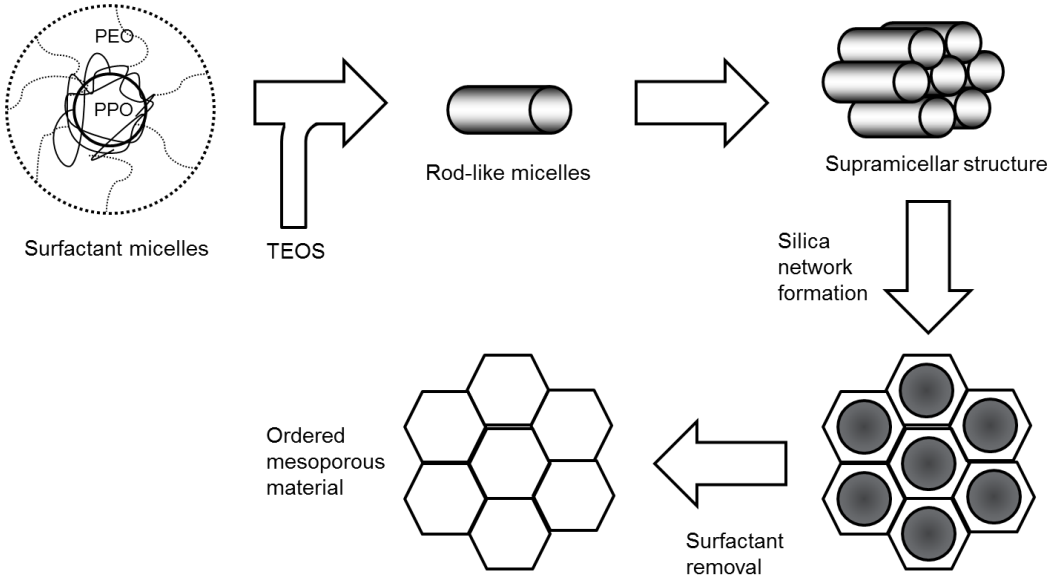

Figure 5.2: Schematic of SBA-15 formation.

To confirm the hexagonal arrangement of the ordered mesopores, low angle XRD was employed. At angles in the region of 2θ = 1º, the diffraction patterns from ordered mesostructures can be observed, allowing for determination of the arrangements of the pores and measurement of the d-spacing between channels (**Figure 5.3**).

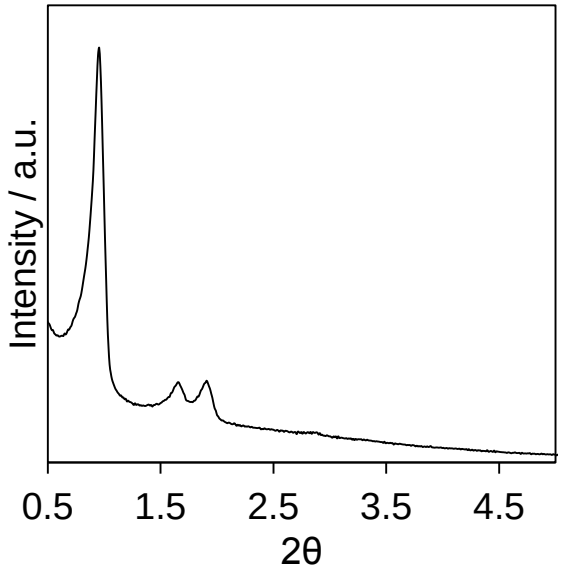

Figure 5.3: Low angle XRD pattern of parent SBA-15.

The peaks at 0.95º, 1.65º and 1.9º correspond to the 100, 111 and 200 planes in the hexagonally symmetrical structure, which has a space group of p6mm. The peak at 100 is used to determine the d-spacing, calculated at 9.24 nm, using Bragg's law (**equation 2.5**).

Using **equation 4.2**, the d-spacing value can be used to calculate the distance between the centres of the pores. A d-spacing of 9.24 nm gives an inter-pore distance of 10.67 nm.

This structure was further confirmed by transmission electron microscopy, which allows for direct observation of the hexagonal framework and long range order of the pore channels (**Figure 5.4**).

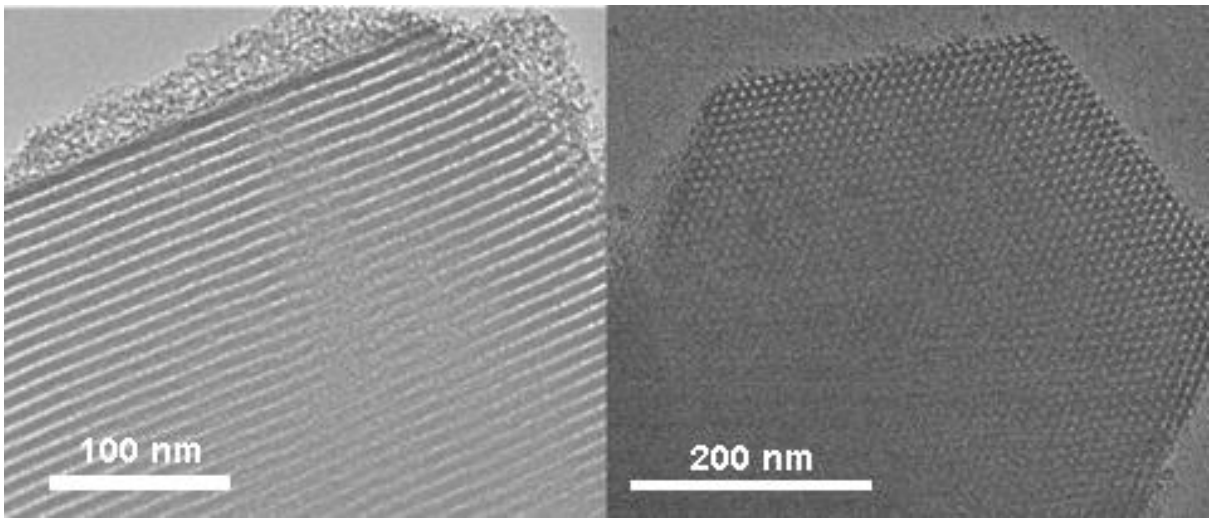

Figure 5.4: TEM images of synthesised SBA-15.

To confirm the high surface area of these materials and determine mesopore size, isotherms were obtained using nitrogen porosimetry (**Figure 5.5**).

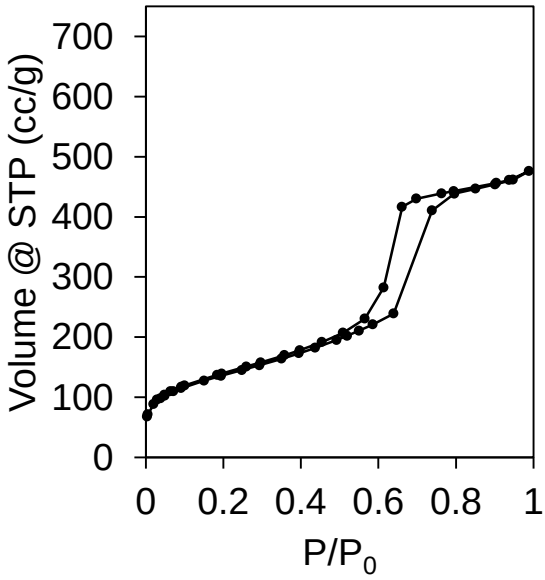

Figure 5.5: Nitrogen adsorption isotherm of synthesised SBA-15.

The adsorption isotherm exhibits a type IV profile with a H1 type hysteresis loop, which are characteristic of mesoporous materials. This feature is the result of the capillary condensation mechanism of filling and emptying pores in the mesopore region.[37] The material exhibited a typically high surface area associated with SBA-15, measured at 830 m^2/g by BET analysis.

Characterisation of the mesopore size range can be achieved applying the BJH method to the adsorption isotherm (**Figure 5.6**), as described in **section 2.6.4**.

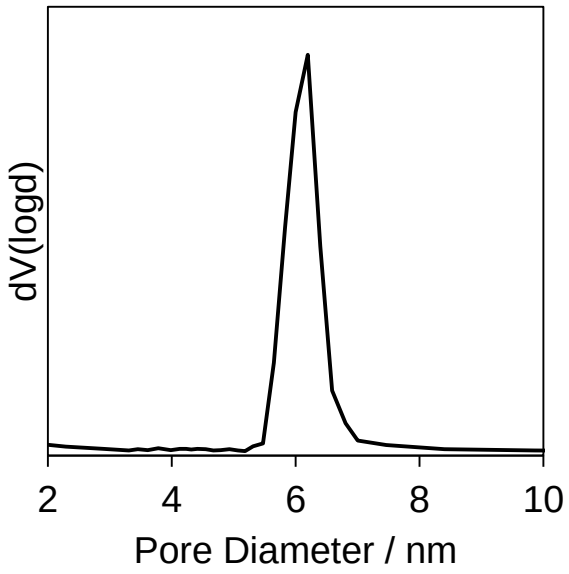

Figure 5.6: BJH profile of synthesised SBA-15.

The BJH profile reports a pore diameter of 6.2 nm, which is consistent with previously reported dimensions for SBA-15 aged at this temperature.[26] A full summary of the properties of the prepared SBA-15 is presented in **table 5.1**.

Material	Surface Area / m^2 g^{-1}	Micropore Surface Area / m^2 g^{-1}	Pore Diameter / nm	Pore Spacing (XRD) / nm	Pore Spacing (TEM) / nm	Wall Thickness / nm
SBA-15	830	292	6.2	10.67	10.4	4.3 ± 0.1

Table 5.1: Summary of properties of synthesised SBA-15.

5.2.1.2. Silver loaded SBA-15

Silver was introduced to these materials using the incipient wetness methodology outlined in **section 2.3.5**, covering a range of weight loadings from 0.5% to 10% nominal loading.

Four different loadings of silver on SBA-15 were prepared and the bulk silver content was measured using EDAX analysis, while the silver surface loadings were measured by XPS. This was compared with the surface silver loadings, shown in **Table 5.2**.

Nominal Ag loading / wt%	Bulk Loading / wt%	Surface loading / wt%
0.5	0.3	0.45
1	0.95	0.56
5	2.4	1.32
10	3.5	2.45

Table 5.2: Bulk and surface silver wt% values, determined by EDAX and XPS.

The bulk analysis reported lower value than the nominal loadings, suggesting that much of the silver was being lost during the impregnation procedure. Some silver is lost due to silver mirroring of the reaction vessel, which could be the reason behind the lower recorded bulk loadings, exacerbated at higher loadings.

The surface-to-bulk loadings are displayed in **figure 5.7**. The surface loading is higher for the lower total loadings, which is potentially suggestive of smaller silver particles covering the surface, which will be more visible by the surface sensitive XPS analysis, due to signal attenuation of silver photoelectrons throughout larger nanoparticles.

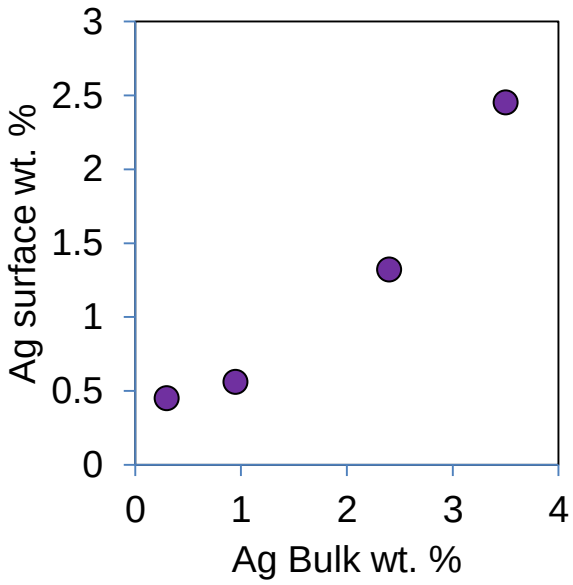

Figure 5.7: Ag surface:bulk wt. %

The surface silver content determined by XPS is observed to be lower than the bulk for the higher loadings suggesting that the majority is contained inside the pores of the SBA-15 material, and hence cannot be observed by XPS analysis. Alternatively, large agglomerates on the surface of the SBA-15 material would give rise to lower

silver signals, and a combination of these two effects could reduce the recorded surface silver loadings.

TEM analyses were employed to obtain an accurate measure of silver particle size and thus dispersion. **Figure 5.8** shows an example of silver particles supported on the SBA-15 support, with an inset exhibiting the lattice fringes of the observed nanoparticles, which was measured to be 2.4 Å; consistent with the fcc Ag (111) facet.

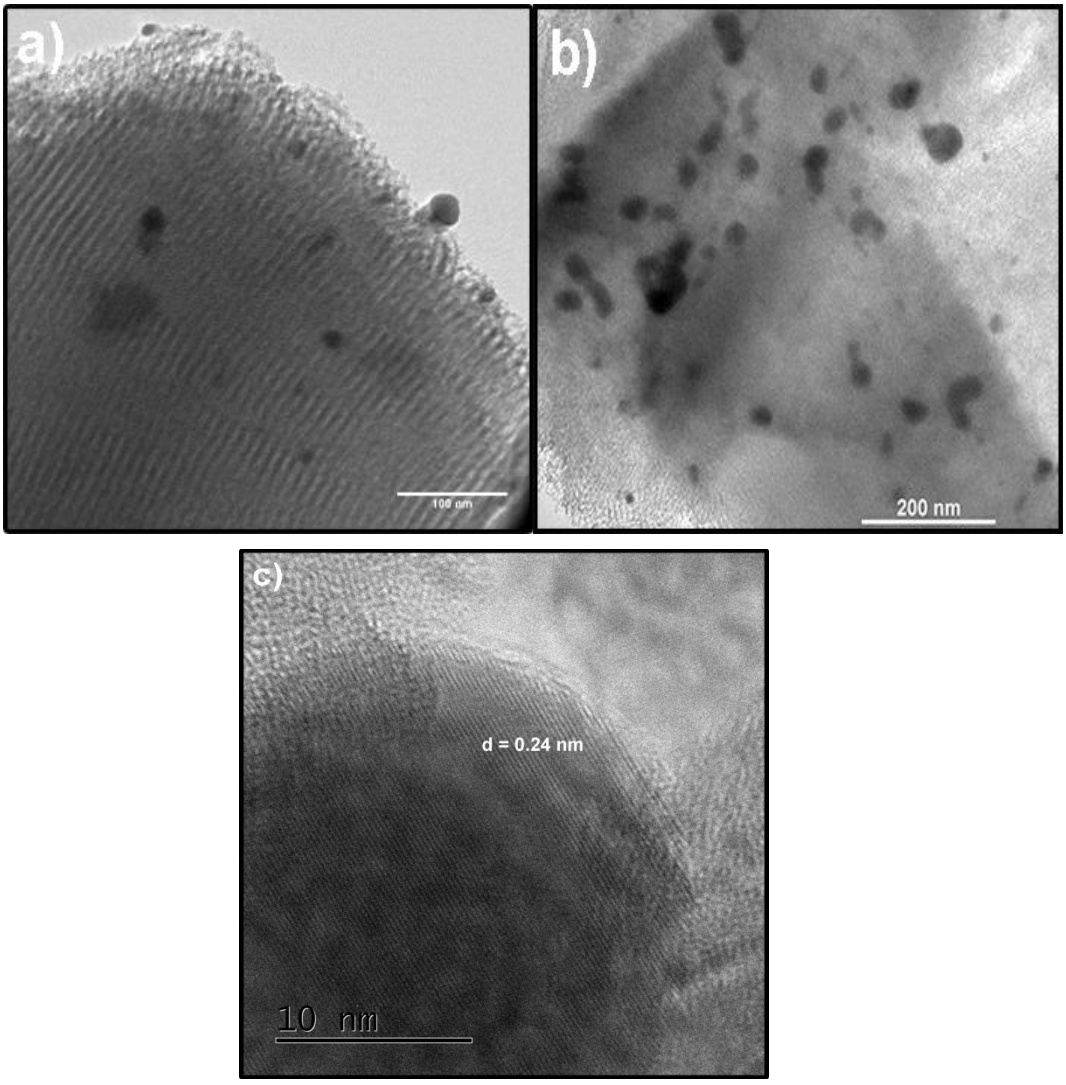

Figure 5.8: Bright field TEM image of Ag- SBA-15 for (a) 0.3% Ag, (b) 3.7% Ag and (c) HR image of Ag nanoparticle (3.5% Ag).

The bright field TEM images were analysed using ImageJ software to obtain a particle size distribution for the silver loaded materials. The compiled distribution histograms and associated statistical distributions are shown in **figure 5.9**. The

monodispersity of these materials is fairly low, with silver particle sizes ranging from very small (5 nm), to larger agglomerates on the surface of the materials.

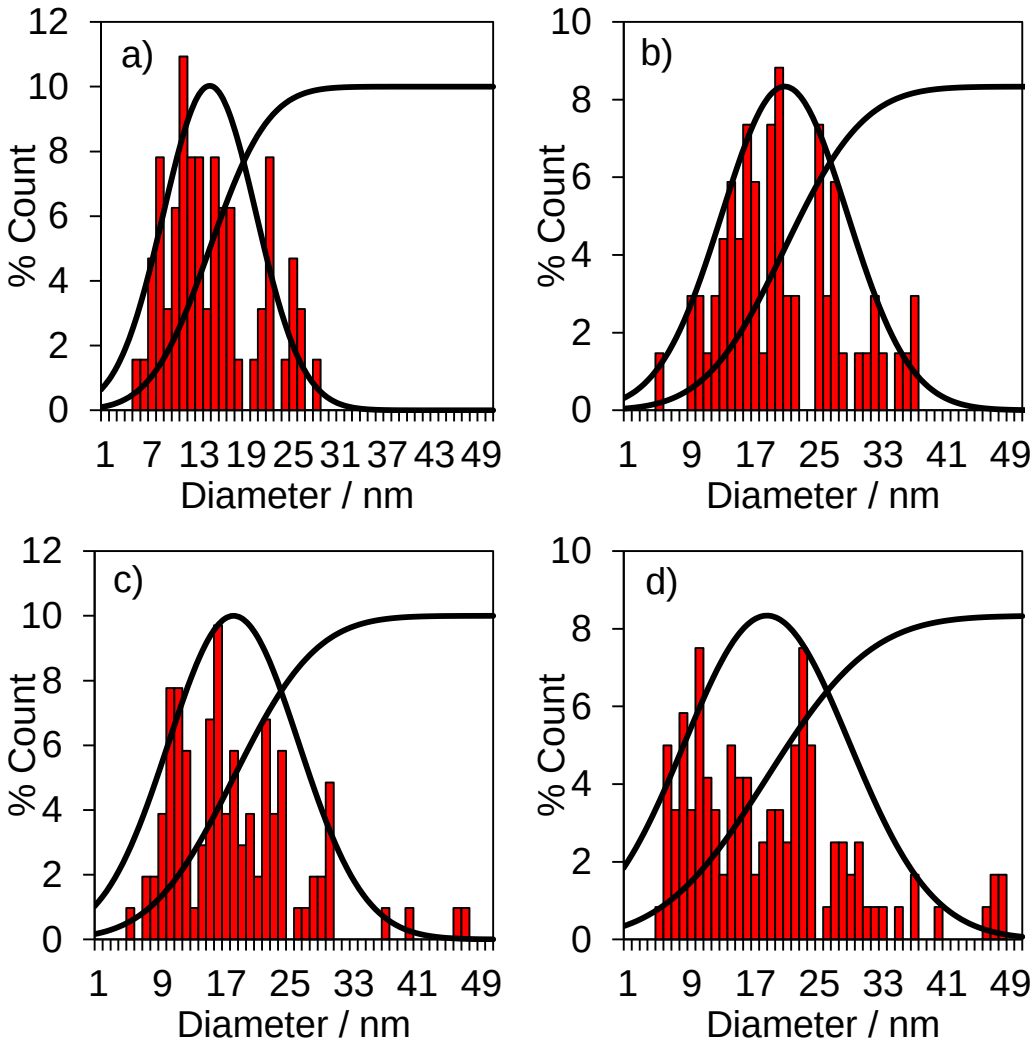

Figure 5.9: Silver nanoparticle size distributions, normal and cumulative statistical distributions for (a) 0.3%, (b) 0.95%, (c) 2.4% and (d) 3.5% Ag on SBA-15, based on counts of >100 particles in all cases.

These particle size distributions are summarised in **figure 5.10**, which reports a minor increase in average particle size, as loading increases, but with increasing dispersities along the series.

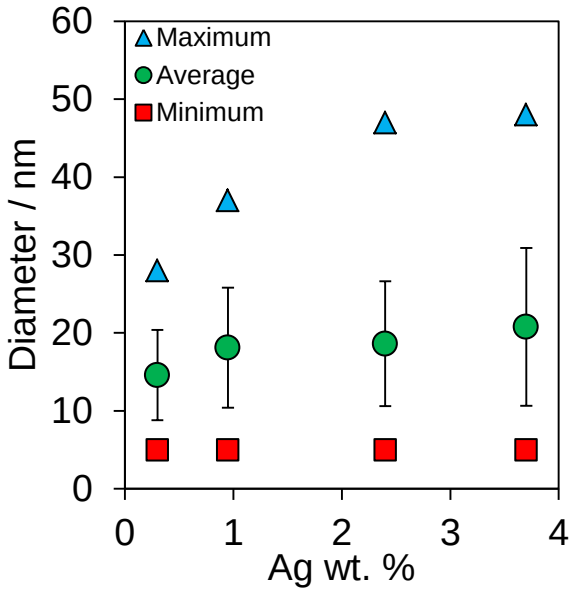

Figure 5.10: Summary of silver nanoparticle size distributions from TEM data for Ag-SBA-15. Error bars from standard deviation of all particle diameters.

X-ray diffraction was used to determine that the support structure maintained its hexagonally structured pore system, determine bulk silver phase and determine average particle size.

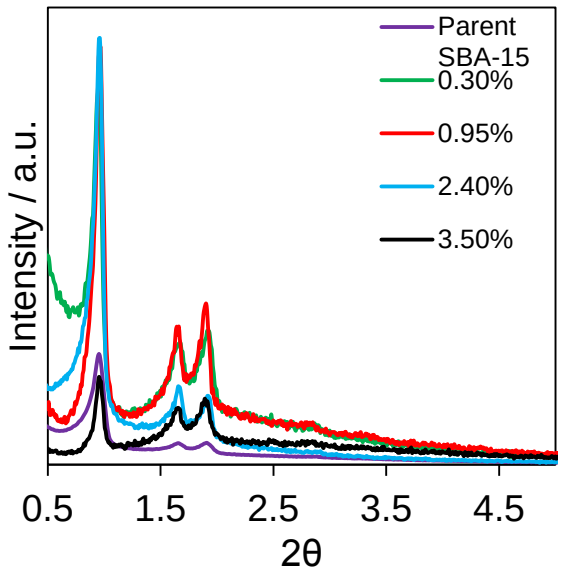

Figure 5.11: Low angle XRD patterns for Ag-SBA-15.

Figure 5.11 displays the low angle XRD patterns for the silver loaded materials, confirming that no structural changes occur during the silver doping process and the p6mm hexagonal symmetry is retained, as well as the inter-pore spacing. The d-spacings are calculated using the Bragg law, and from this, the pore spacings are calculated, using **equation 4.2**. The calculated pore spacings are displayed in **figure 5.12**, and it is clear that these are unchanged from ~10.7 nm as silver loading is increased, as silver loading bears no effect on the pore architecture.

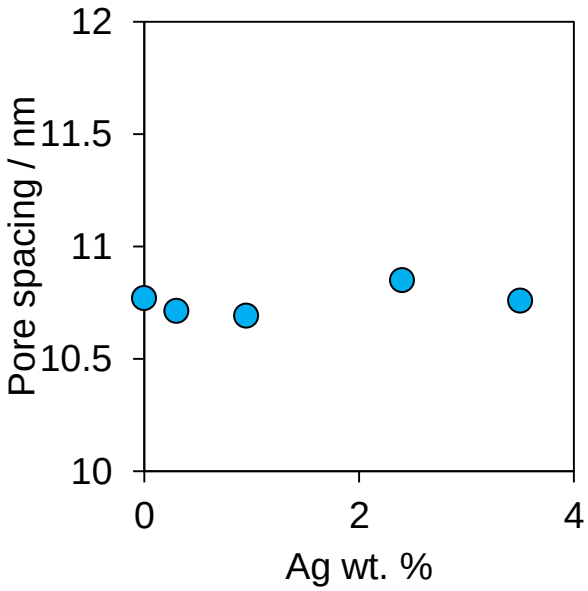

Figure 5.12: Calculated pore spacings from low angle XRD analysis for Ag-SBA-15.

The silver loaded mesoporous silica materials were also studied by wide angle powder XRD, to determine silver phases present in the synthesised composites.

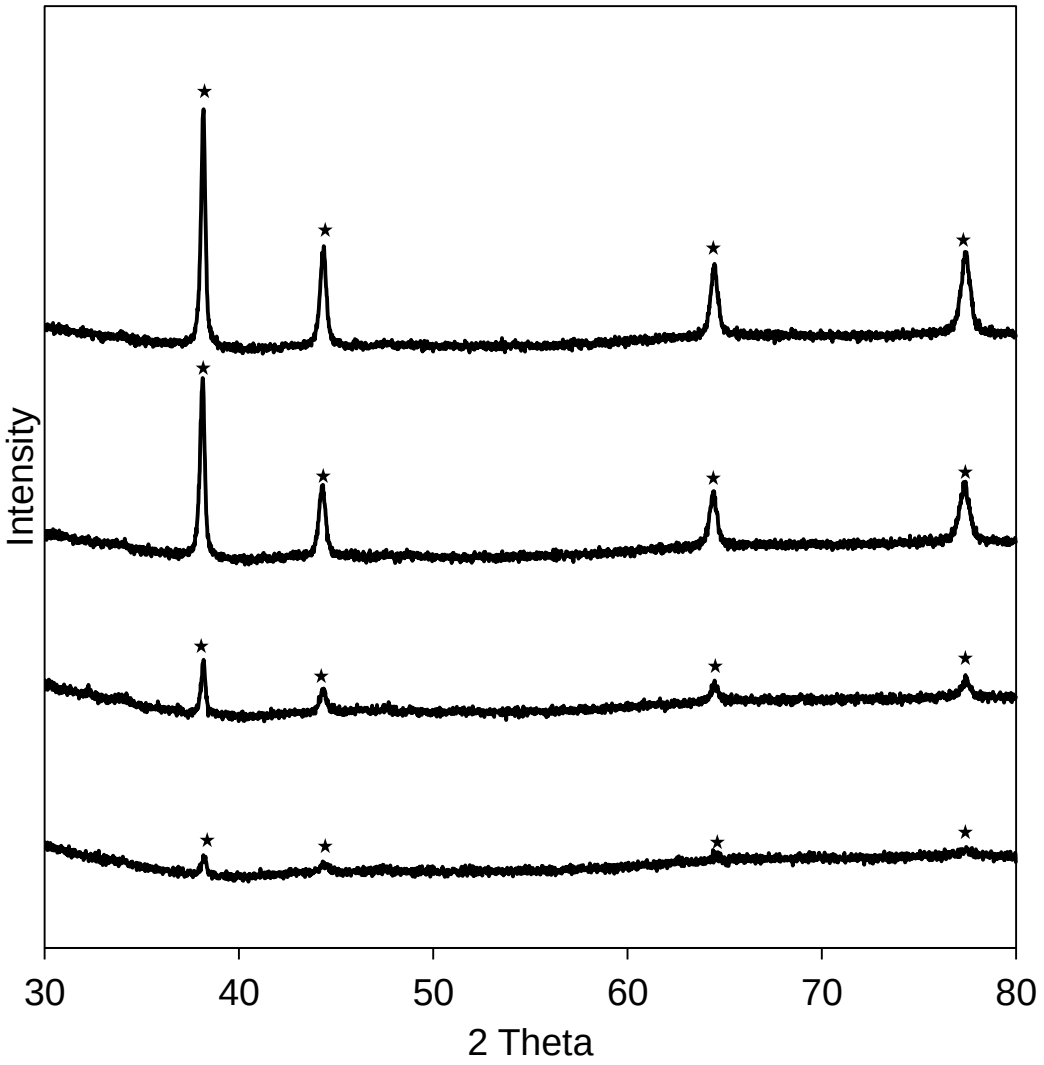

Figure 5.13: Wide angle XRD patterns of silver loaded SBA-15. (*) indicate FCC Ag^0 reflections.

Figure 5.13 shows the XRD patterns over the range 30 to 80°, which shows 4 peaks at 38.1, 44.2, 64.5 and 77.2°, which are consistent with metallic Ag.[38] No reflections were observable for other silver species such as AgO, Ag_2O or carbonates (refer to **chapter 3**, **section 3.2.1**).[39, 40] Using the Scherrer equation (**equation 2.11**), an average particle size can be obtained from the 111 and 200 peaks, which is displayed in **figure 5.14**. The average particle size reported is larger from XRD analysis than that from TEM, although the trend followed is consistent. This could be due to TEM size analysis being a more localised technique, in which areas of large silver nanoparticles may be missed, affecting the calculated average particle size.

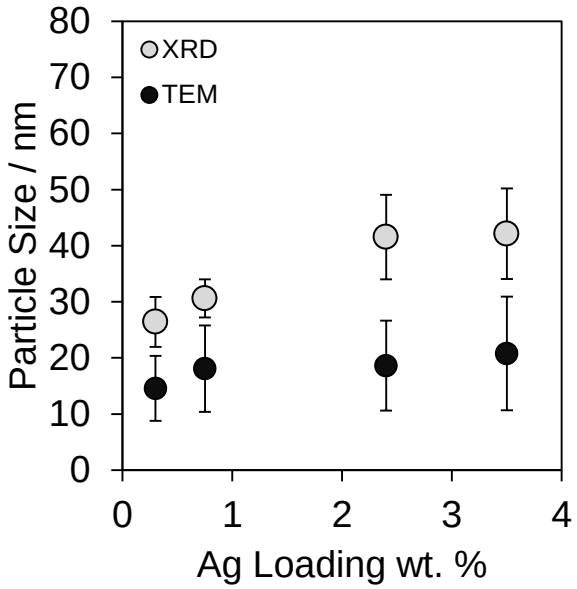

Figure 5.14: Particle sizes determined by XRD and TEM analysis.

Nitrogen porosimetry was performed on these materials to reveal the the effect of silver loading on effective surface areas and pore dimensions, for which adsorption isotherms are displayed in **Figure 5.15**.

From the isotherms, it can be seen that the type IV character and hysteresis loop associated with mesoporous structures is retained, further evidence that the underlying silica structure is unaffected by the silver loading process.

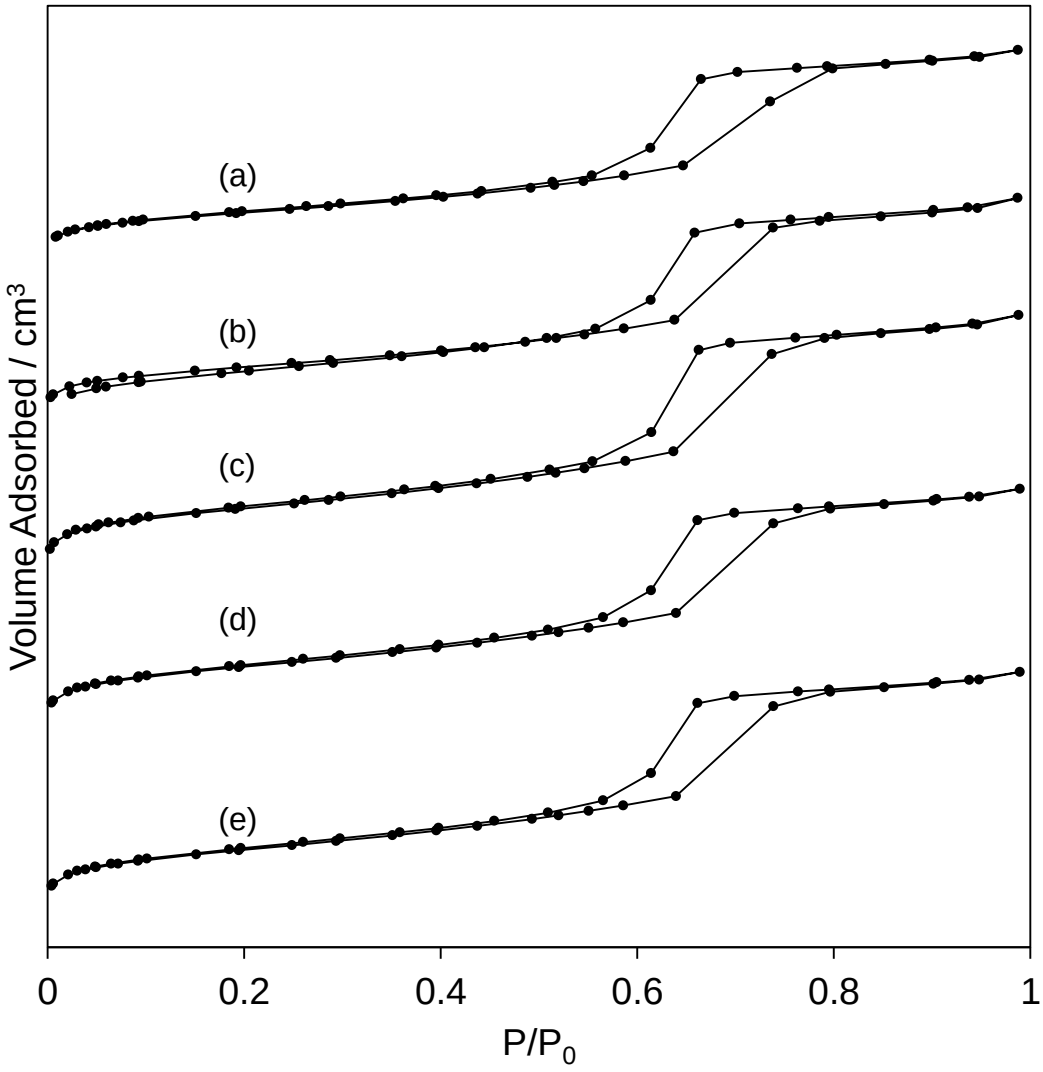

Figure 5.15: Nitrogen adsorption isotherms for silver loaded SBA-15 for (a) 3.5%, (b) 2.4%, (c) 0.95%, (d) 0.3% and (e) 0% Ag loadings.

Looking at the specific surface areas (**Figure 5.16**), however, there is a clear decrease in surface area with silver loading. This could be due to pore blocking by silver nanoparticles reducing the available silica surface, both in the meso- and micro-pore regions. Micropore surface area was calculated using the t-plot method, whilst mesopore surface area was calculated via the BJH method.

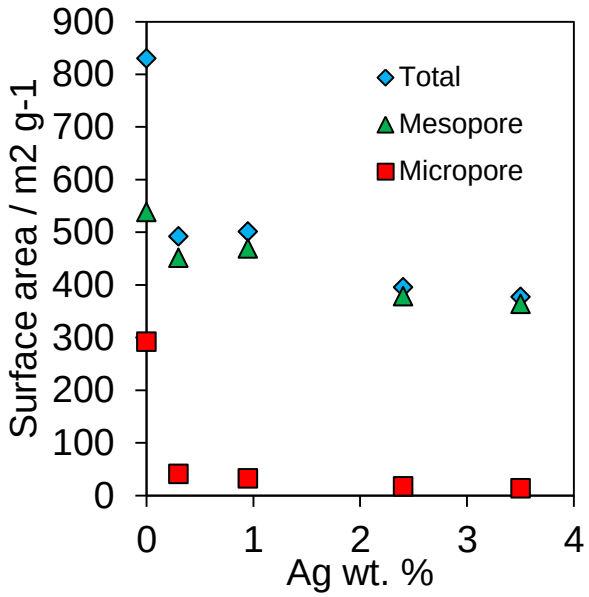

Figure 5.16: Specific surface areas and micropore surface areas from BET, BJH and t-plot analysis of silver loaded SBA-15.

There is a marked decrease in micropore surface area among the silver loaded SBA-15 materials, which appears to have the greatest impact upon total surface area decrease. This suggests that the impregnated silver exists in part within the micropores of the silica support, which has been evidenced in literature regarding metal particle formation within micropore networks.[41, 42]

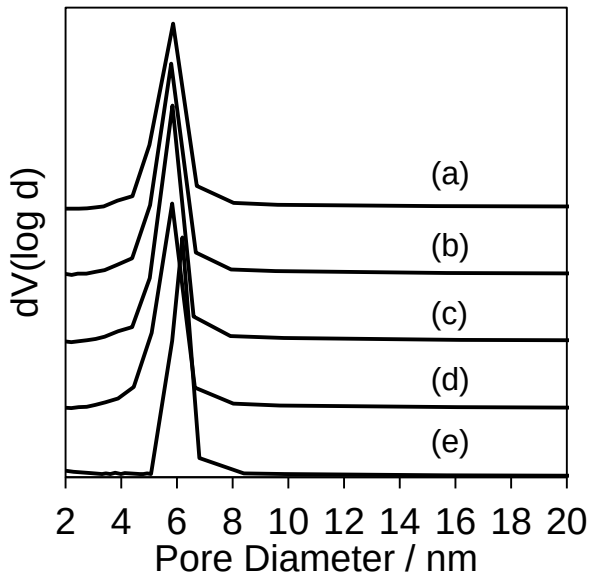

Figure 5.17: BJH profiles for (a) 3.5%, (b) 2.4%, (c) 0.95%, (d) 0.3% Ag and (e) parent SBA-15.

Figure 5.17 reports the BJH profiles created through analysis of the nitrogen adsorption isotherms, which confirms the mean mesopore diameters do not change as a result of silver loading.

XPS was employed to probe the silver species on the surface of the SBA-15 and determine any change in oxidation state as a function of Ag loading, the loadings of which are displayed in **table 5.3**.

Sample	Ag%	Si%	O%	C%
Parent	0	40.69	56.26	3.05
0.3% Ag	0.45	41.17	56.79	1.59
0.95% Ag	0.56	40.57	57.13	1.74
2.4% Ag	1.32	40.56	56.66	1.46
3.5% Ag	2.45	39.76	56.5	1.29

Table 5.3

Figure 5.18 displays the Ag 3d region of the 4 metal loadings, which shows the characteristic $3d_{5/2}$ and $3d_{3/2}$ doublets, having peak area ratios of 3:2 and a doublet separation of 6 eV.[43]

The Ag 3d regions indicate the presence of a single silver species, with a binding energy of 368.2 eV, and a doublet separation of 6 eV, consistent with that of silver (0) metal.[44]

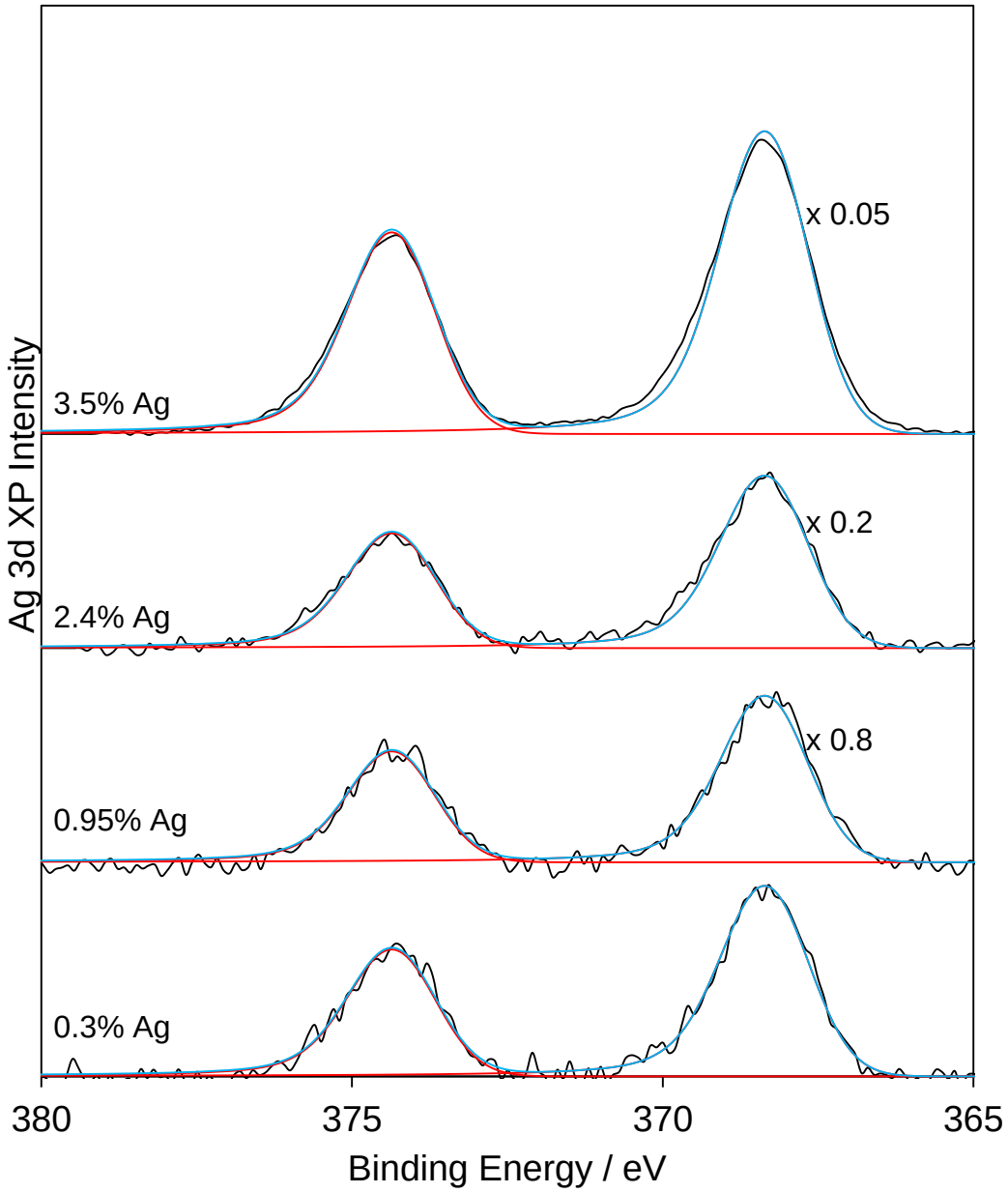

Figure 5.18: Ag 3d XPS stack plot of Ag-SBA-15. Black lines – raw data, red – Ag^0, blue – Ag_2O, green – envelope fit. Scaled to aid presentation.

The Si 2p regions shown in (**figure 5.19**) were fit with 2 peaks for the $2p_{3/2}$ and $2p_{1/2}$ contributions, and a doublet separation of 0.6 eV.[43]

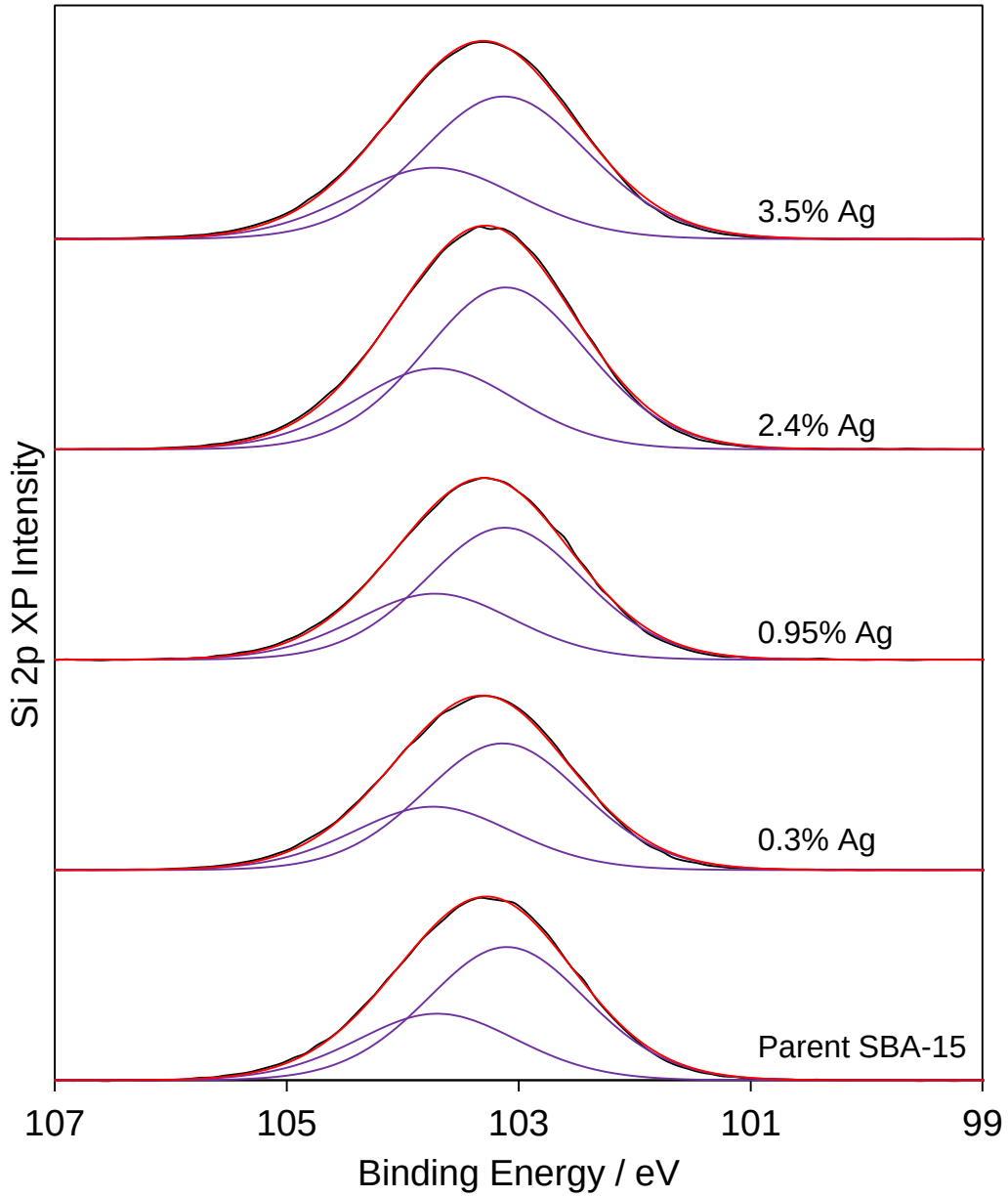

Figure 5.19: Si 2p XPS stack plot of Ag-SBA-15.

The silica supports remains unperturbed by the addition of silver species to the material, which is evident in the 2p regions studied by XPS. The position at 103.3 eV confirms the silica species is SiO_2. There is no evidence in these spectra for additional silicon species.

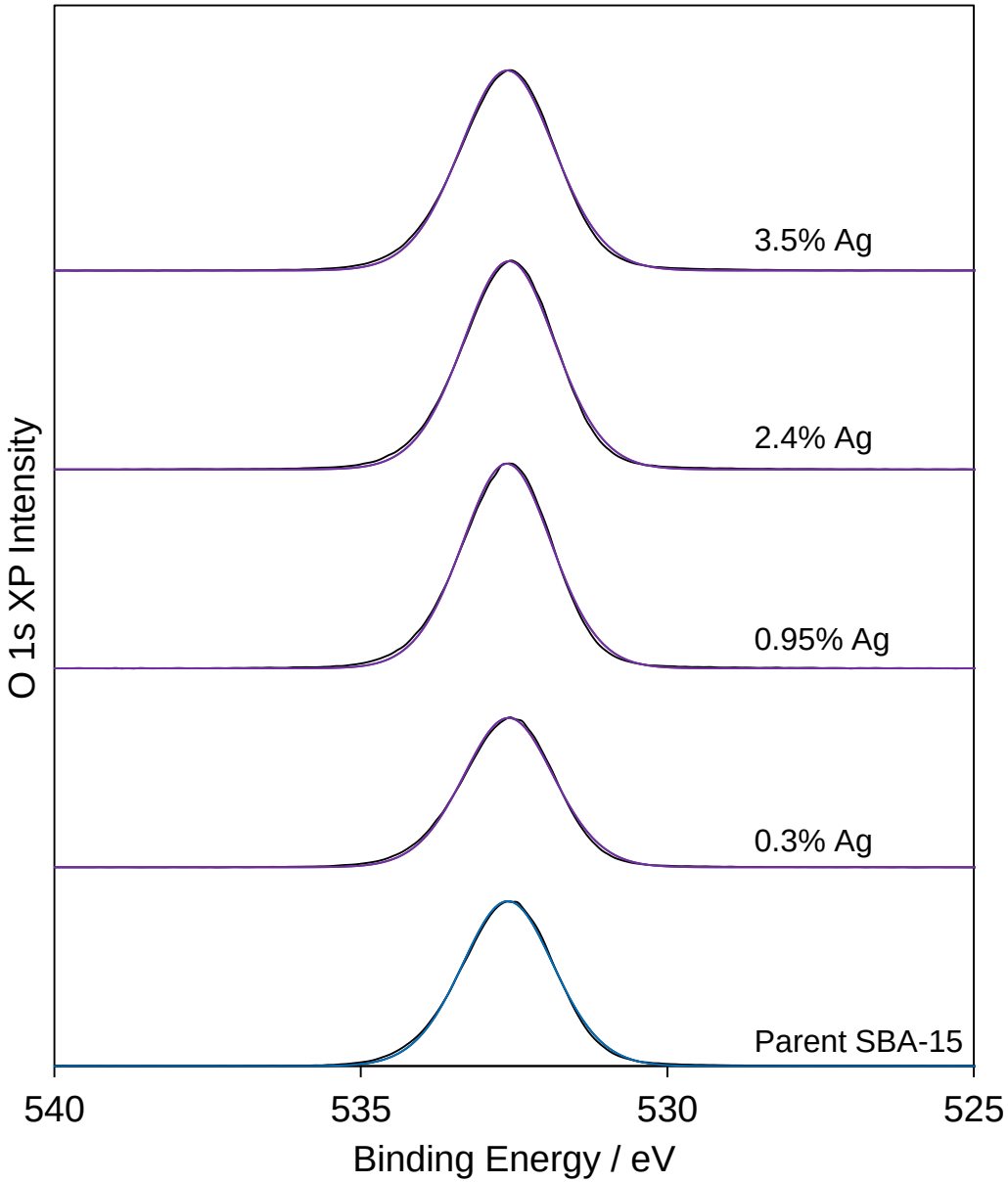

Figure 5.20: O 1s XPS stack plot of Ag-SBA-15.

Figure 5.20 displays the O 1s regions of Ag-SBA-15 which exhibits a singular peak at 533.3 eV, consistent with the binding energy of oxygen species in silica frameworks. No additional oxygen species are evident within the XPS spectra.

5.2.1.3. Titania grafted SBA-15

The grafting procedure of titania onto mesostructured silica was performed using a modified procedure by Landau *et al* and is described in **section 2.3.4**.[45] This involved using a titanium (IV) alkoxyl precursor under anhydrous conditions to hydrolyse and condense with surface silanol species, activated by the addition of a tertiary amine base (triethylamine). The hydrolysis/condensation step is an S_N2 reaction involving surface hydroxyls and the titanium (IV) metal centre, during which a molecule of alcohol is removed (**figure 5.21**).

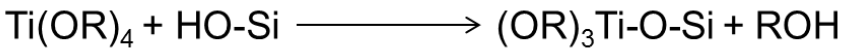

Figure 5.21: Hydrolysis/condensation of titanium alkoxide precursor with silanol species.

Confirmation of incorporation of titania upon the silica was obtained via bulk elemental analysis in the form of EDX, the results of which are summarised in **table 5.4**.

	Ti wt. %	Si wt. %	O wt. %
Bulk	8.3	39.2	53.5
Surface	11.65	35.7	52.65

Table 5.4: Elemental composition of titania grafted SBA-15 (3 cycles) from EDX analysis.

To ensure that more than a monolayer of titania was formed, the grafting procedure was performed three times, producing a layer of titania. The phase was, however, not identifiable by powder XRD, due to the ultrathin nature being undetectable (**Figure 5.22**).

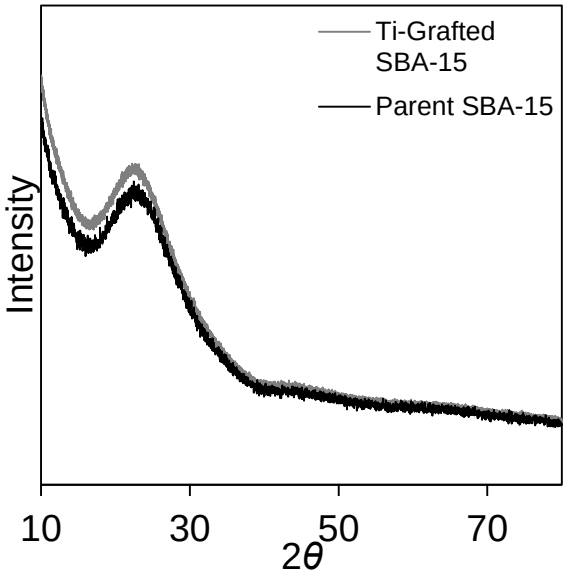

Figure 5.22: Wide angle XRD patterns from titania grafted SBA-15 (3 cycles).

Low angle XRD patterns (**figure 5.23**) of the grafted materials were taken to ensure that multiple heat treatments of the materials had no detrimental effect on the hexagonal pore structure of the base silica. The pore spacing also remained at ~10.7 nm.

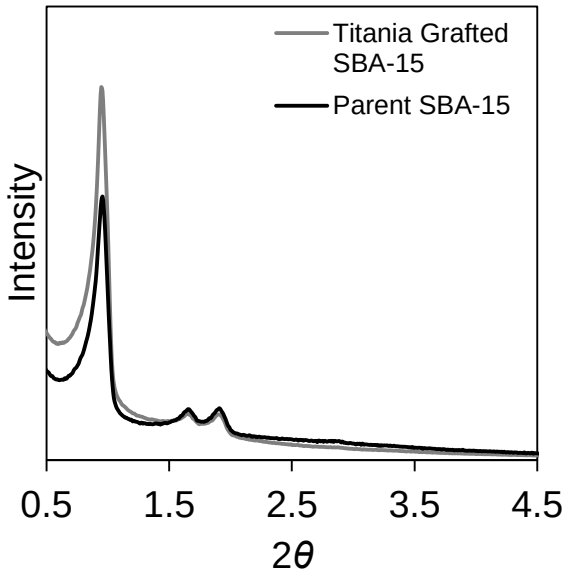

Figure 5.23: Low angle XRD patterns from titania grafted SBA-15 (3 cycles) and parent SBA-15.

Nitrogen porosimetry was used to determine any changes in pore diameter as a direct result of titania grafting. Supposing that thin layers of titania are indeed grafted

onto the surface of the silica, one would expect the pore size to incrementally diminish with subsequent layers of titania.

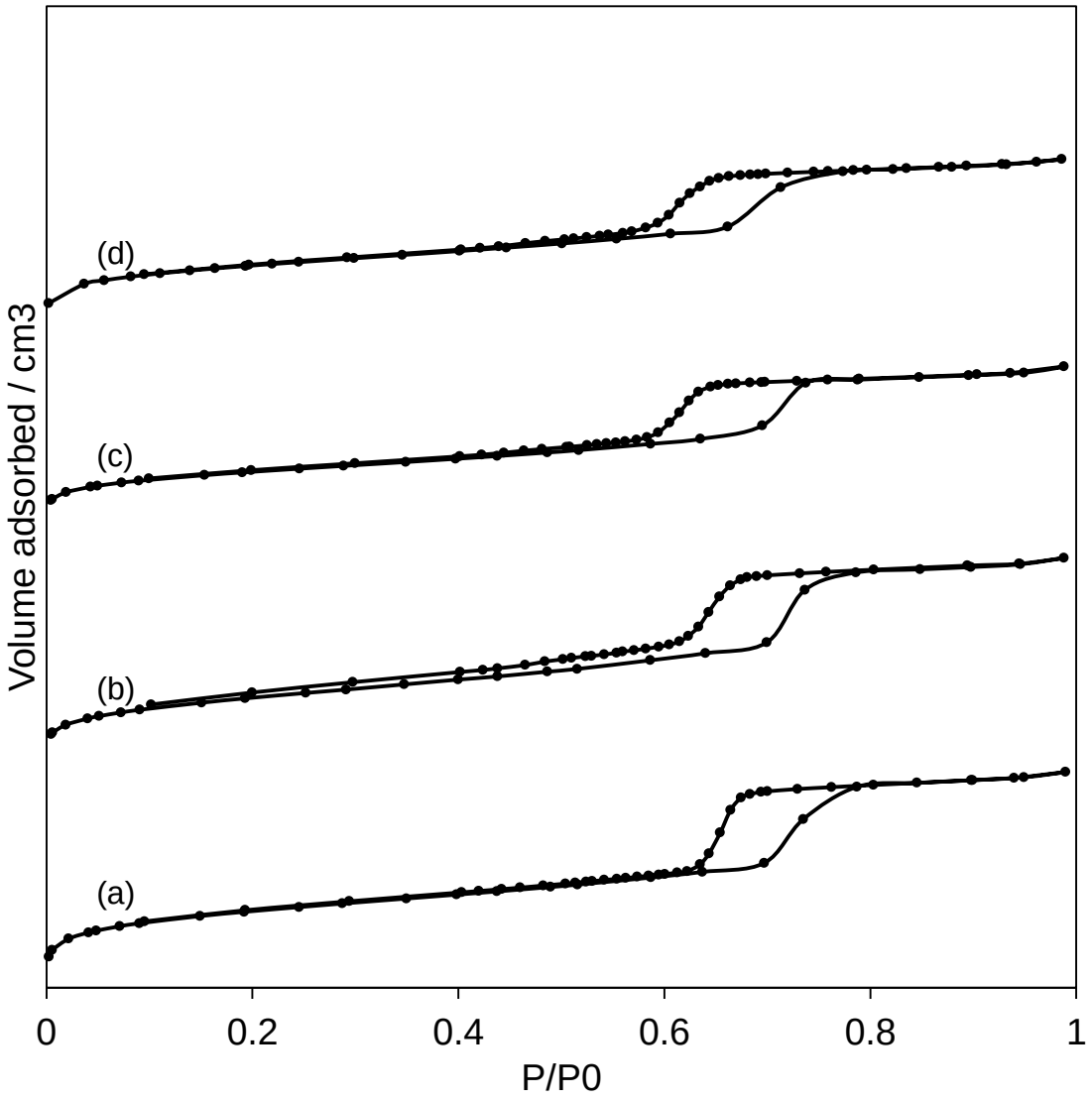

Figure 5.24: Nitroen adsoption isotherms for (a) parent SBA-15, (b) one graft cycle of titanium dioxide, (c) 2 grafts cycles and (d) 3 graft cycles.

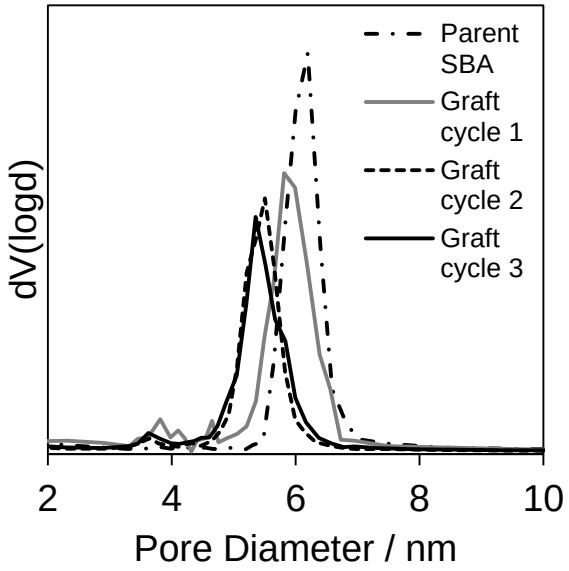

Figure 5.25: BJH pore size distributions from titania grafted silica.

The pore size distributions shown in **figure 5.25** indicate a decreasing pore size with consecutive graftings, which supports the idea that the titania is being applied as an even coating on the surface of the silica. The average pore size decrease is calculated as a fraction of a monolayer of titania and reported in **table 5.5,** assuming a monolayer thickness of 0.355 nm.[46] Small contributions below the average pore size indicate the titania coverage is not entirely uniform.

Graft Cycle	Cumulative Pore Diameter Decrease / nm	Number of Titania Monolayers
1	0.4	1.1
2	0.7	1.9
3	0.85	2.3

Table 5.5: Pore size decrease and subsequent number of monolayers calculated per graft cycle.

The pore diameter decrease for graft cycles 1 and 2 suggest that the material is almost uniformly coated with 1 monolayer of titania, however the BJH analysis for the 3rd cycle of grafting suggests that there is only partial monolayer coverage. After 3 cycles of grafting, there is a calculated average of 2.3 monolayers of titania.

Effects on surface area, micropore and mesopore surface area are displayed in **figure 5.26**.

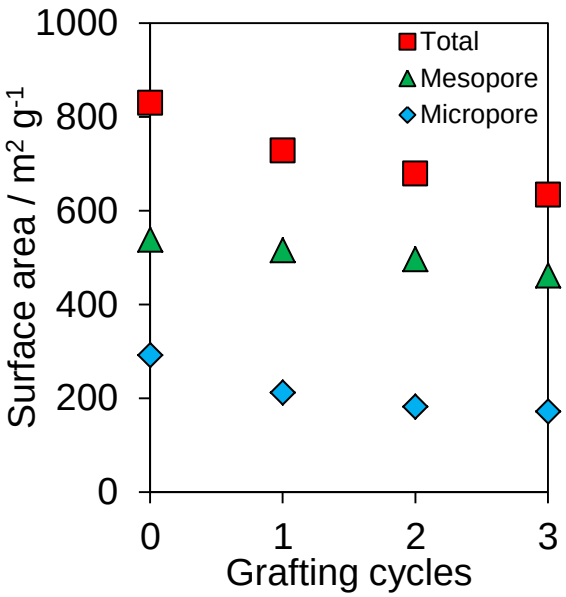

Figure 5.26: Total, mesopore and micropore surface areas of titania grafted SBA-15.

A decreasing trend can be clearly observed in the porosimetry analysis, which is consistent with the idea of pore shrinkage due to an increase in the thickness of titania grafted onto the surface of the SBA-15. The microporous surface area is seen to decrease to the greatest degree after the first cycle, and decrease by smaller amounts during subsequent treatments, however, the titania layers appear to retain some microporous character throughout the grafting procedure. The overall surface area loss arises from a combination of the filling of micropores, as well as pore shrinkage due to additional titania layers.

XPS analysis was used to probe the ultrathin titania layers to determine information regarding the titania oxidation state and coverage (**figure 5.27**). A summary of the elemental composition is presented in **table 5.6** which reports a greatly increase titania composition, indicative of a surface species.

Ti wt. %	Si wt. %	O wt. %
11.65	35.7	52.65

Table 5.6: Surface elemental composition of titania grafted SBA-15 (3 cycles)

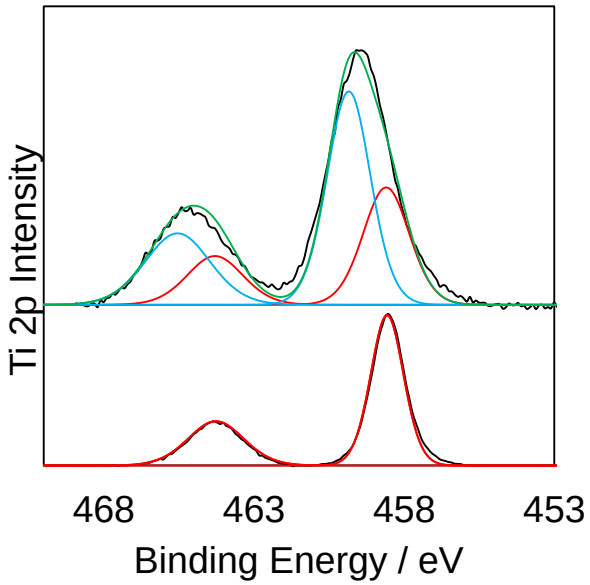

Figure 5.27: Ti 2p XPS analysis for titania grafted SBA-15 (3 cycles).

The Ti 2p region was fit using line shapes obtained from a commercial anatase material (P25, Degussa), which recorded a Ti $2p_{3/2}$ peak position of 458.8 eV, consistent with literature values.[47] A shift to higher binding energies is associated with the formation of Ti-O-Si bonds, resulting in the two sets of peaks exhibited in the Ti 2p spectra[48] caused by a decrease in the positive charge of the titania species within the Ti-O-Si formation compared to that of anatase.[49] The Ti $2p_{1/2}$ peak exhibits a different FWHM to that of the $2p_{3/2}$ peak due to the Coster-Kronig effect, the broadening of $2p_{1/2}$ peaks due to LMM decay processes.[50]

The oxygen 1s region (**figure 5.28**) displayed an asymmetry which was accounted for by fitting the spectra with peaks for bulk silicon dioxide at 533.1 eV and for titanium dioxide at 530 eV, with the line shapes and positions taken from analysis of the parent SBA-15 and P25 commercial anatase. A third feature was fit between the two peaks from SiO_2 and TiO_2, which is thought to be the bridging oxygens, Ti-O-Si.[49]

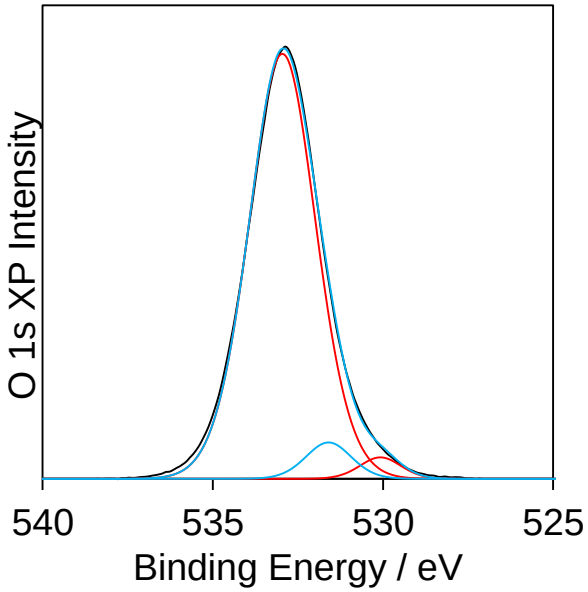

Figure 5.28: O 1s XPS analysis for titania grafted SBA-15.

The Si 2p region was analysed (**figure 5.29**), and fit with a Si 2p doublet ($2p_{3/2}$ = 103.6 eV, doublet separation = 0.6 eV). Additionally, a secondary silicon phase was fit at a higher binding energy, attributed to Si-O-Ti species. This secondary species at a lower binding energy is resultant from electronic alterations to the silicon environment within the bridging layer.[51]

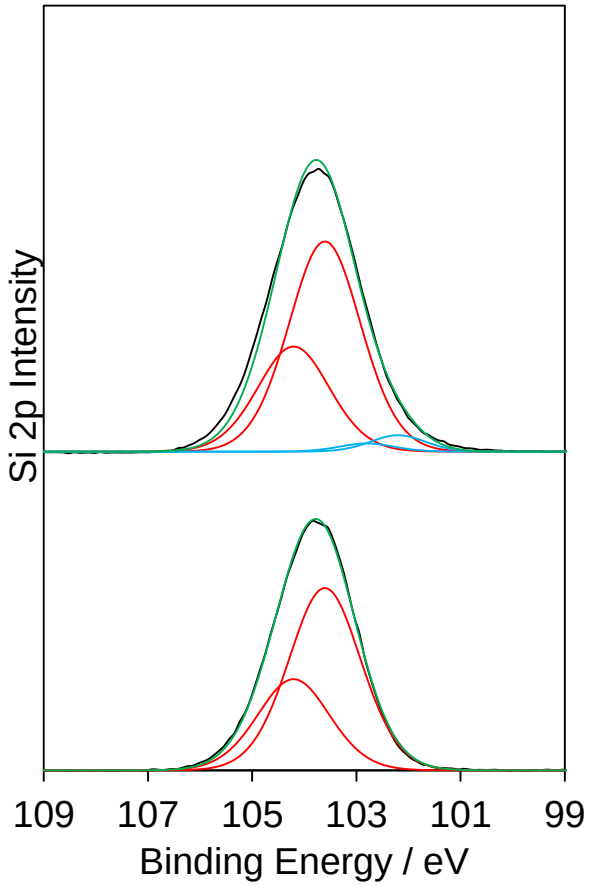

Figure 5.29: Si 2p XPS analysis for titania grafted SBA-15 (top) and parent SBA-15 (bottom).

To study the grafted titania layer, TEM analysis was used in order to look for the possible undesirable existence of large agglomerates of titania, rather than thin grafted layers.

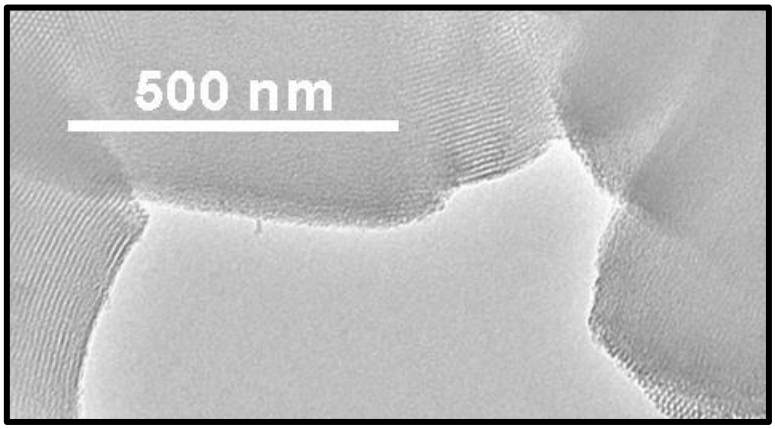

Figure 5.30: TEM image of titania grafted SBA-15.

No large titania particles were observed in the TEM analysis, suggesting titania observed via elemental analysis is the result of thin, grafted layers, supporting the absence of diffraction patterns from XRD analysis. Clear regions of hexagonally arranged pore structures were observed, as well as channels consistent with ordered mesoporous structure. A summary of the material properties is presented in **table 5.7**.

Material	Surface Area / m^2 g^{-1}	Micropore Surface Area / m^2 g^{-1}	Pore Diameter / nm	Pore Spacing (XRD) / nm	Pore Spacing (TEM) / nm	Wall Thickness / nm
Ti-SBA-15	634	172	5.35	10.8	10.3	5.4 ± 0.1

Table 5.7: Summary of properties of synthesised Ti-SBA-15.

5.2.1.4. Silver loaded titania grafted SBA-15

Silver was introduced to SBA-15 with 3 grafting cycles of titania using the incipient wetness methodology as with pure SBA-15, covering a range of weight loadings from 0.5% to 10% nominal loading. The silver content was measured in both the surface and bulk, by XPS and EDAX respectively, and is shown in **table 5.8**.

Nominal Ag Loading / wt. %	Bulk Ag Loading / wt. %	Surface Ag Loading / wt. %
0.5	0.3	0.74
1	0.9	1.11
5	2.3	2.39
10	3.7	3.82

Table 5.8: Ag surface and bulk content in silver loaded, titania-grafted SBA-15.

The weight loadings for silver determined by EDAX analysis are lower than the nominal loadings, and are consistently lower when compared with the silver loaded SBA-15 samples produced in the previous section. This, again, is attributed to silver mirroring of reaction vessels during the synthetic procedure.

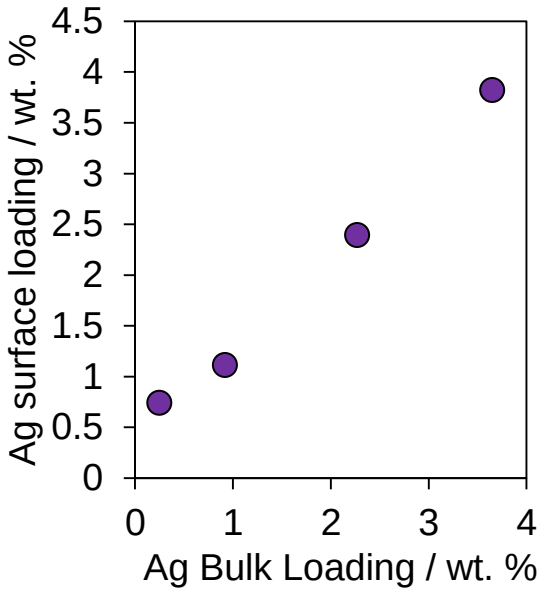

Figure 5.31: Ag surface wt. % vs bulk wt. %, recorded by XPS and EDAX respectively.

The surface to bulk profile displayed in **figure 5.31** exhibits a trend suggestive of increasing particle size. The surface to bulk ratio increases as bulk loading decreases, as the smaller particles are more visible by XPS analysis. Large silver particles will report lower surface loadings due to increased attenuation of silver photoelectrons throughout the large silver particles.

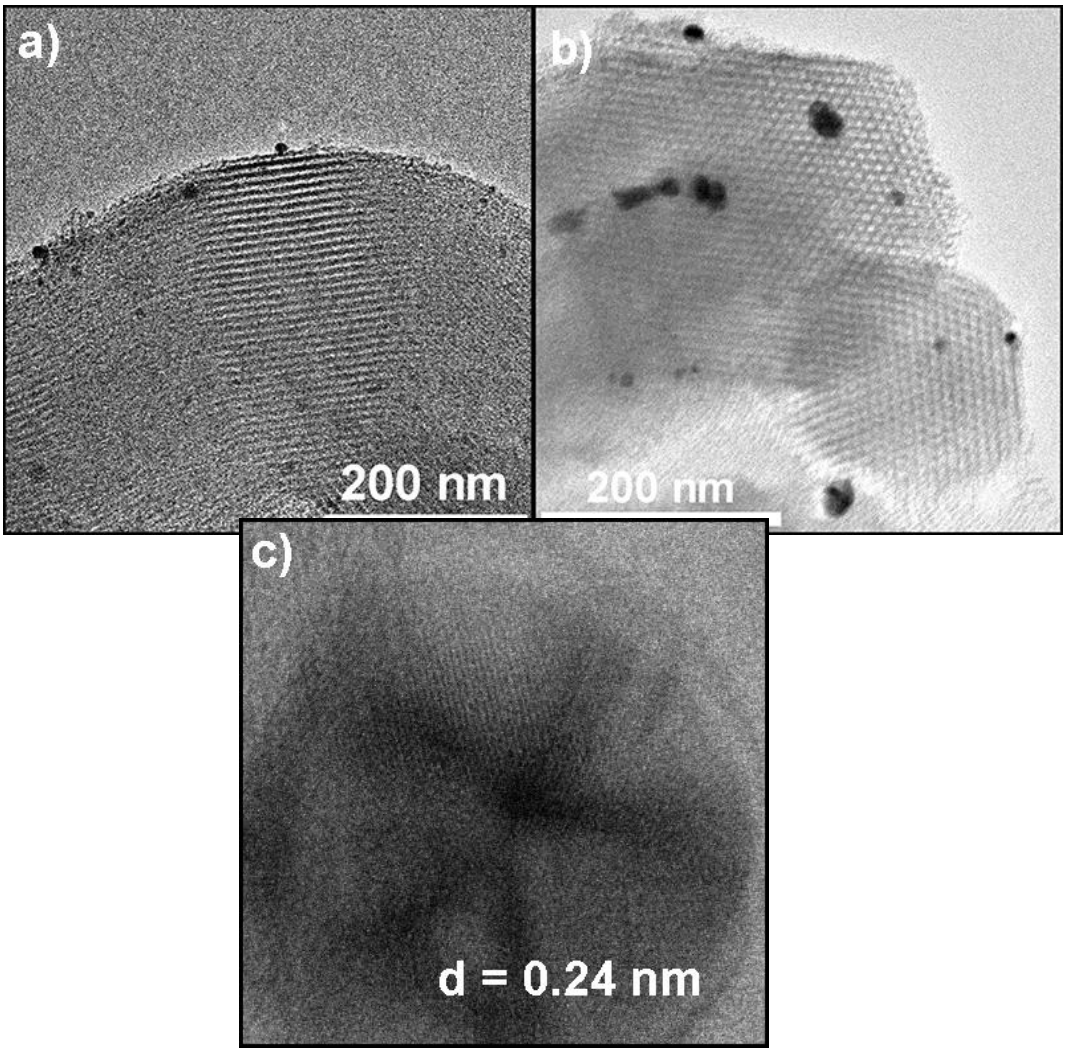

Figure 5.32:Bright field TEM image of Ag-Ti-SBA-15 for (a) 0.3%, (b) 3.7% Ag and HR image of Ag nanoparticle (3.7% Ag).

Bright field TEM images of the silver particles deposited onto the inorganic support materials are exhibited in **figure 5.32**, in which a contrast between the darker silver nanoparticles and the lighter titania-grafted SBA is evident. **Figure 5.32 (c)** shows a HRTEM image of one of the silver nanoparticles, including observed lattice fringes, which were measured to be 0.24 nm, which was identified as the silver metal (111) facet.[52]

There is a slight increasing trend in particle size and dispersity seen across the series, as with the Ag-SBA-15 series, which supports the trend witnessed in the silver surface to bulk ratios determined. Full size histogram distributions are presented in **figure 5.33**.

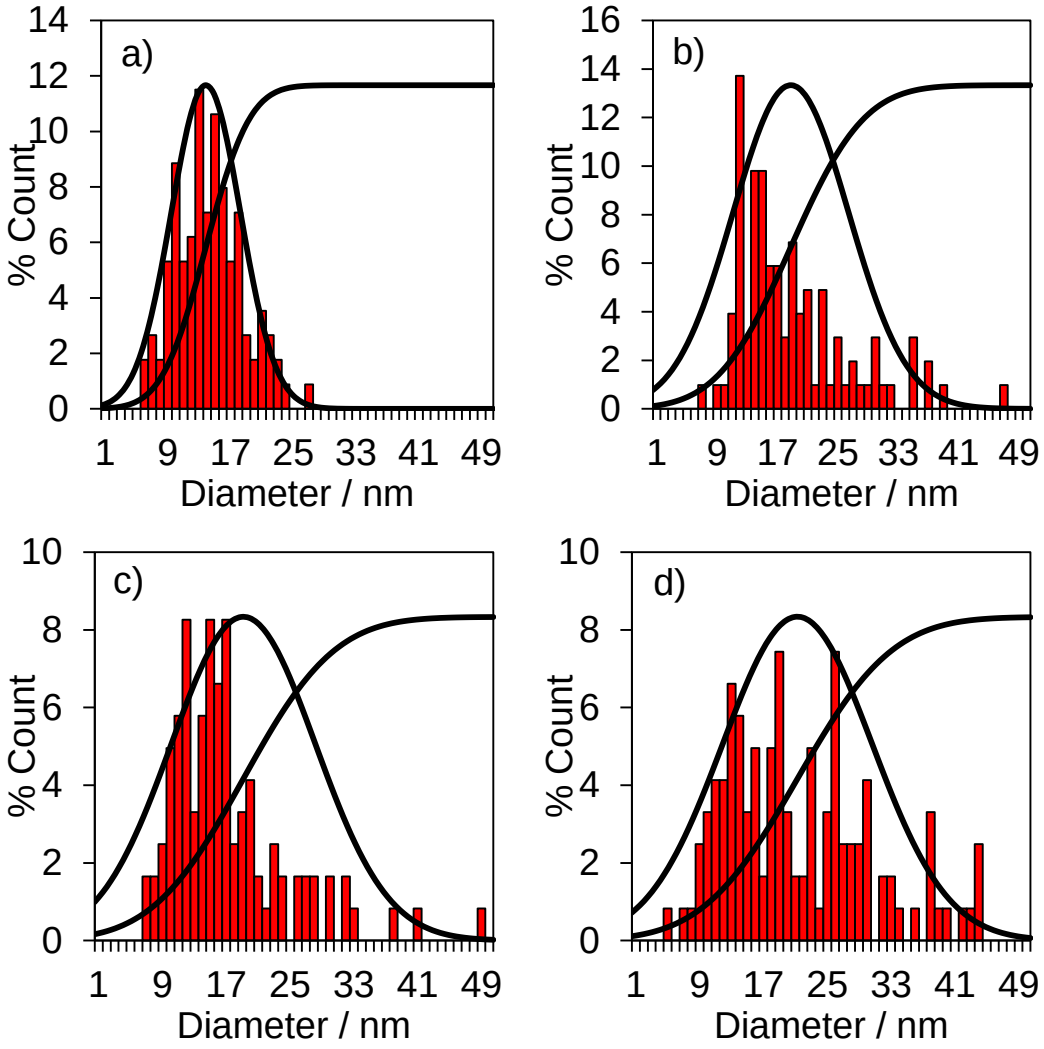

Figure 5.33: Silver nanoparticle size distributions, normal and cumulative distributions for Ag-Ti-SBA15 materials determined by bright field TEM for bulk silver loadings of a) 0.3%, b) 0.9%, c) 2.3% and d) 3.7%.

Within the size distributions, it can be seen that the size distributions become more diverse as silver loadings increase, with a greater number of large agglomerates appearing for the samples of a higher loading. A summary of these histograms is provided in **figure 5.34**.

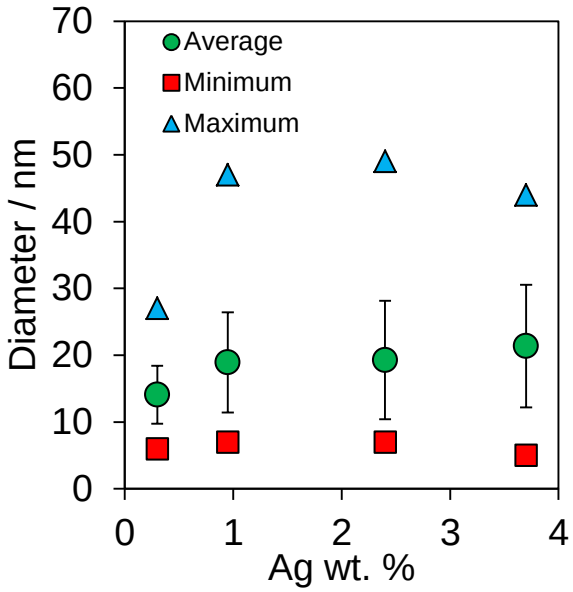

Figure 5.34: Summary of silver nanoparticle size distributions from TEM data for Ag-Ti-SBA-15, based on counts of >100 particles in all cases.

Low angle XRD was employed to determine no detrimental effects were observed to the hexagonal pore structure and pore spacings of the silver impregnated materials (**figure 5.35**). All materials recorded a characteristic low angle XRD pattern associated with a hexagonally arranged ordered mesoporous structure of space group *p6mm*.

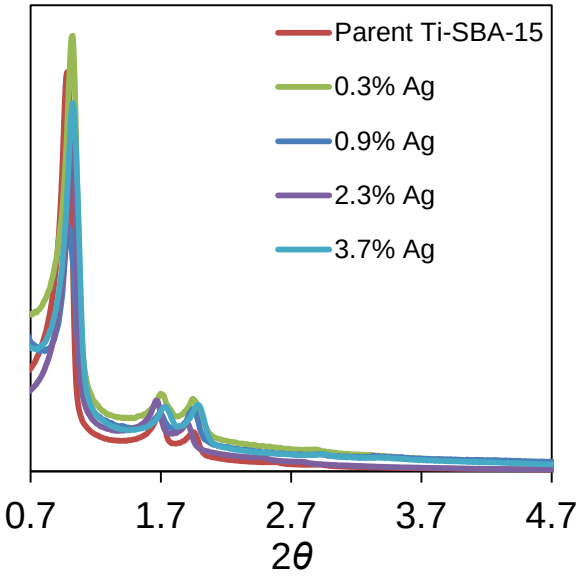

Figure 5.35: Low angle XRD patterns for Ag-Ti-SBA-15.

The silver speciation was studied by wide angle XRD analysis, to identify the dominant silver phases composing the produced nanoparticles and the recorded diffraction patterns are displayed in **figure 5.36**.

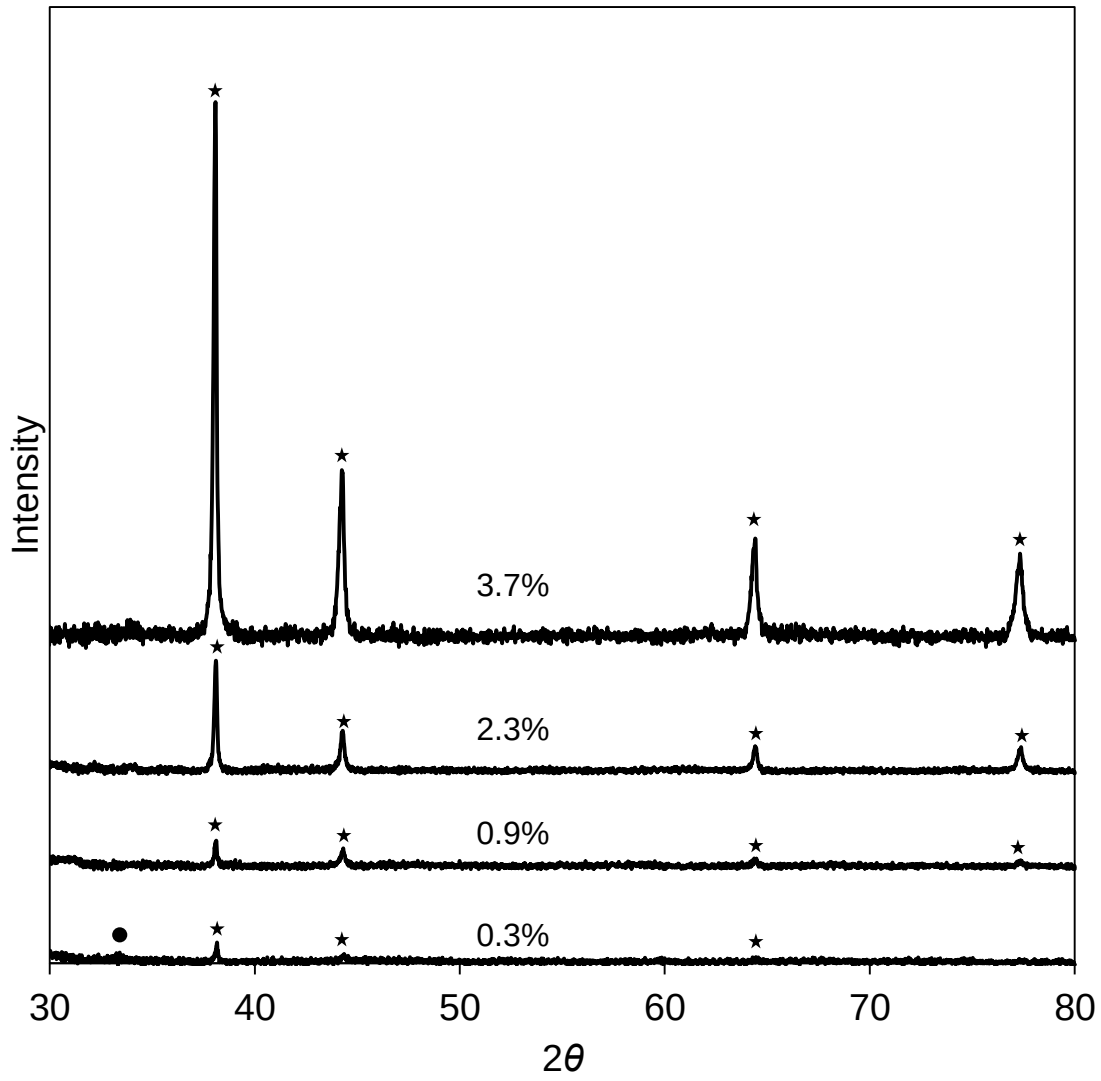

Figure 5.36: Wide angle powder XRD patterns for Ag-Ti-SBA-15. (*) indicate Ag^0 FCC reflections (●) indicate Ag_2CO_3 reflections.

Wide angle XRD analysis of the silver loaded titania grafted SBA-15 materials (**figure 5.36**) indicated the silver was present mostly as silver metal, with a (111) reflection appearing at 38.15 ± 0.05°, corresponding to a d-spacing of 2.35 Å, which is consistent with literature values for silver metal.[52] Additionally, in the 0.3 % material, a very small reflection can be seen at 32.5°, which suggests the presence of silver carbonate species.[40] That this peak is very small indicates that the silver carbonate

reported is of very small crystallite size (< 2-3 nm) and/or at loadings too low to resolve using this instrumentation. The sizes of the silver crystallites were determined vie the Scherrer equation and compared with those obtained by TEM analysis (**figure 5.37**).

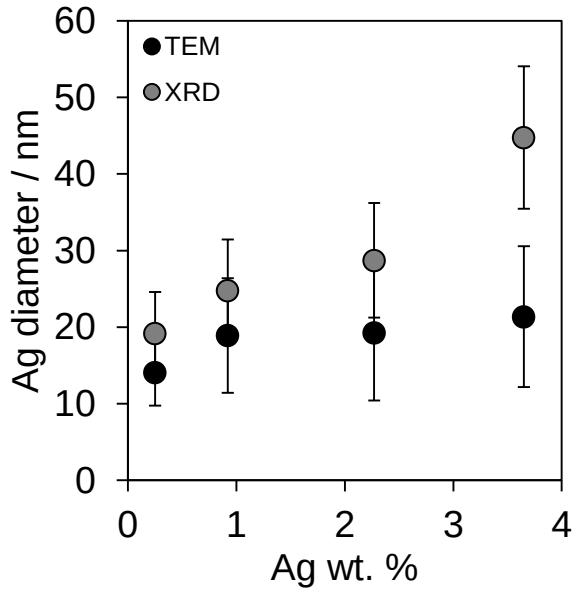

Figure 5.37: Silver particle sizes, as determined by XRD and TEM for Ag-Ti-SBA-15.

Discrepancies in the reported sizes between TEM and XRD analysis increase with silver loading. This is likely due to the differences between the local TEM analysis and bulk XRD analysis, with XRD able to volume average a larger area of material, and hence will detect areas of larger crystallites which may have not been observed by electron microscopy. There is, however, a trend of increasing overall particle size, with larger loadings accumulating an increased number of large agglomerates of silver on the external inorganic surface, which in turn inflates the average particle size of the materials. The materials do not display a high degree of monodispersity, with particle sizes spanning large ranges, similar to that observed in the pure SBA-15 materials. This is hoped to produce a system with a range of dissolution rates to lead to a silver ion delivery system with quick, yet sustained silver release.

Nitrogen adsorption porosimetry was employed to determine the effect of silver loading on the pore network on the titania grafted SBA-15.

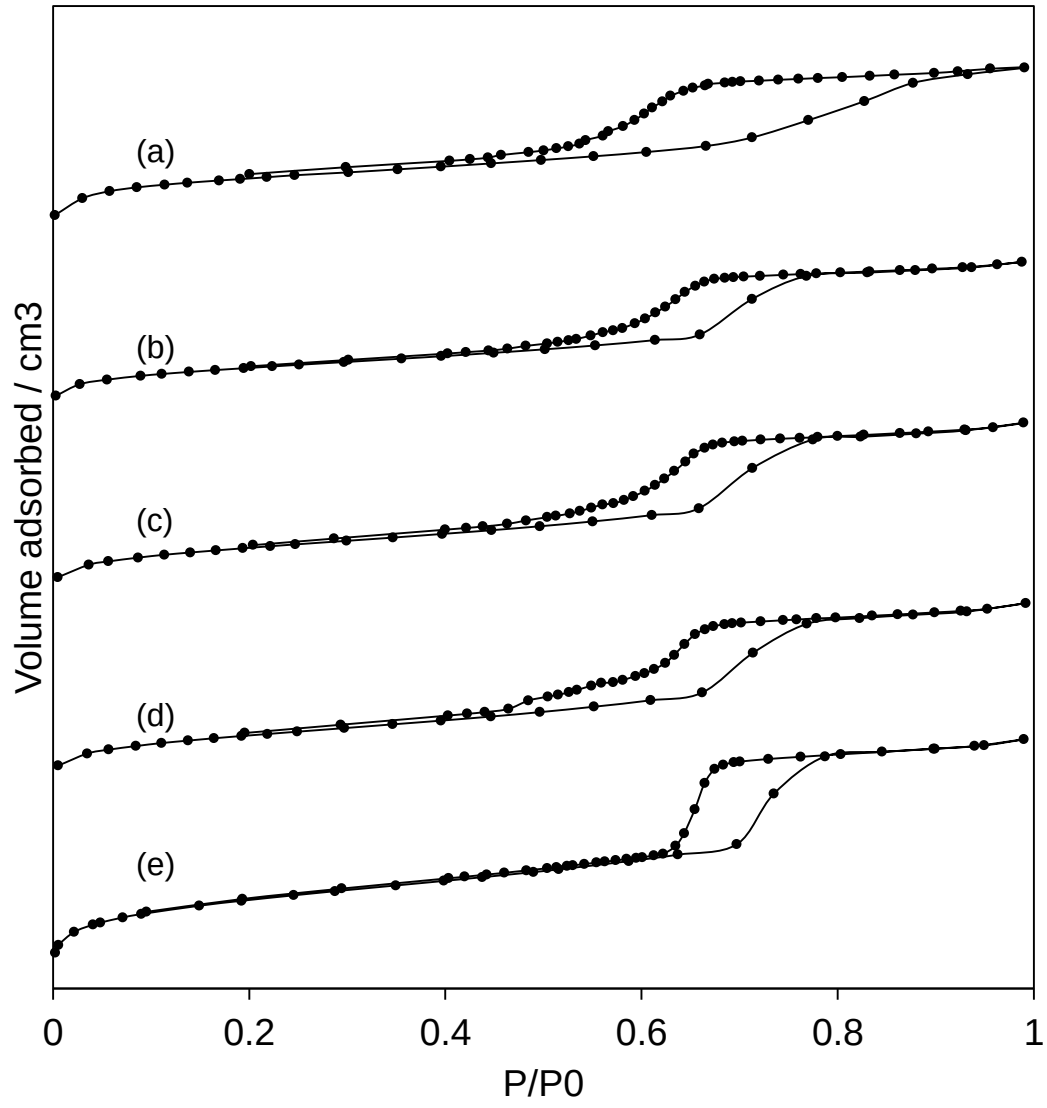

Figure 5.38: Nitrogen adsorption isotherms for (a) 3.7%, (b) 2.3%, (c) 0.9%, (d) 0.3% and (e) 0% Ag-Ti-SBA-15.

The isotherms in **figure 5.38** exhibit the typical type IV shape associated with hexagonally mesostructured SBA-15 type materials, including the H1 type hysteresis loop indicative of the monodisperse pore structure. As the silver loading increases, this shape becomes more perturbed, suggesting that the loaded silver is residing in large amounts within the pore network.

Looking at the recorded surface areas obtained by applying the BET equation to the recorded isotherms, as well as the micropore surface areas from t-plot analysis, a trend of decreasing total surface area can be witnessed (**figure 5.39**). The micropore surface

area suffers a slight initial decrease upon loading (0.25 wt. % Ag), which would suggest the micropore regions are becoming filled with silver to a small degree. This initial remains constant throughout the remaining loadings, which could indicate that while some silver is initially deposited into the micropores, further silver particles form in the majority either within the mesopores or on the external surface.

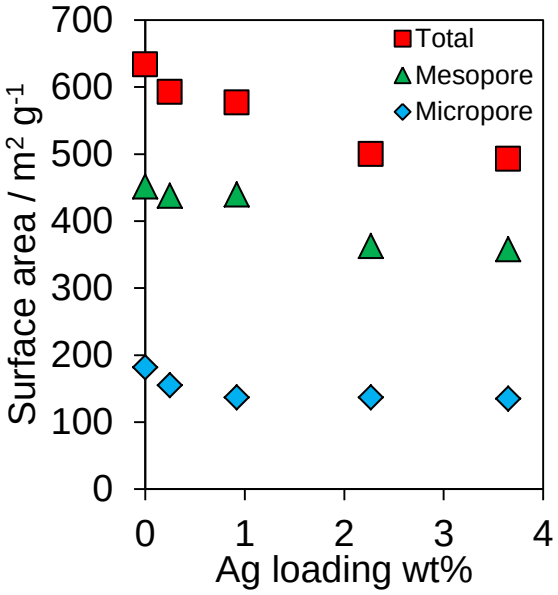

Figure 5.39: Total, mesopore and micropore surface areas of Ag-Ti-SBA-15.

The mesopore volume exhibits a decreasing trend with silver loading, which supports the idea that further loading past the initial filling of mesopores, silver particles form within the pores in the meso-sized region.

The effect of the silver deposited within the mesopore network can be detected by looking at the BJH profiles of the loaded materials. **Figure 5.40** displays the compiled BJH profiles of Ag-Ti-SBA-15.

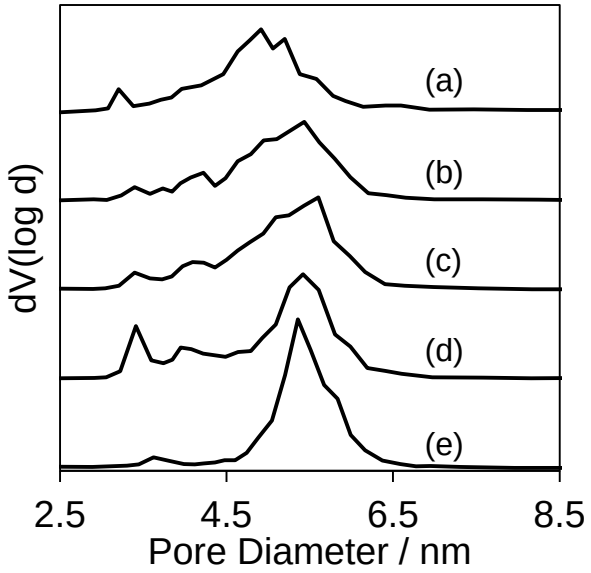

Figure 5.40: BJH profiles for (a) 3.7%, (b) 2.3%, (c) 0.9%, (d) 0.3% and (e) 0% Ag-Ti-SBA-15.

Pore size distributions from BJH analysis indicate a shift to lower pore diameters, with pores appearing below the mean pore diameter determined for the parent material. This would suggest the presence of some silver particle within the pore network, potentially indicative of nanoparticles encompassed within the mesopore network.

The Ag 3d regions were investigated by XPS analysis and are exhibited in **figure 5.41**. The Ag $3d_{5/2}$ and Ag $3d_{3/2}$ peaks are clearly visible and set to peak ratios of 3:2, with a doublet separation of 6 eV, with all spectra calibrated to adventitious carbon at 284.7 eV. As with the previous series, there are two regions visible in the recorded spectra. These are attributed to to silver metal (red lines) at 368.1 eV and silver carbonate (blue lines) at 369.7 eV.

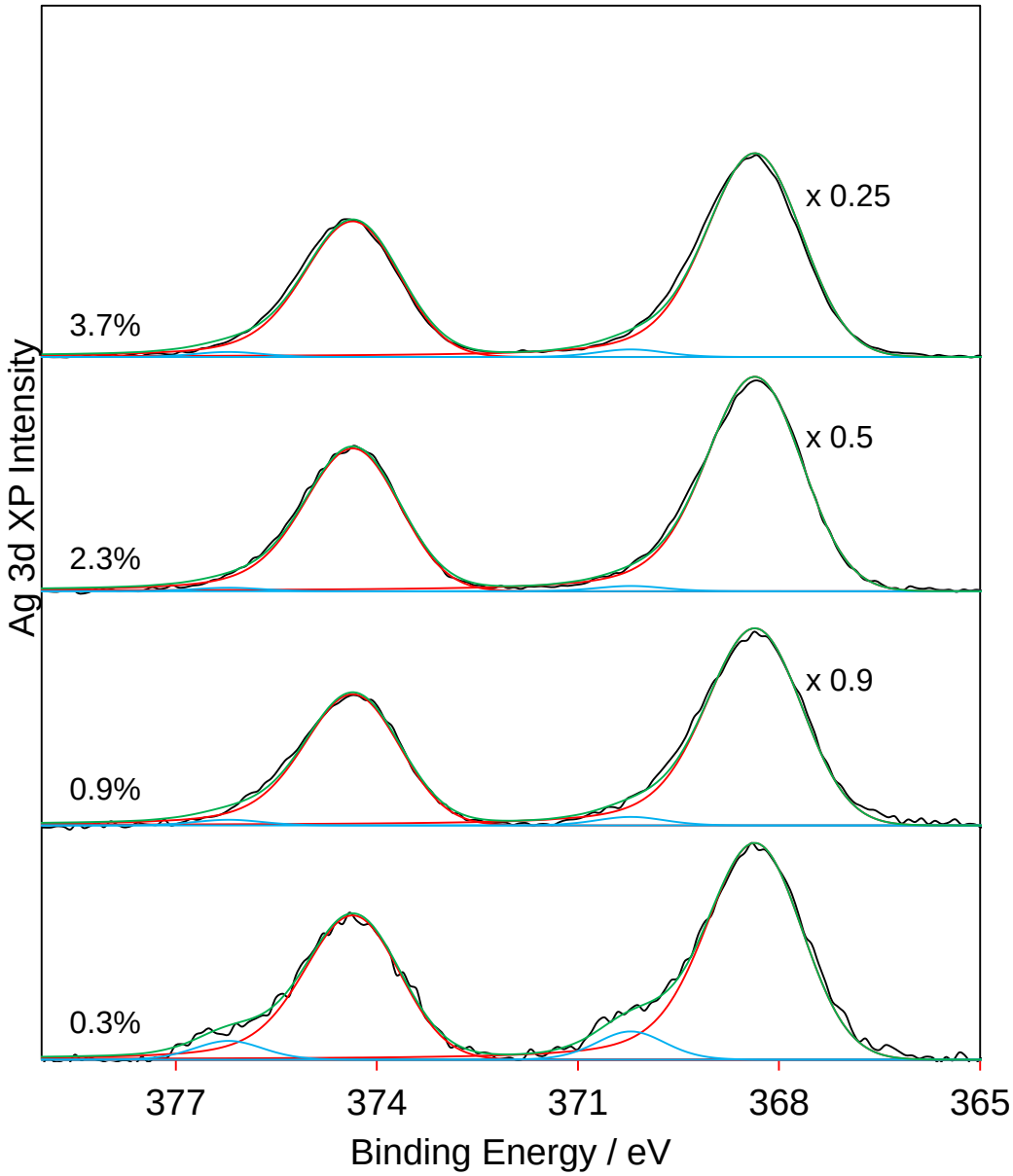

Figure 5.41: Ag 3d XPS stack plot for Ag-Ti-SBA-15.

The total percentage of silver carbonate attributed species is found to decrease as silver loading increases (**figure 5.42**). With a decreasing proportion of silver carbonate as weight loading and average particle size increases (and hence surface area decreases), the carbonate species has been assigned as a surface species. Small carbonate surface coverage would also explain the lack of distinct carbonate peaks exhibited within the XRD diffractograms.

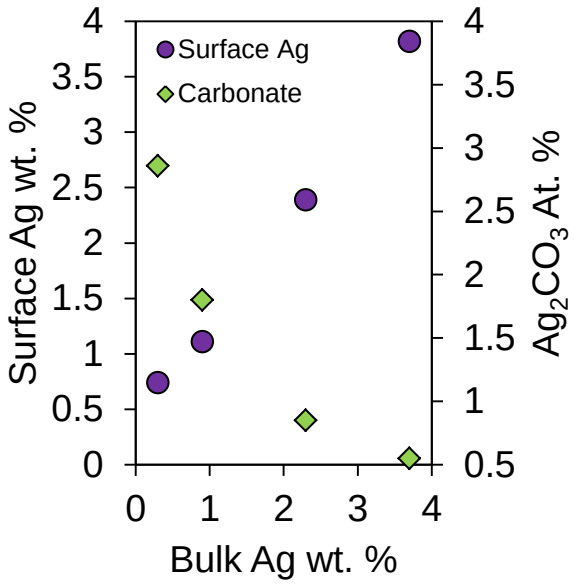

Figure 5.42:Surface carbonate and total surface silver loadings vs bulk Ag wt. % for Ag-Ti-SBA-15.

This decrease in carbonate composition is likely due to it being a surface species that forms when the surface of Ag is oxidised. Titania supports have been shown to exhibit improved promotion of the formation of oxidised species on metal nanoparticle surface compared to silica supports due to enhanced acidity.[53] Ag oxides are known to be slightly basic and will adsorb CO_2 from the atmosphere to form a carbonate.[54, 55] Thus, as Ag loading and particle size increases, the proportion of surface carbonate will decrease as the contribution from the underlying metal increases. This assignment supports the observation of XRD diffractograms, in a small, broad peak corresponding to silver carbonate was observed.

C 1s regions are shown in **figure 5.43**, which indicate a growing species at 288 eV with decreasing silver content. This is consistent with a silver carbonate species, supporting the assignment of the secondary silver species.[56]

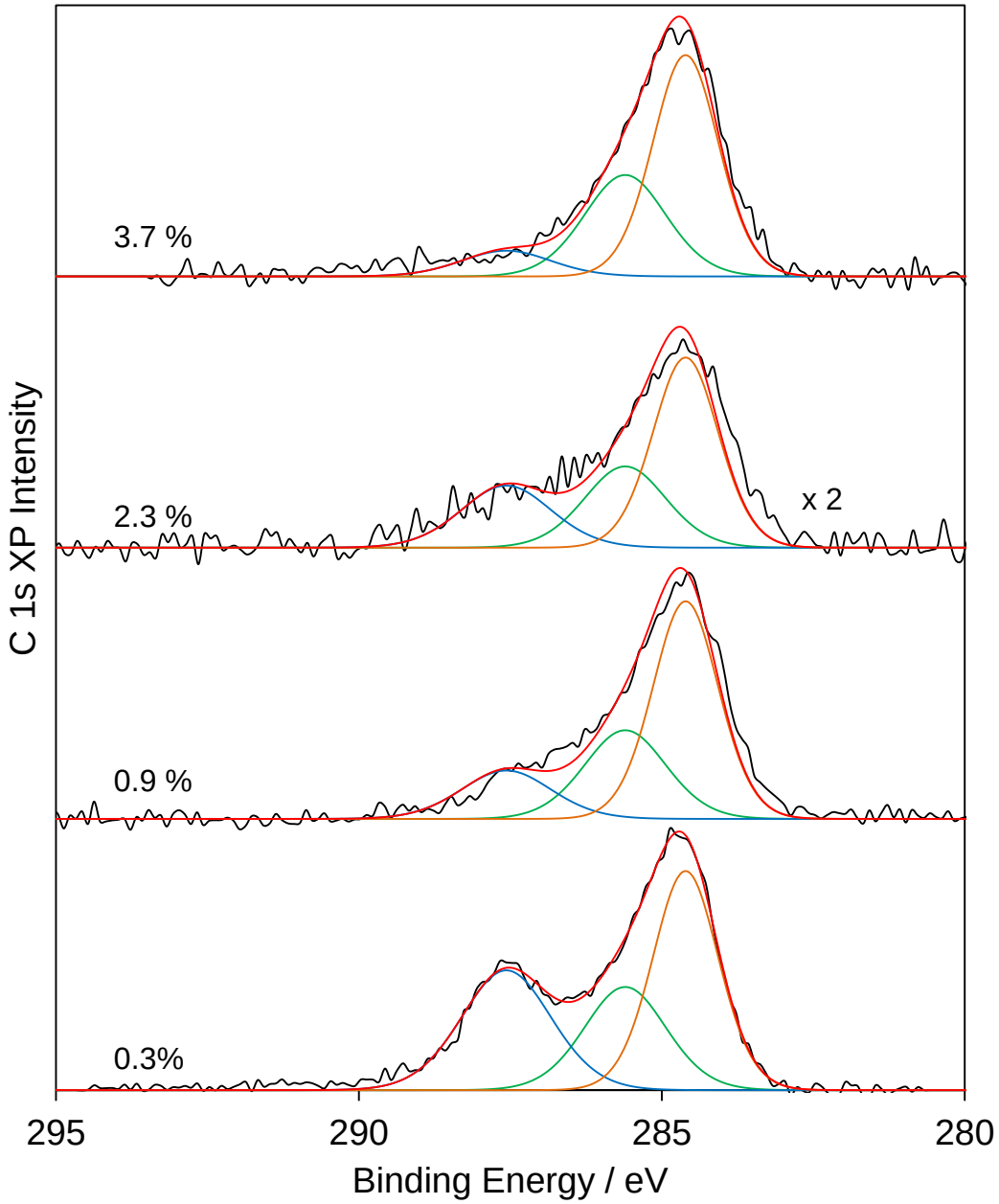

Figure 5.43: C 1s XPS stack plot of Ag-Ti-SBA-15.

. The titanium 2p regions (**figure 5.44**) were analysed, in order to determine any changes to the titanium species. The $2p_{3/2}$ and $2p_{1/2}$ peaks were fit with peak area ratios of 2:1 and a doublet separation of 5.7 eV. There is no visible change within any of the recorded titanium regions, suggesting the chemical environment of the surface titania remains unperturbed by the introduction of silver species.

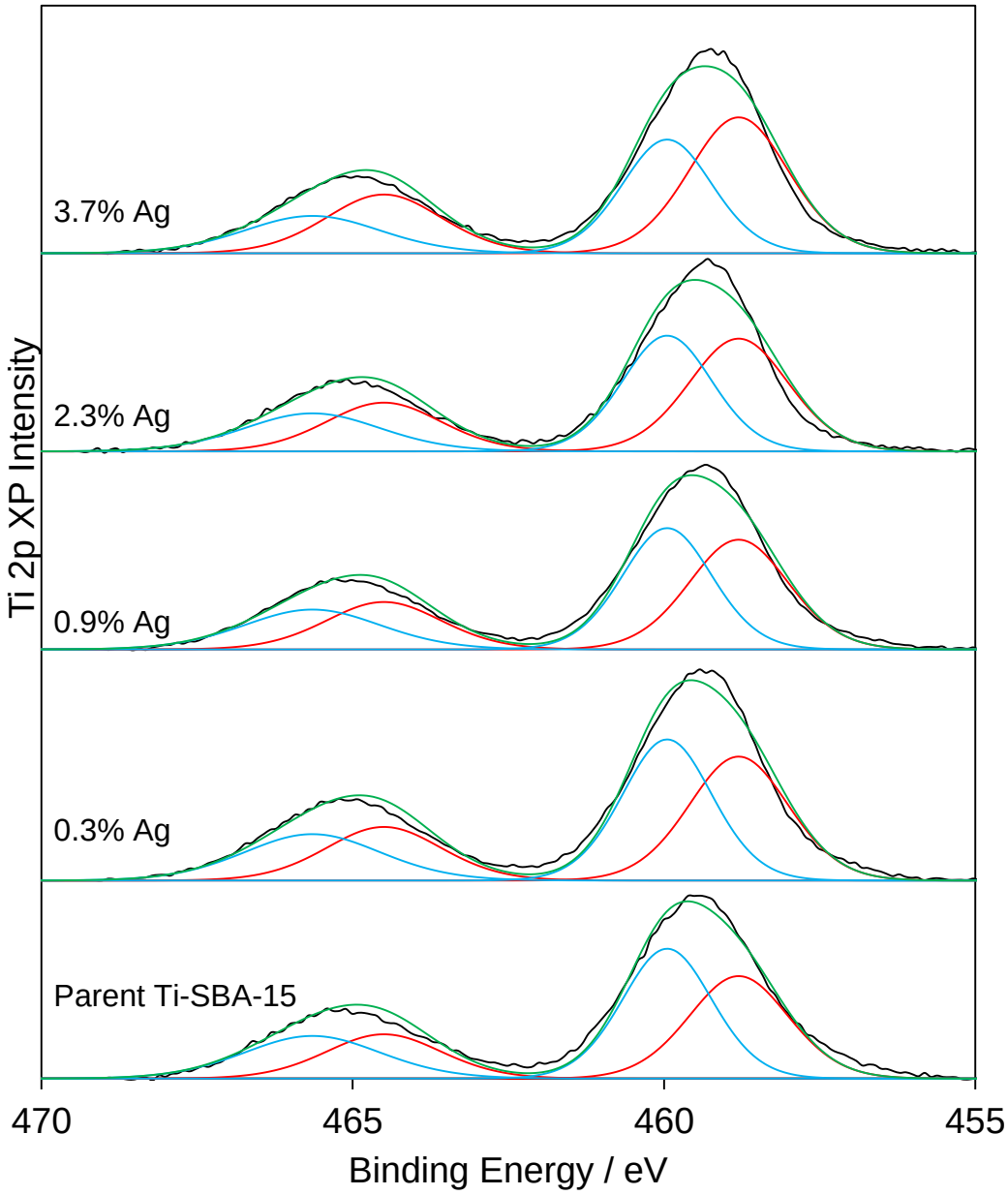

Figure 5.44: Ti 2p XPS stack plot for Ag-Ti-SBA-15.

The titanium to silicon ratios were recorded for the loaded samples, to ensure no sintering of surface titanium species was observed (**table 5.9**). The surface titanium to silicon ratio was not found to vary to any significant degree.

Bulk Ag wt. %	Ti:Si (XPS)
0	0.32
0.3	0.35
0.9	0.37
2.3	0.29
3.7	0.29

Table 5.9: Ti:Si ratios from XPS analysis.

5.2.1.5. Macroporous titania grafted SBA-15

Macropores were introduced to the synthesised SBA-15 materials using a polystyrene bead templating synthesis in an attempt to increase the available external titania surface area able to interact with bacteria and inhibit cell growth or promote cell death. Additionally, macropores improve mass transport within the support structure, aiding diffusion.

The polystyrene beads were prepared as described in **section 2.3.2** and introduced to the synthesis of SBA-15 prior to grafting to introduce macroporosity as described in **section 2.3.3,** a schematic of which is presented in **figure 5.45.**

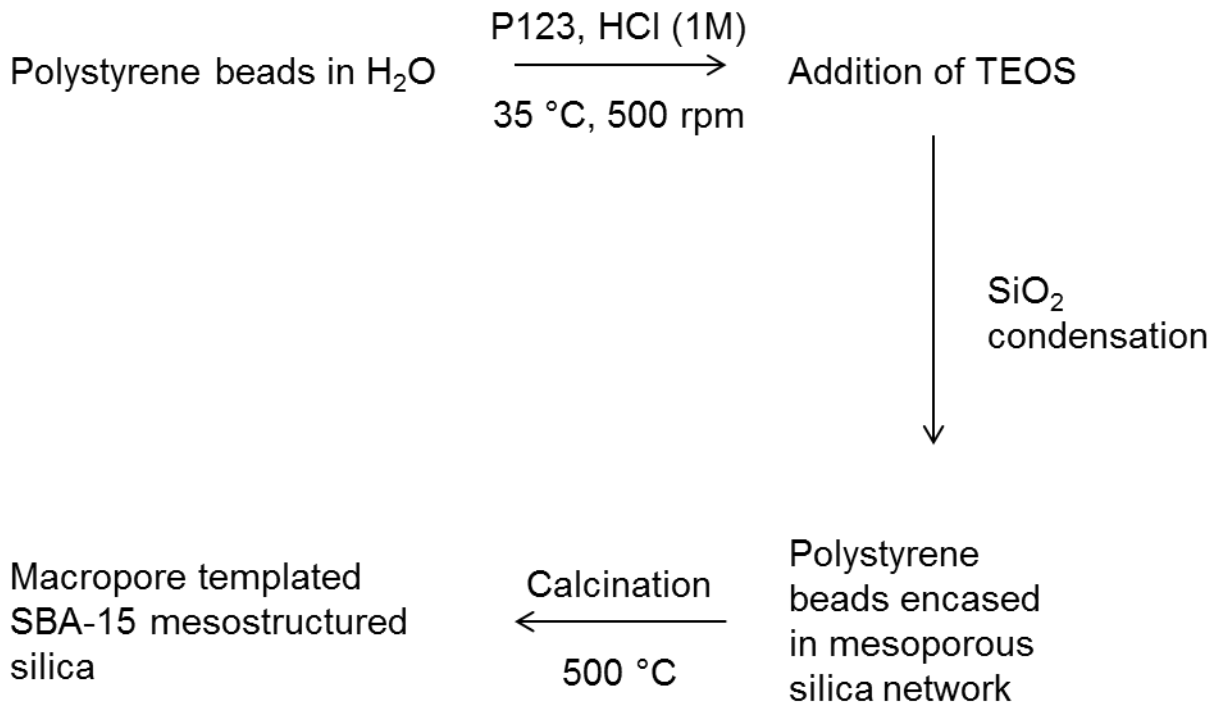

Figure 5.45: Schematic of macroporous SBA-15 synthesis.

Low angle XRD analysis confirmed the presence of an ordered pore arrangement with hexagonal symmetry and p6mm space group (**Figure 5.46**).

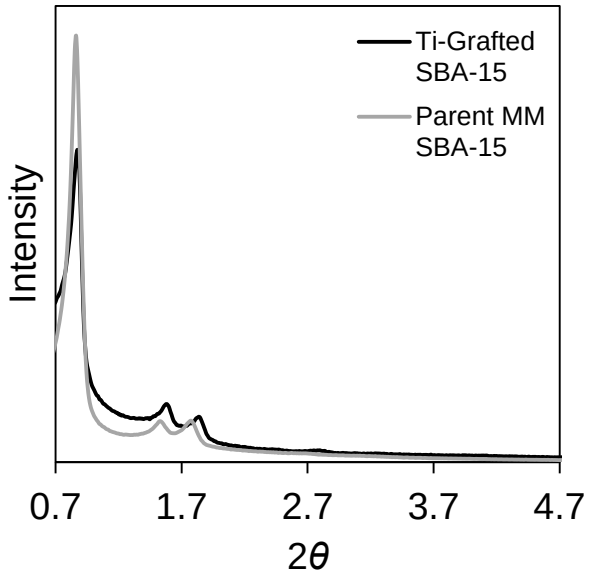

Figure 5.46: Low angle XRD pattern for macroporous SBA-15 and titania grafted SBA-15 (3 cycles).

The grafting of titania onto the surface of the macroporous SBA-15 was achieved using the same method as in **section 5.2.1.3.** The pore arrangement was observed by low angle XRD analysis to ensure the grafting procedure did not affect the hexagonal arrangement of the grafted material.

To try and identify the phase of the prepared titania grafted layer on the hierarchically porous structure, wide angle XRD was run on the parent material and grafted material (3 cycles) and is displayed in **figure 5.47**. There were no visible reflections identified from titania phases within the XRD analysis, which is suggestive of an ultrathin layer coverage.

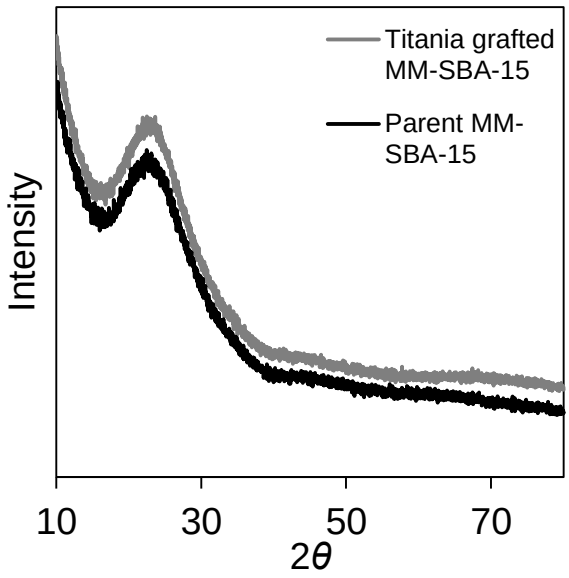

Figure 5.47: Wide angle XRD patterns from macroporous titania grafted SBA-15.

To observe the growth of a layer of titania upon the surface of the silica, nitrogen adsorption porosimetry was performed on the samples. **Figure 5.48** Shows the recorded isotherms.

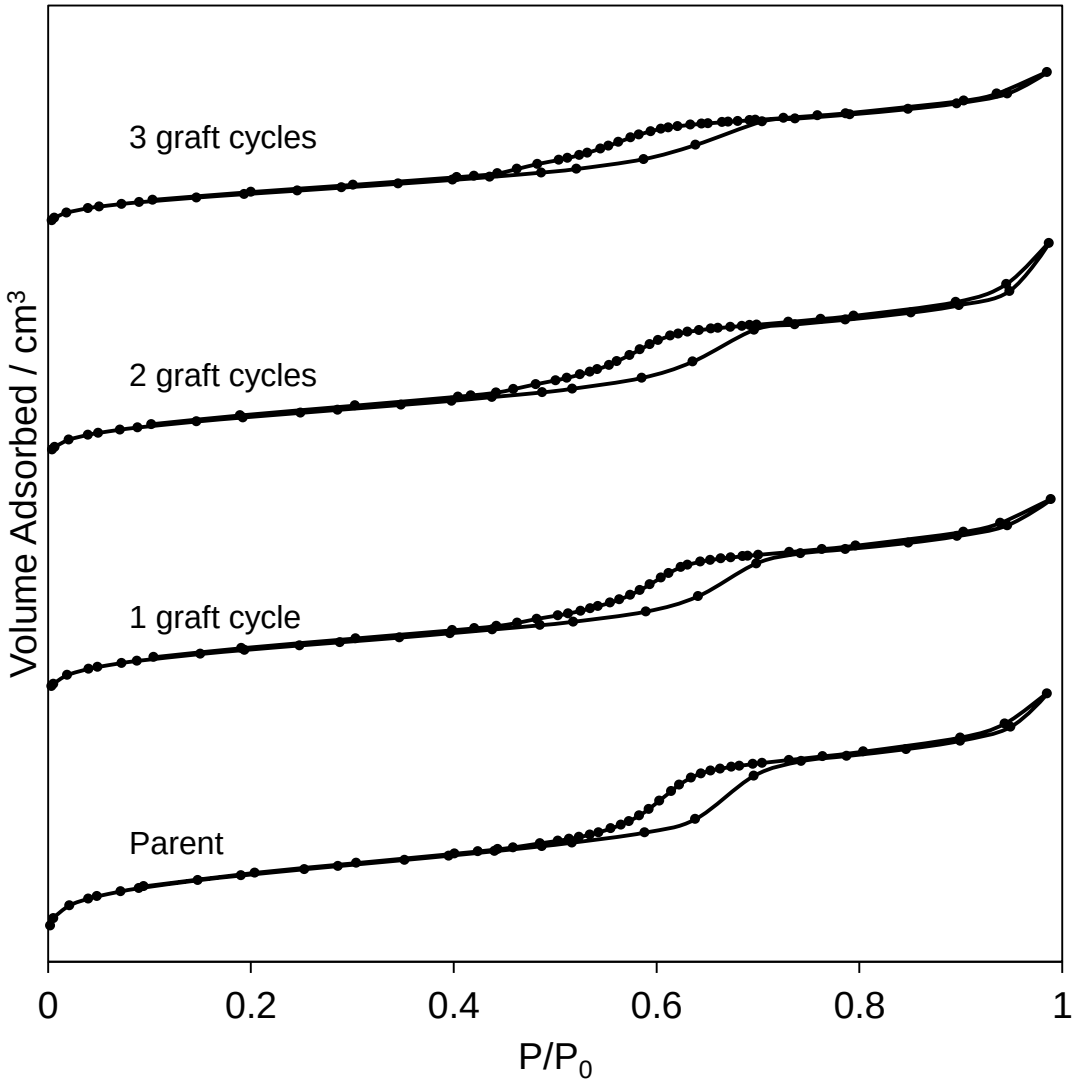

Figure 5.48: Nitrogen adsorption porosimetry on Ti-grafted meso/macro SBA-15.

The isotherms retain a type IV shape, characteristic of mesoporous materials, including a H1 hysteresis loop which is associated with the presence of ordered, monodisperse pore networks, with an increasing adsorption at high partial pressure, suggesting the presence of macropores. The BJH method was applied to these isotherms to observe the pore size distribution (**figure 5.49**).

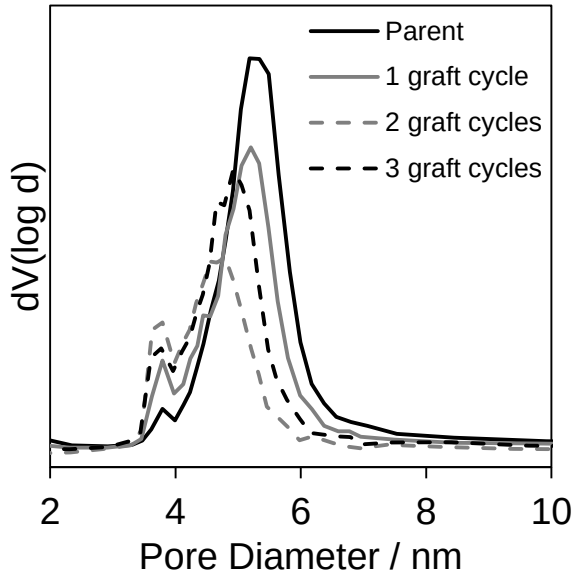

Figure 5.49: BJH pore size distributions for Ti-grafted meso/macro SBA-15.

The pore size distributions indicate that the prepared materials do not have an entirely monodisperse pore network, with a small amount of pores existing at a lower diameter to those of the average, possibly due to contraction of the P123 micelles near to the polystyrene bead regions. The grafting of titania appears to reduce the overall pore size, initially by an insignificant margin, contrary to that observed in the mesoporous material, possibly due to condensation occurring mainly within the large macroporous voids, and subsequently, the second and third grafting cycles reduce the pore diameter to an eventual 2 monolayers of titania (**table 5.10**).[46]

Graft cycle	Cumulative Pore Diameter Decrease / nm	Cumulative Number of Monolayers
1	0.02	0.06
2	0.3	0.85
3	0.7	1.98

Table 5.10: Pore size decrease and subsequent number of monolayers calculated per graft cycle.

The surface area and microporous surface area was recorded, and was found to decrease in a similar manner to that observed for the non-macroporous material (**figure 5.50**).

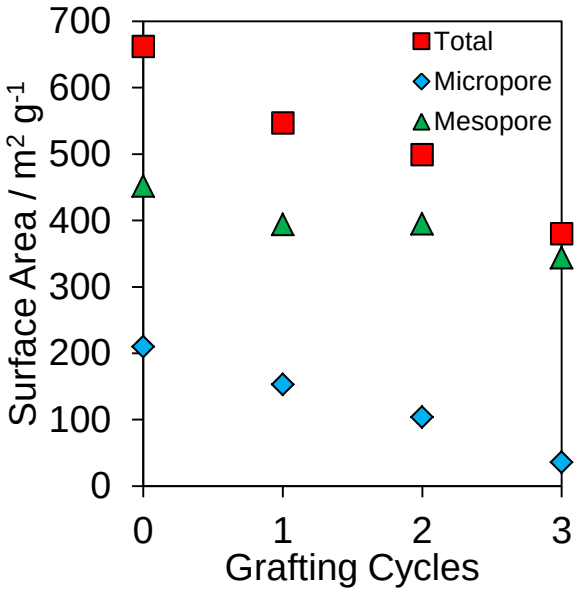

Figure 5.50: Total, mesopore and micropore surface areas of titania grafted macroporous SBA-15.

The Ti 2p region (**figure 5.51**) was fit using line shapes obtained from a commercial anatase material (P25, Degussa), which recorded a Ti $2p_{3/2}$ peak position of 458.8 eV, consistent with reported data for anatase Ti^{4+}.[47] A secondary peak of higher binding energy was fit, representing the formation of Ti-O-Si bonds, resulting in the two sets of peaks exhibited in the Ti 2p spectra[48] caused by a decrease in the positive charge of the titania species within the Ti-O-Si formation compared to that of anatase.[49]

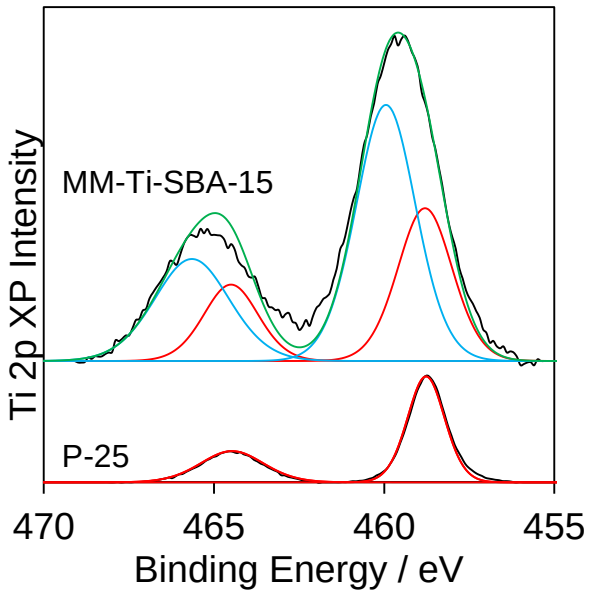

Figure 5.51: Ti 2p region from XPS analysis of macroporous titania grafted SBA-15 and a commercial titania (P-25 – anatase).

Analysis of the oxygen 1s regions (**figure 5.52**) confirmed the presence of three oxygen species, at 532.3 eV, oxygen was detected in the form of silicon dioxide, whilst a secondary peak appeared at 530 eV, which corresponds to titanium dioxide and finally, the bridging oxygens at 531.9 eV.[49]

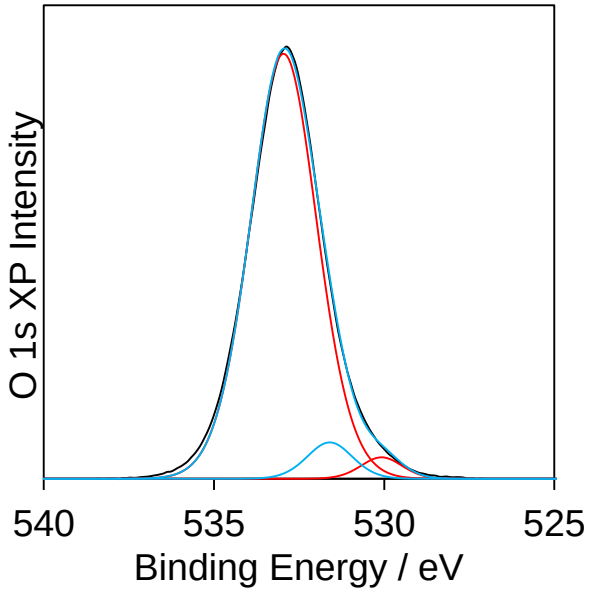

Figure 5.52: O 1s region from XPS analysis of macroporous titania grafted SBA-15.

The XPS spectra from of the silicon regions (**figure 5.53**) reported a peak shift from 103.3 eV, corresponding to silicon dioxide, for the parent MM-SBA-15. The peak was fit with two sets of Si 2p doublets with a doublet separation of 0.6 eV, one corresponding to Si-O-Si, and a second, with a $2p_{3/2}$ peak at 104 eV, corresponding to Si-O-Ti.

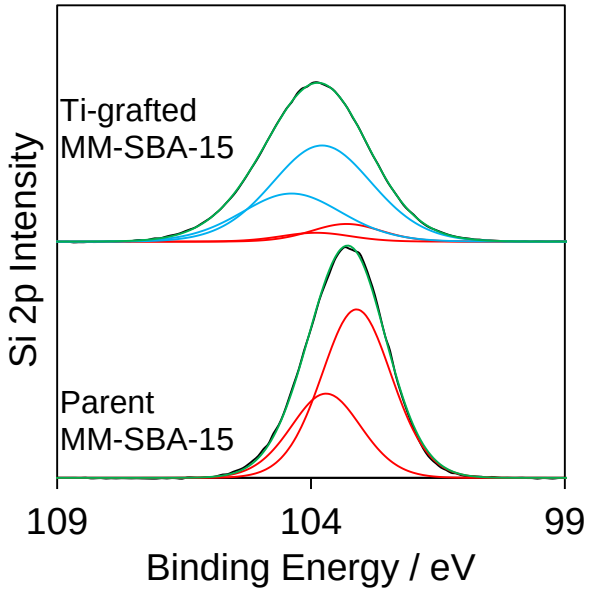

Figure 5.53: Si 2p region from XPS analysis of titania grafted MM-SBA-15 and parent MM-SBA-15.

Following removal of the polystyrene and surfactant template by calcination, the material was studied using TEM, to confirm the presence of macropores and observe the pore channels of SBA-15 (**Figure 5.54**).

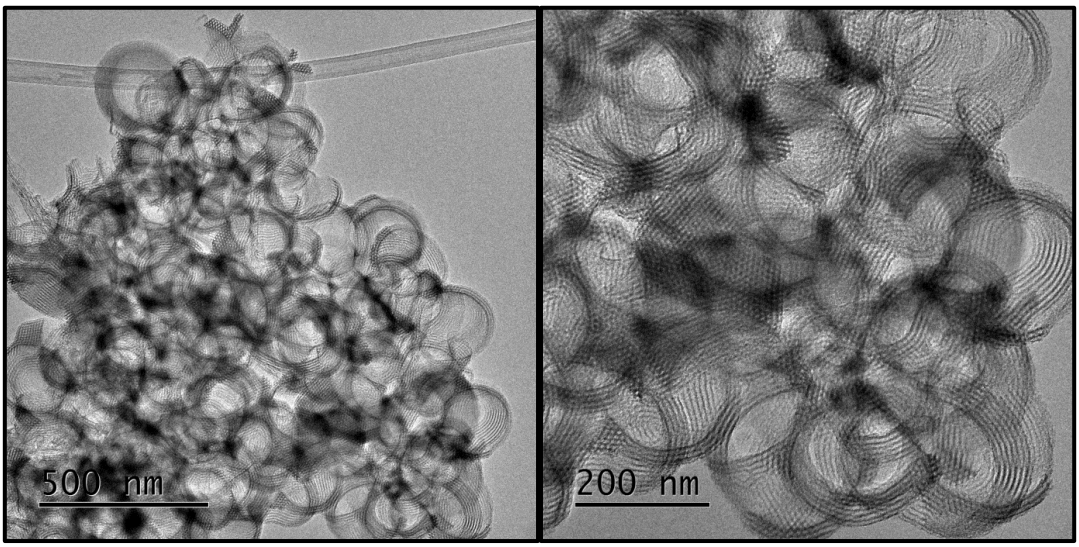

Figure 5.54: TEM image of macroporous SBA-15, before titania grafting (left) and after titania grafting (right).

Following titania grafting, there was no observable evidence of large particle formation of titania throughout the material. This supports the formation of a thin layer of titania on the surface of the hierarchically porous SBA-15. A summary of the

material properties of the synthesised MM-Ti-SBA-15 material supports is presented in **table 5.10**.

Material	Surface Area / m^2 g^{-1}	Micropore Surface Area / m^2 g^{-1}	Pore Diameter / nm	Pore Spacing (XRD) / nm	Pore Spacing (TEM) / nm	Wall Thickness / nm
MM-Ti-SBA-15	380	36	4.5	12.9	12.1	8.4 ± 0.1

Table 5.10: Summary of properties of synthesised MM-Ti-SBA-15.

5.2.1.6. Silver loaded macroporous titania grafted SBA-15

Following the successful grafting of a layer of titania onto the surface of the hierarchically porous structure, the sample was loaded with silver nanoparticles, by the wet impregnation method used in previous sections. The prepared material was analysed by TEM, to determine particle sizes and morphologies. Bright field TEM images are displayed in **figure 5.55**, whereby the silver nanoparticles can be clearly defined from the titania/silica support due to the large differences in contrast.

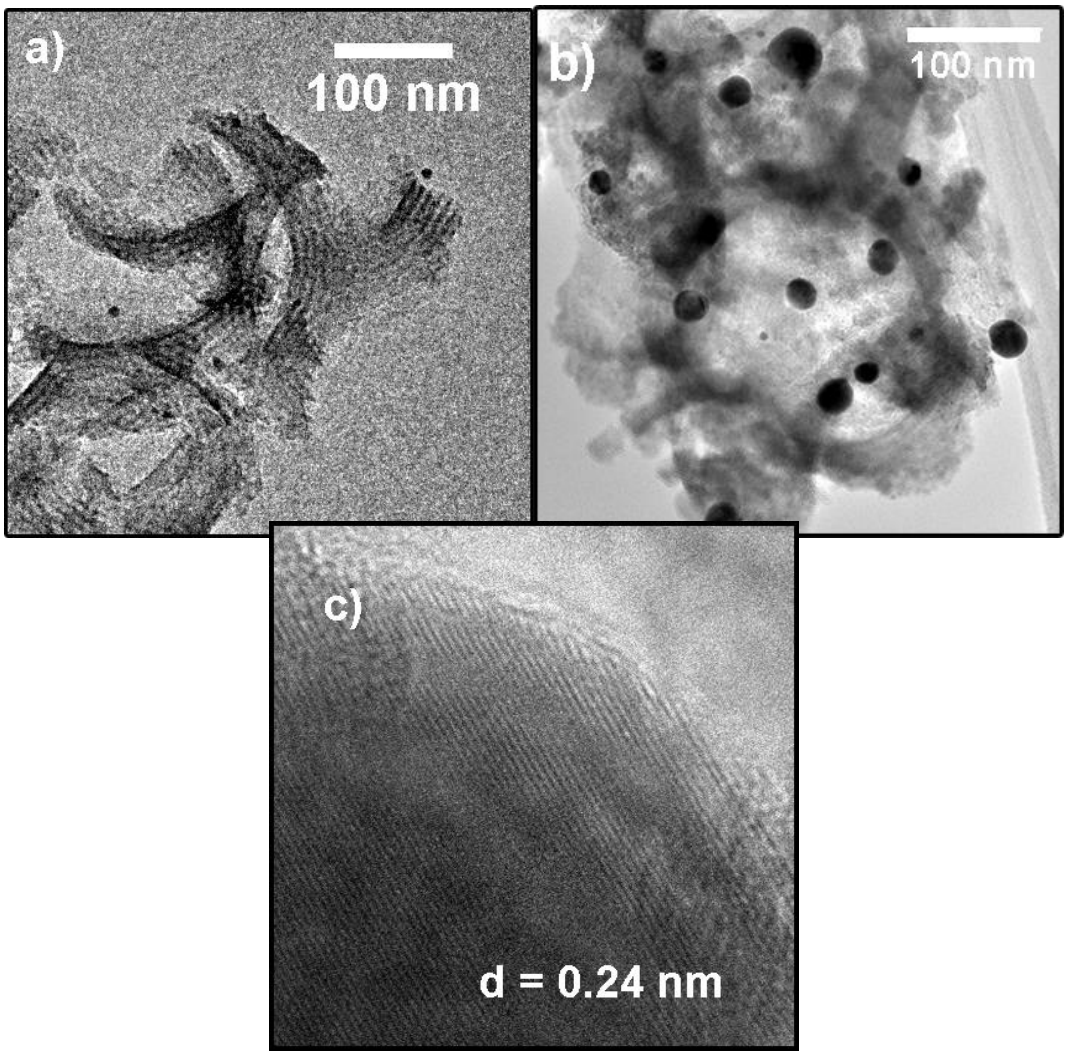

Figure 5.55:Bright field TEM image of Ag-Ti-SBA-15 for (a) 0.28%, (b) 3.65% Ag and HR image of Ag nanoparticle (3.64% Ag).

A clear difference in the approximate average particle sizes can be observed in the electron micrographs. The lowest loading of silver (0.28 wt. %) displays very small, spherical nanoparticles, which seem to exist within the pore network of the material, whereas a number of large agglomerates can be witnessed in the electron micrograph of the highest loading (3.64 wt. %). This is reflected upon viewing of the recorded size distribution histograms, which indicate that whilst most particles in all samples tend towards the small regime, and contained within the pore structure of the materials, but that as loading increases, the number of large agglomerates, external to the pore network appear.

The third TEM image is a HRTEM picture of a silver nanoparticle from the 3.64 wt. % sample, in which the lattice spacing of the silver can be witnessed. This was measured to be 0.24 nm, which would indicate the 111 plane of silver metal.[52]

There is a small increase in the average particle size across the series, along with an increase in the dispersion, as evidenced by the error bars, taken from standard deviation of the counted particle sizes. This is further evidenced by the particle size distribution histograms, shown in **figure 5.56**, in which it is clear that increasing the loading forms large agglomerates, in greater numbers, along with small silver nanoparticles, formed within the mesopore structure.

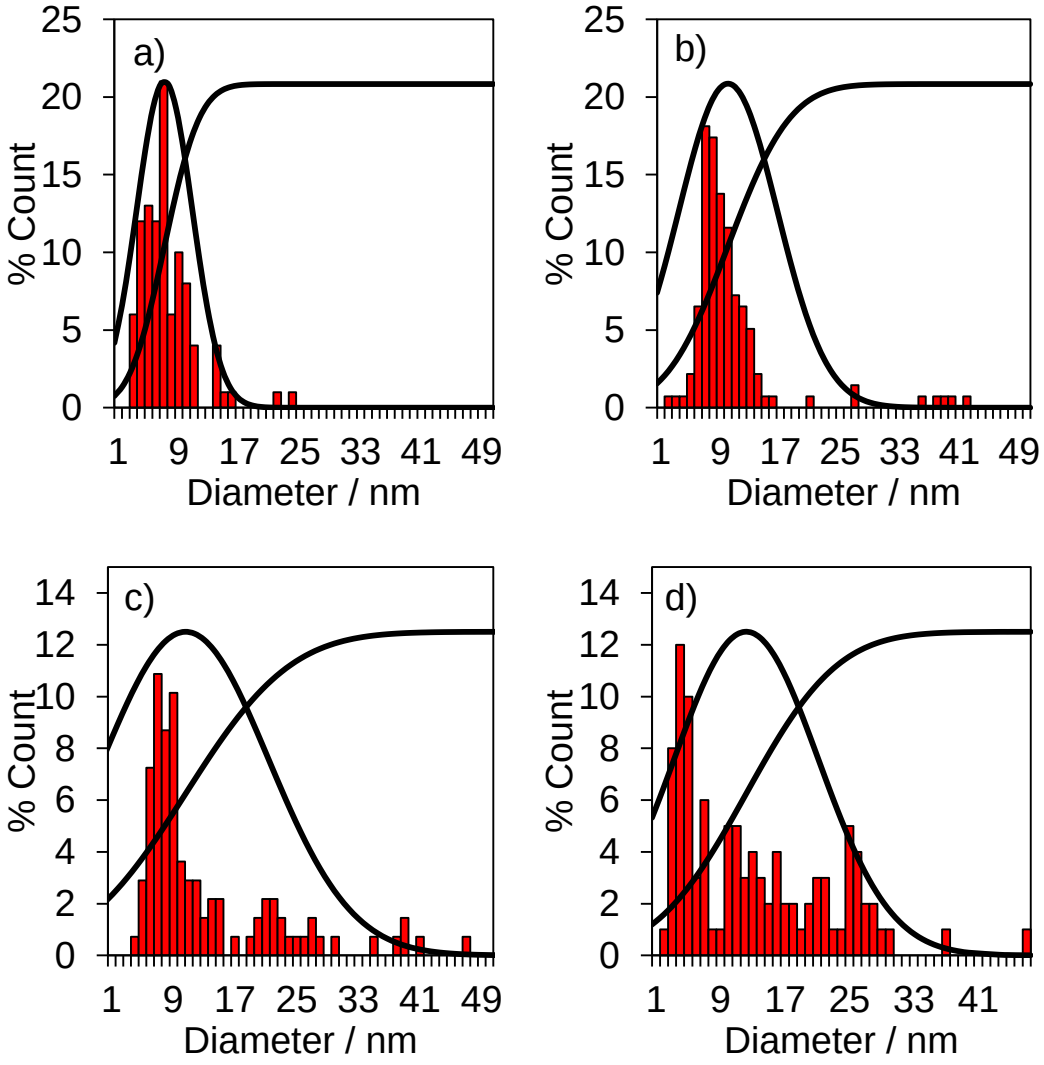

Figure 5.56: Silver nanoparticle size distributions, normal and cumulative distributions for AgTiSBA15 materials determined by bright field TEM for bulk silver loadings of a) 0.28%, b) 0.75%, c) 1.19% and d) 3.65%.

A summary of the particle sizes, which were measured using ImageJ software, is displayed in **figure 5.57**.

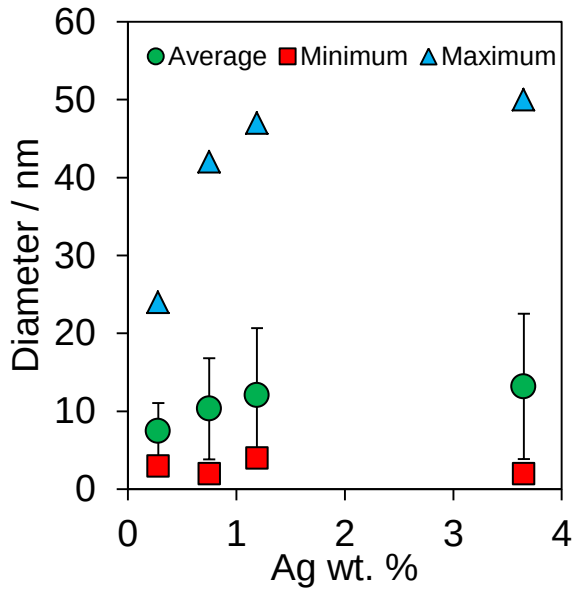

Figure 5.57: Summary of silver nanoparticle size distributions from TEM data for MM-Ag-Ti-SBA-15, based on counts of >100 particles in all cases.

Nitrogen porosimetry was employed to study the internal pore structures, and assess the effect of loading silver nanoparticles onto the prepared supports. The isotherms are displayed in **figure 5.58**.

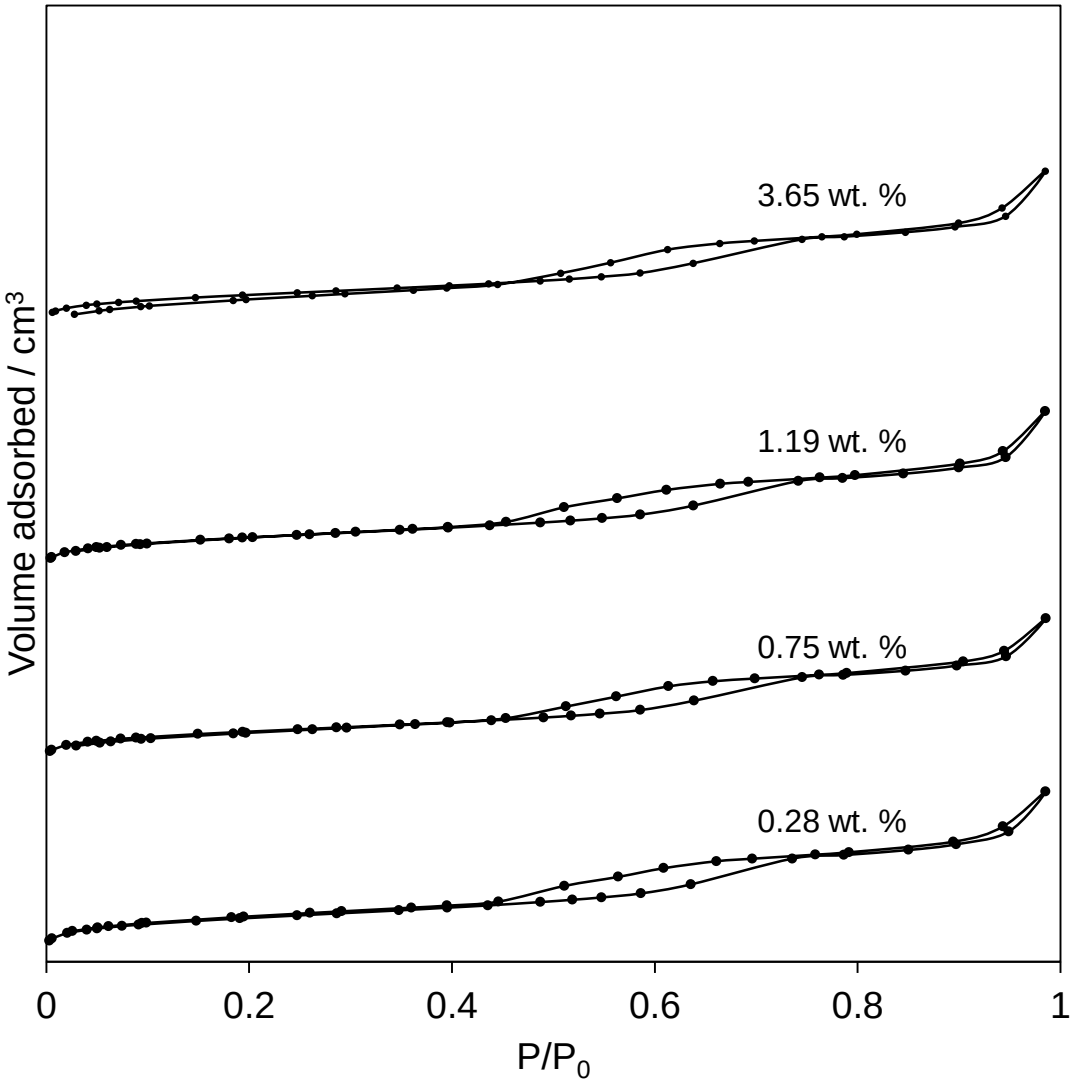

Figure 5.58: Nitrogen adsorption isotherms for Ag-MM-Ti-SBA-15.

The isotherms exhibit a type IV characteristic, which is indicative of a mesoporous material, with a H1 type hysteresis loop which is the result of monodisperse mesopore networks within the material. The isotherms were not altered by a particularly large amount by silver impregnation, although upon analysis of the surface areas utilising the BET equation and the micropore surface area using the t-plot method, it is evident that the silver nanoparticles are, in-fact, blocking a large proportion of micropores and mesopores upon impregnation. The micropore surface areas do not change by a large factor for the different silver loadings, whilst the total surface areas and mesopore surface areas decrease steadily as loading increases (**figure 5.59**).

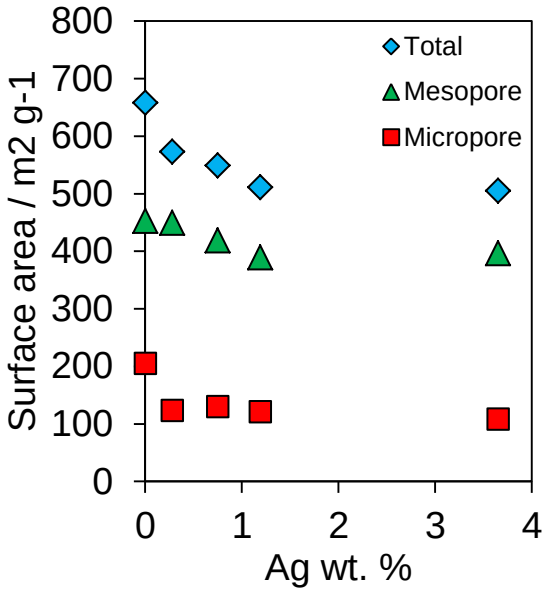

Figure 5.59: Total, meso and micrpore surface areas for Ag-MM-Ti-SBA-15.

This trend in surface area changes could be due to micropores being blocked or filled immediately, upon introduction of silver, however, as seen in the TEM analysis, the main result of further loading with silver is that the number of larger silver agglomerates increases, which would tend to have more of an effect on the mesopore regime, rather than the micropores.

The BJH method was applied, in order to study the pore size distributions and observe how the average pore diameter was affected by the introduction of silver to the pore network (**figure 5.60**).

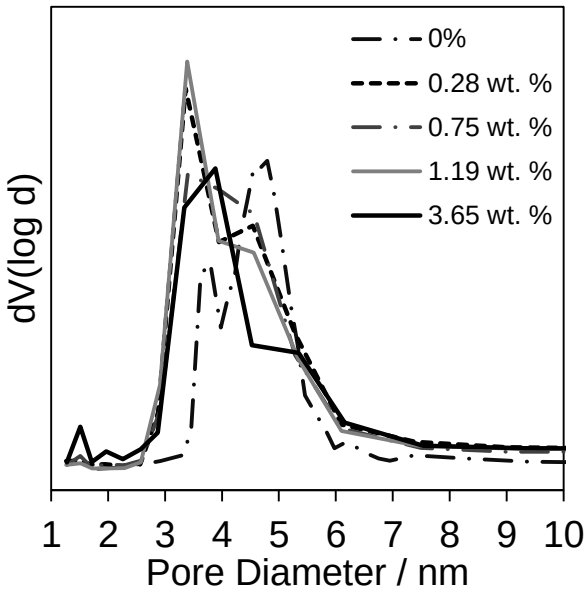

Figure 5.60:BJH pore size distributions for Ag-MM-Ti-SBA-15.

The pore size distribution of the loaded materials indicates pore filling by small nanoparticles. There is a shift to a lower average size, as well as a more polydisperse distribution of sizes. At the highest silver loading, further features appear in the BJH profile, in the form of some reported pores in the region of 1-2 nanometers, which could be due to the presence of an increased number of larger silver particles, which are almost completely filling the pores, leading to the reporting of very small pores.

Powder XRD was used to study the effect of the silver loading upon the pore network, as well as analyse the crystalline phase of the impregnated silver nanoparticles. The recorded low angle XRD patterns are displayed in **figure 5.61**.

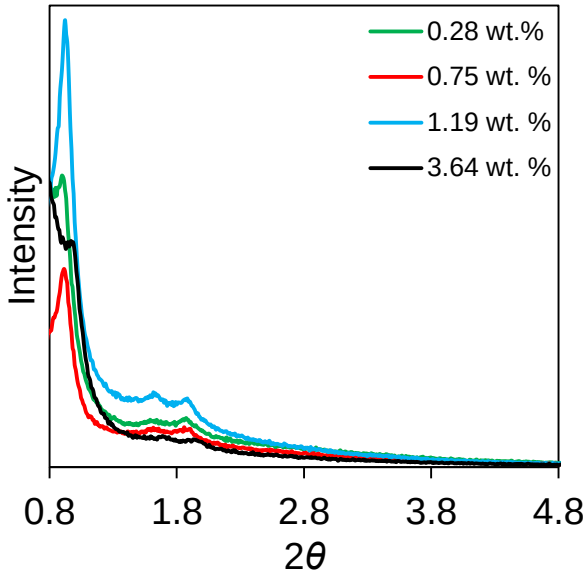

Figure 5.61: Low angle XRD patterns for Ag-MM-Ti-SBA-15.

It can be seen from the low angle XRD diffractograms, that the prepared materials all exhibit the characteristic patterns for a hexagonally arranged pore network with symmetry of *P*6*mm*. It can be concluded that the loading of silver bears no effect on the pore network of the prepared materials. The pore spacings can be calculated from these patterns, using **equation 4.2**. The results of these calculations are displayed in **figure 5.62**.

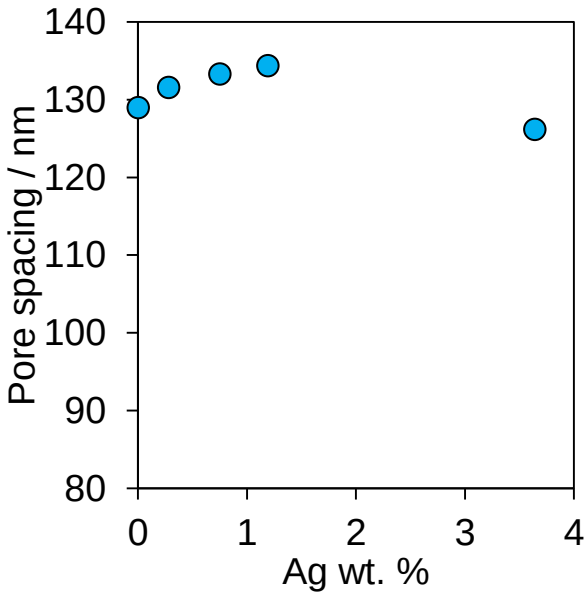

Figure 5.62: pore-spacings calculated form low angle XRD patterns for Ag-MM-Ti-SBA-15.

The pore spacings remain constant across the series, further confirmation of the negligible effect of silver loading on the base support structure.

Wide angle XRD was employed in an attempt to determine the phase of the prepared materials. The recorded patterns are exhibited in **figure 5.63**.

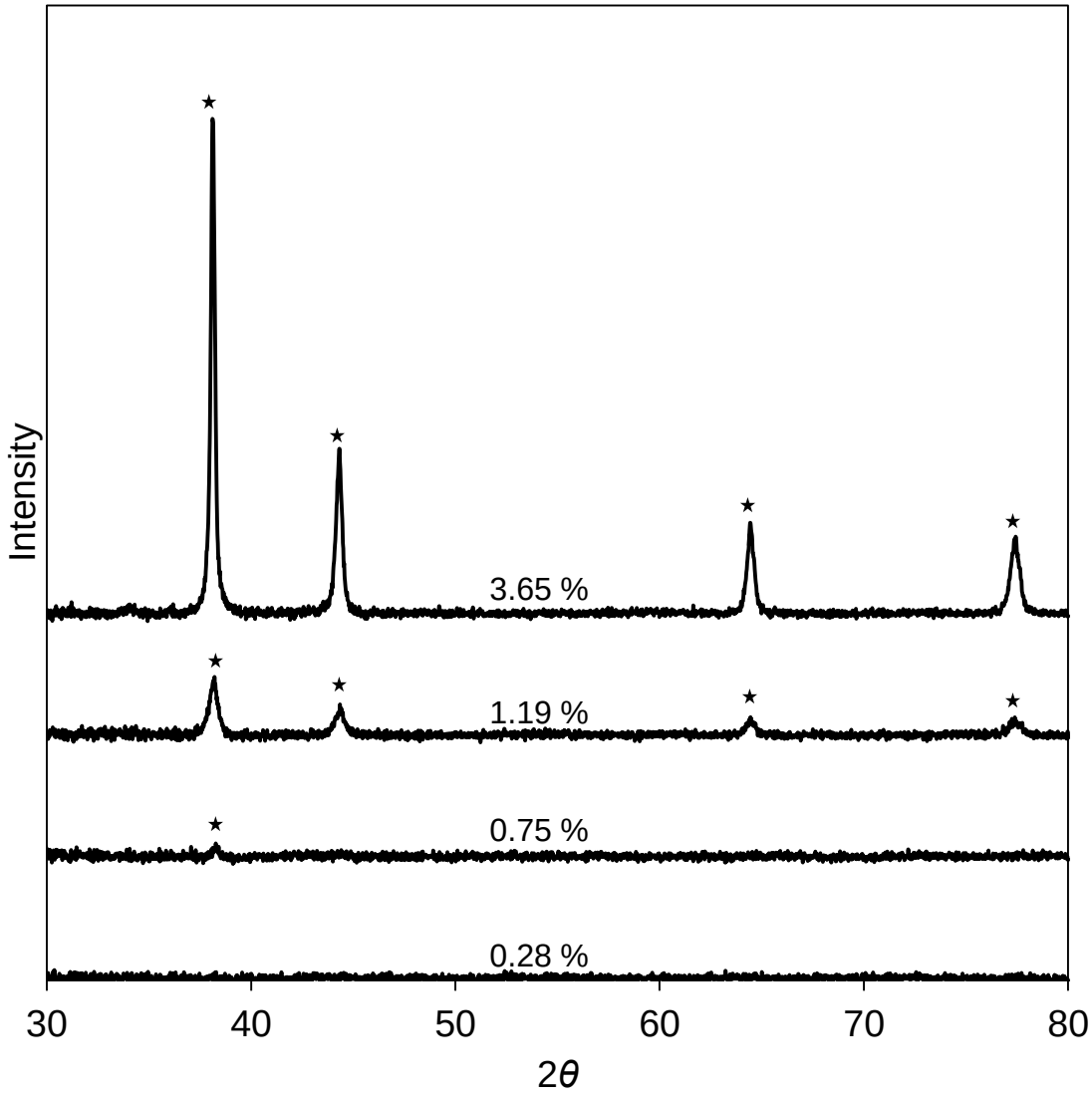

Figure 5.63: Wide angle powder XRD patterns for MM-Ag-Ti-SBA-15.

The powder XRD patterns indicate once again the presence of silver metal, with peaks corresponding to an Ag^0 FCC metal structure. Metal particle sizes were determined via the Scherrer equation and compared to those determined by TEM analysis. The lower loadings, combined with what were ultimately determined to be

lower average particle sizes compared with the non-macroporous materials resulted in very weak diffractions for the lowest 2 samples and, accordingly, FHWM which are difficult or impossible to measure. For the materials with a higher weight percentage of silver, and a greater degree of large silver agglomerates, the XRD patterns record clear, strong reflections existing in a manner suggestive of a majority composition of silver metal. No silver phases were detected for 0.28% MM-Ag-Ti-SBA-15 and hence particle size could not be determined (**figure 5.64**).

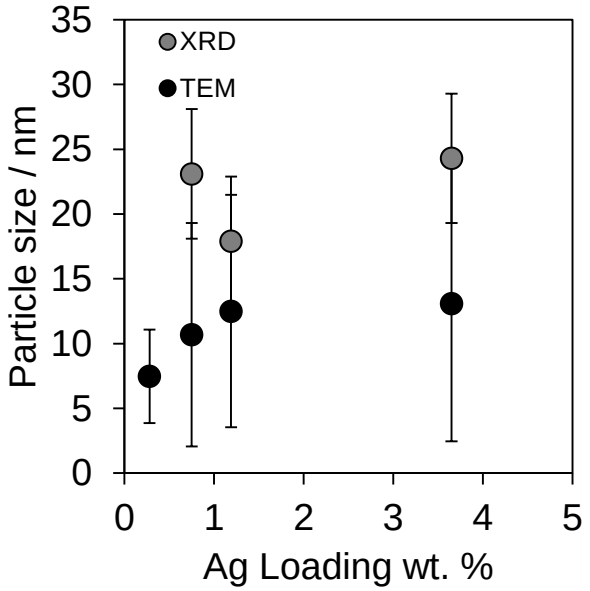

Figure 5.64:Silver particle sizes, as determined by XRD and TEM for MM-Ag-Ti-SBA-15.

Further characterisation of the silver species was achieved using XPS. The silver 3d species were observed to possess the characteristic $3d_{5/2}$ and $3d_{3/2}$ peaks and were fit with peak ratios or 3:2 and a doublet separation of 6 eV. All spectra were calibrated to adventitious carbon at 284.7 eV. A stack plot of the Ag 3d regions is displayed in **figure 5.65**.

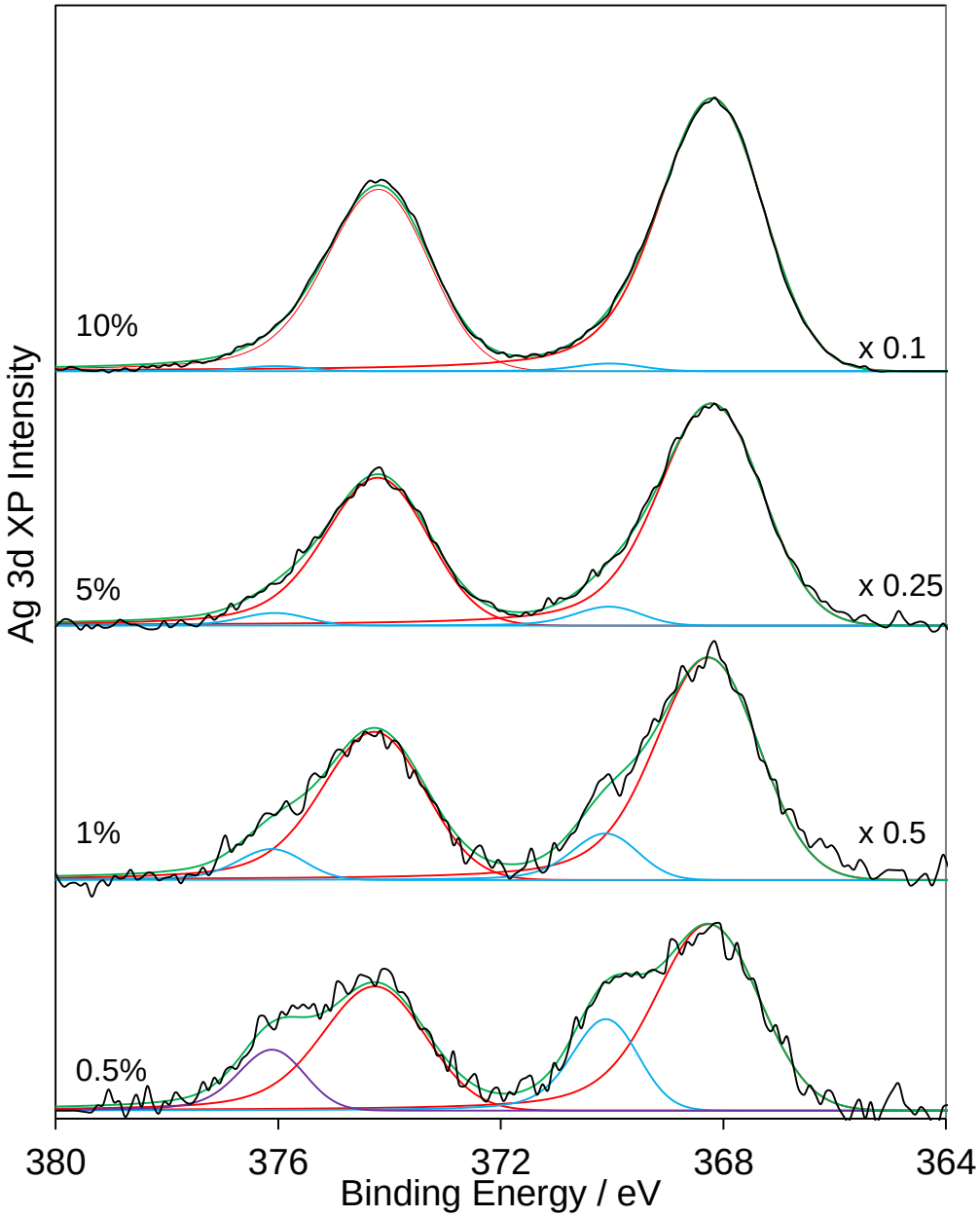

Figure 5.65: Ag 3d XPS stack plot for MM-Ag-Ti-SBA-15.

The XPS spectra from the prepared silver nanoparticles reported clear evidence of a dual oxidation state, as with the previous materials. The Ag $3d_{5/2}$ peak at 368.1 eV was again fit as the silver metal species (red lines), whilst the small shoulders at 370 eV were fit as silver carbonate species (blue lines). The composition of the two species is displayed in **figure 5.66**.

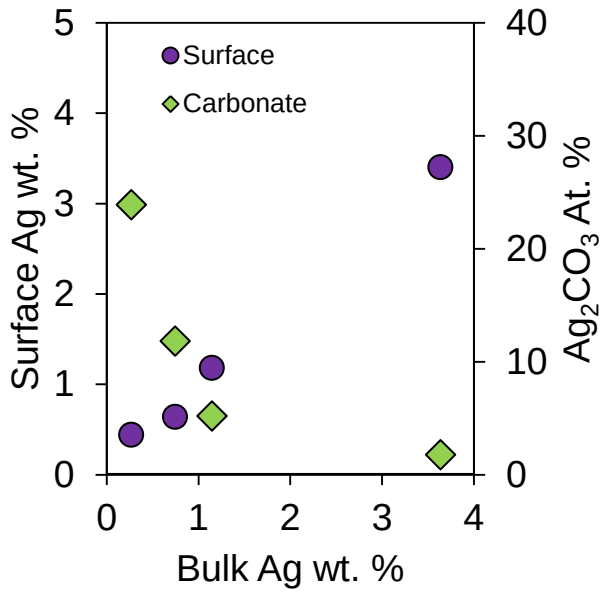

Figure 5.66: Surface carbonate and total surface silver loadings vs bulk Ag wt. % for MM-Ag-Ti-SBA-15.

The total percentage of carbonate species decreases as silver loading increases. This is suggestive of a surface carbonate species, likely existing as a small layer encasing the silver nanoparticles. Upon an average increasing of particle size, due to the presence of large agglomerates as loading increases, the majority of silver observed is that of bulk silver metal, and the carbonate species becomes less pronounced. If the carbonate is a surface species, this data could be explained as a decrease in the total amount of surface silver, with an increase in silver bulk species. Supporting the idea of a surface species of carbonate, is the increased surface carbonate content, compared to the less disperse silver particles within non-macroporous Ag-Ti-SBA-15.

The Ti 2p regions were studied, with the $2p_{3/2}$ and $2p_{1/2}$ peaks fit at area ratios of 2:1 and a doublet separation of 5.7 eV (**figure 5.67**).

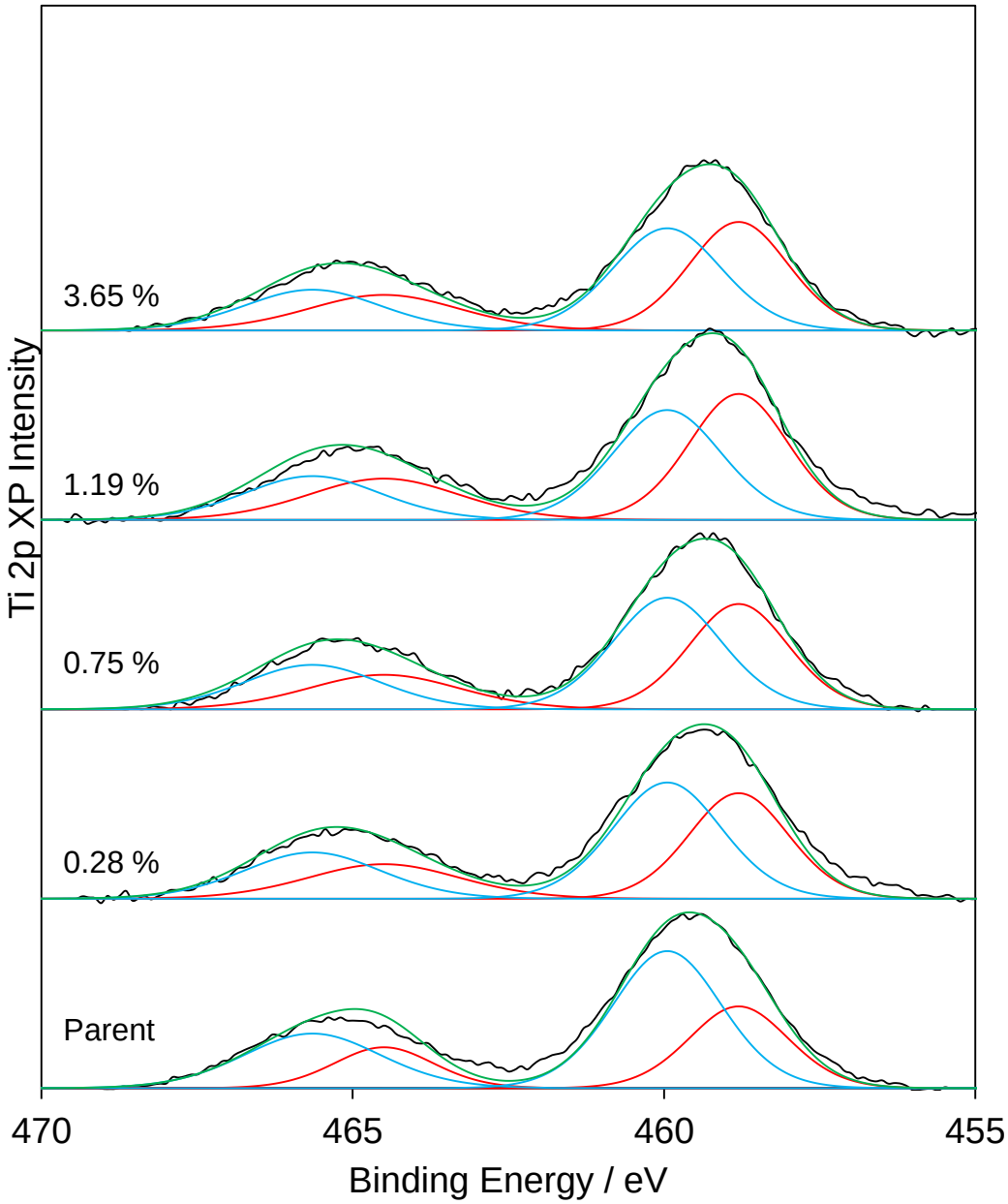

Figure 5.67: Ti 2p XPS stack plot for MM-Ag-Ti-SBA-15.

There is no appreciable change in the titania species upon silver loading, the Ti 2p regions exhibiting both Ti-O-Ti and Ti-O-Si species as witnessed in the parent material. The titania:silicon ratio was not found to change to any significant degree (**table 5.11**).

Bulk Ag wt. %	Ti:Si (XPS)
0	0.26
0.28	0.29
0.75	0.26
1.15	0.25
3.64	0.23

Table 5.11: Ti:Si surface ratios.

A full summary of the three series is presented in **table 5.12**. In this table, it is evident that in all cases, average particle size, determined from TEM analysis, increases with bulk silver loading, as does the polydispersity of particle diameters. All materials display high surface areas, which decrease across all series with bulk silver loading, as pores are blocked by silver particles. In the case of the titania based materials, formation of a surface carbonate species is evident, with the total % of silver in the form of carbonate increasing with decreasing average silver particle diameter, indicative of a surface species.

Material	Surface Area / m^2 g^{-1}	Surface Ag wt. %	% Ag Carbonate	Mean Ag Diameter (TEM) / nm	Standard Deviation of Ag Particle Size / nm
SBA-15	830	-	-	-	-
0.3% Ag	492	0.45	0.00	14.58	5.79
0.95% Ag	501	0.56	0.00	18.09	7.71
2.4% Ag	395	1.32	0.00	18.62	8.01
3.5% Ag	377	2.45	0.00	20.79	10.14
Ti-SBA-15	634	-	-	-	-
0.3% Ag	593	0.74	2.86	14.08	4.32
0.9% Ag	577	1.11	1.80	18.91	7.50
2.3% Ag	500	2.39	0.85	19.27	8.86
3.7% Ag	493	3.82	0.55	21.36	9.19
MM-Ti-SBA-15	380	-	-	-	-
0.28% Ag	373	0.44	23.90	7.48	3.60
0.75% Ag	349	0.64	11.81	10.32	6.48
1.15% Ag	311	1.18	5.18	12.07	8.60
3.64% Ag	305	3.40	1.77	13.19	9.33

Table 5.12: Summary of material properties for all series.

5.2.2. Performance assays

The microbiological performance of the prepared materials was examined by studied the silver ion release rates, via the methodology in **Chapter 2.4**, and correlating them to antibacterial activities, as determined by the methods outlined in **Chapter 2.5**.

5.2.2.1. Silver dissolution

The dissolution of silver ions into solution from the bulk material was investigated in order to study the delivery rates of the active species as a function of time. The materials were all compared to a slow releasing silver compound, silver carbonate, which exhibits dissolution kinetics favourable towards the slow release of active silver species.

The silver release rates were determined using ICP-MS to study the concentration of silver ions in filtered solutions taken at set time intervals from vessels containing the target sample and an aqueous buffer solution of 0.5 M $NaNO_3$. ICP-MS allowed for detection of the incredibly low silver concentrations within the resultant mixture, which were in the sub-ppm range (1-1000 ppb). Due to the limitations of allowed ionic species within the ICP-MS, the experiments could not be run in a simulated bodily fluid solution such as that which was used for antibacterial testing.

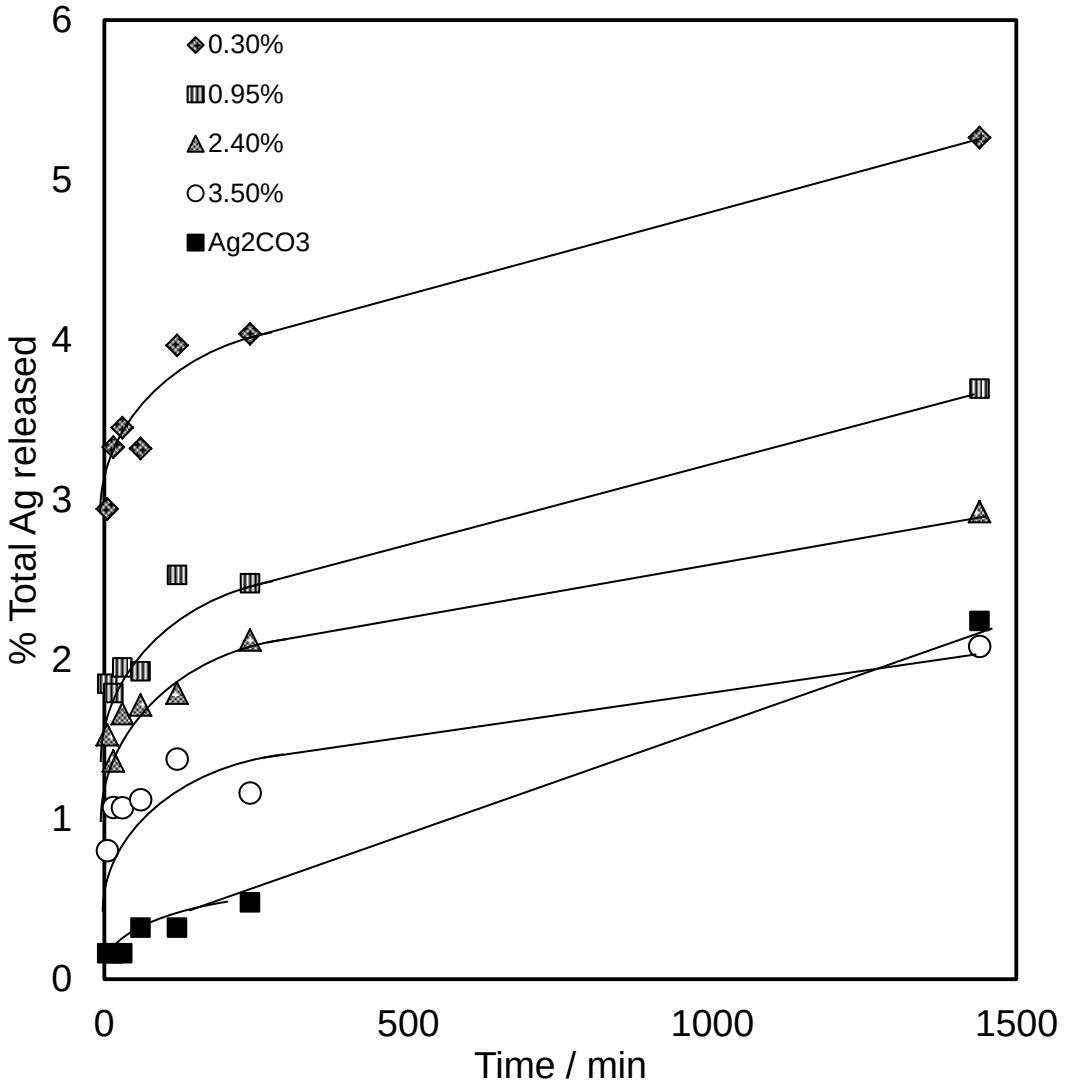

Figure 5.68: Silver ion dissolution rates from Ag-SBA-15, normalised to silver content.

Figure 5.68 displays the silver release profile for the Ag-SBA-15 series of composite materials. Evident from these plots is the fact that the dissolution rates for these materials appear to be incredibly slow, with an initial release reaching a critical concentration of dissolved Ag^+ ions at near to the 4 hour mark of the experiments, after which the silver ion release is significantly retarded. It has been observed in previous studies that this an equilibrium point is reached after around 6 hours of dissolution, prior to a slowed release rate of dissolved silver ions, at which point free silver ions can feither form aggregates, or rejoin existing nanoparticles.[57] This suggess that an initial spike in silver release is followed by a subsequent steady release of silver into solution,

which could result in a material which fulfills both a fast acting and long lasting antibacterial function.[57]

Overall silver percentage released increases as the silver loading decreases, which indicates that the rate of initial release in fact increases as silver loading, and hence average particle size, decreases. This can be assigned as a surface area effect, as the total metal surface area per unit mass increases, silver release rate increases.[58]

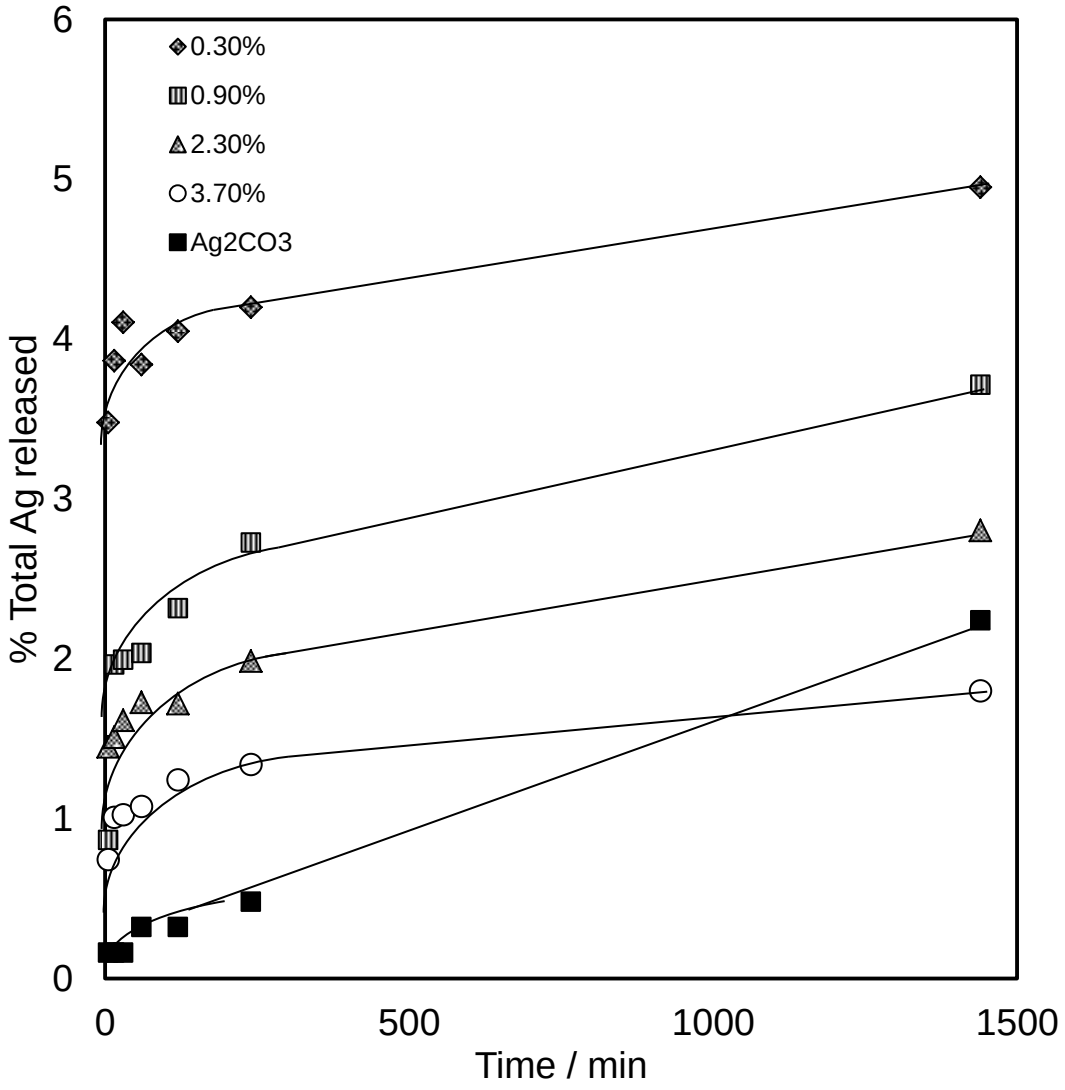

Figure 5.69: Silver ion dissolution rates from Ag-Ti-SBA-15, normalised to silver content.

The dissolution profiles for Ag-Ti-SBA-15 materials are presented in **figure 5.69**. Being that the particle size distributions for the silver loaded, titania grafted mesoporous silica systems are comparible to those of silver nanoparticles deposited

onto conventional SBA-15 materials, it is expected, and is observed, that the dissolution kinetics are not significantly different. As exhibited by the the silver ion release profiles of the mesoporous silica materials, the overall decrease in solid particulate silver increases in magnitude as loading and average particle size decreases.

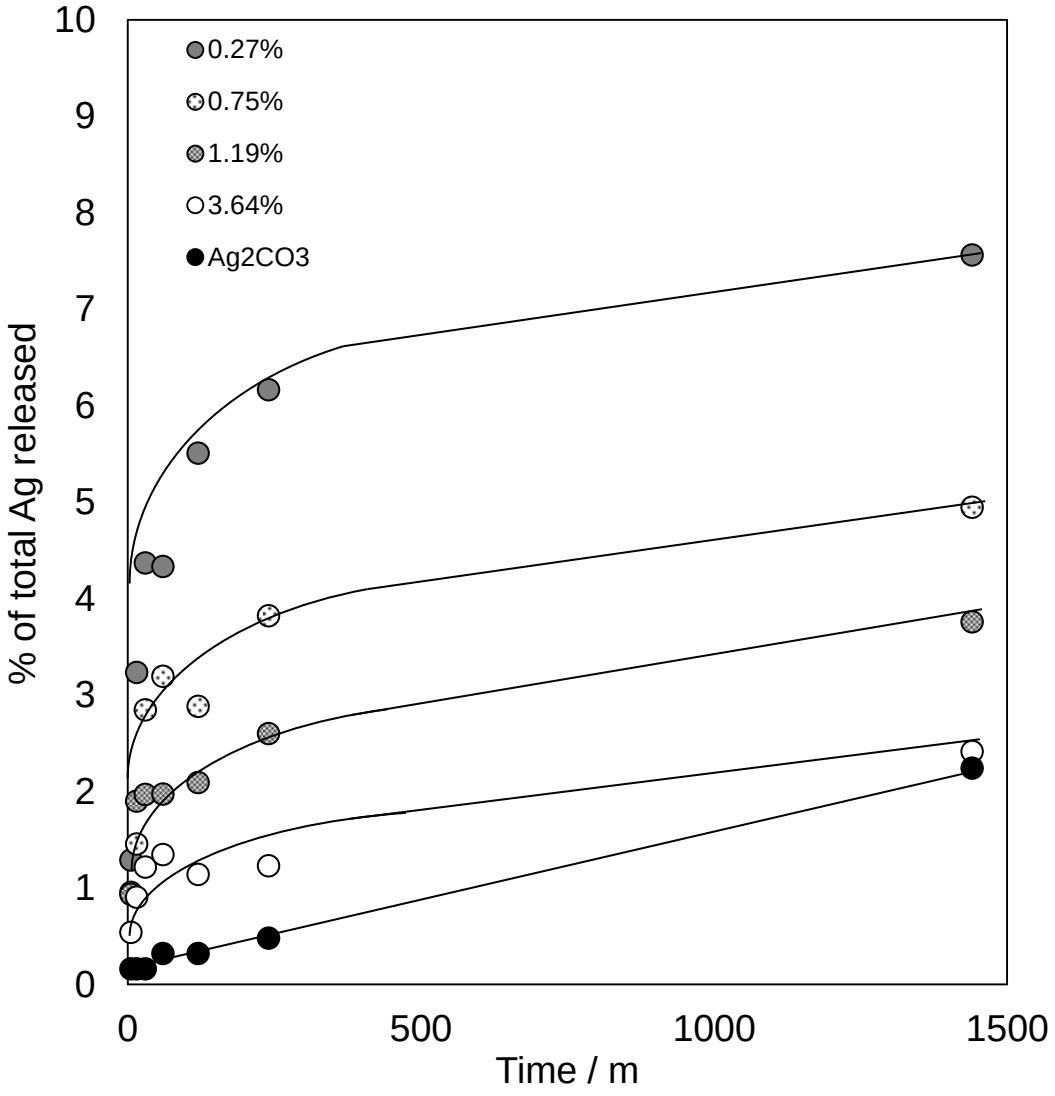

Figure 5.70: Silver ion dissolution rates from MM-Ag-Ti-SBA-15, normalised to silver content.

Figure 5.70 displays the silver ion release profiles for hierarchically porous, titania grafted SBA-15 loaded with silver nanoparticles. A similar trend to that of the previous materials is observed, with an initially faster release rate, followed by an approach of an equilibrium point and subsequent rate decrease. These materials, however, exhibit an increase in overall mass percentage decrease, implying that the initial release of silver

is faster than that of the reported dissolution profiles for the mesoporous materials. This can be ascribed to an overall decrease in average silver particle size, as reported via TEM and XRD analysis of the as synthesised materials.

In order to compensate for alterations in silver particle sizes, the profiles were normalised to total metal surface area, calculated from average particle sizes. These are displayed in **figure 5.71**.

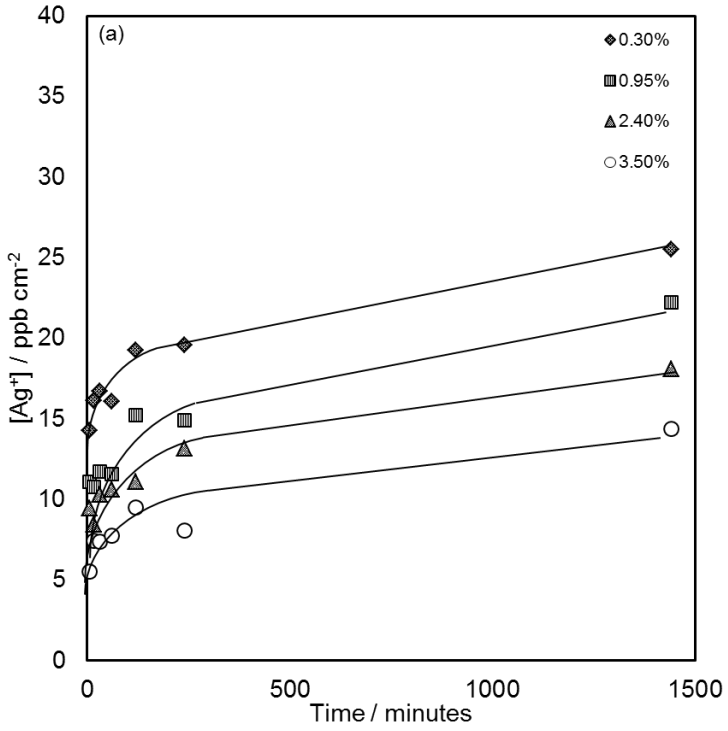

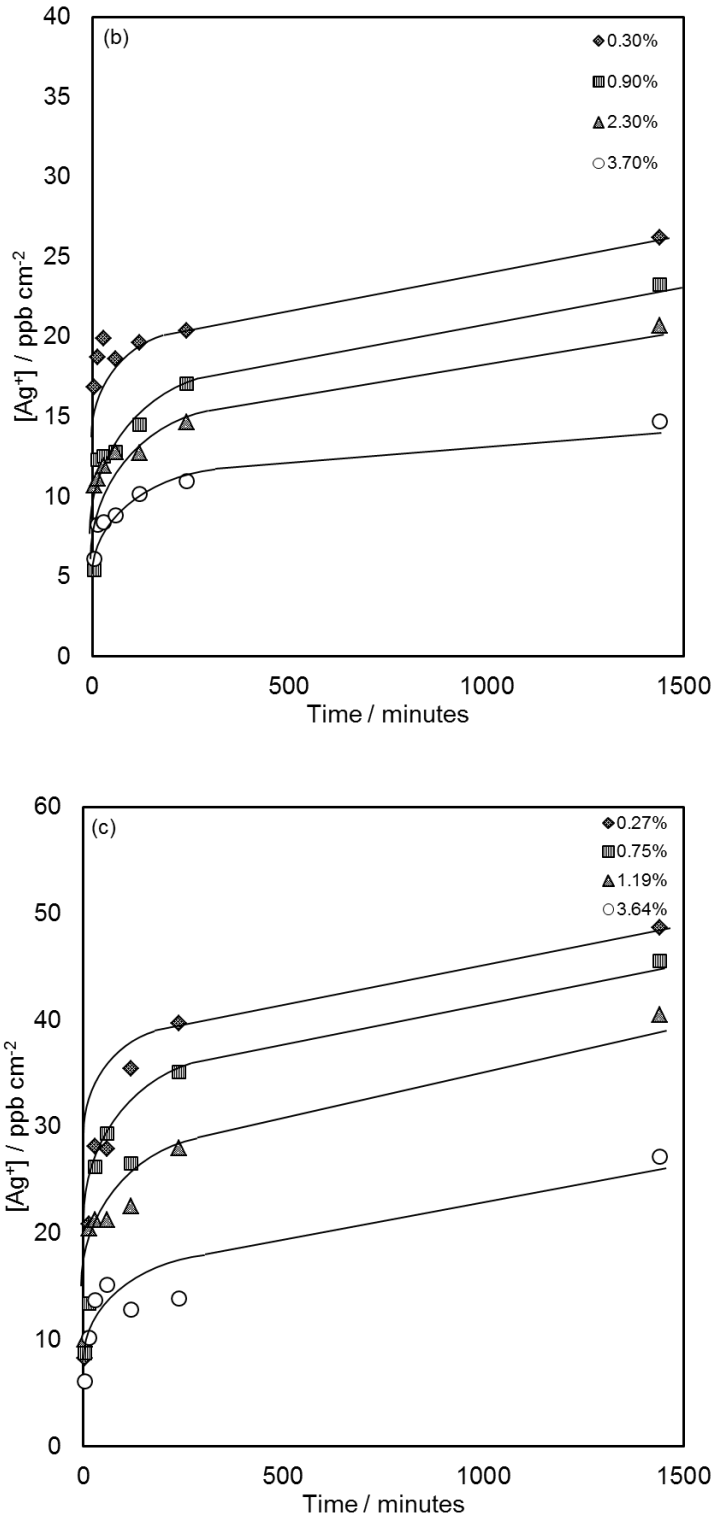

Figure 5.71 Silver ion dissolution profiles for (a) Ag-SBA-15, (b) Ag-Ti-SBA-15 and (c) MM-Ag-Ti-SBA-15 normalised to total metal surface area.

It is observed within the dissolution profiles, normalised to total metal surface area, that the dissolution rates increase for smaller particles. It has been observed previously that particle size can affect silver dissolution kinetics, and that smaller particles are more effective at silver release due to increased surface area per unit mass and these dissolution profiles concur with that.

Support effects upon silver dissolution are primarily relating with the introduction of macropores. These open structures allowed for an increase in silver dispersity, which increased the silver ion release rates as observed above. There was no significant difference between the dissolution of silver from SBA-15 or Ti-SBA-15 materials, suggesting carbonate species bear little effect upon release rates.

5.2.2.2. Antibacterial assays

The antibacterial activity of the prepared materials was studied utilising the profiling methodologies outlined in **section 2.5**. Zones of inhibition, minimum bactericidal concentration and logarithmic reduction experiments were performed to characterise the antibacterial potential of each type of material.

5.2.2.2.1. Zone of inhibition

Zone of inhibition experiments (**figures 5.71** & **5.72**) were performed as a semi-quantitative method for probing antibacterial efficacy. The zone of inhibition test involves spreading a bacterial inoculum onto an agar plate, boring holes into the agar, inserting the material, dispersed in simulated body fluid, into the resulting wells and incubating. After 24 hours at 37^{o}C, the wells will have a clear zone around them where bacteria have not been allowed to grow. This zone can be measured and used as an indicator of antibacterial activity and comparative strength, although this test is heavily limited by diffusion through the agar itself. The zones are reported in millimetres and normalised to total silver content.

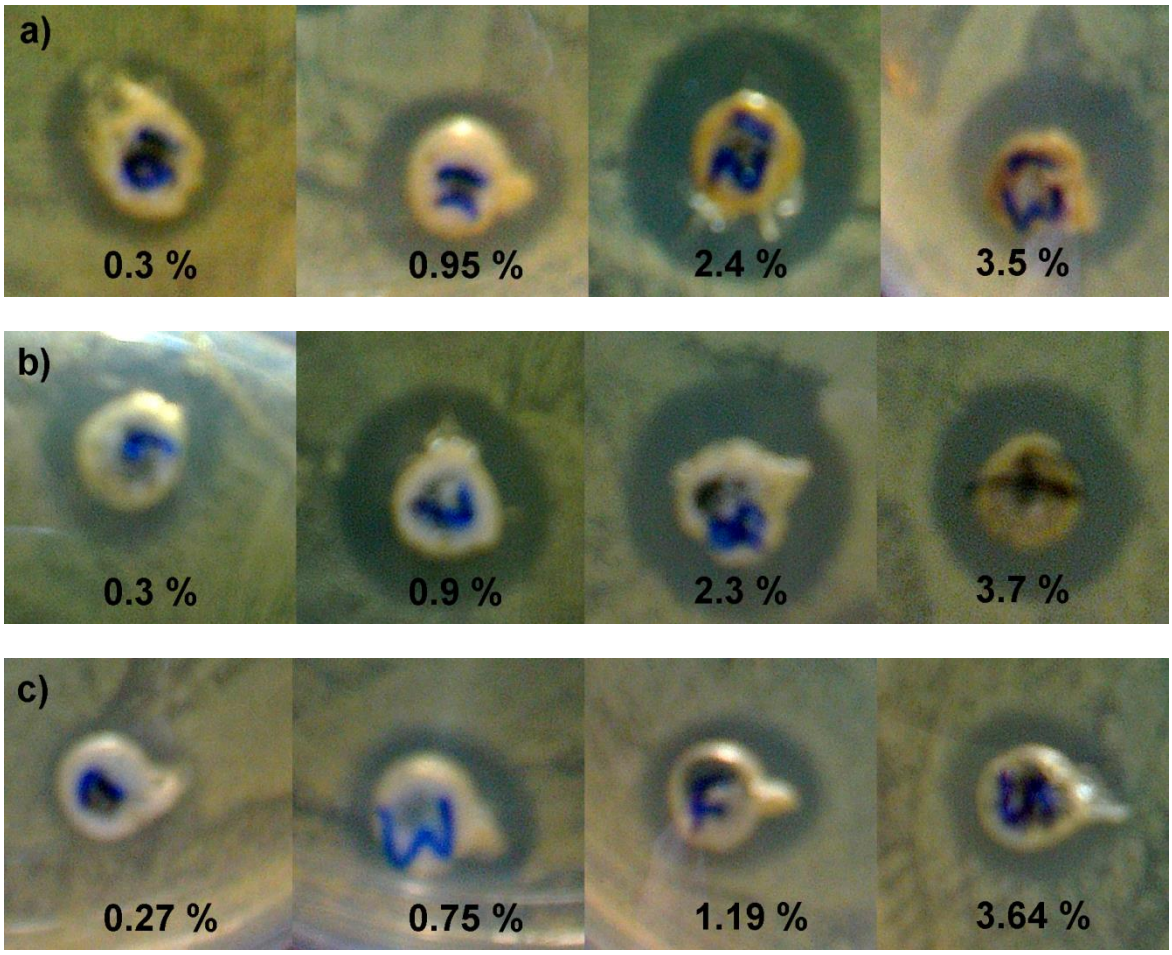

Figure 5.72: Zones of inhibition for (a) Ag-SBA-15, (b) Ag-Ti-SBA-15 and (c) MM-Ag-Ti-SBA-15 against *Staphylococcus aureus.*ATCC 6538

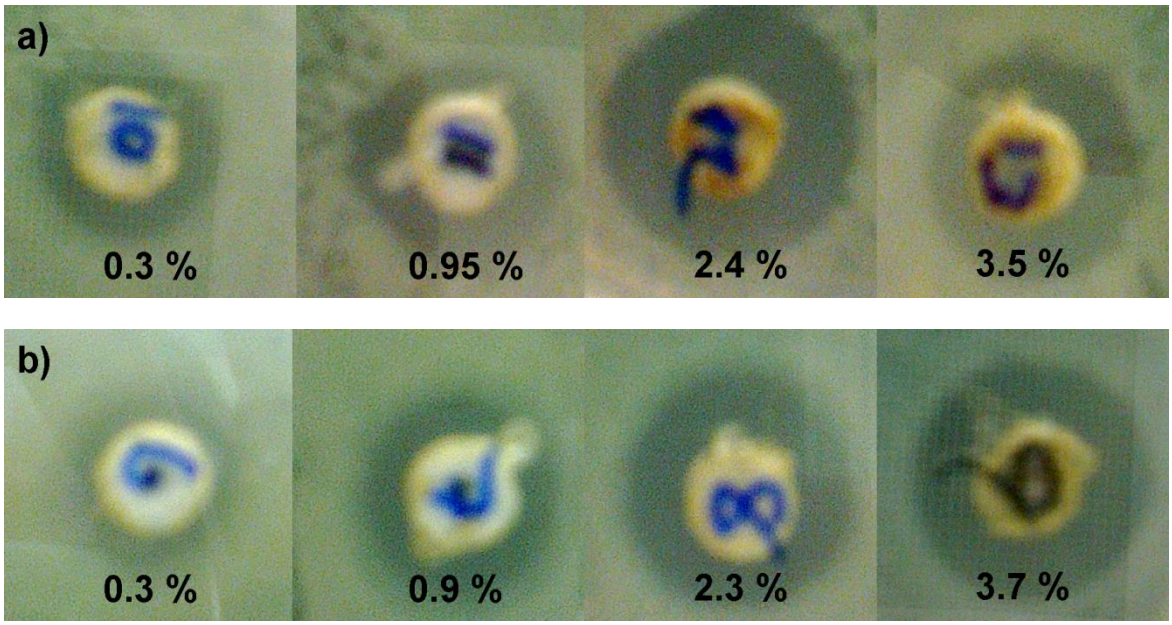

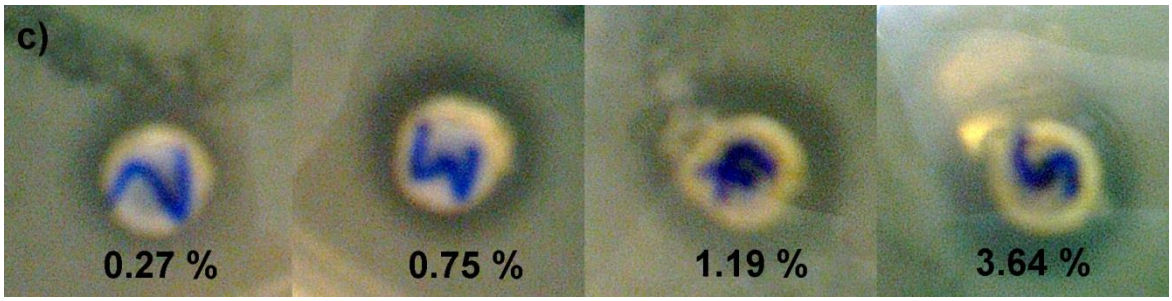

Figure 5.73: Zones of inhibition for (a) Ag-SBA-15, (b) Ag-Ti-SBA-15 and (c) MM-Ag-Ti-SBA-15 against *Pseudomonas aeruginosa* ATCC 15442

The visible rings around the central wells represent the zone in which bacterial growth has been inhibited, which is measured using ImageJ software, calibrated to a ruler. The summary of the measure zones, normalised to bulk silver content, is shown in **figure 5.74**.

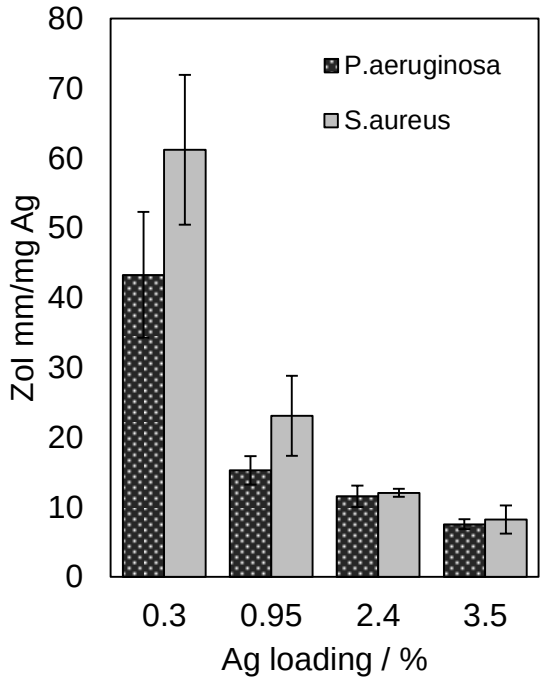

Figure 5.74: ZoI plots for Ag-SBA-15, normalised to bulk Ag content

That the lowest loading material appears to have the greatest activity of the series can be attributed to the limiting effect of silver ion diffuson through the agar, resulting in diminished results for the higher loaded samples.

A similar trend is witnessed for the Ag-Ti-SBA-15 materials, as evidenced in **figure 5.75**;

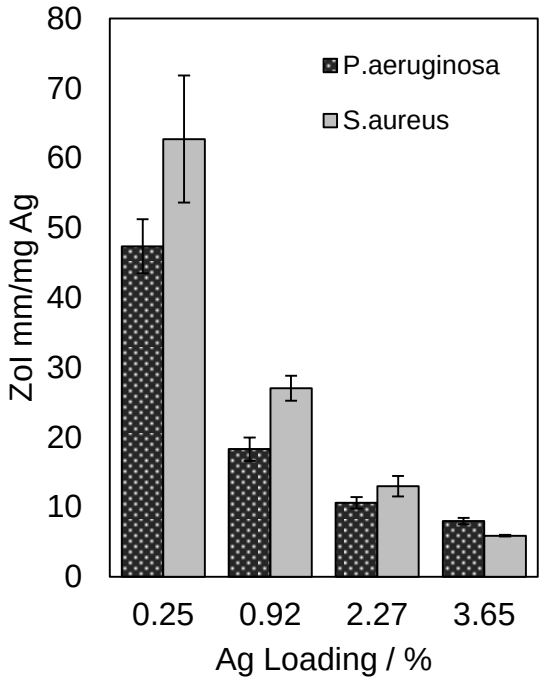

Figure 5.75: ZoI plot for Ag-Ti-SBA-15, normalised to bulk Ag content

That the lowest loadings exhibit this level of antibacterial efficacy is not only indicative of the antibacterial potency of silver ions, but also the effective delivery from the nanocomposites.

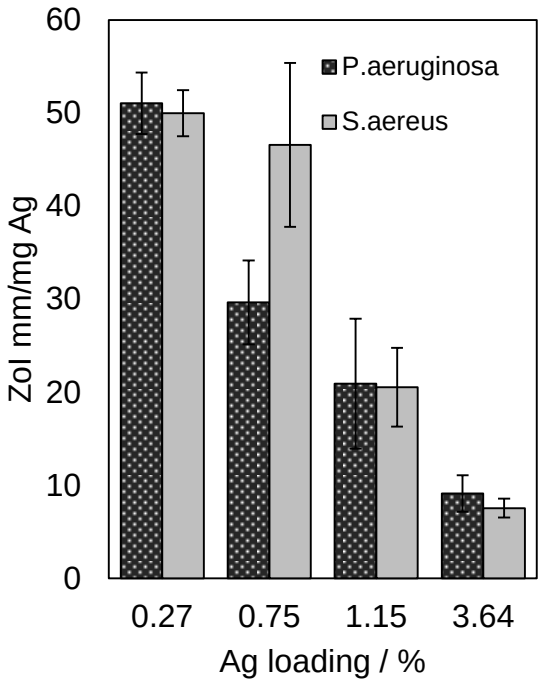

Figure 5.76: ZoI plot for Ag-MM-Ti-SBA-15, normalised to bulk Ag content.

The results from the hierarchically porous material follow a similar general trend, although the lowest loading material was found to exhibit slightly lower than expected zone sizes. The semi-quantitative nature of these zone of inhibition tests, however, lessens the significance of the results when compared with the logarithmic reduction results later on. A summary of these zones, normalised to total silver content is summarised in **figure 5.77**.

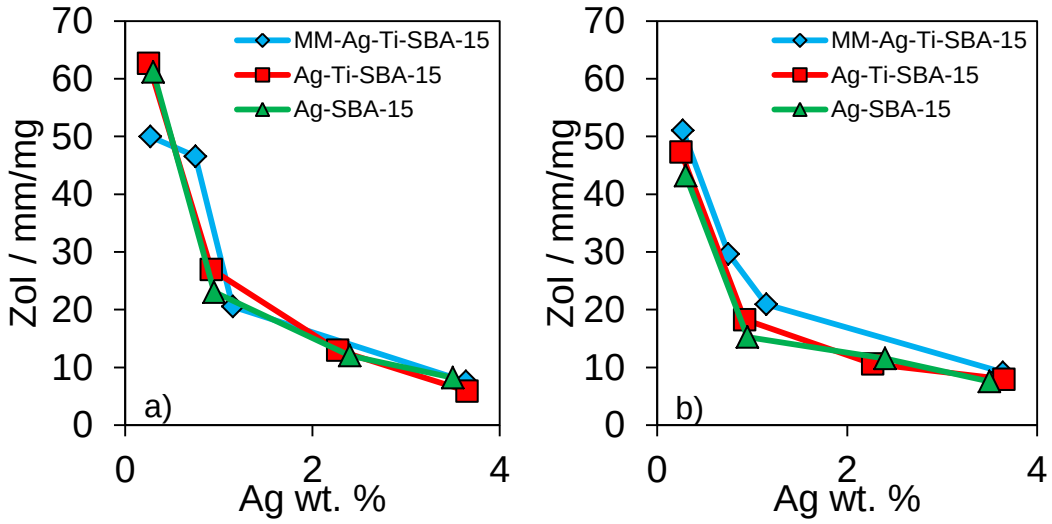

Figure 5.77: Zones of inhibition against (a) *S.aureus* and (b) *P.aeruginosa*.

From these plots, the hierarchically porous materials appear to exhibit a slight performance increase against both organisms at lower loadings, with the exception of 0.28 % MM-Ag-Ti-SBA-15, which appears to be less effective per unit mass than the mesoporous materials. This could be due to the relatively small zones exhibited by these loadings, in which small errors may have a greater effect on the final calculated zone.

5.2.2.2.2. Minimum bactericidal concentration

Study of the lower limits of antibacterial activity was performed to determine suitable concentration ranges to study during the logarithmic reduction experiments which would allow for a reasonable time period to study.

This was performed as described in **section 2.5.2** and involved preparing solutions containing the target organism at a known concentration, along with the test material at a variety of concentrations to determine a break point, below which the material was not considered antibacterial. These solutions were incubated with agitation at 37^{o}C for 24 hours, before being plated out and the bacterial colonies counted.

The solutions were made using a serial dilution technique and the materials were dispersed into a solution of microorganisms in the following concentrations; 1, 0.1, 0.01, 0.001 and 0.0001 mg/ml. The materials were in contact with the microorganisms over a 24 hour time frame, at which point a sample of the solution was taken and spread onto an agar plate before being incubated at 37^{o}C prior to counting the viable organisms.

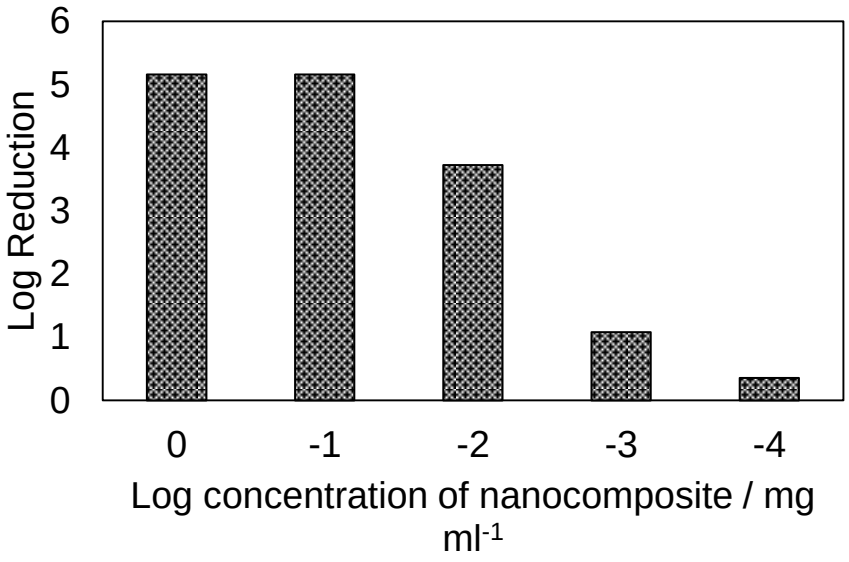

Figure 5.78 Logarithmic reductions for 0.3% Ag-SBA-15 at a range of concentrations after 24 hours.

The material studied was 0.3% Ag-SBA-15 (**figure 5.78**), so as to provide a lower limit for MBC of the SBA-15 based materials. At concentrations of 0.001 and below, the material falls below the 3-fold log reduction threshold which is the standard requirement for a sample to be considered an antibacterially active material.

5.2.2.2.3. Validity of neutralisation

In order to quantify the antibacterial activity of these materials as a function of time and correlate this to silver loading, a logarithmic reduction assay was required. This is a commonly used technique, involving adding a known number of microorganisms to the target material and determining the number of bacteria which are exterminated by plating out serial dilutions of the test solution at set time intervals. Due to the low concentrations of colonies required for counting purposes, serial dilution is required which can lead to possible inaccuracies during the process. It is for this reason that the samples are tested at least three times, for each time point.

Prior to performing a quantitative logarithmic reduction assay on these materials, a neutraliser was required which was able to render the silver materials incapable of killing the target organisms, allowing for a snapshot of antibacterial activity at the

desired time points. For this, a solution of STS was examined as described in **section 2.5.2.3**.

STS is a solution of 1% Tween20, 0.85% sodium chloride and 0.4% sodium thioglycolate. Sodium thioglycolate is known to neutralise silver due to the high affinity of silver for thiol moieties.[59, 60] The mechanism behind the antibacterial activity of silver is known to be connected with the interaction with thiol groups; silver ions and thiol groups in enzymes and proteins are a large part of the inactivation of said enzymes and proteins, leading to cell death.

The STS agent was effective in neutralising the antibacterial effects of the silver-silica materials, following 24 hours of contact, plus an incubation period, against both *P.aeruginosa* and *S.aureus*. The solution was therefore considered a viable option for the logarithmic reduction experiments.

5.2.2.2.4. Logarithmic reduction

Logarithmic reduction experiments allowed for a more quantitative representation of the synthesised materials and was performed as described in **section 2.5.4**. 10 mg of the each of the materials were agitated in a 1 ml solution of simulated body fluid and the target organism at 37^{o}C and samples removed at set intervals in order to determine the viable count of living organisms at that point and obtain the reduction of bacteria as a function of time.

Figure 5.79 displays the logarithmic reduction of viable cell count of *S.aureus* in the presence of silver loaded SBA-15 materials.

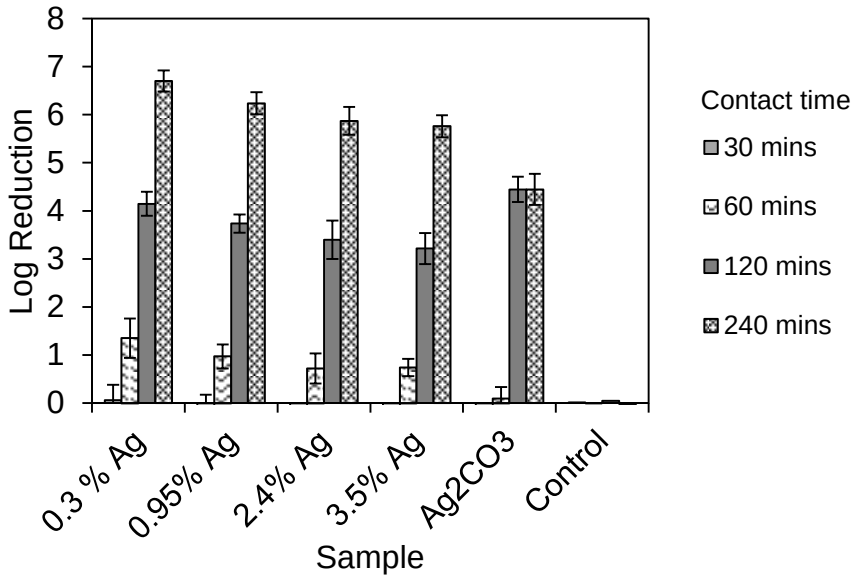

Figure 5.79: Logarithmic reduction of *Staphylococcus aureus* ATCC 6538 as a function of time in the presence of Ag-SBA-15, normalised to total silver content present.

There is an increasing antibacterial function with decreasing silver loading, when normalised to bulk silver content, which is consistent with the observed trends from silver ion dissolution profiles. This is an expected trend when considering that the silver ions are attributed with antibacterial functionality. The materials display a 3-fold log reduction in viable cell count within 2 hours of contact with the target organism, and all materials recorded a complete reduction in bacterial cells within 4 hours.

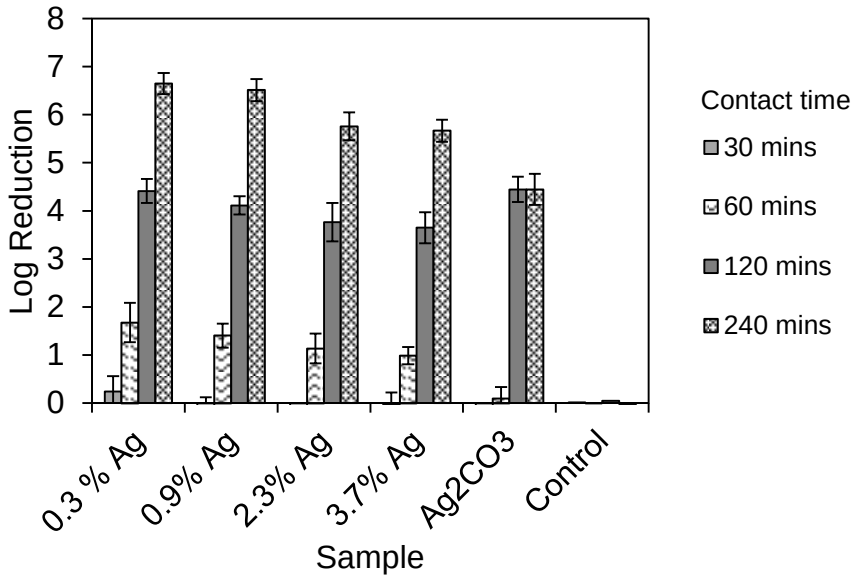

Figure 5.80: Logarithmic reduction of Staphylococcus aureus ATCC 6538 as a function of time in the presence of Ag-Ti-SBA-15, normalised to total silver content present.

Upon study of the logarithmic reductions for the silver loaded mesoporous titania grafted species (**figure 5.80**), we can observe a similar trend to that witnessed with the previous series. In this sample, however, there is a slight increase in the logarithmic reduction after 2 hours. Consideration of the silver dissolution profiles similarities, and the normalisation to bulk silver content, suggests the possibility of an enhanced antibacterial activity from the titania species. Titania has been shown to exhibit an antibacterial force of its own accord, due to the formation of core-hole species when excited by radiation of wavelengths of around 385 nm (UVA, band gap energy, $E_g \approx$ 3.2 eV) and below, meaning that the material can be activated somewhat in the presence of natural light.[61] This appearance of photochemically active species can perform oxidation reactions with cell components, such as coenzyme A, or produce reactive oxygen species which in themselves, can cause cell damage though redox reactions with prokaryotic and eukaryotic cells.[18, 61]

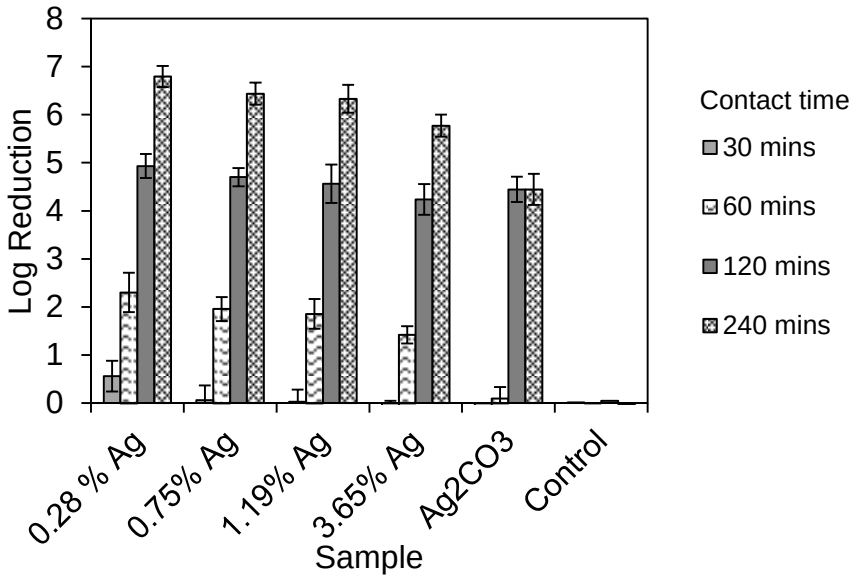

Figure 5.81: Logarithmic reduction of Staphylococcus aureus ATCC 6538 as a function of time in the presence of MM-Ag-Ti-SBA-15, normalised to total silver content present.

In **figure 5.81**, the logarithmic reduction function of silver loaded, titania coated, hierarchically porous silica based nanocomposites materials are presented. Further from the previous two profiles, it is evident that the identical trend is followed, with regards to increasing silver ion release resulting in an increase in cell morbidity. In the post 2 hour mark, interestingly, the log reduction of viable cell count displays an approximate 10-fold increase over the pure silica based materials. The possibility of an increasing silver release function resulting in an increase in antibacterial efficacy of this magnitude is present, however there also exists a prospect that this increase is also the result of the surface titania layer, with a more open and accessible structure, resulting from the introduction of macropores into the material, is enhancing the recorded bacterial morbidity function.

The viable count of the target organism reached a 3-fold reduction after 2 hours for all samples. For this reason, this data point was plot, normalised to total surface area of silver, calculated from average particle diameters determined by TEM analysis and mass of silver in the sample (**figure 5.82**).

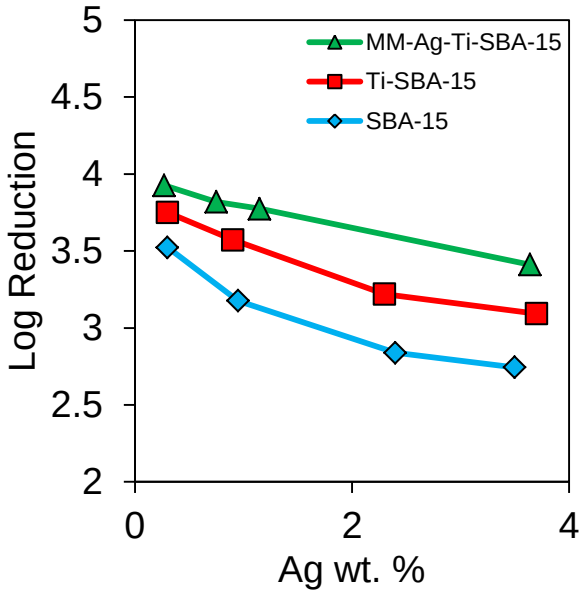

Figure 5.82: Logarithmic reductions after 120 minutes, normalised to total surface area.

It was decided to attempt to determine bactericidal effects arising from inorganic support species, and subsequent ROS generation or photocatalysed redox reactions, and distinguish them from the primary mode of action, silver ion release. In order to assess this, 10 mg of the three supports, with and without silver, were introduced to 1 ml solutions of *Staphylococcus aureus* in simulated body fluid solution, incubated for 2 hours at 37^{o}C, and the viable cell count recorded and logarithmic reduction determined (**figure 5.83**). As an additional point of interest, these materials were studied in the presence, and absence, of natural light.

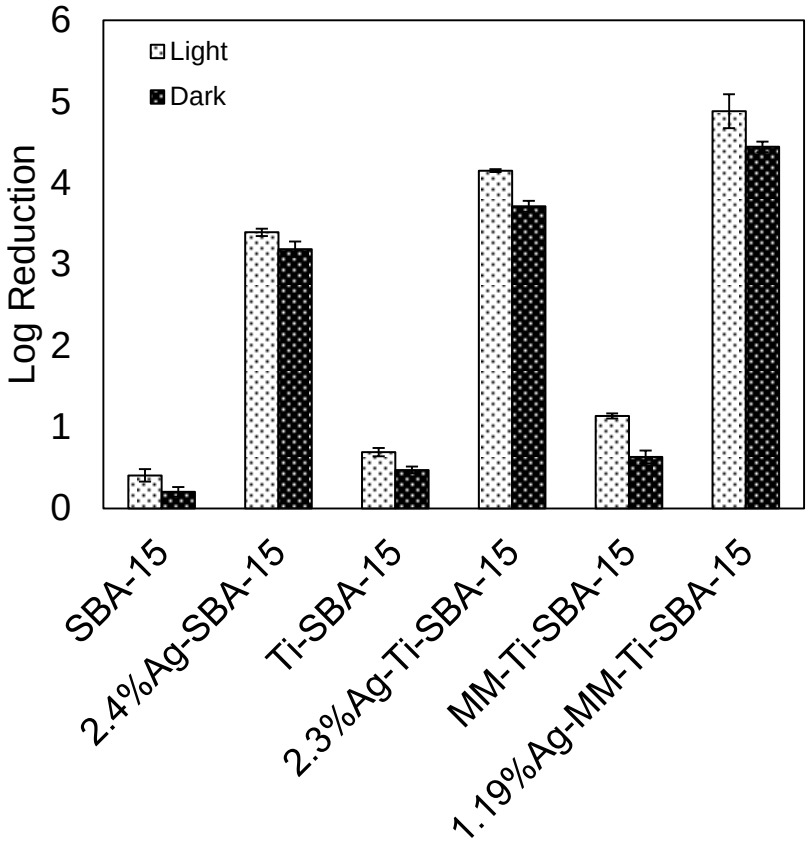

Figure 5.83: Logarithimic reduction of *Staphylococcus aureus*

It is observed in the recorded reduction functions for these materials, that there is indeed a small contribution towards antibacterial efficacy from the support materials developed. MM-Ti-SBA-15 exhibited more than a 10-fold decrease in viable cell count, when exposed to visible light, whilst the mesoporous material recorded slightly under a 10-fold reduction. These comparisons alone highlight the effect of the open macroporous structure and the advantageous nature of the subsequent nanostructured support. When compared with the pure SBA-15 material, the increase in antibacterial function indicates the secondary antibacterial function awarded to the grafted material by titania layer coverage. This trend can additionally be observed within the silver loaded species, wherein an increase in total logarithmic reduction, normalised to silver content, displays a similar increase in efficacy to those recorded by support materials alone.

A secondary point of interest within the results of these experiments, lies within the decrease in antibacterial function exhibited in the absence of a source of light. Upon

removal of electromagnetic radiation, the reduction in cell count is diminished, suggesting that the antibacterial strength follows suit. That there is witnessed a reduction in viable cells even in the absence of light could be attributed to a base formation of reactive oxygen species which, although enhanced by prhotocatalytic means in the presence of light, exists across all series as an intrinsic property of these materials in solution.[62] Additionally, oxide based support materials on the nanoscale have been found to exhibit cellular toxicity as a result of interference with, and damage of, cell membranes as a function of size and independent from ROS generation, suggesting materials in this size regime can disrupt cells and cause cell death.[63]

5.3. Conclusions

Mesoporous silica based materials were synthesised using an organic framework templating mechanism which is widely known and used within many materials chemistry associated fields. Further modification to these oxide supports was introduced in the form of macroporosity, enhancing the external surface area, and a grafted layer of titanium dioxide, believed to be in the form of anatase, introduced via sequential anhydrous grafting procedures. The produced layer of titania was found to be roughly 2.5 nm in thickness from nitrogen adsorption studies.

Silver particles were found to be deposited onto oxide based supports via a thermal treatment process with poor monodispersity, forming particulate silver over a large size range. The form of the silver was mainly silver metal, although contributions from silver carbonate, attributed to surface silver carbonate formation, were observed. Introduction of silver into the macroporous system allowed for a greater degree of monodispersity over the silver nanoparticle size regime, with a greater percentage of silver particles observed within the mesopore framework by electron micrography. Larger agglomerates of silver particles were observed as bulk loading increased, introducing a greater range of particle sizes and altering the dissolution kinetics.

To assess the suitability of these materials for application within the desired field, the materials were subjugated to a series of performance tests. The first of these was to study the silver ion release kinetics, and correlate them with determined particle

characteristics. The materials were observed to exhibit favourable silver release rates for lower bulk silver loadings, initially attributed to slight decreases in overall silver particle diameter. Upon normalisation of the dissolution profiles to calculated total surface areas, it became clear that these release kinetics were indeed affected by particle dispersion, as predicted. Silver carbonate species did not increase dissolution rates to any significant degree.

The materials antibacterial efficacy was determined via a series of microbiological assays, including zone of inhibition testing, which reported clear inhibition for all samples monitored, with a zone size dependant on silver loading. Minimum bactericidal concentration, determined for the least active material, reported that the material will exhibit antibacterial action beyond a 3-fold log reduction at concentration beginning between 0.01 and 0.001 mg/ml. Further quantitative analysis of the antibacterial action as a function of time indicated a silver loading dependant efficiency, favourable towards lower loadings, and hence smaller particles, as suggested by the results of the silver ion dissolution experiments. Further to this, effects outside and beyond the actions associated with silver ion release were studied, in order to determine advantageous performances from the synthesised support materials. From these studies, it was determined that the macroporous materials, with a surface grafted layer of titania, exhibited favourable antibacterial efficacy when compared to pure silica SBA-15 and titania enhanced mesoporous SBA-15, due to improved silver particle dispersities and hence silver ion release rates. The macroporous materials were also the most potent antibacterial agents in the absence of silver particles, recording over a ten-fold decrease in viable cell count in the presence of light.

5.4 References

1. J. J. Buckley, A. F. Lee, L. Olivi and K. Wilson, *Journal of Materials Chemistry*, 2010, **20**, 8056-8063.
2. J. J. Buckley, P. L. Gai, A. F. Lee, L. Olivi and K. Wilson, *Chemical Communications*, 2008, 4013-4015.
3. C. Kneuer, M. Sameti, E. G. Haltner, T. Schiestel, H. Schirra, H. Schmidt and C.-M. Lehr, *International journal of pharmaceutics*, 2000, **196**, 257-261.

4. A. Galarneau, H. Cambon, F. Di Renzo and F. Fajula, *Langmuir : the ACS journal of surfaces and colloids*, 2001, **17**, 8328-8335.

5. C. P. Vinod, K. Wilson and A. F. Lee, *Journal of Chemical Technology and Biotechnology*, 2011, **86**, 161-171.

6. J. Dhainaut, J.-P. Dacquin, A. F. Lee and K. Wilson, *Green Chemistry*, 2010, **12**, 296-303.

7. K. N. Rao, A. Sridhar, A. F. Lee, S. J. Tavener, N. A. Young and K. Wilson, *Green Chemistry*, 2006, **8**, 790-797.

8. A. M. Busuioc, V. Meynen, E. Beyers, P. Cool, N. Bilba and E. F. Vansant, *Catalysis Communications*, 2007, **8**, 527-530.

9. W. Wang and M. Song, *Microporous and Mesoporous Materials*, 2006, **96**, 255-261.

10. W. Wang and M. Song, *Materials Research Bulletin*, 2006, **41**, 436-447.

11. X. Chen, X. Cheng, A. H. Soeriyadi, S. M. Sagnella, X. Lu, J. A. Scott, S. B. Lowe, M. Kavallaris and J. J. Gooding, *Biomaterials Science*, 2014, **2**, 121-130.

12. I. I. Slowing, J. L. Vivero-Escoto, C.-W. Wu and V. S.-Y. Lin, *Advanced drug delivery reviews*, 2008, **60**, 1278-1288.

13. I. I. Slowing, B. G. Trewyn, S. Giri and V. Y. Lin, *Advanced Functional Materials*, 2007, **17**, 1225-1236.

14. J. Wei, J. Shi, H. Pan, W. Zhao, Q. Ye and Y. Shi, *Microporous and Mesoporous Materials*, 2008, **116**, 394-399.

15. S.-W. Song, K. Hidajat and S. Kawi, *Langmuir : the ACS journal of surfaces and colloids*, 2005, **21**, 9568-9575.

16. J. Dhainaut, J.-P. Dacquin, A. F. Lee and K. Wilson, *Green Chemistry*, 2010, **12**, 296-303.

17. J. Thiel, L. Pakstis, S. Buzby, M. Raffi, C. Ni, D. J. Pochan and S. I. Shah, *Small*, 2007, **3**, 799-803.

18. K. Page, R. G. Palgrave, I. P. Parkin, M. Wilson, S. L. P. Savin and A. V. Chadwick, *Journal of Materials Chemistry*, 2007, **17**, 95-104.

19. X. You, F. Chen, J. Zhang and M. Anpo, *Catal Lett*, 2005, **102**, 247-250.

20. C. W. Dunnill, K. Page, Z. A. Aiken, S. Noimark, G. Hyett, A. Kafizas, J. Pratten, M. Wilson and I. P. Parkin, *Journal of Photochemistry and Photobiology A: Chemistry*, 2011, **220**, 113-123.

21. L. A. Brook, P. Evans, H. A. Foster, M. E. Pemble, A. Steele, D. W. Sheel and H. M. Yates, *Journal of Photochemistry and Photobiology A: Chemistry*, 2007, **187**, 53-63.

22. T. Bala, G. Armstrong, F. Laffir and R. Thornton, *Journal of Colloid and Interface Science*, 2011, **356**, 395-403.

23. L. Zhao, H. Wang, K. Huo, L. Cui, W. Zhang, H. Ni, Y. Zhang, Z. Wu and P. K. Chu, *Biomaterials*, 2011, **32**, 5706-5716.

24. T. Matsunaga, R. Tomoda, T. Nakajima and H. Wake, *FEMS Microbiology Letters*, 1985, **29**, 211-214.

25. C. M. A. Parlett, D. W. Bruce, N. S. Hondow, M. A. Newton, A. F. Lee and K. Wilson, *ChemCatChem*, 2013, **5**, 939-950.

26. C. M. A. Parlett, D. W. Bruce, N. S. Hondow, A. F. Lee and K. Wilson, *ACS Catalysis*, 2011, **1**, 636-640.

27. D. Tian, G. Yong, Y. Dai, X. Yan and S. Liu, *Catal Lett*, 2009, **130**, 211-216.

28. M. Boutros, J.-M. Trichard and P. Da Costa, *Applied Catalysis B: Environmental*, 2009, **91**, 640-648.

29. A. Doadrio, E. Sousa, J. Doadrio, J. Pérez Pariente, I. Izquierdo-Barba and M. Vallet-Regı, *Journal of Controlled Release*, 2004, **97**, 125-132.

30. Z. Luan, M. Hartmann, D. Zhao, W. Zhou and L. Kevan, *Chemistry of materials*, 1999, **11**, 1621-1627.

31. M. B. Yue, Y. Chun, Y. Cao, X. Dong and J. H. Zhu, *Advanced Functional Materials*, 2006, **16**, 1717-1722.

32. S. Ruthstein, V. Frydman and D. Goldfarb, *The Journal of Physical Chemistry B*, 2004, **108**, 9016-9022.

33. S. Ruthstein, V. Frydman, S. Kababya, M. Landau and D. Goldfarb, *The Journal of Physical Chemistry B*, 2003, **107**, 1739-1748.

34. M. Impéror-Clerc, P. Davidson and A. Davidson, *Journal of the American Chemical Society*, 2000, **122**, 11925-11933.

35. P. Petrov, J. Yuan, K. Yoncheva, A. H. E. Müller and C. B. Tsvetanov, *The Journal of Physical Chemistry B*, 2008, **112**, 8879-8883.

36. D. Zhao, Q. Huo, J. Feng, B. F. Chmelka and G. D. Stucky, *Journal of the American Chemical Society*, 1998, **120**, 6024-6036.

37. J. Rouquerol, F. Rouquerol and K. S. Sing, *Adsorption by powders and porous solids*, Academic press, 1998.

38. H. W. Lu, S. H. Liu, X. L. Wang, X. F. Qian, J. Yin and Z. K. Zhu, *Materials Chemistry and Physics*, 2003, **81**, 104-107.

39. G. I. Waterhouse, G. A. Bowmaker and J. B. Metson, *Physical Chemistry Chemical Physics*, 2001, **3**, 3838-3845.

40. G. Dai, J. Yu and G. Liu, *The Journal of Physical Chemistry C*, 2012, **116**, 15519-15524.

41. C.-M. Yang, H.-A. Lin, B. Zibrowius, B. Spliethoff, F. Schüth, S.-C. Liou, M.-W. Chu and C.-H. Chen, *Chemistry of materials*, 2007, **19**, 3205-3211.

42. C. Parlett, D. W. Bruce, N. S. Hondow, M. A. Newton, A. F. Lee and K. Wilson, *ChemCatChem*, 2013, **5**, 939-950.

43. X. Nist, 1997.

44. A. M. Ferraria, A. P. Carapeto and A. M. Botelho do Rego, *Vacuum*, 2012, **86**, 1988-1991.

45. M. V. Landau, E. Dafa, M. L. Kaliya, T. Sen and M. Herskowitz, *Microporous and Mesoporous Materials*, 2001, **49**, 65-81.

46. X.-C. Guo and P. Dong, *Langmuir : the ACS journal of surfaces and colloids*, 1999, **15**, 5535-5540.

47. I. Georgiadou, N. Spanos, C. Papadopoulou, H. Matralis, C. Kordulis and A. Lycourghiotis, *Colloids and Surfaces A: Physicochemical and Engineering Aspects*, 1995, **98**, 155-165.

48. R. Castillo, B. Koch, P. Ruiz and B. Delmon, *Journal of Materials Chemistry*, 1994, **4**, 903-906.

49. G. Lassaletta, A. Fernandez, J. P. Espinos and A. R. Gonzalez-Elipe, *The Journal of Physical Chemistry*, 1995, **99**, 1484-1490.

50. R. Nyholm, N. Martensson, A. Lebugle and U. Axelsson, *Journal of Physics F: Metal Physics*, 1981, **11**, 1727.

51. C. M. A. Parlett, L. J. Durndell, A. Machado, G. Cibin, D. W. Bruce, N. S. Hondow, K. Wilson and A. F. Lee, *Catalysis Today*, 2014, **229**, 46-55.

52. A. Kirkland, D. Jefferson, D. Duff, P. Edwards, I. Gameson, B. Johnson and D. Smith, *Proceedings of the Royal Society of London. Series A: Mathematical and Physical Sciences*, 1993, **440**, 589-609.

53. A. Venezia, F. Liotta, G. Pantaleo, A. Beck, A. Horvath, O. Geszti, A. Kocsonya and L. Guczi, *Applied Catalysis A: General*, 2006, **310**, 114-121.

54. C. Xu, Y. Liu, B. Huang, H. Li, X. Qin, X. Zhang and Y. Dai, *Applied Surface Science*, 2011, **257**, 8732-8736.

55. T. L. Slager, B. J. Lindgren, A. J. Mallmann and R. G. Greenler, *The Journal of Physical Chemistry*, 1972, **76**, 940-943.

56. J. S. Hammond, S. W. Gaarenstroom and N. Winograd, *Analytical Chemistry*, 1975, **47**, 2193-2199.

57. Y.-J. Lee, J. Kim, J. Oh, S. Bae, S. Lee, I. S. Hong and S.-H. Kim, *Environmental Toxicology and Chemistry*, 2012, **31**, 155-159.

58. W. Zhang, Y. Yao, N. Sullivan and Y. Chen, *Environmental Science & Technology*, 2011, **45**, 4422-4428.

59. S. Y. Liau, D. C. Read, W. J. Pugh, J. R. Furr and A. D. Russell, *Letters in Applied Microbiology*, 1997, **25**, 279-283.

60. J. R. Furr, A. D. Russell, T. D. Turner and A. Andrews, *Journal of Hospital Infection*, 1994, **27**, 201-208.

61. H. A. Foster, I. B. Ditta, S. Varghese and A. Steele, *Applied microbiology and biotechnology*, 2011, **90**, 1847-1868.

62. V. Brezová, S. Gabčová, D. Dvoranová and A. Staško, *Journal of Photochemistry and Photobiology B: Biology*, 2005, **79**, 121-134.

63. K. Yu, C. Grabinski, A. Schrand, R. Murdock, W. Wang, B. Gu, J. Schlager and S. Hussain, *J Nanopart Res*, 2009, **11**, 15-24.

Chapter 6: Conclusions and Future Work

6. Conclusions and Future Work

6.1. Conclusions

Silver remains a widely used and key material in the fight against hospital acquired infections such as MRSA. While improvements in hygiene standards and prevention of patient cross contamination have led to a decrease in the number of reported HAIs in the UK, global infection rates are high, morbidity rates from HAIs increasing, and conventional antibiotic treatments are proving increasingly ineffective. New presentation formats of silver-containing functional materials with lower silver content (and hence reduced patient concern and environmental impact) yet superior bactericidal action, and easier clinical application, therefore remain in great demand.

Silver has been used as an antibacterial agent for centuries and has regained the interest of the scientific and medical communities recently due to the rise of these so-called ‘superbugs’. The use of silver carries the benefits of low toxicity at low concentrations, as well as the intrinsic ability to exhibit broad spectrum antimicrobial activity, with no bacterial resistance yet reported. Silver has therefore found use in many commercial wound dressings, and a protocol for controlling silver release to minimal levels and regulating this to a degree so as to extend activity lifetimes.

Silver-silica core shell devices, synthesised via a reverse micelle microreactor process, have shown admirable properties for these applications, possessing a wide array of tuneable properties in the form of monodisperse silver nanoparticle of adjustable diameter, adjustable silica shell thicknesses and the ability to enhance the intrinsic porosity within the silica matrix. From the nanocomposites materials, a slow and steady release of silver ions is released, through an oxidative dissolution process from the surface of silver nanoparticle cores, which suggest potential material lifetimes of the order of months. The composites exhibit a high degree of antimicrobial activity against two strains of bacteria, representing Gram-positive and Gram-negative organisms, in the form of *Staphylococcus aureus* and *Pseudomonas aeruginosa*. There appears to be some slight effect upon silver release rates with decreasing silver core size, likely due to higher silver surface areas being prevalent within smaller silver cored materials and this trend is reflected within the antimicrobial results. Furthermore, larger

silica shells retard silver release, slowing kill rates, attributed to inhibited diffusion through larger silica shells. Core-shell nanocomposites with the largest shells exhibited the slowest rate of silver release, but still achieved the industry target minimum of a three-fold log reduction (99.9 %) in viable bacterial cell count between 2 and 4 hours of contact time with target organisms. This suggests that the lifetime of these slow releasing silver ion delivery systems can indeed be increased through control over composite dimensions, with larger silica shells retarding silver release and conversely increasing operational lifetime, and yet maintain a high degree of antimicrobial activity.

A combination of thermal followed by base etching protocol using a PVP protecting agent designed to open intrinsic pores and enhance silver release rates and bacterial kill rates was unsuccessful in augmenting the antimicrobial efficacy or silver release rate from core-shell nanocomposites as hoped. Thermal treatment in the presence of PVP led to silver release rates improving alongside associated antibacterial performance, although base etching led to falling release rates and antibacterial performance, despite higher surface areas and increased surface silver visibility by XPS suggesting a decrease in silica network density.

Core-shell devices designed with intrinsic mesopores through the use of an organic template were also prepared. Silver metal nanoparticles were observed following a chemical reduction via hydrazine, which inhibited the formation of silver bromide. Aniline and formaldehyde were also explored as safer reductants, but both were unable to suppress silver bromide formation. Increasing the bulk silver loading had no effect upon the resultant size of silver nanoparticles, which were consistently around 15 nm, and hence enhanced release rates and antimicrobial activity solely reflected the silver content not morphology. A mesitylene porogen was utilised to enhance silver release and antibacterial function through increasing the diameter of mesopores within the silica shell. The resultant pore size, determined from porosimetry, increased linearly with mesitylene concentration up to 17 mM, affording an average pore diameter of 3.9 nm. Release rates and associated antimicrobial function of silver nanoparticle cores within these enlarged pore structures improved with pore diameter, indicative of accelerated silver ion diffusion as a consequence of a higher surface area of accessible silver.

Considering the two critical variables of silver loading and mesopore diameter, suggests that high silver loadings and attendant large mesopores should afford a

nanocomposite with a long lifetime (due to a large silver reservoir) and faster silver release rates due to increased exposure of surface silver. Stable core-shell composite structures with silver loading approaching 10 wt. %, were developed, which may offer significant advantages in terms of production costs compared with commercial antimicrobial additives. It is estimated that for a standard 40m batch of polyurethane foam wound dressing, the cost of materials for manufacture of these mesoporous core shell materials is roughly £150. Commercial products such as Reliameds silver alginate dressing and Smith and Nephews Acticoat range cost between an estimated £750 and £2400 for an equivalent amount of dressing, which would suggest these materials have market potential. Further to this, a much lower loading of silver can be afforded, due to retarded silver delivery, reducing leached silver ion concentration (as much as ~400 ppm after 10 days for Acticoat 7) into wound environments without compromising additive lifetime.

Dual-functional antimicrobials in the form of meso- and hierarchical silica-titania nanocomposites supports, loaded with silver nanoparticles through a wet impregnation method were prepared and the material properties assessed. These materials were compared to one another and it was concluded that macroporous, titania grafted mesoporous silica not only facilitates the production of smaller metal nanoparticles, which themselves exhibited superior silver release rates and antimicrobial functionalities, but also possess an inherent improvement in antimicrobial activity in the absence of loaded silver nanoparticles due to titania surface reactions, including ROS generation.

The nature of the produced silver particles was found to be strongly affected by the support material, with mesoporous silica structures favouring silver metal nanoparticles, while the more acidic titania supports promoted carbonate formation upon the surface of the silver nanoparticles, determined by XPS analysis. Hierarchically porous, titania grafted SBA-15 was observed to promote the formation of silver nanoparticles of the highest dispersity, forming the majority of particles below 10 nm for all materials, with an increasing number of agglomerates appearing in higher loadings. These materials were seen to exhibit the highest carbonate content, consistent with the assignment of carbonate as a surface species. This surface carbonate species was ultimately not found to affect silver ion release rates in any way, with metal and carbonate structures leaching silver ions at near identical rates. Average particle size of

the impregnated nanoparticles, however, was a major factor in silver release rates, with release kinetics of smaller particles observed to be vastly improved when compared with larger silver particles. This trend was also observed within the antibacterial studies, with smaller particles exhibiting higher effective antimicrobial kill rates.

6.2. Future Work

Incorporation of these materials into wound dressings, to ensure compatibility with polyurethane foam dressing production process and assess material functionality within commercial foams would be a vital process going forwards. Initial tests performed with an experimental set-up simulating foam production suggested the incorporation of all materials bore no significant detrimental effect on foam stability, which is positive going forwards that these materials can be included within the polymer foam network without damaging the excellent properties of the dressings which make them so attractive as wound care management systems.

With mesoporous core-shell devices possessing the greatest potential, considering ease of manufacture, lifetime, ability and cost, more research into these materials would be of great interest. Investigation of further tuning of material properties, such as eventual average silver core size could lend further control to silver release rates and minimise loaded silver content/material content within eventual commercial products. Additional functionality, in the form of adjusting the inorganic surrounding matrix of the shell is of great interest. It was seen in **Chapter 5**, that titanium dioxide surfaces enhance the antimicrobial activity of the produced materials, hence applying a surface layer of titania, or incorporating titanium dioxide into the shell or even replacing the entire shell with TiO_2 would make for an interesting materials and applications study for their use in the field of antimicrobials. Calcium phosphate based inorganic materials, such as hydroxyapatite, or Bioglass-type silica composites, also raise an interesting option for pursuit, with these mineral-incorporated silicas being more biocompatible and having been shown to aid wound healing rates.